2020

Raman Scattering, Synchrotron Terahertz/Far-Infrared Spectroscopic Investigation and Electrical Transport Properties of Aerographite and Single-Walled Carbon Nanotube Aerogel

Hao Zhang

University of Wollongong

UNIVERSITY
OF WOLLONGONG
AUSTRALIA

Raman Scattering, Synchrotron Terahertz/Far-Infrared Spectroscopic Investigation and Electrical Transport Properties of Aerographite and Single-Walled Carbon Nanotube Aerogel

Hao Zhang
B. Eng., M. Sc.

Supervisors:
Associate Professor Joseph Horvat
Senior Professor Roger A. Lewis
James M. Skinner Professor of Science Arjun G. Yodh (University of Pennsylvania)

This thesis is presented as part of the requirements for the conferral of the degree:
Doctor of Philosophy

This research has been conducted with the support of

a University Postgraduate Award and an International Postgraduate Tuition Award

University of Wollongong

Faculty of Engineering and Information Sciences

School of Physics and Institute for Superconducting and Electronic Materials

March 2020

“When you are face to face with a difficulty, you are up against a discovery.”

— **Lord Kelvin (William Thomson)**
Scottish mathematical physicist and engineer

Abstract

The body of this thesis comprises seven chapters, including four research chapters (Chapters 3–6) which are preceded by a chapter of background and a chapter of physical principles of experimental techniques and are followed by a concluding chapter which provides a perspective that contextualizes all of this submitted work.

The first substantive part of this thesis consists of Chapter 3. This detailed work is concerned with Raman spectra of Aerographite, graphite oxide, kish graphite and graphite flakes, investigated with different laser excitation energies. The Raman spectra all exhibit the typical graphitic features of the G, D, D′ and 2D bands. The D and 2D bands show a "blue-shift" with laser excitation energy, E_L, while the G bands are invariant. The dependence of the intensity ratio I_D/I_G on λ_L^4 is linear for graphite flakes and kish graphite, while it saturates at the longest λ_L for Aerographite and graphite oxide. An explanation of this unexpected behavior is sought within the double resonant Raman scattering model, considering the disorder-induced broadening of peaks in the phonon density of states.

The second part of this thesis appears in Chapter 4. This is concerned with the investigation of the temperature dependence of synchrotron THz/Far-IR and Raman scattering spectra of Aerographite and SWCNT aerogel. Specifically, the THz/Far-IR spectra were acquired in the energy range of 7–1000 cm^{-1} from 6–300 K. Raman spectra were measured in the frequency range of 100–4000 cm^{-1} using a 514 nm laser over the temperature range 80–300 K. The positions of the main Raman features (D and G) in both Aerographite and SWCNT aerogel display the behavior of "red-shifting" with increasing temperature. This is attributed to the C-C bond stretching, which is due to thermal expansion of the lattice and anharmonic couplings of phonon modes. The 2D peak of both Aerographite and SWCNT aerogel shows a "blue-shifting" effect with increasing temperature. The explanation of this is proposed to be either through an increase of the distance between covalently bonded C structures and related charge redistribution, or through the double resonant Raman scattering mechanism. In addition, multiple low frequency Raman peaks (that is, in the THz region) are also identified and assigned.

The third part of this thesis comprises Chapter 5. This details the temperature dependent electrical transport properties of Aerographite and SWCNT aerogel over the temperature range 2–300 K with different magnetic field strengths (in the range 0–9 T, in steps of 2 T). The experimental results show that the resistance falls as the temperature increases as an exponential function. Such strong temperature dependence is characteristic of some form of hopping or tunneling conduction behavior. Two physical models, fluctuation-induced tunneling conduction (FITC) and variable range hopping (VRH), are employed to explicate the possible electrical conduction mechanisms occurring in Aerographite and SWCNT aerogel, respectively. It is found that structural disorder and the charge carrier density of electrons, which are modified by their structural symmetries and electronic band structures, both play important roles in the temperature dependent electrical transport properties of Aerographite and SWCNT aerogel.

The fourth and final part of this thesis appears in Chapter 6. This details an investigation on designing a novel double-network hydrogel network. The basis is of PDOPA–PAM hydrogel which exhibits autonomous self-healing properties. This is then infiltrated with SWCNT hydrogel precursor. The result is a L-DOPA-PAM-SWCNT hydrogel hybrid network. The double-network hydrogel has improved mechanical robustness and electrical properties which exhibit sensitivity to pressure. The piezoresistive effect of the resultant L-DOPA-PAM hydrogel was studied under ambient conditions. A physical explanation is proposed to describe the observed pressure- and time-sensitive electrical properties of the L-DOPA-PAM hydrogel. It is suggested the dominant mechanisms responsible for the remarkable pressure- and time- sensitivities are a combination of polymer creep and the quantum tunneling effect.

Acknowledgments

I would like to express my gratitude for all the help that I received during my PhD journey. Without it, I would not have reached this point in a challenging but memorable experience in my life.

First, I wish to express my sincere appreciation to my respective PhD supervisors in the School of Physics and the Institute for Superconducting and Electronic Materials (ISEM) at the University of Wollongong (UOW), Associate Professor Joseph Horvat and Senior Professor Roger A. Lewis for their excellent supervision, encouragement, and guidance. They provided me with a precious opportunity to pursue my PhD degree in the fascinating fields of Terahertz Science and Condensed Matter Physics. Their patience, enthusiasm, and encouragement gave me the energy to overcome the difficulties encountered in my research. Thanks, Joseph and Roger, for giving me the freedom to pursue what I wish to do!

Secondly, I would like to thank my PhD associate supervisor, the James M. Skinner Professor of Science, Arjun G. Yodh, who is in the Department of Physics and Astronomy and the Laboratory for Research on the Structure of Matter (LRSM) at the University of Pennsylvania (UPenn), USA. I also should thank Professor Mohammad F. Islam from the Department of Materials and Engineering, Carnegie Mellon University, USA. Thanks, Arjun and Mohammad, for introducing me into the area of Soft Matter and Soft Nanomaterials and providing me with powerful support!

Thirdly, I thank the National Computational Infrastructure (NCI, Australia) and Senior Professor Chao Zhang (UOW) to kindly provide high-performance computing resources, and my fellow group members in the Terahertz Science and Solid State Physics group in the School of Physics and the ISEM, UOW, and the Soft Matter group in the Department of Physics and Astronomy and the LRSM, UPenn, including Mr. Jie Tian (Data analysis, UOW), Mr. Mohanad Mohammed (PPMS, UOW), Dr. Julian Steele (Raman Spectroscopy, UOW), Dr. Andrew Squires (THz-TDS, UOW), Mr. Sunchao Huang (Data Analysis, UOW), Mr. John Mabon (THz-TDS, UOW), Mr. Jarrod Colla (FTIR Spectroscopy, UOW), Ms. Nana Liu (AFM, UOW), and Dr. Chandan Mishra (Optical Microscope, UPenn) for all their advice and support. I would also like to thank Dr. Tania Silver (UOW) for her critical reading of my PhD thesis.

I also wish to thank our collaborator-Prof. Yogendra Mishra, who is in the Institute for Materials Science, Christian-Albrecht University of Kiel, Germany, for providing his excellent samples of Aerographite. I also need to acknowledge the professional assistance that I received from staff and technicians, including Dr. Dominique Appadoo (THz/Far-IR Beamline, Australian Synchrotron), Dr. Anne Rich (Raman Spectroscopy, Mark Wainwright Analytical Centre, University of New South Wales), Dr. Matthew Brukman (THz Raman Spectroscopy, Singh Center for Nanotechnology, UPenn), Dr. Sepidar Sayyar (DMA, UOW), Mr. Steve Szewczyk (DMA, UPenn), Mr. Tony Romeo (FE-SEM, UOW), Mr. Martin Morillas (Laboratory and Workshop Assistance, UOW) and Mr. Peter Ihnat (Laboratory Assistance, UOW).

To my all friends in China, Australia and USA, thanks for sharing happiness and kind help, especially Mr. Geng Li (Lenovo), for the high-performance computing support. I should take this opportunity to thank the University of Wollongong for its financial support of my PhD studies via a University Postgraduate Award (UPA) and an International Postgraduate Tuition Award (IPTA), as well as the Australian Synchrotron Research Program (AS181/THz/Far/IR/13120).

Finally, I owe gratitude to my parents, Mrs. Xin-Lin Fan and Mr. Chong-Neng Zhang, who have been standing by me and encouraging me to pursue my dreams all the time! My greatest thanks must be delivered to my wife, Dr. Qiao Yan. I thank you for your deepest love, unconditional support, and for our mutual inspiration! Your passion for science and life enabled me to go ahead even further! All my achievements really belong to both of us.

Certification

I, Hao Zhang, declare that this thesis submitted in fulfilment of the requirements for the conferral of the degree of Doctor of Philosophy, from the University of Wollongong, is wholly my own work unless otherwise referenced or acknowledged. This document has not been submitted for qualifications at any other academic institution.

_____

Hao Zhang

27th March 2020

List of Abbreviations

AFM	Atomic force microscope
ATR	Attenuated total reflection
BS	Beam splitter
CCD	Charge-coupled device
CDF	Cumulative distribution function
CVD	Chemical vapor deposition
CW	Continuous wave
DAST	Diethylaminosulfurtetrafluoride
DFG	Different frequency generation
DFT	Density function theory
DMA	Dynamic mechanical analysis
DOPA	3,4-dihydroxyphenyl-L-alanine
DOS	Density of states
DR	Double resonance
DTGS	Deuterium tryglycine sulfate
EDA	Ethylenediamine
EO	Electro-optic
EPC	Electron-phonon coupling
ETO	Electrical transport option
FELs	Free electron lasers
FE-SEM	Field emission scanning electron microscope
FFT	Fast-Fourier transform
FITC	Fluctuation-induced tunneling conduction
FT	Fourier transformation
FTIR	Fourier transform infrared spectroscopy
FTS	Flame transport synthesis
FWHM	Full width at half maximum
FWM	Four-wave mixing
HOPG	Highly oriented pyrolytic graphite
HPHT	High pressure, high temperature
HWP	Half-wave plate
IR	Infrared
iTO	In-plane transverse-optical
KA	Kohn anomaly
K-K	Kramers-Kronig
L-B	Landauer-Büttiker
LBM	Layer breathing mode
L-DOPA	3,4-Dihydroxy-L-phenylalanine

LO	Longitudinal optical
MCT	Mercury cadmium telluride
MEMS	Microelectromechanical system
MWCNT	Multi-walled carbon nanotube
N.A.	Numerical aperture
NLO	Nonlinear optics
OD	Optical density
PAM	Polyacrylamide
PAMPS	Poly (2-acrylamido, 2-methyl, 1-propanesulfonic acid
PC	Photoconductive
PDOPA	Polydopamine
PDOS	Phonon density of states
PET	Polyethylene terephthalate
PPMS	Physical properties measurement system
PXRD	Powder X-ray diffraction
PVA	Polyvinyl alcohol
PVB	Polyvinyl butyral
QPM	Quasi-phase-matching
RBM	Radial breathing mode
SDBS	Sodium dodecylbenzene sulfonate
SEM	Scanning electron microscope
SNR	Signal to noise ratio
SSA	Specific surface area
SWCNT	Single-walled carbon nanotube
TES	THz emission spectroscopy
TEM	Transmission electron microscope
THz	Terahertz
THz-QCLs	THz-Quantum cascade lasers
THz-TDS	THz time-domain spectroscopy
TO	Transverse optical
TPO	THz parametric oscillator
TPX	Polymethylpentene
TRTS	Time-resolved THz spectroscopy
TTO	Thermal transport option
UCF	Universal conductance fluctuation
UV	Ultraviolet
VRH	Variable range hopping
XRD	X-ray diffraction

Table of Contents

Abstract **2**

1 Background **20**

1.1 Outline of Thesis 20

1.2 Aerogels 21

1.2.1 Overview of Aerogels 21

1.2.2 Physical and Chemical Properties 22

1.3 Carbon Aerogels 23

1.3.1 Aerographite (Graphite Aerogel) 23

1.3.2 Graphene and Graphene-inspired Aerogel 24

1.3.3 Carbon Nanotube Aerogel 24

1.3.4 Nanodiamond Aerogel 25

1.4 Terahertz Techniques 26

1.4.1 Terahertz Radiation in the Electromagnetic Spectrum 26

1.4.2 Synchrotron Radiation as a THz Source Based on Relativistic Electrons 27

1.4.3 Terahertz Detection 27

1.4.3.1 Photoconductive Antenna 28

1.4.3.2 Electro-optic Sampling 28

1.4.3.3 Thermal Detectors 28

1.4.4 Terahertz Spectroscopy 29

2 Physical Principles of Experimental Techniques **31**

2.1 Terahertz Spectroscopy of Condensed Matter 31

2.1.1 Physical Phenomena in Electronic Materials in the THz Region 31

2.1.2 Absorption and Dispersion 32

2.2 Phonon Modes and Symmetry 33

2.2.1 Phonons and Phonon Modes 33

2.2.2 Infrared and Raman Activity 34

2.2.3 Selection Rules 35

2.2.4 Phonon Modes in sp^2 Carbon Materials 36

2.2.5 Phonon Dispersion of sp^2 Carbon Materials 38

2.2.6 Raman Spectroscopy of sp^2 Carbon Materials 39

2.2.7 Double Resonant Raman Scattering Process 41

2.3 Quantum Transport in Mesoscopic Systems 42

2.3.1 Temperature Dependence of the Electrical Conductivity 42

2.3.2 Quantum Tunneling 43

2.3.2.1 Barrier Transmission and Tunneling 43

2.3.3 Hopping Conduction 44
2.3.3.1 Hopping Probabilities 44
2.3.3.2 Variable Range Hopping Conduction 45
2.3.4 Landauer-Büttiker Formula 47
2.4 Experimental Methods 48
2.4.1 Fourier Transform Infrared Spectroscopy 48
2.4.2 THz/Far-IR Beamline of the Australian Synchrotron 49
2.4.3 Raman Spectroscopy 51
2.4.4 Physical Properties Measurement System 52
2.4.5 X-ray Diffraction 55
2.4.6 Field Emission Scanning Electron Microscope 56
2.4.7 Atomic Force Microscope 56
2.4.8 Dynamic Mechanical Analysis 57
2.4.9 Uncertainty of Measurements 58

3 Double Resonant Raman Scattering and Disorder-induced Band Dispersion for Aerographite and Graphitic Systems at Different Excitation Energies 59
3.1 Introduction 59
3.2 Experimental Details 60
3.2.1 Sample Preparation 60
3.2.2 Sample Characterization 60
3.3 Results and Discussion 61
3.3.1 Field Emission Scanning Electron Microscope 61
3.3.2 X-ray Diffraction 61
3.3.3 Raman Scattering Spectra 63
3.3.4 Analysis of Raman Spectra by Peak Fitting and Deconvolution 67
3.3.5 Quantifying Analysis of Defects and Disorder via Raman Spectra Reported for Ion Bombardment sp^2 Carbon Systems 73
3.3.6 Analysis of Laser Excitation Energy Dependence of I_D/I_G for Aerographite 74
3.4 Conclusion 82

4 Temperature Dependent Synchrotron Terahertz/Far-Infrared and Raman Scattering Spectral Studies of Aerographite and Single-Walled Carbon Nanotube Aerogel 84
4.1 Introduction 84
4.2 Experimental Details 85
4.2.1 Materials Preparation 85
4.2.2 Measurements of Spectra 86
4.3 Results and Analysis 87
4.3.1 IR and Raman Phonon Activity Overview for Graphite and SWCNTs

.....87
4.3.2 THz/Far-IR Spectra 88
4.3.3 Raman Spectra 95
4.3.3.1 Aerographite 95
4.3.3.2 SWCNT Aerogel 96
4.3.4 Temperature Dependence of Raman and Synchrotron THz/Far-IR Spectra 97
4.3.4.1 Temperature Dependence of Raman Spectra 98
4.3.4.2 Temperature Dependence of Synchrotron THz/Far-IR Spectra ..102
4.4 Discussion on Synchrotron THz/Far-IR and Raman Spectra.....103
4.4.1 Activation of New IR Bands by Disorder and Defects in Aerographite and SWCNT Aerogel 103
4.4.2 van der Waals Force for Thermal Expansion of Aerographite and SWCNT Aerogel 105
4.5 THz Raman Spectra of Graphite Flakes and SWCNT Aerogel……. 106
4.6 Conclusion.....109

5 Temperature Dependent Electrical Transport Properties of Aerographite and Single-Walled Carbon Nanotubes Aerogel 111
5.1 Introduction 111
5.2 Physical Models 112
5.2.1 Fluctuation-induced Tunneling Conduction Model 112
5.2.2 Variable-range Hopping Model.....113
5.2.3 Percolation Theory 114
5.3 Experimental Details 116
5.3.1 Sample Preparation.....116
5.3.2 Structural and Morphological Characterization 116
5.3.3 Temperature Dependent Resistance Measurements 118
5.4 Discussion of Results 123
5.4.1 Fluctuation-induced Tunneling Conduction Model for Aerographite…… 124
5.4.2 Variable-range Hopping Model for SWCNT Aerogel 125
5.5 Conclusion.....128

6 Self-healing and Piezoresistive Properties of Polydopamine-based Single-Walled Carbon Nanotube Hydrogel Hybrid Network 130
6.1 Introduction 130
6.1.1 Sol-Gel Transition 131
6.1.2 Classes of Gel 131
6.1.3 Hydrogels 131
6.1.4 Mussel-inspired Hydrogels: Cross-linked Network Precursor.....132

6.2 Principle and Methodology 133
6.2.1 Metal-catecholate Complexes with SWCNT Hydrogel 133
6.3 Catechol-functionalized Precursor with SWCNT Hydrogel 136
6.3.1 Chemicals and Materials Synthesis 137
6.3.2 Reaction Mechanism of L-DOPA-PAM Hydrogel 137
6.3.3 Synthesis of L-DOPA-PAM-SWCNT Hydrogel Hybrid Network 137
6.4 Characterization of Obtained Samples 139
6.4.1 Optical Microscopy 139
6.4.2 Raman Spectroscopy 140
6.4.3 Dynamic Mechanical Properties (Rheology)-Compression Test 141
6.4.4 Piezoresistive Effect 143
6.5 Conclusion 147

7 Conclusion and Outlook 148
7.1 Conclusion 148
7.2 Outlook 149

References 151

Appendix 1: List of Publications 179

Appendix 2: MATLAB Code for FTIC and VRH Fittings 181

List of Tables

1.1 A brief summary of the differences between THz-TDS, FTIR and Raman spectroscopy…… 30

1.2 The detailed comparison between the THz-TDS and FTIR systems…….30

2.1 Frequency of a photon of Boltzmann energy at different temperatures…….31

2.2 IR activity of phonon modes in polar and non-polar solids……...35

2.3 Raman active and IR active modes of carbon nanotubes……...…38

3.1 Raman band positions of graphitic materials by different photon energies from 1.96 eV to 2.81 eV……..……...65

3.2 Spectral parameters obtained from the single-peak fitting of Raman spectra of Aerographite…….69

4.1 Assignments and frequency behavior for Raman modes of SWCNT aerogel……..….97

4.2 Assignments for the THz Raman modes of SWCNT aerogel…….…….109

5.1 Values of fitting parameters obtained from applying the FITC model to Aerographite……..119

5.2 Values of Fitting parameters obtained from applying the VRH model to SWCNT Aerogel..121

List of Figures

1.1 (a) Aerogel in hand; (b) a brick supported on an aerogel block with excellent mechanical properties [4] ……...…...……21

1.2 The differences between a sol, a gel, and an aerogel [6] ……...…....22

1.3 TEM image of Aerographite - with its fine mesh structure [14] ……...24

1.4 SEM and TEM images of SWCNT aerogel [17] ...……...25

1.5 The THz band in the electromagnetic spectrum [25] ……26

1.6 (a) Electron beam travelling through a magnet emitting synchrotron radiation collected at the beam line detector. (b) An electron travelling in an arc “sees” an electrical field pulse. (c) Power spectrum given by Fourier transform of electrical field pulse. (d) The THz/Far-IR Hutch at the Australian Synchrotron [29] ……27

1.7 The operation principle of a bolometer. (a) Schematic diagram of a bolometer [21]. (b) A liquid helium cooled silicon bolometer……29

2.1 The Lorentzian oscillator model [22] ……....32

2.2 Dispersion curves for the acoustic and optical phonon branches [44] ……..….34

2.3 The phonon modes in 3D graphite at zone center [48] ……36

2.4 Three types of SWCNTs: (a) “armchair”; (b) “zig-zag”; and (c) “chiral” [46] ……....37

2.5 Phonon dispersion curves in graphite and graphene [47,52] ...…….....….....39

2.6 The Double resonant Raman scattering process [61] ……...41

2.7 Schematic illustration of a FTIR Spectrometer [82] ……..……...49

2.8 The Brüker IFS125HR FTIR spectrometer at the Australian Synchrotron…….…….…..50

2.9 Optical scheme of the Brüker IFS125HR FTIR spectrometer [83] ……..……50

2.10 Schematic illustration of the closed-loop cryostat [84] ……..51

2.11 The Renishaw inViaTM Raman microscope……...52

2.12 The Quantum Design PPMS DynaCool™ System…….…….53

2.13 The cryostat control system, the chamber temperature control system, and the magnetic field control system [86] …….…….53

2.14 (a) Sample pucks for different measurements; sample mounted on pucks which are inserted in the sample chamber [86] …...……...54

2.15 (a) PPMS probe; (b) PPMS probe which is inserted in the sample chamber [86]...……54

2.16 (a) Schematic diagram of a four-wire probe circuit; (b) Equivalent circuit diagram of a four-wire probe [86]…….54

2.17 The GBC Powder X-ray Diffractometer.....56

2.18 The FE-SEM (JSM 7500FA) ……..…….56

2.19 The MFP-3D™ AFM...……57

2.20 The physical principle of DMA measurement [90]...……...57

2.21 The DMA 242 E Artemis.……58

3.1 FE-SEM Images of Aerographite……...…..…..……...……...…61

3.2 XRD Spectra of Aerographite and Graphitic Materials…….62

3.3 Raman Spectra of Graphitic Materials Excited by Different Photon Energies from 1.96 eV to 2.81 eV……..……...64

3.4 Raman Spectra of Aerographite Excited by Different Photon Energies from 1.96 eV to 2.81 eV…….……65

3.5 Peak Positions of the D and 2D Bands as a Function of Laser Excitation Energies of Aerographite ……67

3.6 Peak Fitting for Raman Spectra of Aerographite by Different Photon Energies from 1.96 eV to

2.81 eV……68

3.7 Peak Fitting for Raman Spectra of Graphitic Materials by Different Photon Energies from 1.96 eV to 2.81 eV……..70-72

3.8 I_D/I_G of Aerographite as a Function of Laser Wavelengths, as Measured at Different Spots on the Sample.……...75

3.9 I_D/I_G of Aerographite and Graphitic Materials as a Function of Four Power of Laser Excitation Wavelengths.……75

3.10 Dependence of I_D/I_G on Laser Wavelength for Kish Graphite and Graphite Flakes……..…….……..……...……...……..…...……...…….76

3.11 Dependence of I_D/I_G on Laser Wavelength for Aerographite and Graphite Oxide...……...76

3.12 C_A as a Function of E_L of Aerographite……78

3.13 Peak Positions of the G and D Bands as a Function of Excitation Energy for Aerographite, Graphite Flakes, graphite Oxide and Kish Graphite……78

3.14 Schematic Diagram of Double Resonant Raman Scattering…….……..…….….79

3.15 Schematic Diagram of Double Resonant Raman Scattering with Electron Defect States…...80

3.16 PDOS of Ideal Graphite and Graphite with Point Defects from 1200-1650 cm^{-1}...……..…82

4.1 Optical Images of Aerographite and SWCNT Aerogel…….…….……...86

4.2 Synchrotron THz/Far-IR Raw Spectra of Aerographite on a Log-Scale at Various Temperature, from 6 K to 300 K…...……..…….....89

4.3 Synchrotron THz/Far-IR Raw Spectra of SWCNT Aerogel on a Log-Scale at Various Temperature, from 6 K to 300 K……...…...89

4.4 THz/Far-IR Transmittance Spectra of Aerographite from 30–200 cm^{-1} at Various Temperature, from 6 K to 300 K……...…….91

4.5 THz/Far-IR Transmittance Spectra of Aerographite from 90–300 cm^{-1} at Various Temperature, from 6 K to 300 K……..…….....91

4.6 THz/Far-IR Transmittance Spectra of Aerographite from 400–700 cm^{-1} at Various Temperature, from 6 K to 300 K……..……92

4.7 THz/Far-IR Transmittance Spectra of Aerographite from 800–1000 cm^{-1} at Various Temperature, from 6 K to 300 K……..……..……..92

4.8 THz/Far-IR Transmittance Spectra of SWCNT Aerogel from 30–200 cm^{-1} at Various Temperature, from 6 K to 300 K……...……...93

4.9 THz/Far-IR Transmittance Spectra of SWCNT Aerogel from 90–300 cm^{-1} at Various Temperature, from 6 K to 300 K……..……..…...…93

4.10 THz/Far-IR Transmittance Spectra of SWCNT Aerogel from 400–750 cm^{-1} at Various Temperature, from 6 K to 300 K……..….....94

4.11 THz/Far-IR Transmittance Spectra of SWCNT Aerogel from 800–1000 cm^{-1} at Various Temperature, from 6 K to 300 K……...…….....….94

4.12 Raman Spectra of Aerographite at 514 nm Laser Excitation…….……...…...95

4.13 Raman Spectra of SWCNT Aerogel at 514 nm Laser Excitation…….……...……96

4.14 Raman Spectra for Aerographite under a Laser Excitation at 514 nm at Various Temperatures, from 80 K to 300K…….…….....99

4.15 Raman Spectra for SWCNT Aerogel under a Laser Excitation at 514 nm at Various Temperatures, from 80 K to 300K……..……..……99

4.16 Temperature Dependent Evolution of Raman Peak Positions of Aerographite from 80–300 K……...…..100

4.17 Temperature Dependent Evolution of Raman Peak Positions of SWCNT Aerogel from 80–300 K……..….101,101

4.18 Synchrotron THz/Far-IR Peak Positions of Aerographite and SWCNT Aerogel vs. Temperature from 6–300 K……...…….…....103

4.19 THz Raman Spectra of Graphite Flakes and SWCNT Aerogel…….…....107

5.1 FE-SEM Images of Aerographite…….……117

5.2 FE-SEM Images of SWCNT Aerogel…….…….117

5.3 Temperature dependent resistance of Aerographite with different magnetic field strengths from 2–300 K in the “No Overshoot” temperature approach mode……...…….118,119

5.4 Temperature dependent resistance of SWCNT aerogel with different magnetic field strengths from 2–300 K in the “No Overshoot” temperature approach mode…….....120

5.5 (a) The *I-V* characteristics curve of Aerographite with different magnetic field strengths at different temperatures. (b) The *I-V* characteristics of SWCNT aerogel with different magnetic field strengths at different temperatures……...122,123

5.6 (a) Schematic illustration for the insulating junction between two conducting segments (shaded areas) with the effective area A for the tunnel process and separation *w*, which may be regarded as a parallel-plate capacitor. (b) Schematic representation of the parabolic potential barrier of height V_0 and width w between two conducting segments. The dashed lines denote the corresponding rectangular barrier…….…….124

5.7 Tapping mode AFM image of SWCNT on a silicon surface. The SWCNTs suspension was prepared at 0.1 mg/mL by the tip sonicator……...……...…126

6.1 The chemical structure of protein bound DOPA containing the catechol side chain……...132

6.2 Designed chelation chemical structures based on different functional groups targeted to self-healing properties. (a) PEO/PEG backbone, pendent with catechol unit, o-Phenylenediamine, (S)-(-)-1,1′-Bi(2-naphthol) and (R)-(+)1,1′-Bi(2-naphthol) via chelation reactions; (b) PAM backbone, pendent with catechol unit, o-Phenylenediamine, (S)-(-)-1,1′-Bi(2-naphthol) and (R)-(+)1,1′-Bi(2-naphthol) via chelation reactions……134

6.3 Metal-catechol coordination polymer networks precursor. Metal ions cross-linkers were used to establish different polymer networks with color changes. (a) Dynamic metal–catechol coordination complexes explored as polymer crosslinks; (b) Sample preparation protocol……..135

6.4 Images of PEO-catechol-Co^{2+} hydrogel undergo self-healing after physical damage. (a) and (b) Finger printing on the sample, which will disappear without external influence after 2 hours; (c) and (d) Physical damage (knife wound) on the sample, which will repair without external actuation after 2 hours……136

6.5 Synthetic process and reaction mechanism of the L-DOPA–PAM hydrogel…….…….137

6.6 Synthetic process and reaction mechanism of L-DOPA-PAM-SWCNT hydrogel hybrid network……...138

6.7 Synthetic process of L-DOPA-PAM-SWCNT hydrogel hybrid network……139

6.8 Optical microscopy images of L-PDOPA-PAM hydrogel. (a) reference: colloid particles, d = 4 micron; (b) Leica DMRX optical microscopy 10x lens; (c) and (d) Zeiss Axiovert 135 optical microscopy of L-PDOPA-PAM hydrogel using 100x lens with immersion oil……....140

6.9 Raman spectra of L-DOPA-PAM-SWCNT hydrogel hybrid network and SWCNT aerogel.141

6.10 Frequency dependent modulus of L-DOPA-PAM-SWCNT hydrogel hybrid network…....142

6.11 tan δ curves of L-DOPA-PAM-SWCNT hydrogel hybrid network…….…….143

6.12 Electrical resistance as a function of pressure and time of L-DOPA–PAM hydrogel ..……..…….145

6.13 Electrical resistance as a function of pressure of L-DOPA–PAM hydrogel ……....146

6.14 Electrical resistance vs. pressure of L-DOPA–PAM hydrogel measuring at 40s with error bars……....147

Chapter 1

Background

1.1 Outline of Thesis

Chapter 1 introduces background information on carbon aerogels and THz techniques. In the Chapters 3 to 5, Raman scattering results of Aerographite and graphitic materials at different excitation energies, synchrotron THz/Far-IR and temperature dependent Raman scattering spectral studies, and electrical transport properties of Aerographite and SWCNT aerogel are presented, respectively. Application work related to the novel polymer and SWCNT hydrogel network, and is electrical and mechanical properties, are reported in Chapter 6.

Chapter 2 explains the physical principles of experimental techniques, covering physical phenomena of electronic materials in the THz region, phonon modes of sp^2 carbon materials, quantum tunneling, electron transport and mesoscopic quantum transport. A brief introduction to characterization methods is also included: Raman spectroscopy, Synchrotron THz/Far-IR spectroscopy, PPMS, PXRD, FESEM, AFM, and DMA.

Chapter 3 reports an investigation of room temperature Raman scattering results and disorder-induced bands dispersion for Aerographite and graphitic materials at different excitation energies. Raman spectra exhibit typical graphitic features with the G, D, D′ and 2D bands. D and 2D bands show “blue-shift”, while G bands are invariant with laser excitation energy. The dependence of the intensity ratio I_D/I_G varies with λ_L^4 (where λ_L is the excitation laser wavelength) for graphite flakes and kish graphite, while it saturates at greatest λ_L for Aerographite and graphite oxide. A physical model based on the double resonant scattering, which considers the disorder-induced broadening of Raman peaks in the phonon density of states, is proposed to explain this behavior.

Chapter 4 presents an investigation of the temperature dependence of synchrotron THz/Far-IR and Raman spectra of Aerographite and SWCNT aerogel. New IR absorption bands of Aerographite and SWCNT aerogel were observed in the temperature range from 6 K to 300 K. Variable temperature Raman results reveal frequency shifts of phonon modes with the change of temperature over this range. Raman peak positions of Aerographite and SWCNT aerogel show a “red-shift” with increasing temperature. In contrast, the 2D peak of Aerographite and SWCNT aerogel show a “blue-shift” with temperature. The results are explained by a model invoking van der Waals bonding.

Chapter 5 reports the temperature dependent resistance and electrical transport properties of Aerographite and SWCNT aerogel in the temperature range from 2–300 K under different magnetic field strengths. The experimental results show that the resistance falls as temperature increases according to an exponential function. Strong temperature dependence is characteristic of

some form of hopping or tunneling conduction behavior. Two physical models are employed to understand the possible electrical conduction mechanisms in Aerographite and SWCNT aerogel.

Chapter 6 focuses on an investigation on designing and producing a novel double-network functional hydrogel network, which exhibits self-healing properties, then further infiltrating with SWCNT hydrogel precursor to form L-DOPA-PAM-SWCNT hydrogel hybrid network. The final product has useful electrical properties.

Chapter 7 summarizes all the results and provides a perspective for future work.

1.2 Aerogels

Aerogels were firstly created in 1931 by S. S. Kistler, an American scientist and chemical engineer [1]. There are also referred to as “frozen smoke” or “solid smoke”. They are composed of up to 99.8% air with the remainder being a solid polymer network. Aerogels have a large surface-area-to-volume ratio (500–1,500 m^{-1}), low density (as low as 0.001 g/cm^3), low mean free path for diffusion, low refractive index (n = 1.02), low thermal conductivity (as low as 0.015 W/mK), low dielectric constant and low acoustic velocity (as low as 100 m/s) [2,3].

1.2.1 Overview of Aerogels

Aerogels are a kind of materials with ultralight and highly porous characters. Usually they can be fabricated through making wet gels dry to remove the background liquid, but keep the network. Microscopically, aerogels are made of tenuous networks of clustered nanoparticles. Because of the unique properties, aerogels can be used in versatile and tailorable 3D architectures to enable the advantageous technologies, that is the combination of nano scale, high surface area, and inclusion of multiple functionalities. Various aerogels have been confirmed to have excellent performance in various applications, such as aerospace engineering, thermal insulation, energy storage and conversion, catalysis, and supercapacitor, etc. Fig. 1.1 (b) shows a 2.5 kg brick supported on a 2.0 g aerogel block with excellent mechanical properties [4].

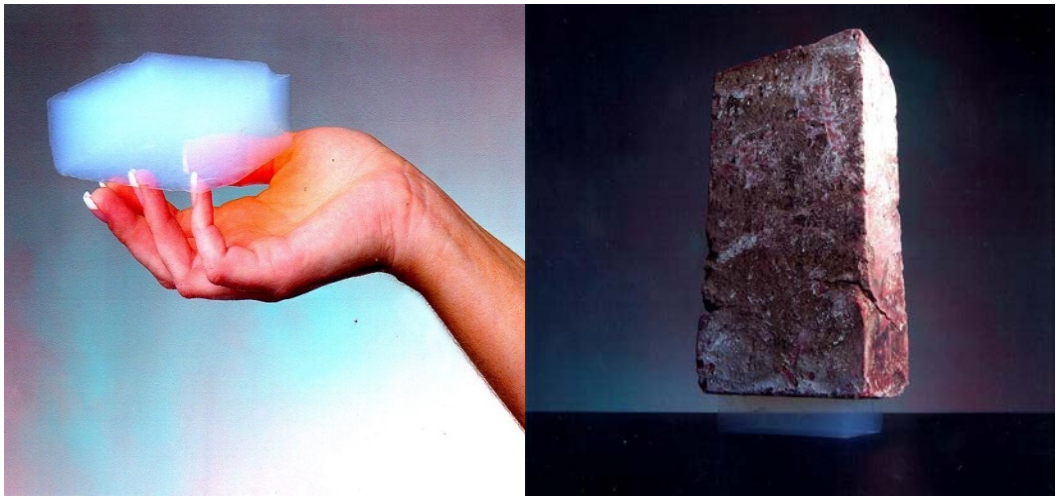

Figure 1.1: (a) Aerogel in hand. (b) Aerogel supporting a brick [4].

1.2.2 Physical and Chemical Properties

Due to their microstructure, aerogels have many excellent physical and chemical properties that may be used in various applications [2,3,5]. Generally, a two-step preparation method will be employed to prepare various aerogels: first a sol-gel process and second a drying step under special conditions (e.g. a high temperature environment). In more detail, firstly, a solution is used to create the gel, and then the liquid component is removed via critical point drying, which removes the liquid slowly to maintain the structural shape. In this step, the liquid component is replaced by air. The drying process is controlled by permeability and capillary stress, which are controlled by Darcy's law and Laplace's law, respectively [2].

Sol: "Liquid solution" – a colloidal system of liquid character in which the dispersed particles are either solids or large molecules with sizes in the colloidal range ($1 - 1{,}000$ nm) [6].

Gel: "Nanostructured material" – a colloidal system of solid character in which the dispersed substance forms a continuous, coherent framework that is interpenetrated by a system consisting of kinetic units smaller than colloids [6]. Usually a gel contains a small amount of the dispersed phase ($1 - 3$ wt %) and exhibits the properties of rigidity and elasticity. The assembly of several units into junction results, in different cases, from the effects of valence bonds, hydrogen bonds, dipole forces, van der Waals forces, and surfactants. According to the different media containing the dispersed phase, gels may be classified into hydrogels and aerogels (for water and air, respectively) [2]. Fig. 1.2 shows the differences between a sol, a gel, and an aerogel [6].

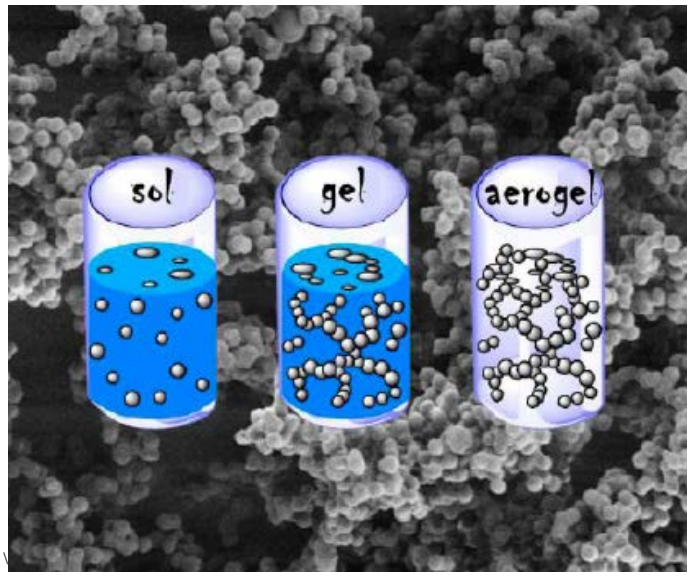

Figure 1.2: The differences between sol, gel, and aerogel [6].

Hydrogels are formed through the cross-linking of hydrophilic polymer chains within an aqueous environment. They hold a large amount of water while maintaining their structure [7,8]. This gelation can be achieved through a variety of mechanisms, such as physical entanglement of polymer chains, electrostatic interactions, and covalent chemical cross-linking [7,8]. The

hydrophilicity of the network exists due to the presence of functional groups, e.g. -NH_2, -COOH, -OH, -$CONH_2$, - CONH, and -SO_3H [7]. Aerogels are obtained when the liquid within the hydrogel is removed above its critical temperature and pressure [2]. In this process, the liquid is transformed at its critical temperature into a fluid without liquid-vapor phases being present as the pressure is raised [2]. The fluid within the gel can be slowly extracted at temperatures and pressures above the critical conditions to obtain an air-filled gel structure [2]. Because there is no distinction between the liquid and the vapor, there is no surface tension or capillary pressure developed during drying [2]. This enables the gel to be dried with very little shrinkage and the gel matrix to remain nearly intact [2]. Aerogels also contain large amounts of homogeneous dispersed air within their structure.

1.3 Carbon Aerogels

Carbon aerogels hold a unique combination of ultralow density, large surface area, high electrical conductivity, thermal and chemical robustness, and good mechanical properties [9,10]. The discovery of carbon allotropes, such as graphite, graphene, carbon nanotubes and nanodiamond, has provided a further opportunity to develop novel aerogels based on carbon allotrope materials. The properties relate directly from the assembly of amorphous sp^2 carbons into a highly porous, low-density aerogel. Carbon aerogels have been shown to have advantages in hydrogen and energy storage, supercapacitors and batteries, capacitive desalination, and electro-catalysis [11].

1.3.1 Aerographite (Graphite Aerogel)

Mecklenburg *et al.* firstly developed an ultra-light weight graphite aerogel based on a single-step chemical vapor deposition (CVD) synthesis method for the fabrication from a freely adjustable zinc oxide (ZnO) tubular network [12,13]. Fig.1.3 shows a transmission electron microscope (TEM) image of Aerographite, which is a fine mesh with an ultra-low density of 0.18 mg/cm^3 [14]. It is produced through following steps:

(1) The ZnO networks are fabricated by using a flame transport synthesis (FTS) approach. A mixture of Zn and polyvinyl butyral (PVB) powder is rapidly heated in a muffle-type furnace to 900 °C in ambient air. The mixture ignites causing Zn to travel and react with ZnO nanostructures along the way inside the flame. The product of the FTS is a white powder of ZnO tetrapod material. As a 3D interconnected network, the ZnO powder is compressed into a well-defined volume and re-heated for 5 h at 1,150 °C.

(2) ZnO networks mixed with metal micro particles are fabricated by homogenously mixing metal micro particles (Al, Bi, Cu, Fe and Sn) with ZnO tetrapod powder before compressing and re-heating. The weight ratio between the ZnO tetrapod powder and the metal micro particles is 20:1. The volume and density of the ZnO networks is 1 cm^3 and 0.3 g/cm^3, respectively.

(3) Aerographite is fabricated by template-based CVD growth. Graphitic carbon is grown at 760°C on top of the ZnO network while simultaneously removing the ZnO template. Toluene is used as the carbon source, and hydrogen gas is used for ZnO reduction. The porous ZnO

network acts as sacrificial template, and thus, the architecture of Aerographite material is mainly decided by the structural morphology of the sacrificial ZnO template.

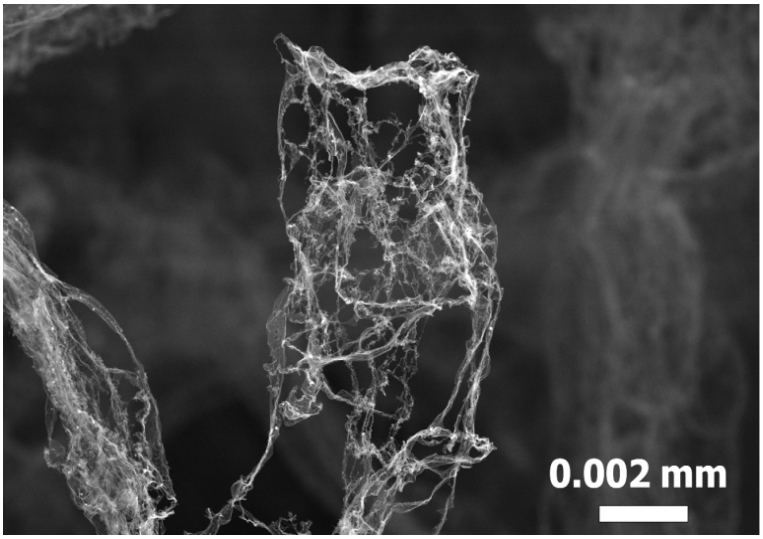

Figure 1.3: TEM image of Aerographite - with its a fine mesh structure [14].

1.3.2 Graphene and Graphene-inspired Aerogel

Graphite oxide is widely used to prepare graphene aerogels because its affordability and ease of processing. Several groups have reported different synthesis strategies for graphene aerogels based on graphite oxide. Xu *et al.* reported a hydrothermal method in which an aqueous graphite oxide suspension is heated to 180 °C in a pressure vessel for 12 h to simultaneously reduce and gel the graphene oxide [15]. Graphene aerogels have also been produced via a freeze-drying method [15]. Worsley *et al.* used a resorcinol and formaldehyde (RF) sol–gel process to form a carbonaceous "glue" between the graphene sheets in the aerogel. Thermal treatment at 1050 °C under inert gas converted both the RF and the graphite oxide to sp^2 carbon [15]. H. Hu *et al.* introduced ethylenediamine (EDA) into the graphite oxide colloidal solution. After the graphite oxide dispersion was transformed into graphene hydrogel, the solvent was removed from the graphene hydrogel to produce a graphene aerogel [15]. Worsley *et al.* also developed methods to synthesize highly crystalline graphene oxide-based graphene aerogels via high-temperature processing, as is common in commercial graphite production [15].

Gao *et al.* prepared graphene-inspired aerogels via freeze-drying aqueous solutions of multi-walled carbon nanotubes (MWCNTs) and giant graphene oxide sheets, followed by the chemical reduction of giant graphene oxide sheets into graphene using hydrazine vapor [16]. They also developed highly stretchable neat carbon aerogels with a retractable 200% elongation through hierarchical synergistic assembly [16]. Worsley *et al.* produced periodic graphene aerogel micro-lattices, possessing an architecture acquired via a 3D printing technique [16].

1.3.3 Carbon Nanotube Aerogel

Bryning *et al.* firstly reported the creation of SWCNT aerogel from aqueous gel precursors by critical point drying and freeze-drying approaches [17]. They used a surfactant to disperse SWCNTs, and then washed them in water to remove the surfactant [17]. This resulted in 3D SWCNTs with superior mechanical properties. Fig.1.4 shows scanning and transmission electron microscope (SEM and TEM) images of SWCNT aerogel with a mass concentration of 7.5 mg/mL [17]. The density of SWCNT aerogel is low, 2.3 mg/cm^3, measured from the final mass and dimensions of the aerogel.

(1) SWCNT powders were suspended in deionized water using surfactant at a concentration of 1 mg/mL; the mass ratio of SWCNTs with sodium dodecylbenzene sulfonate (SDBS) surfactant was 1:10. The solution was then tip-sonicated for 1 h at 100 W. The SWCNTs dispersion was centrifuged at 1,500 rpm for 30 min [17].

(2) SWCNTs suspensions were concentrated by evaporating and then pouring them into circular molds, then the surfactant was removed [17]. Different concentrations of ethanol solutions were used to replace the water in the samples.

(3) SWCNT hydrogel was dried by the critical-point dryer to obtain the SWCNT aerogel.

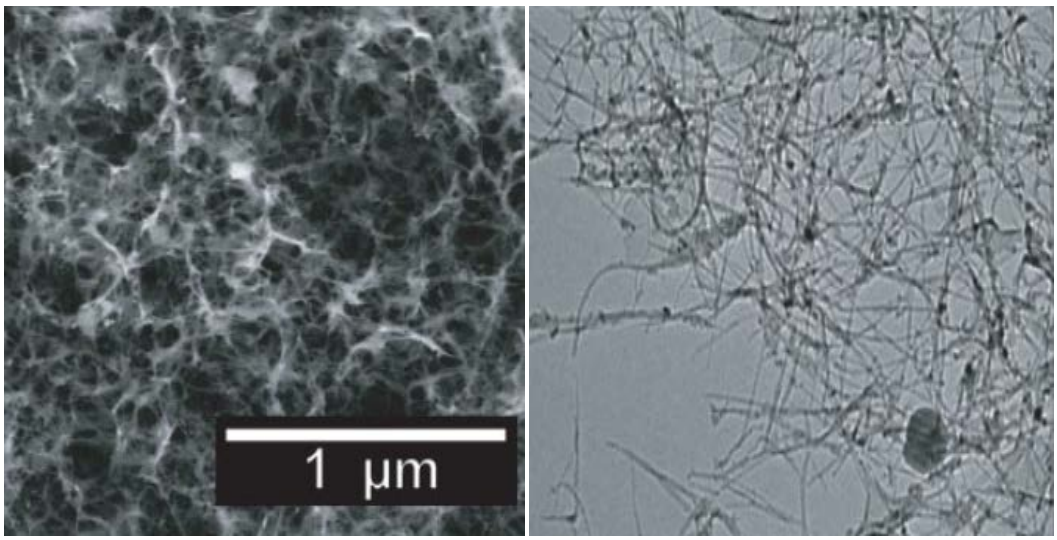

(a) SEM (b) TEM

Figure 1.4: SEM and TEM images of SWCNT aerogel [17].

SWCNT aerogel prepared by this method could support thousands of times its own weight after polyvinyl alcohol (PVA) reinforcement, depending on the processing conditions. Its electrical conductivity was as high as 1 S/cm [17]. Kim *et al.* further investigated the mechanical and thermal characteristics of SWCNT aerogel. The specific surface area (SSA) of the SWCNT aerogel is 1,291 m^2/g at a density of 7.3 mg/mL. The compressive and tensile moduli of SWCNT aerogel with a density of 9.9 mg/mL are 0.22 MPa and 0.21 MPa, respectively. The thermal properties are also greatly enhanced [18]. Zou *et al.* prepared ultralight multi-walled carbon nanotube (MWCNT) aerogel from a wet gel of dispersed pristine MWCNTs [19].

1.3.4 Nanodiamond Aerogel

Pauzauskie *et al.* firstly reported high pressure, high temperature (HPHT) synthesis to form a nanodiamond aerogel from an amorphous carbon precursor [20]. Phase transition from amorphous-to-crystalline is achieved by subjecting the amorphous precursor aerogel of density 0.04 g/cm^3 to a high pressure until it reaches the diamond state in the phase diagram [20]. Materials are heated to temperatures around 1,580 K through a laser-heated diamond anvil cell to overcome the kinetic barriers [20]. Manandhar *et al.* also proposed the rapid sol–gel synthesis of nanodiamond aerogel at standard temperature and pressure [20]. The surface areas of nanodiamond aerogel cross-linked with resorcinol and formaldehyde (RF) was larger than 589 m^2/g [20].

1.4 Terahertz Techniques

Since the 1970s, developments in electronics and photonics have provided new materials and techniques that can access the THz spectrum. THz spectroscopy provides a powerful method to study vibrational modes and validate theoretical molecular structures in semiconductors. It allows the measurement of the lifetime of carriers and doping concentrations. Its use in plasmas provides a better understanding of electron ionization and collision processes on the picosecond (ps) time scale.

1.4.1 Terahertz Radiation in the Electromagnetic Spectrum

Terahertz (THz) radiation is electromagnetic radiation in a frequency interval from 0.1 to 10 THz (0.03 mm to 3 mm wavelength, 3 to 300 cm^{-1}), a frequency range lies between the microwave and infrared (IR) regions of the electromagnetic spectrum [21-23]. The lack of suitable technologies for THz sources and detectors led to the THz band being called the “THz gap” [21-23]. As part of the electromagnetic spectrum, radiation at 1 THz radiation has a period of 1 ps, an angular frequency of 6.28×10^{12} rad/s, a wavelength of 300 μm, a wavenumber of 33 cm^{-1}, a photon energy of 4.1 meV, and an equivalent temperature of 47.6 K [24-26].

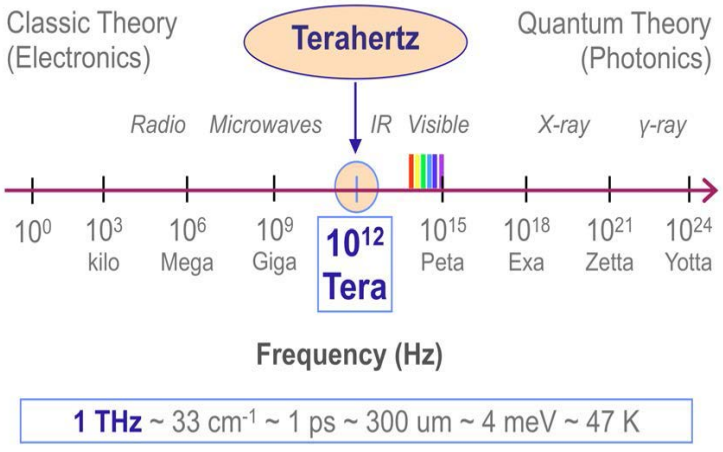

Figure 1.5: The THz band in the electromagnetic spectrum [25].

The “THz gap” arises from the nature of sources and detectors both on the optical (high frequency)

side and the electronic (low frequency) side [22]. THz radiation is now available in both continuous wave (CW) and pulsed (or time-domain) forms, down to single-cycles or less, with peak power up to 10 MW [24]. The unique nature of THz waves has triggered the development of THz technology for various applications [24]:

• THz waves have low photon energies and cannot lead to photoionization in biological tissues. THz waves are considered safe for both samples and operator [24].

• THz waves have longer wavelengths than visible and IR waves. This means THz waves are less affected by Mie scattering [24]. Most dry dielectric materials are transparent to THz waves [24]. THz waves are considered very promising for non-destructive evaluation applications.

• Many molecules exhibit strong absorption and dispersion in the THz region due to dipole-allowed vibrational transitions, which are specific to the molecule and enable THz spectral fingerprints [24].

• Coherent THz signals can be detected in the time domain by mapping transient electric fields for amplitude and phase, which provides access to THz spectroscopy [24].

1.4.2 Synchrotron Radiation as a THz Source Based on Relativistic Electrons

A synchrotron is a vacuum electronic radiation source based on electric charges moving freely [27]. Whenever relativistic light charged particles are bent in a magnetic field, synchrotron radiation is emitted with very bright light across the electromagnetic spectrum from X-rays to IR. Synchrotron radiation has several unique properties: a wide spectral coverage (energies ranging from IR to hard X-rays), extremely intense and highly collimated, highly polarized, and emitted in very short pulses for enabling time-resolved studies [28-30]. This highly collimated and intense synchrotron source provides an ideal setup to study thin samples in transmission or reflection in the THz region. Fig. 1.6 (a–c) shows an outline of the principle of synchrotron radiation [28-30], and (d) is a photo of the THz/Far-IR hutch at the Australian Synchrotron.

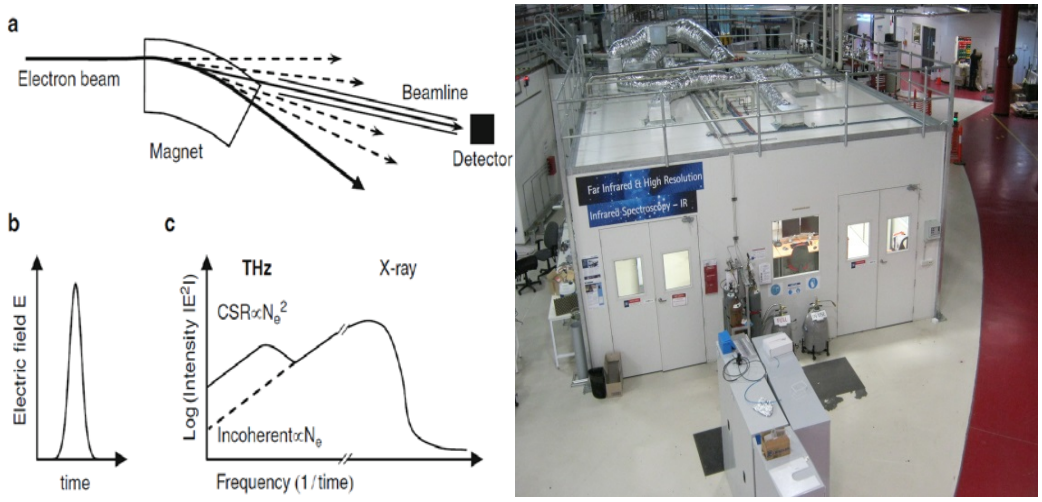

Figure 1.6: (a) Electron beam travelling through a magnet emitting synchrotron radiation collected at the beam line detector. (b) An electron travelling in an arc "sees" an electrical field pulse. (c) Power spectrum given by Fourier transform of electrical field pulse. (d) The THz/Far-IR Hutch at the Australian Synchrotron [29].

1.4.3 Terahertz Detection

THz detection schemes are classified into coherent and incoherent techniques [22]. The main difference is coherent detection could measure the amplitude and phase of the electrical field, whereas incoherent detection measures intensity [22,31].

1.4.3.1 Photoconductive (PC) Antenna

A PC antenna can be used not only for THz generation, but also for broadband THz pulse detection in the time domain. The THz field induces photocurrent in a PC gap when an optical probe pulse injects photo carriers [22]. The induced photocurrent is proportional to the amplitude of the THz field. The voltage between the two electrodes of the PC antenna will be proportional to the electric field of the THz wave at the time of arrival of the optical probe pulse [22].

1.4.3.2 Electro-optic Sampling

Electric-optic (EO) sampling measures the actual electrical field in the time domain based on the Pockels effect, which is a linear electro-optic effect [22]. A THz field induces birefringence in a nonlinear optical crystal, which is proportional to the field amplitude. This effect can be used for the detection of THz waves [22].

1.4.3.3 Thermal Detectors

Inherent THz detectors are thermal detectors, such as bolometers, Golay cells, and pyroelectric detectors. In these thermal detectors, electromagnetic radiation is absorbed and produces heat. A change in temperature produces a change in some physical quantity, which could be measured. The most widely used thermal detector is the bolometer, which measures heat by a change in its electrical resistance and operates in the cryogenic temperature range [21-23]. A bolometer is equipped with an electrical resistance thermometer with heavily doped semiconductor elements (e.g. carbon, silicon, and germanium) [32,33]. A liquid helium cooled silicon-based bolometer is employed to detect signals in the 300-700 cm^{-1} region. This detector comes with an IR light collecting cone assembly, vacuum-sealed wedged window, field of view baffling, and low noise electronics [21]. Fig. 1.7 demonstrates the operation principle of a bolometer [21].

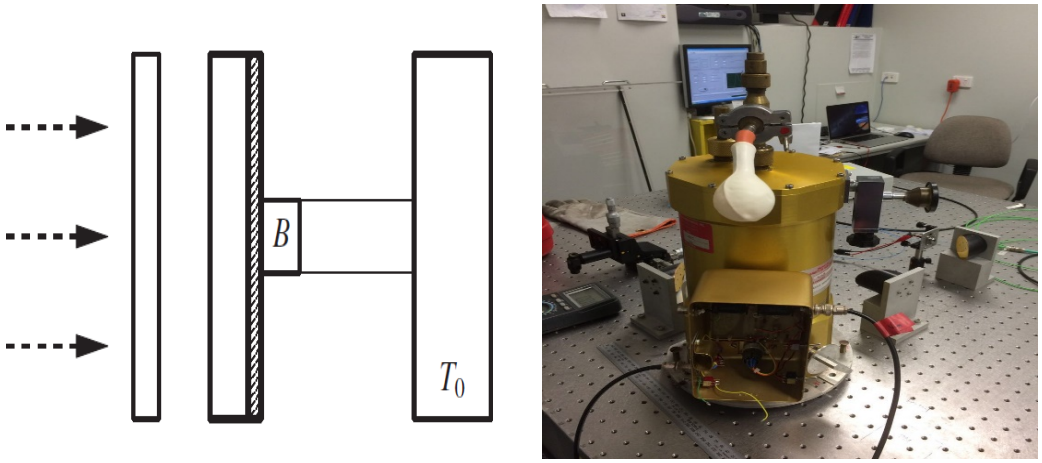

(a) (b)

Figure 1.7: The operation principle of a bolometer.
(a) Schematic diagram of a composite bolometer [21].
(b) The liquid helium cooled silicon bolometer at the UOW THz Science Laboratory.

1.4.4 Terahertz Spectroscopy

One of the primary research motivations to develop THz science and technology is to extract the characteristics of materials (rich physical and chemical phenomena) [34] and their spectral properties in the THz regime. THz spectroscopy is a powerful tool to detect amplitude and phase information simultaneously from coherent electromagnetic radiation in the THz range [21]. Because its broadband capability, unique time-resolved feature, and strong immunity to background noise in its observation of THz material interactions, THz spectroscopy is widely used on a huge variety of materials to aid our understanding of materials, identify chemical compounds, and demonstrate applications for THz sensing and imaging [35].

Other common vibrational spectroscopic methods are Raman spectroscopy and Fourier-transform infrared spectroscopy (FTIR). Raman spectroscopy employs a laser to excite samples and collects the Raman scattering (inelastic scattering) light to analyze in the Raman spectrometer [25]. Raman scattering effect causes a shift of the excitation frequency that can be associated with vibrational modes of samples [25]. FTIR measures indirectly in time domain interferometry in the IR band. In a typical FTIR measurement, a broadband source illuminates the sample. The light then passes to a far-IR beam splitter and focusing and collimating form optical parts for far-IR. Light returning from the sample is mixed with a reference beam in an interferometer (typically a Michelson interferometer) [25]. An interferogram is obtained by scanning the length of one optical arm, from which a spectrum can be obtained through Fourier transformation (FT) [25,36].

One of the main differences between FTIR and Raman spectroscopy with respect to THz time-domain spectroscopy (THz-TDS) is both Raman and FTIR spectroscopy measure energy whereas THz-TDS measures electric field [25]. On the other hand, FTIR and Raman require the use of models and indirect computation, such as the Kramers-Kronig (K-K) transformation, to retrieve

the complex dielectric constant [25]. A brief summary of the differences between THz-TDS, FTIR and Raman spectroscopy is shown in Table 1.1 [25].

	Advantages	**Disadvantages**
FTIR	High frequency resolution (~cm^{-1}) High sensitivity Broadband (up to 100 THz)	No coherent detection Need cryogenic conditions for high sensitivity No real-time data rate
Raman	High frequency resolution (~cm^{-1}) Room temperature operation High sensitivity High selectivity	No coherent detection
THZ-TDS	Room temperature operation Coherent detection (amplitude and phase) High selectivity Real-time data rate	Low frequency resolution than FTIR (~10 cm^{-1}) Narrow bandwidth than FTIR

Table 1.1: A brief summary of THz-TDS, FTIR, and Raman spectroscopy, adapted from [25].

Zhang *et al.* compared THz-TDS with FTIR from the aspects of radiation source, detector, signal to noise ratio (SNR), dynamic range of power, bandwidth, frequency resolution, peak power, source stability, data acquisition time, availability, and uniqueness [36]. The SNR values suggested that THz-TDS is advantageous at low frequencies under 3 THz (100 cm^{-1}), while FTIR works better at frequencies above 5 THz (167 cm^{-1}). Table 1.2 shows a detailed comparison between the THz-TDS and FTIR systems [36].

	THz-TDS	**FTIR**
Dynamic Range of Power (< 3THz)	$>10^8$	~300
Bandwidth	Far IR	Far IR-Visible
Frequency Resolution	~ 0.1 cm^{-1}	~ 0.1 cm^{-1}
Peak Power	e^{-3} W	e^{-7} W
Source Stability	Good	Not Good
NEP < 3 THz	$\sim 10^{-16}$ W•$Hz^{1/2}$	$\sim 8\times10^{-16}$ W•$Hz^{1/2}$
Data Acquisition Time	minutes	minutes
Uniqueness	Coherent pulse	Broader spectrum
Availability	Initial stage	Mature, easy

Table 1.2: The detailed comparison between THz-TDS and FTIR systems [36].

Chapter 2

Physical Principles of Experimental Techniques

2.1 Terahertz Spectroscopy of Condensed Matter

2.1.1 Physical Phenomena in Electronic Materials in the THz Region

1. Boltzmann Energy

The Boltzmann energy is defined as

$$E = k_B T \tag{2.1}$$

where k_B is the Boltzmann constant.

	Temperature (K)	Frequency (THz)	Energy (meV)
One Kelvin	1	0.020836644	0.08617343
He boils	4.2	0.088	0.36
	10	0.20836644	0.8617343
One meV	11.60451	0.24179894	1
	20	0.41673288	1.723469
One THz	47.992373	1	4.135667
	50	1.0418322	4.308672
Nitrogen boils	77.4	1.61	6.67
	100	2.0836644	8.617343
Water melts	273.15	5.6915	23.538
Triple point	273.16	5.6917	23.539
Room temperature	293.15	6.1083	25.262
	300	6.2509932	25.85203

Table 2.1: Frequency of a photon of Boltzmann energy at different temperatures [34]. The equivalent photon energy is found from $f = E/h$.

2. Phonon Energies

Assume a harmonic electric field variation is described using a time dependence of the form exp(-$i\omega t$). The harmonic oscillator dielectric function combined with the free-carrier term is [34]:

$$\begin{aligned}\epsilon(\omega) &= \epsilon(\infty) + \frac{\omega_t^2[\epsilon(0) - \epsilon(\infty)]}{\omega_t^2 - \omega^2 + i\gamma\omega} - \frac{\epsilon(\infty)\omega_p^2}{\left(\omega^2 + i\gamma_p\omega\right)} \\ &= \epsilon_1(\omega) + i\epsilon_2(\omega) \\ &= (n+i\kappa)^2\end{aligned} \tag{2.2}$$

where ω_t is the transverse optical (TO) phonon frequency, γ is the damping term, ω_p is the plasma frequency, and γ_p is the plasma damping term [34].

According to the real part of the refractive index n and the extinction coefficient κ, we could calculate the reflectance R [34]:

$$R = \frac{(n-1)^2-\kappa^2}{(n+1)^2+\kappa^2} \tag{2.3}$$

The plasma term allows the charge-carrier density N to be determined through $\omega_p^2 = \frac{Ne^2}{m^*\varepsilon_0\varepsilon(\infty)}$, where is m^* the effective mass of the charge carrier. The THz reflectivity spectra of undoped polar materials yield the TO and longitudinal optical (LO) phonon energies [34].

3. Electron-Phonon Interactions

THz spectroscopy provides information on electron-phonon interactions and ultrafast carrier dynamics of electrons and phonons in semiconductors and low-dimensional materials [37-41]. THz-TDS is employed to determine a function $\alpha^2F(\omega)$, which characterizes the electron-phonon coupling and the phonon density of states (PDOS), the transport-weighted electron-phonon coupling constant λ_{tr}, the temperature dependence of the electron-phonon mass enhancement, T_0, and the electronic degrees of freedom related to the plasma frequency ω_p [39]. The coupling of a zone-center phonon with a bound-state to bound-state transition results in a "Fano resonance", which is a discrete state in resonance with a continuum state [42].

2.1.2 Absorption and Dispersion

Frequency dispersion behavior could be described by the Lorentzian oscillator model, which is based on the classical theory of light-matter interaction and is used to describe frequency dependent polarization due to bond charge [22]. The binding force behaves like a mass-spring system, given the displacement is small enough [22]. Electrons react to an electromagnetic field by vibrating like damped harmonic oscillators. Fig. 2.1 describes the Lorentzian oscillator model [22].

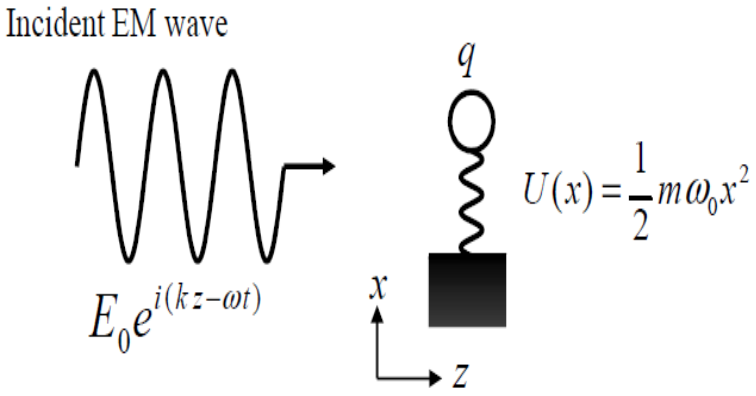

Figure 2.1: The Lorentzian oscillator model [22].

The equation of motion could be expressed as:

$$m\frac{d^2x}{dt^2} + m\gamma\frac{dx}{dt} + m\omega_0^2 x = qE(t) = qE_0\exp(-i\omega t) \tag{2.4}$$

where q is the charge, m is the mass, γ is the damping constant, and ω_0 is the resonance frequency. $m\frac{d^2x}{dt^2}$ is the acceleration force; $m\gamma\frac{dx}{dt}$ is the viscous force; $m\omega_0^2 x$ is the Hooke's force; and $qE(t)$ is the electrical driving force. The solution to the equation of motion (2.4) yields the expression for the amplitude of oscillation, depending on photon energy ω:

$$x(t) = x_0 \exp(-i\omega t) \tag{2.5}$$

$$x_0 = \frac{qE}{(\omega_0^2 - \omega^2) + i\gamma\omega} \tag{2.6}$$

$$x(\omega) = \frac{q/m}{\omega_0^2 - \omega^2 - i\gamma\omega} E_0 exp(-i\omega t) \tag{2.7}$$

According to Maxwell's equations, the dispersion relation is [22]

$$k^2 = \varepsilon\mu\omega^2 \tag{2.8}$$

where ε is the total permittivity, which is $\varepsilon_0\varepsilon_r$, where ε_0 is the absolute permittivity and ε_r is the relative permittivity (or the dielectric constant); μ is the magnetic permeability.

The complex amplitude of the wave vector:

$$k(\omega) = k_R(\omega) + ik_I(\omega) = \sqrt{\epsilon_r(\omega)}\frac{\omega}{c} \tag{2.9}$$

The plane wave propagating along the *z*-axis:

$$\vec{E}(z,t) = \vec{E}_0 exp\,[i(kz - \omega t)] = \vec{E}_0 e^{-\frac{\alpha}{2}z} e^{-i\omega(t-\frac{n}{c}z)} \tag{2.10}$$

The absorption coefficient α (ω) is the imaginary part of the dielectric constant:

$$\alpha(\omega) = Im\{k(\omega)\} = \frac{2\kappa\omega}{c} = \frac{4\pi\kappa}{\lambda} \tag{2.11}$$

2.2 Phonon Modes and Symmetry

2.2.1 Phonons and Phonon Modes

A phonon is a quantized vibration mode, which is an elementary excitation can be treated as a quasiparticle in a solid. The phonon modes are subdivided into two categories (according to whether their vibrations are perpendicular or parallel to the propagating direction of the wave, as specified by the wave vector $\vec{q}$) [44]: acoustic (A) or optical (O); transverse (T) or longitudinal (L).

The energy of the phonon is given by $\varepsilon = \hbar\omega$ (2.12)

The momentum of the phonon is $p = \frac{h}{\lambda}$ (2.13)

$$\vec{p} = \hbar\vec{q} \tag{2.14}$$

where λ is the wavelength, $\lambda = \frac{2\pi}{q}$, where $\vec{q}$ is the wave vector.

The average number of phonons in a mode at thermal equilibrium is

$$\bar{n} = \frac{1}{e^{\frac{\hbar\omega}{kT}} - 1} \tag{2.15}$$

Average number of phonons depends on the temperature: $T = 0$, $\bar{n} = 0$; so $\bar{n}$ increases with increasing T. Phonons can be created by raising temperatures, and average number of phonons in the system is not conserved [43]. A phonon mode is defined by the displacements of atoms inside the unit cell. The symmetry of a phonon belongs to the irreducible representation in direct product of a vector and the representation generated by a permutation of the equivalent atom positions in the unit cell [43].

2.2.2 Infrared and Raman Activity

When phonons have resonant frequencies in the IR region, the modes that interact directly with light are IR active. Phonon modes that are IR active can be derived by group theory and selection rules. In general, it is the optical modes rather than the acoustic modes that are IR active. These optically active phonons can absorb light at their resonant frequency. Conservation laws require that photons and phonons have the same energy and momentum [44]:

$$\omega = ck \tag{2.16}$$

$$\vec{k} = \vec{q} + \vec{Q} \tag{2.17}$$

where ω is the phonon angular frequency, $\vec{k}$ is the photon wave vector, $\vec{q}$ is the phonon wave vector, and $\vec{Q}$ is a reciprocal lattice vector.

Acoustic phonon modes have zero energy at the center of the Brillouin zone, and do not contribute to IR absorption. Optical modes have some energy at $\vec{q}$=0, decreasing with increasing $\vec{q}$, and become flat near the surface of the Brillouin zone. Only the optical modes at or near the center of the Brillouin zone could contribute to IR absorption or emission [44]. Selection rules govern whether a certain transition is allowed or forbidden, depending on whether the transition matrix element is non-vanishing or vanishing respectively. Fig. 2.2 shows the dispersion curves for acoustic and optical phonons. Angular frequency ω of acoustic and optical phonons is plotted with the wave vector $\vec{q}$ in the first Brillouin zone. Resonant absorption take place when phonon frequency ω and wave vector $\vec{q}$ match. Phonons and photons have the same frequency, and $\vec{q}$ is satisfied when the dispersion curves intersect [44].

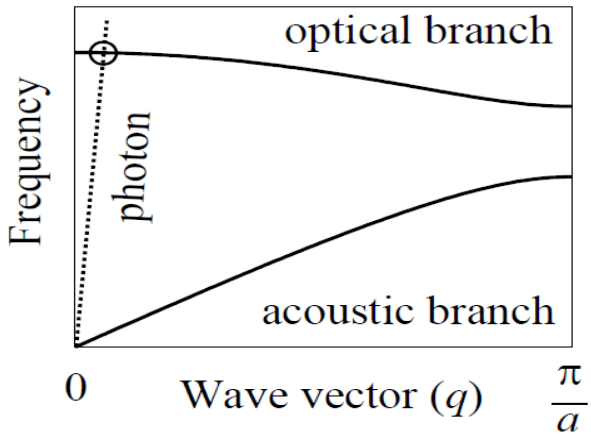

Figure 2.2: Dispersion curves for the acoustic and optical phonon branches [44].

Electromagnetic waves are transverse and can only apply driving forces to transverse vibrations. They can only couple to the TO phonon modes. The LO phonon modes are important to the IR properties. Solids have some ionic character to their TO phonons to be optically active because phonons and electron-phonon couplings through the driving force provided by the light wave. Because there is ionicity generated from the bonding, bonds with an ionic character are polar bands. The asymmetric electron cloud between atoms creates a dipole that can interact with electric fields. IR activity induces an electric dipole moment due to the change in atomic positions. Table 2.2 summarizes the IR activity of phonon modes in polar and non-polar solids.

Mode	Polar Solid	Non-polar Solid
Longitudinal Acoustic (LA)	NO	NO
Transverse Acoustic (TA)	NO	NO
Longitudinal Optic (LO)	NO	NO
Transverse Optic (TO)	YES	NO

Table 2.2: IR activity of phonon modes in polar and non-polar solids [44].

Raman scattering is an inelastic light scattering process under emission or absorption from optical phonons [44]. Energy and momentum must be conserved in the scattering process. Because optical phonons have less dispersion near $\vec{q} = 0$, inelastic light scattering can only probe the phonon modes with $\vec{q} \approx 0$. Raman scattering gives little information on the dispersion of optical phonons, and its main use is to determine the frequencies of the LO and TO modes near the Brillouin zone center [44]. Scattered light is examined for the presence of Stokes scattering (phonon emission) at frequency $(\omega - \omega_v)$ and of anti-Stokes scattering (phonon absorption) at frequency $(\omega + \omega_v)$.

2.2.3 Selection Rules

Selection rules are used to determine whether an optical phonon is Raman active, IR active or not. A vibrational mode is Raman active or not, which depends on whether the electron-phonon matrix element between the initial and final states for the Raman perturbation vanishes [45]:

$$\langle \Psi_f | | H'_{Raman} | \Psi_i \rangle \tag{2.18}$$

where Ψ_f is the final state corresponding to the normal mode that we are trying to excite, H'_{Raman} is the Raman perturbation energy operator, which has the transformation properties of a symmetric second rank tensor, and Ψ_i is the initial state, generally taken as the ground state which has the full symmetry of the Schrödinger equation group. A mode will be Raman active if the direct product $(\Psi_i \oplus \Psi_f)$, where H'_{Raman}transforms as a second rank symmetric tensor, contains the irreducible representation for the final state Ψ_f.

Crystals have long range order and can be categorized into 32 classes according to their point group symmetry [44]. Neumann's principle (or the principle of symmetry), which is *any macroscopic physical property must have at least the symmetry of the crystal structure*, is used to interpret the link between physical properties and point group symmetry [44]. The rule of mutual

exclusion means that crystals possesses inversion symmetry. In the centrosymmetric crystals, the vibrational modes must either have even or odd parity under inversion symmetry. The odd parity modes are IR active, while the even parity modes are Raman active [44]. In the non-centrosymmetric crystals, some vibrational modes are both IR and Raman active, and others can be neither IR active nor Raman active [44]. The interaction of light with lattice vibrations demonstrates IR active modes cause a change in the local dipole moment while Raman active modes cause a change in the local polarizability [45].

2.2.4 Phonon Modes in sp^2 Carbon Materials

Carbon-based materials are found in variety of allotropes, e.g. fullerenes (0D), carbon nanotubes (1D), graphene (2D), and graphite (3D) [46]. It is because a carbon atom can form several distinct types of valence bonds, where the chemical bonds refer to the hybridization of atomic orbitals. Each carbon atom has six electrons, which occupy $1s^2$, $2s^2$ and $2p^2$ atomic orbitals. Mixing of *2s* and *2p* atomic orbitals is called hybridization, whereas the mixing of a single *2s* electron with n = *1, 2, 3, 2p* electrons is called sp^n hybridization [46]. Three possible hybridizations occur in carbon: *sp* (two-fold), sp^2 (three-fold) and sp^3 (four-fold) [46].

Graphite is a layered material with individual graphene layers, which are the 3-D interlayer AB stacking order (the Bernal structure) in the most common form of graphite. Each unit cell of graphite has four carbon atoms, so there are twelve zone center lattice modes, and it belongs to the D_{6h}^4 group. Phonon modes of graphite at the Γ point can be expressed as [47]:

$$\Gamma_{\text{Graphite}} = A_{2u}(IR) + 2B_{2g} + E_{1u}(IR) + 2E_{2g}(R) \qquad (2.19)$$

where the A_{2u} and E_{1u} representations are the translations of the plane; the B_{2g} mode is an optical mode where the carbon atoms move perpendicular to the plane; and E_{2g} is the in-plane optical mode. Phonon modes are two double degenerate Raman active E_{2g} modes (1582 and 47 cm^{-1}); two IR active A_{2u} and E_{1u} modes (868 and 1588 cm^{-1}); and the other two are "silent" B_{2g} modes (neither Raman active nor IR active, one is at 127 cm^{-1} and another occurs at 870 cm^{-1}) [48].

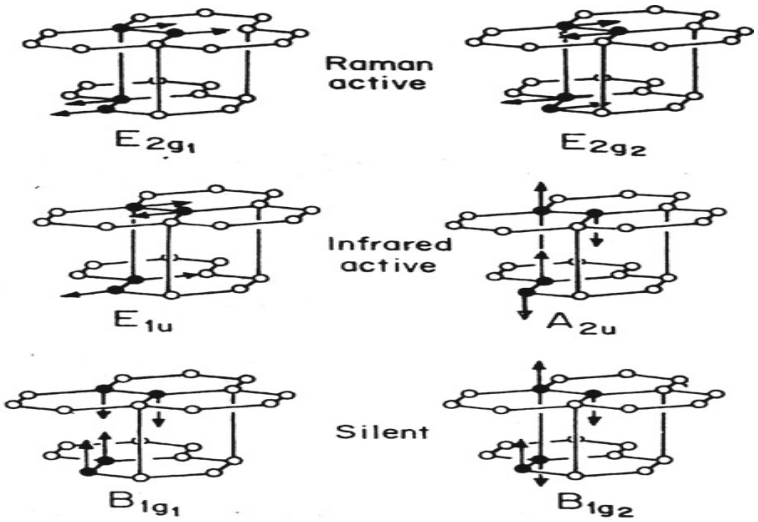

Figure 2.3: The phonon modes in 3D graphite at zone center $\vec{q}$=0 [48].

A SWCNT could be viewed as a graphene sheet rolled up into a seamless cylinder with one atomic layer in thickness, and microns in length along the cylinder axis. Physical properties of carbon nanotubes depend on how the graphene sheet is rolled up [45,46]. The structure of carbon nanotube is uniquely determined by the chiral vector $\overrightarrow{C_h}$ which spans the circumference of the cylinder when the graphene layer is rolled up into a tube [45].

$$\overrightarrow{C_h} = n\overrightarrow{a_1} + m\overrightarrow{a_2} \equiv (n, m) \tag{2.20}$$

where the vectors $\overrightarrow{a_1}$ and $\overrightarrow{a_2}$ are lattice vectors of the unit cell of the graphene layer, which contains two distinct carbon atom sites, while *n* and *m* are arbitrary integer numbers. The carbon nanotube can also be characterized by its diameter d_t and chiral angle θ, which determine the length $C_h = |\overrightarrow{C_h}| = \pi d_t$ of the chiral vector and its orientation on the graphene layer [46],

$$d_t = a\sqrt{n^2 + nm + m^2}/\pi \tag{2.21}$$

$$\tan\theta = \sqrt{3m}/(2n + m) \tag{2.22}$$

Because of the six-fold symmetry of the graphene layer, all nonequivalent CNTs can be characterized by the (*n, m*) pairs of integers where $0 \leq m \leq n$ [46]. The notation (*n, m*) defines the atomic coordination for the 1D unit cell of carbon nanotubes [49]. The carbon nanotubes are classified as achiral carbon nanotubes ($m = 0$ *or* $m = n$), which are known as armchair carbon nanotubes ($m = n$) (Fig. 2.4 (a)), zig-zag carbon nanotubes ($m = 0$) (Fig. 2.5 (b)) and chiral carbon nanotubes ($0 < m < n$) (Fig. 2.4 (c)), respectively.

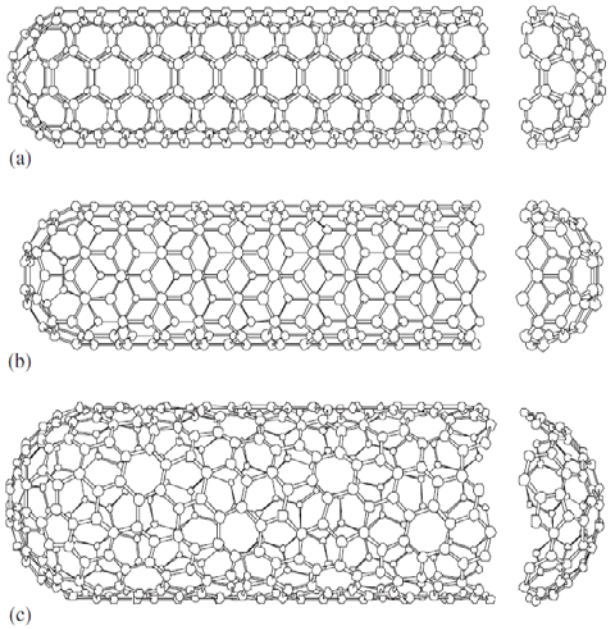

Figure 2.4: Schematic diagram of three types of SWCNTs:
(a) “armchair”. (b) “zig-zag” and (c) “chiral” [46].

Number of the Raman active and IR active vibrational modes for carbon nanotubes could be predicted by group theory based on the lattice structure and its symmetry [50]. Table 2.3 summarizes number and symmetries of the Raman active lattice vibrational modes for different carbon nanotubes [50,51].

	Nanotube Structure	Point Group	Raman Active	IR Active
Armchair	armchair (*n*; *n*) *n*: even	D_{nh}	$4A_{1g} + 4E_{1g} + 8E_{2g}$	$A_{2u} + 7E_{1u}$
	armchair (*n*; *n*) *n*: odd	D_{nd}	$3A_{1g} + 6E_{1g} + 6E_{2g}$	$2A_{2u} + 5E_{1u}$
Zigzag	zigzag (*n*; 0) *n*: even	D_{nh}	$3A_{1g} + 6E_{1g} + 6E_{2g}$	$2A_{2u} + 5E_{1u}$
	zigzag (*n*; 0) *n*: odd	D_{nd}	$3A_{1g} + 6E_{1g} + 6E_{2g}$	$2A_{2u} + 5E_{1u}$
Chiral	chiral (*n*; *m*) $n \neq m \neq 0$	C_{N}	$4A + 5E_1 + 6E_2$	$4A + 5E_1$

Table 2.3: Raman active and IR active modes of carbon nanotubes [51].

Phonon modes of SWCNTs can be expressed as [51]:

$$\Gamma_{\mathrm{SWCNTs}} = A_{2\mathrm{M}}(IR) + 2B_{2g} + 2E_{1\mathrm{M}}(IR) + 2E_{2g}(R) \tag{2.23}$$

For armchair SWCNTs (with even *n = 2j* having D_{nh} symmetry),

$$\Gamma_{\mathrm{armchair\ SWCNTs-2j}} = 4A_{1g} + 2A_{1u} + 4A_{2g} + 2A_{2u} + 2B_{1g} + 4B_{1u} + 2B_{2g} + 4B_{2u} + 4E_{1g} + 8E_{1u} + 8E_{2g} + 4E_{2u} + \cdots + 4E_{(\mathrm{j}-1)g} + 8E_{(\mathrm{j}-1)u} \tag{2.24}$$

For zigzag SWCNTs (with even *n = 2j* having D_{nh} symmetry),

$$\Gamma_{\mathrm{zig-zag\ SWCNTs-2j}} = 3A_{1g} + 3A_{1u} + 3A_{2g} + 3A_{2u} + 3B_{1g} + 3B_{1u} + 3B_{2g} + 3B_{2u} + 6E_{1g} + 6E_{1u} + 6E_{2g} + 6E_{2u} + \cdots + 3E_{(\mathrm{j}-1)g} + 6E_{(\mathrm{j}-1)u} \tag{2.25}$$

For armchair and zigzag SWCNTs (with odd *n = 2j+1* having D_{nd} symmetry),

$$\Gamma_{\mathrm{armchair\ and\ zig-zag\ SWCNTs-2j+1}} = 3A_{1g} + 3A_{1u} + 3A_{2g} + 3A_{2u} + 6E_{1g} + 6E_{1u} + 6E_{2g} + 6E_{2u} + \cdots + 6E_{\mathrm{j}g} + 6E_{\mathrm{j}u} \tag{2.26}$$

For chiral SWCNTs (with even *n = 2j* having D_{nh} symmetry),

$$\Gamma_{\mathrm{chiral\ SWCNTs-N}} = 6A + 6B + 6E_1 + 6E_2 \ldots + 6E_{\left(\frac{\mathrm{N}}{2}\right)-1} \tag{2.27}$$

According to Table 2.3, the Raman and IR selection rules for SWCNT imply the numbers of Raman and IR active modes do not depend on the carbon nanotube diameter and chirality, though the total number of finite frequency phonon modes …(6*N*-4) is different, depending on the chirality and diameter [51]. Selection rules indicate there are only 15 or 16 Raman active modes and 6 to 9 IR active modes for SWCNT, despite the large number of vibrational modes [51].

2.2.5 Phonon Dispersion of *sp²* Carbon Materials

Phonon dispersion curves are the frequency versus wave vector plots for lattice vibrations in the crystal. Phonon dispersion curves in crystals along the high-symmetry direction of the Brillouin zone can be measured by neutron scattering and high-resolution X-ray scattering techniques [43]. Fig. 2.5 shows the phonon dispersion curves in graphite and graphene [47,52]. At the zone center (Γ point), the in-plane iTO and LO optic modes are degenerate at the Γ point [47,52]. The

degenerate zone-center LO and iTO phonon modes belong to the E_{2g} representation and are Raman active modes. The phonon comes from the iTO branch is nondegenerate at the *K* point [47,52]. The LO and LA phonon branches meet each other at the *K* point in the Brillouin zone, resulting in a doubly degenerate phonon mode [47,52].

(a) Phonon dispersion in graphite.

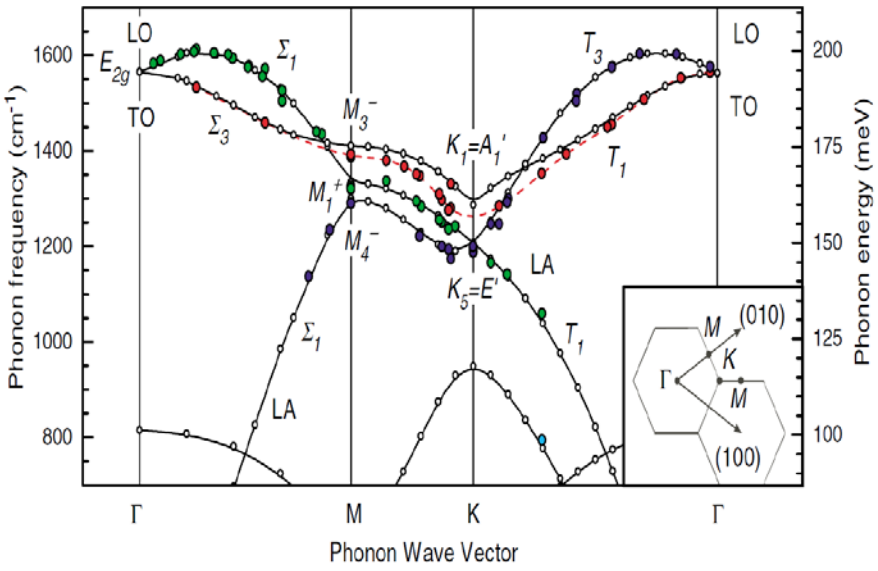

(b) Phonon dispersion in graphene.

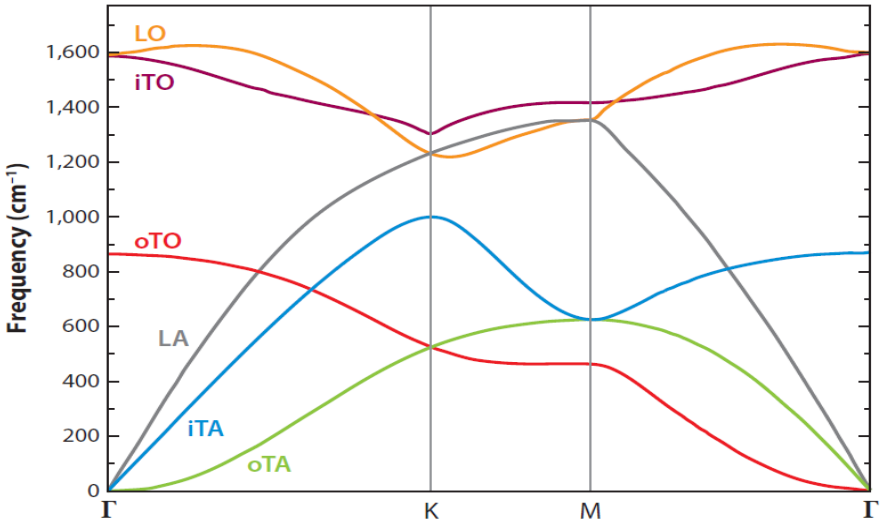

Figure 2.5: Phonon dispersion in graphite and graphene [47,52].

2.2.6 Raman Spectroscopy of sp^2 Carbon Materials

Raman spectroscopy is a powerful tool to provide information on crystallite size, chemical impurities, optical energy gap, elastic constants, defects and other disorder, edge structure, chirality, curvature, metallic or semiconducting behavior [53,54]. Raman spectroscopy measures phonon frequencies through the shift in the wavelength of inelastically scattered photons. Raman spectrum depends on the bond disorder, the presence of sp^2 rings or chains, and the ratio of sp^2/sp^3 [53,54].

In general, typical Raman features in sp^2 carbon materials include the G band around 1580 cm^{-1}, which is common to all sp^2 carbon materials. The radial breathing mode (RBM) makes the diameter and optical transition energy analysis of CNTs possible, and the D and G′ bands are significant for providing information on electronic and geometrical structures through the double resonance Raman scattering process [53].

1. Tangential Mode - G band.

Stretching of the C-C bonds in sp^2 carbon materials gives rise to the tangential G band Raman feature (with A_{1g}, E_{1g}, and E_{2g} symmetry) [53]. The multi-peak Lorentzian features are associated with the doubly degenerate (iTO and LO) phonon mode at the Brillouin zone center that is Raman active in the range of 1530-1620 cm^{-1} for sp^2 carbon structures. The G band is sensitive to strain effects and could be used to probe modification roles in the flat structure in sp^2 carbon systems. The G band could be used for (1) diameter characterization; (2) to distinguish between metallic and semiconducting SWCNTs, through differences in their Raman line shapes; (3) to probe the charge transfer arising from doping a SWCNT; and (4) to study selection rules in the Raman scattering processes and geometries [54-57].

2. Disorder Induced Mode - D Band.

Disorder and defects (such as hetero-atom, vacancies, impurities, etc.) in sp^2-hybridized carbon systems leads to the appearance of the D peak in the range of 1280-1350 cm^{-1}, which is a dispersion effect of the incident laser energy (1.0 eV$< E_{laser} <$ 4.5 eV) [53,58-60]. The relative intensity of the D band to the G band provides a probe to determine the in-plane crystallite size or the disorder amount. Both the D and the G′ bands are related to non-zone center phonons, and the dispersive behavior in a double resonance Raman process [53]. The intensity ratio I_D/I_G for the D band and G band is used to characterize the defect quality in sp^2 carbon materials.

3. Dispersive Mode - G′ (2D, overtone of D) Band: Double Resonance Process.

A strong Raman features appears in the range of 2500-2800 cm^{-1} in sp^2 carbon materials. It is the G′ (2D) Band, which is a second-order Raman process (overtone of the D band) and exhibits a strong frequency dependence (highly dispersive) on the excitation laser energy, E_L. An isolated SWCNT shows different G′ (2D) features, where the number of peaks and their frequencies depend on (*n*, *m*) because of both curvature-induced strain and quantum confinement effects [52,59]. For SWCNT bundles, the D band shows an overlap of many peaks from different (*n*, *m*) carbon nanotubes in resonance with E_L, and a step or oscillatory behavior superimposed on the linear E_L dependence of both ω_D and $\omega_{G'}$ in graphite [53,55].

4. Radial Breathing Mode (RBM).

Radial breathing mode (RBM) (appearing at 120 $cm^{-1} < \omega_{RBM} <$ 350 cm^{-1} for SWCNTs within 0.7 nm $< d_t <$ 2 nm) results in vibrations of each carbon atom in the radial direction. The RBM frequency (ω_{RBM}) is inversely proportional to the CNT diameter [53],

$$\omega_{\mathrm{RBM}} = \frac{A}{d_{\mathrm{t}}} + B = \frac{227}{d_{\mathrm{t}}}\sqrt{1 + C_{\mathrm{e}} d_{\mathrm{t}}^2} \tag{2.28}$$

Where C_{e} represents effects of the environment and has values from 0.05 to 0.07; and A and B are parameters determined experimentally.

For SWCNT bundles, d_{t} = 1.5 ± 0.2nm, A = 234 cm^{-1} nm, and B = 10 cm^{-1} (where B is an upshift in ω_{RBM} assigned to tube-tube interactions). For isolated SWCNT, A = 248 cm^{-1} nm and B = 0 [50]. The RBM is used to determine nanotube diameters and probe electronic structures through its intensity (I_{RBM}). Moreover, the (n, m) indices and optical transition energies (E_{ii}) of an individual SWCNT will be assigned when considering resonance conditions [53,55].

2.2.7 Double Resonant Raman Scattering Process

The Double resonance Raman scattering arises from the intervalley or intra-valley scattering who one or two phonons and one defect play role in the scattering of the excited electron [61-64]. The double resonant Raman scattering consists of four steps [62,63]: (a) an electron-hole pair excitation; (b) inelastic scattering of the electron (or the hole) by a phonon; (c) elastic scattering of the electron (or hole) by a defect; and (d) recombination of the excited electron and hole. In the defect-induced double resonance Raman scattering process, two of three intermediate states in the conduction band which are visited by the electron are real electronic state, and sattisfied by resonance of an electronic state with either the incident or scatted photons, give raise to a double resonant Raman process (electron-photon and electron-phonon scattering) [62,63]. The electronic state are visited in the conduction band, which are determined by the energy diffrence between the electronic bands by the conservation of momentum and by obeying selection rules [61,64,65].

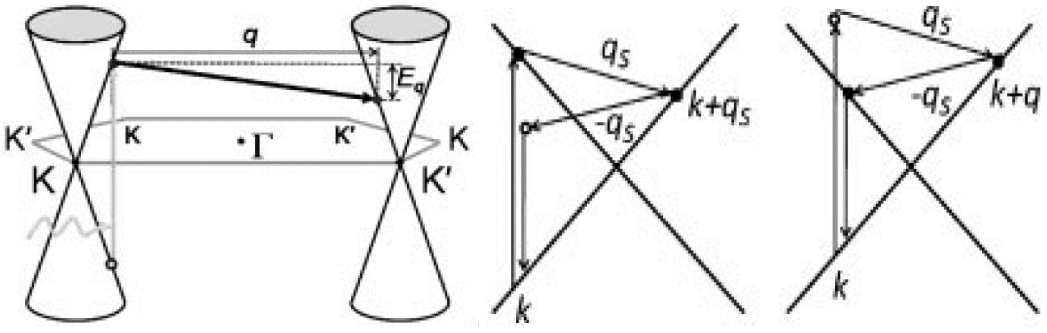

(a) (b)

Figure 2.6: The Double resonant Raman scattering process [61].
(a) Light-induced electron-hole formation and one electron-one phonon scattering process in the double resonant Raman process. (b) Double resonance with the incident and scattered light.

Fig. 2.6 shows the schematic diagram of the double resonant Raman scattering process, which is near the Fermi level at the K and K' points in the Brioullin zone. The first step is an electron with momentum $\vec{k}$ and energy $E_i(\vec{k})$ is excited by an incident photon with excitation energy E_i from the valence band state a to a conduction band sate b, which is results in an electron-hole pair creation at the $\vec{k}$ point matching the energy diffrence between a and b ($a \rightarrow b$). A photon will interact with

an electron, whose energy will increase up to the high avablible energy level. Because photon carries a little momutum, the momentum of an electron remains almost unchanged. In this process, the scattering probaility is proportional to the electron DOS, and the resonant condition is that

$$E_i(\vec{k}) = E_{\text{laser}}, \tag{2.29}$$
$$E(\vec{k}+\vec{q}) = E_i(\vec{k}) - \hbar\omega_{\text{ph}}(\vec{q}),$$

The second step is an electron inelastic scattering process by emitting a phonon with momentum $\vec{q}$ and energy $E(\vec{q})$ from state *b* to an intermediate state *c* (*b*→*c*). The electron-phonon interaction will change momentum $\vec{k}$and energy $E(\vec{k})$ to momentum $\vec{k}+\vec{q}$ and energy $E(\vec{k}+\vec{q})$, respectively. The scattering probability is proportional to the PDOS, and the resonant condition is that

$$E_i(\vec{k}) = E_{\text{laser}}, \tag{2.30}$$
$$E(\vec{k}+\vec{q}) = E_i(\vec{k}) - \hbar\omega_{\text{ph}}(\vec{q}),$$

In the elastic scattering process from sate *c* to virtrual state *d* (*c*→*d*), an electron will be mediated and modified by a lattice defect. Due to the size of a lattice defect is larger than that of an electron, the change of enery can be negliable while the change of mometum will play the main role. The subsequent recombination by an electron-hole will be taken place if the momutum of state *d* is equal and opposite wave vector $\vec{q}$ to the momutum of the hole. The scattering probablity is proportional to the defects DOS, and the resonant condition is that

$$E_i(\vec{k}) = E_{\text{laser}}, \tag{2.31}$$
$$E(\vec{k}+\vec{q}) = E_i(\vec{k}),$$

In the process of virtural state *d* to *a* (*d*→*a*), an electron is scatted back to the same initial sate in the conduction band with momentum $\vec{k}$ and energy $E_i^s(\vec{k})$ to satisfy the conservation of monmutum and selection rules. A photon is emitted by an electron and recombine with the photo-induced hole. The total scattering probility is proportional to the probability of electron DOS and phonon DOS due to the defect DOS is smaller. The resonant condition is that

$$E_i(\vec{k}) = E_{\text{laser}}, \tag{2.32}$$
$$E(\vec{k}+\vec{q}) = E_i(\vec{k}).$$
$$E_i^s(\vec{k}) = E(\vec{k}+\vec{q}) - \hbar\omega_{\text{ph}}(\vec{q}).$$

2.3 Quantum Transport in Mesoscopic Systems

2.3.1 Temperature Dependence of the Electrical Conductivity

In the view of phonons, the electrical conductivity is primarily controlled by electrons scattering around E_F by phonons with electron speed of $V_F = (\frac{2E_F}{m_e})^{\frac{1}{2}}$ and momentum of $m_e V_F$. The electrical conductivity σ is proportional to the mean collision time, τ, of the electrons, $\sigma \propto \tau$. If we take on average *N* collisions to randomize the electron's momentum, and τ is the mean time between the scattering processes, the effective scattering time is $N\tau$ and $\sigma \propto N\tau$.

For the electrical conductivity at low temperature, defect and boundary scattering play the dominate role, and σ is independent of temperature. At high temperatures above the Debye temperature ($T > T_D$), phonon concentration n_{phonon}increase with *T* [48,66]:

$$\sigma \propto \tau \propto \frac{1}{n_{\text{phonon}}} \propto \frac{1}{T} \tag{2.33}$$

At a higher temperature but still below the Debye temperature ($T < T_D$), phonon concentration n_{phonon} follows $n_{\text{phonon}} \propto T^5$, and the mean phonon energy $\bar{E}_{\text{phonon}} \propto T$. Average phonon momentum $\hbar$K is proportional to temperature. *N* times collisions will take place with momentum of electrons changing by $2m_eV_F$ from -m_eV_F to m_eV_F, the electrical conductivity is [48,66]

$$\sigma \propto N\tau \propto \frac{N}{n_{\text{phonon}}} \propto \frac{1}{T^5} \tag{2.34}$$

$$N = \frac{(2m_eV_F)^2}{(\hbar K)^2} \propto \frac{1}{T^2} \tag{2.35}$$

2.3.2 Quantum Tunneling

2.3.2.1 Barrier Transmission and Tunneling

Quantum tunneling is the penetration of a particle through a potential energy barrier by virtue of the particle's wave-like behavior. Considering that an electron moves with a mass *m* and energy $E = \frac{\hbar^2k^2}{2m}$, if it encounters a potential barrier:

$$V(x) = \begin{cases} 0, & x < 0, x > a \\ V_0, & 0 \le x \le a \end{cases} \tag{2.36}$$

And if the energy of the electron is less than the potential barrier ($V_0 > E$), the electron will tunnel through the barrier to appear on the other side. The probability of tunneling depends on the height and width of the potential barrier. The wave function could be expressed as

$$\Psi(x,t) = \Psi(x)e^{-\frac{iEt}{\hbar}} \tag{2.37}$$

This wave function is the solution of the Schrödinger equation [67]:

$$-\frac{\hbar^2}{2m}\Psi'' + V(x)\Psi = E\Psi \tag{2.38}$$

$$\begin{cases} \Psi'' + k^2\Psi = 0, x < 0, x > a \\ \Psi'' - \beta^2\Psi = 0, \quad 0 \le x \le a \end{cases} \tag{2.39}$$

In combination with the boundary condition, the solution of the equation (2.38) is

$$\Psi(x) = \begin{cases} Ae^{ikx} + Re^{-ikx}, x < 0 \\ De^{ikx}, x > a \end{cases} \tag{2.40}$$

$$\Psi(x) = Be^{\beta x} + Ce^{-\beta x}, 0 < x < a \tag{2.41}$$

where the *A* item is the incident wave, the *R* is the reflected wave, and the *D* item is the transmitted wave, $k = \frac{\sqrt{2mE}}{\hbar}, \beta = \frac{\sqrt{2m(V_0-E)}}{\hbar}$.

The transmission coefficient *T* (the probability of tunneling) and the reflection coefficient *R* (the probability of reflection) are defined as [67]

$$T = \left|\frac{D}{A}\right|^2 = \frac{(\gamma-\gamma^*)^2}{e^{2\beta a}+e^{-2\beta a}-(\gamma^2+\gamma^{*2})} \quad (2.42)$$

$$R = \left|\frac{R}{A}\right|^2 = \frac{(e^{\beta a}-e^{-\beta a})^2}{e^{2\beta a}+e^{-2\beta a}-(\gamma^2+\gamma^{*2})} \quad (2.43)$$

$$\left|\frac{D}{A}\right|^2 + \left|\frac{R}{A}\right|^2 = 1 \quad (2.44)$$

where $\gamma = \frac{\beta+ik}{\beta-ik}, \gamma^* = \frac{\beta-ik}{\beta+ik} = \frac{1}{\gamma}, |\gamma| = 1$. In practice, $e^{2\beta a} \gg 1$, (2.42) could be simplified to

$$T = \left|\frac{D}{A}\right|^2 \approx |\gamma-\gamma^*|^2 e^{-2\beta a} = \frac{16E(V_0-E)}{V_0^2} e^{-\frac{2a\sqrt{2m(V_0-E)}}{\hbar}} \quad (2.45)$$

If $V_0 < E$, $$\beta = \frac{\sqrt{2m(V_0-E)}}{\hbar} = \frac{i\sqrt{2m(E-V_0)}}{\hbar} = i\alpha \quad (2.46)$$

$$\gamma = \frac{\alpha+k}{\alpha-k}, \gamma^* = \frac{\alpha-k}{\alpha+k}, \gamma\gamma^* = 1 \quad (2.47)$$

$$(\gamma-\gamma^*)^2 = (\frac{4\alpha k}{\alpha^2-k^2})^2 \quad (2.48)$$

When an electron encounters a potential energy barrier of height V_0 greater than its energy *E*, the electron will tunnel through the barrier with a certain probability, which depends on the energy and width of the barrier. For a wide potential barrier, the probability of tunneling is proportional to exp(-2α*a)*. This means that the wider or higher the potential barrier, the smaller the probability of the electron tunneling will be [66,67].

2.3.3 Hopping Conduction

Anderson reported that all electron states will be localized in the system if disorder is strong enough, and the wave function envelop will exponentially decay with increasing distance [68],

$$|\psi(\vec{r})| \propto \exp(-|\vec{r}-\vec{r}_0|/\xi) \quad (2.49)$$

where $\vec{r}_0$ is the central position of local states; and ξ is the localization length. In a strongly disordered system, active electron states are all localized states. At $T = 0$, electrons are non-mobile and cannot contribute to current transport beyond the localized length. At $T \neq 0$, electrons will "hop" from one localized state to another to generate hopping conduction based on two mechanisms of thermal activation (up in energy) and tunneling (across in space) [69,70].

2.3.3.1 Hopping Probabilities

We consider two electrons located at $\vec{R}_i$ and $\vec{R}_j$ with energy of ε_i and ε_j, respectively. If $\varepsilon_i > \varepsilon_j$, the energy difference between the two localized states is $\varepsilon_{ij} = \varepsilon_j - \varepsilon_i$, and the distance between the two localized states $\vec{r}_{ij} = |\vec{R}_j - \vec{R}_i|$.

Hopping is a quantum process in which the electron travels from one local state to another with phonon assistance. According to the energy conservation law, the probability of hopping is proportional to the number of phonons at energy ε_{ij}; and to the probability of tunneling between

these two states. If we assume that all localized states have the same localization length ξ, the probability of hopping between the *i* and *j* states is:

$$\gamma_{ij} = \gamma_0 \exp\left(-\frac{2r_{ij}}{\xi}\right) n(\varepsilon_{ij}),\ \varepsilon_{ij} > 0 \tag{2.50}$$

$$n(\varepsilon_{ij}) = \frac{1}{e^{\frac{\varepsilon_{ij}}{k_B T}} - 1} \tag{2.51}$$

where γ_0 is related to ε_{ij} and r_{ij}, and $n(\varepsilon_{ij})$ is the distribution of phonons, the Planck distribution.

If $k_B T \ll \varepsilon_{ij}$, this will be simplified to the Boltzmann distribution: *exp (-*$\frac{\varepsilon_{ij}}{k_B T}$*)*. The hopping process will take place only if there are electrons located in the *i* state and the *j* state is empty. The number of electrons hopping from *i* to *j* per unit time is

$$\Gamma_{ij} = \gamma_0 \exp\left(-\frac{2r_{ij}}{\xi}\right) \exp\left(-\frac{\varepsilon_{ij}}{k_B T}\right) f_i(1 - f_j) \tag{2.52}$$

$$f_i = \frac{1}{e^{\frac{\varepsilon_i - \mu}{k_B T}} + 1} \tag{2.53}$$

where f_i is the Fermi-Dirac distribution function and μ is the mobility of electrons.

2.3.3.2 Variable Range Hopping Conduction

Mott reported that, in the low temperature range, hopping conduction mainly takes place in the local states around the Fermi energy ε_F [71,72]. According to (2.65), the number of electrons hopping from *i* to *j* per unit time will be determined by the distance in space between the *i* and *j* states, $r_{ij} = r$, and the energy difference $\varepsilon_{ij} = \Delta\varepsilon$ in the low temperature range. When the phonons cannot provide enough energy as the temperature decreases, the probability of hopping in the states that have a longer distance between the electrons and smaller energy difference between them $\Delta\varepsilon$, will be larger than for the others. The average energy differences can be estimated by

$$\Delta\varepsilon \sim \frac{1}{g(\varepsilon) r^d} \tag{2.54}$$

where g (ε) is the DOS, and d is the system dimensionality.

According to (2.56) and (2.58), the characteristic parameters in the hopping process will vary with the temperature. The phonon factor with increased the thermal activation $\exp(-\frac{\Delta\varepsilon}{k_B T})$ will provide larger contribution than with a decreased overlap factor of the wave function, $\exp(-\frac{2r}{\xi})$. This means that electrons will select the final states that hold similar energies over a large range to increase the probability of hopping. The most probable hopping range r_0 could be found from

$$\frac{d}{dr}\left[\frac{2r}{\xi} + \frac{1}{g(\varepsilon_F) r^d k_B T}\right] = 0 \tag{2.55}$$

where $g(\varepsilon_F)$ is the DOS at ε_F, and *d* is the system dimensionality.

The approximate solution of (2.55) is

$$r_0 \approx \left[\frac{\xi}{g(\varepsilon_F) r^d k_B T)}\right]^{\frac{1}{d+1}} \tag{2.56}$$

This process is the variable range hopping (VRH) because hopping range varies with temperatures. The electrical resistivity for hopping is determined by the overlap factor of the electron wave function at r_0. Assuming the hopping conductivity corresponds to the most probable hopping,

$$\sigma \propto e^{-C(\frac{T_0}{T})^{\frac{1}{d+1}}} \tag{2.57}$$

$$k_B T_0 \sim \frac{1}{g(\varepsilon)\xi^d}, T \ll T_0 \tag{2.58}$$

where *C* is a constant for a 1D system.

For a 3D system, the relationship between the electrical resistivity (ρ) and temperature obeys Mott's $T^{\frac{1}{4}}$ law:

$$\rho(T) = \rho_0 exp[(\frac{T_0}{T})]^{\frac{1}{4}} \tag{2.59}$$

$$T_0 = \frac{\beta}{k_B g(\varepsilon_F)\xi^3} \tag{2.60}$$

According to the percolation theory [73], the hopping process is mapped onto a random-resistor network. Values of resistors are changed randomly, and it considers electrical percolation thresholds and percolation possibilities in strongly disordered systems with local states are then considered. This will be used in Chapter 5 and we describe it in more detail here. In the random-resistor network, the hopping resistance between two local states R_{ij} is related to the distance and energy differences between the local states by exponential relationships. Total resistance will be determined by smallest resistance branches in this percolation network. This process can be repeated until the resistance percolation threshold, R_c, is reached since only the resistance paths below R_c are considered in the random-resistor network:

$$\frac{2r_{ij}}{\xi} + \frac{\varepsilon_{ij}}{k_B T} \leq \eta \tag{2.61}$$

$$r_{max} = \frac{1}{2}\xi\eta,\ \varepsilon_{max} = k_B T \tag{2.62}$$

Hopping will take place in the local states from $\varepsilon_F - \varepsilon_{max}$ to $\varepsilon_F + \varepsilon_{max}$, and the number of local states around r_{max} is [74]

$$n(\eta) = 2g(\varepsilon_F)\varepsilon_{max} r_{max}^d = \frac{1}{2^{d-1}} g(\varepsilon_F) k_B T \xi^d \eta^{d+1}. \tag{2.63}$$

The hopping electrical resistivity is [74]

$$\rho = \rho_0 e^{\eta_c}, \tag{2.64}$$

where *d* is the system dimension, and the percolation threshold is $\eta_c = [\frac{2^{d-1} n_c}{g(\varepsilon_F) k_B T \xi^d}]^{\frac{1}{d+1}}$, $\beta = 4n_c$.

For a 2D system, *d=2*, $\frac{1}{d+1} = \frac{1}{3}$; and for a 1D system, *d=1*, $\frac{1}{d+1} = \frac{1}{2}$.

The hopping process is related to two processes: the thermal activation, which change the energies of local electron states, and the quantum tunneling, which changes the mobility. At low temperature ($T < T_0$), the number of thermally accessible states becomes smaller, and it forces the tunneling distances to become larger. Since the tunneling distance could be continuously increased as temperature decreases, this conduction is "variable range hopping". In the high temperature

range ($T > T_0$), variable range hopping undergoes a transition to fixed range hopping, and the electrical resistivity is mainly determined by the thermal activation of phonons (with the limiting factor the tunneling distance) [74],

$$\rho \propto e^{\frac{-\Delta\varepsilon_\xi}{k_B T}} \tag{2.65}$$

The energy difference between two close local states $\Delta\varepsilon_\xi$ is [74]

$$\Delta\varepsilon_\xi \sim \frac{1}{g(\varepsilon) r^d} \tag{2.66}$$

When the Fermi energy ε_F is close to the mobility edge, ε_c, $(\varepsilon_c - \varepsilon_F) < \Delta\varepsilon_\xi$,

$$\rho \propto e^{-\frac{(\varepsilon_c - \varepsilon_F)}{k_B T}} \tag{2.67}$$

At T=0, the quantum tunneling will play the main role in the mobility between local states. If the sample size $L \gg \xi$, the electrical resistance is [74]

$$R \propto e^{\frac{L}{\xi}} \tag{2.68}$$

2.3.4 Landauer-Büttiker Formula

The Landauer-Büttiker (L-B) formula describes the electrical conductance in mesoscopic systems based on transport properties that are results of carrier interaction with the sample edges, and the electrical conductivity is expressed by transmittance T and reflectivity R [75-77]. It is used in Chapter 5 to get the relationship between voltage and current through the SWCNT aerogel.

The mesoscopic system has a size of $L \leq L_\varphi$ between the microscopic and the macroscopic sizes [78]. The main characteristic of a mesoscopic system is the preservation of wave characteristics, e.g. interference and phase memory. There are two important length scales in the transport properties of mesoscopic systems: 1) the dephasing time, τ_φ, which is determined by electron-dopant scattering; and 2) the dephasing length, L_φ, which is determined by electron-phonon scattering (0.1− 1 μm). The relationship between the dephasing lengths L_φ and dephasing time τ_φ is [74]

$$L_\varphi = (D\tau_\varphi)^{\frac{1}{2}} \tag{2.69}$$

For the 3D system, diffusion coefficient is $D = \frac{v_F l}{3}$, where l is the elastic scattering mean free path.

The L-B formula describes the electrical conductance in mesoscopic systems based on transport properties resulting in the interaction of carriers with the sample edges, and the electrical conductivity is expressed by the transmittance T and the reflectivity R [75-77].

In a coherent system with a size smaller than L_φ, two terminals are connected two ideals lead on two sides to electron reservoirs with chemical potentials μ_1 and μ_2, and the relationship between voltage and chemical potential is $V = \frac{\mu}{-e}$. If the width of the conductive area is w, the electron energy is [74]

$$E_n = \frac{\hbar^2}{2m^*}(\frac{n\pi}{w})^2 \quad (2.70)$$

The wave function in the direction of *x* is

$$\Psi_n(x) = Ae^{ikx} + Be^{-ikx} \quad (2.71)$$

Total energy of electrons is

$$E = \frac{\hbar^2}{2m^*}(\frac{n\pi}{w})^2 + \frac{\hbar^2}{2m^*}k^2 \quad (2.72)$$

When the Fermi energy of the electrons is larger than E_n, there are *n* sub-energy levels, namely, *n* channels.

When there is a small difference between chemical potentials μ_1 and μ_2, $\Delta\mu = \mu_1 - \mu_2 \ll \mu_1$, current will be generated by electrons in motion from μ_1 to μ_2 [74]:

$$I = n(-e)v = \left(\frac{dn}{dE}\right)\Delta\mu(-e)\frac{1}{\hbar}\frac{\partial E}{\partial k}T = -\frac{e}{h}[(1-R)\mu_1 - T\mu_2] = \frac{e^2}{h}[(1-R)V_1 - TV_2] \quad (2.73)$$

When $\frac{dn}{dE}$ is the DOS of electrons, the electrical conductance is quantized in units of $\frac{e^2}{h}$. Such quantization is seen to arise directly from the finite width of the conduction channel, which acts as an electronic waveguide [70].

For multi-channel conductance, the L-B formula is [78-80]

$$I_i = \frac{2e}{h}[(1 - R_{ii})\mu_i - \sum_{j\neq i} T_{ji}\mu_j] \quad (2.74)$$

where I_i is the outgoing current in the i^{th} channel; $R_{ii} = \sum_{n,m} R_{ii,mn}$ is the probability of an incoming electron in the i^{th} channel; $T_{ji} = \sum_{n,m} T_{ij,mn}$ is the probability of an incoming electron from the i^{th} channel being transmitted into the j^{th} channel. If $\mu_0 = \varepsilon_F$, $\mu_i = eV_i$, the Landauer-Büttiker formula is expressed in terms of the voltage V_i:

$$I_i = \frac{2e^2}{h}[(N_i - R_{ii})V_i - \sum_{i\neq j} T_{ij}V_j] \quad (2.75)$$

2.4 Experimental Methods

2.4.1 Fourier Transform Infrared Spectroscopy

IR spectroscopy measures the absorption of IR light by vibrations and can provide a "chemical fingerprint" with absorption peaks which correspond to the frequencies of vibrations involving the bonds of atoms in materials [81]. Fourier Transform Infrared (FTIR) spectroscopy is based on interference of radiation between two beams to yield an interferogram. Basic components of an FTIR spectrometer are the source, interferometer, detector, amplifier, and analog-to-digital convertor [82]. The most common interferometer used in an FTIR spectrometer is a Michelson interferometer, which consists of two perpendicular plane mirrors, one of which can travel in a direction perpendicular to the plane (Fig. 2.7).

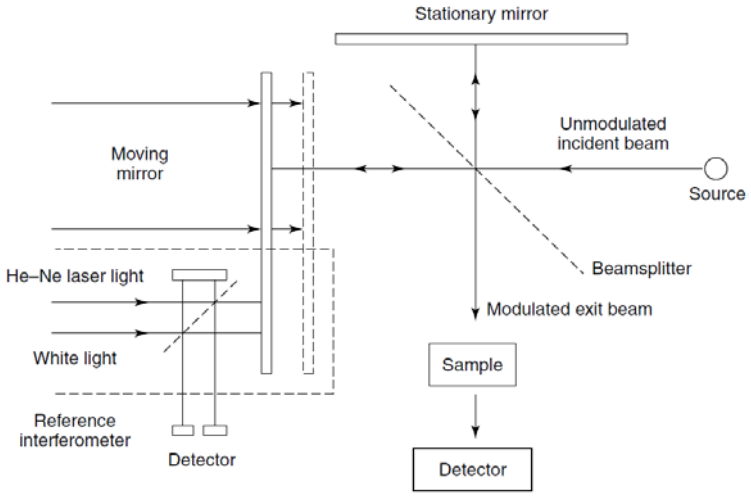

Figure 2.7: Schematic illustration of a FTIR Spectrometer [82].

In general, the FTIR spectrometer uses a Globar source and a pyroelectric detector incorporating deuterium triglycine sulfate (DTGS) in a temperature-resistant alkali halide window for the mid-IR region (400-4000 cm^{-1}). Mercury cadmium telluride (MCT), which is operating at liquid nitrogen temperatures, is used for especially the sensitive detection in mid-IR range. In the far-IR range (below 400 cm^{-1}), a high-pressure mercury lamp can be used as the light source, and Ge or InSb detectors, operating at liquid helium temperature, are employed [82].

The essential equations for FTIR spectroscopy are [82]

$$I(\delta) = \int_0^{+\infty} B(\bar{\nu})\cos(2\pi\bar{\nu}\delta)\, d\bar{\nu} \tag{2.76}$$

$$B(\bar{\nu}) = \int_{-\infty}^{+\infty} I(\delta)\cos(2\pi\bar{\nu}\delta) d\delta \tag{2.77}$$

where $I(\delta)$ is the intensity received at the detector; $B(\bar{\nu})$ is the spectral irradiance (in W m^{-1}). Equation (2.76) shows the variation in power intensity as a function of the difference in path length, δ, which is an interference pattern; and equation (2.81) shows the variation in intensity as a function of wavenumber [82].

The most important type of experiment to obtain an FTIR spectrum is producing an interferogram with and without a sample in the beam and transforming the interferogram into spectra of (a) the signal pass with a sample and (b) the signal pass without a sample. The ratio of (a) to (b) is the transmittance of the sample in the IR range. The resolution of a FTIR is determined by the maximum path difference between two arms.

2.4.2 THz/Far-IR Beamline in the Australian Synchrotron

THz/Far-IR beamline at the Australian Synchrotron covers the spectral range from THz to mid-IR regions. The Australian Synchrotron is an advanced third-generation accelerator with a 3 GeV storage ring with a horizontal emittance of 10.4 nm rad^{-1} [83]. A combination of radially polarized edge radiation and linearly polarized light is coupled to a Brüker IFS125HR FTIR spectrometer (Brüker Optics, Ettlingen, Germany). Fig. 2.8 is an image of the IFS125HR FTIR spectrometer.

Figure 2.8: The Brüker IFS125HR FTIR spectrometer at the THz/Far-IR Beamline, Australian Synchrotron.

The optical layout of the Brüker IFS125HR FTIR spectrometer is shown in Fig. 2.9. There are four different components in this spectrometer: the source, the interferometer, the sample chamber, and the detector. Experiments conducted at the Australian Synchrotron consist of phase transitions from 6 to 300 K. A spectral range of 25 to 700 cm^{-1} is achieved using 6 μm and 75 μm beam splitters. A helium cooled silicon-based thermo-electronic bolometer detector is employed to detect the THz/Far-IR signals. The NEP (noise equivalent power, $W/Hz^{1/2}$) of the detector is ~1.2 x 10^{-13} [33]. Low temperature experiments are conducted in a He closed-loop cryostat with a variable temperature insert (Cryo Industries of America, Inc., Manchester, NH, USA), equipped with diamond windows from 5 to 300 μm. Fig. 2.10 shows a schematic illustration of this closed-loop cryostat [84]. Sample chamber is filled with helium gas as a working medium for heat exchange. High precision target temperatures as low as 6 K are achieved by stepping by 10 K from 300 K.

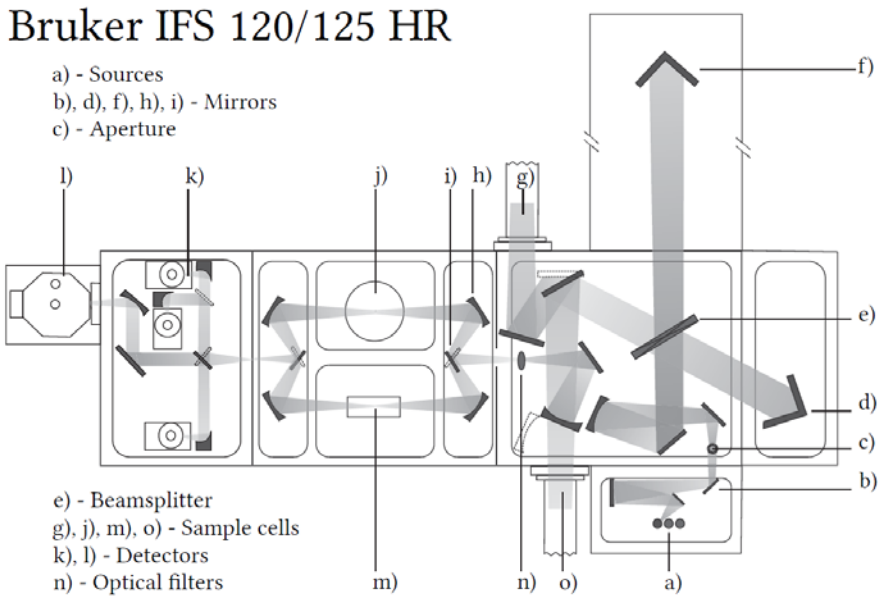

Figure 2.9: Optical scheme of the Brüker IFS125HR FTIR spectrometer [83].

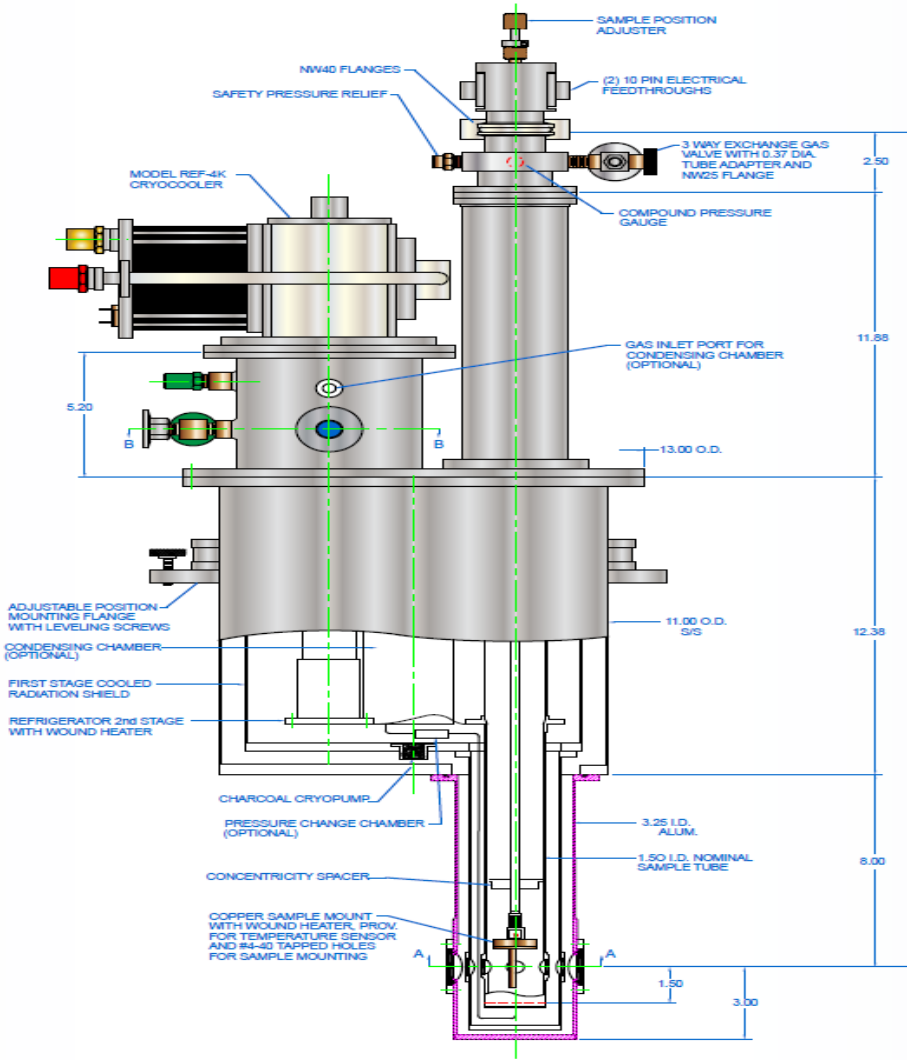

Figure 2.10: Schematic illustration of the closed-loop cryostat with a variable temperature insert [84].

2.4.3 Raman Spectroscopy

Raman scattering effect is inelastic scattering of excitation light by molecules. Interaction of a molecule with photons causes vibrations of its chemical bonds, leading to specific energy shifts in the scattered light can be identified in its Raman feature. Changes in molecular polarizability are required during the vibration for the Raman scattering effect to occur. Raman spectroscopy measures the wavelength shift of light due to vibrations. It provides information on peak intensity to quantity of a specific compound, peak shift to identify stress and strain states, peak width to reflect the degree of crystallinity, and polarization state (crystal symmetry and orientation). Typically, the components of a Raman spectrometer system are [85]:

• single and multi-wavelengths laser;

• lenses to focus the light onto samples and to collect the scattered light;

• filters to purify the reflected and scattered light so that only the Raman light is collected;

• diffraction gratings or prisms;

• sensitive detector.

The inVia^{TM} confocal Raman microscope (Renishaw plc, Gloucestershire, UK) is a Raman spectrometer coupled to a microscope (Fig. 2.11), which focuses a laser source onto specific areas, and then collects the light scattered off the sample surface and directs it through a Raman spectrometer. The capabilities of the Renishaw inVia^{TM} Raman microscope are:

• Standard modes: 514 nm Argon ion laser and 532 nm diode laser with 1,800 l/mm gratings.

• Standard mode laser spot size is 1.5 microns at 50× magnification.

• 325 nm, 442 nm, 633 nm, 785 nm, and 830 nm wavelength options.

Figure 2.11: The Renishaw inVia^{TM} Raman microscope at The Mark Wainwright Analytical Centre, UNSW.

2.4.4 Physical Properties Measurement System

The Physical Properties Measurement System (PPMS) DynaCool^{TM} is a multi-functional, and variable temperature control system that is optimized to perform a variety of physical properties measurements (Fig. 2.12). The DynaCool^{TM} PPMS is equipped with a ^{4}He-based temperature control system and gas flow technology [86].

Main Features [86]:

• Magnetic Field Range: 9 T and 14 T magnets available (-90,000 to 90,000 Oe for 9 T magnet; -140,000 to 140,000 Oe for 14 T magnet);

• Temperature range: No use of cryogenic liquids. 1.8 to 400 K (No overshoot, fast and sweep modes);

• Pressure: High vacuum (<10^{-4} torr);

• 25 mm diameter sample space;

• Electrical Transport Option (ETO): Resistance, Hall Effect, *I-V* Curves, Electrical Resistivity, Magnetoresistance, Critical Current, Differential Resistance $\frac{dV}{dI}$ vs. I_{bias} and $\frac{dI}{dV}$ vs. V_{bias};

• Thermal Transport Option (TTO): Thermal Conductivity, Heat Capacity, Seebeck and Nest Effects.

Figure 2.12: The Quantum Design PPMS DynaCool™ System at the ISEM, UOW.

Fig. 2.13 schematically illustrates the inside workings of the Quantum Design PPMS DynaCool™, including the cryostat control system, the chamber temperature control system, and the magnetic field control system [86]. Resistance measurements can be made with both in the ETO and the Resistivity options, respectively. In the ETO, measurements are performed using a 4-wire configuration with 2 channels at a time. The sample puck includes pre-mapped pads I_+, I_-, V_{A+}, V_{B+}, and V_- on both channel 1 and channel 2 (Fig. 2.14). Electrical contact with the sample and the channel input pads is provided via wire bonding and soldered and silver-painted wires. The resistivity option enables a 4-wire resistance measurement with 3 channels at a time. The sample puck includes pre-mapped pads for + and – current and voltage channels 1-3 [86].

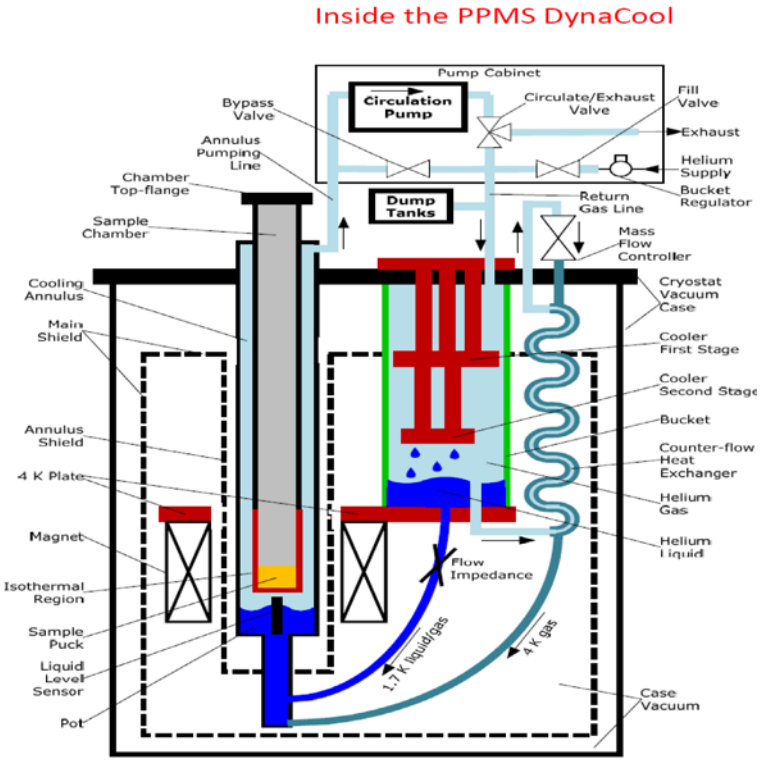

Figure 2.13: Inside view of the Quantum Design PPMS DynaCool™ [86].

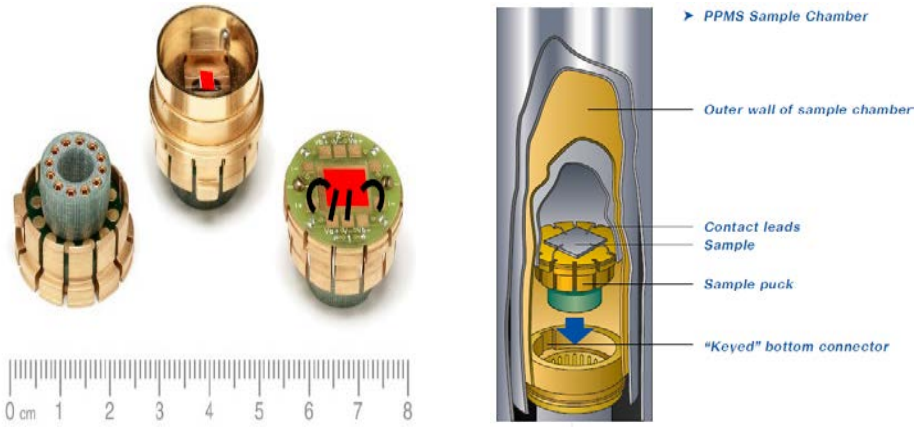

Figure 2.14: (a) Sample pucks (2.4 cm in diameter) for different measurements. (b) Sample mounted on pucks which inserts in the sample chamber [86].

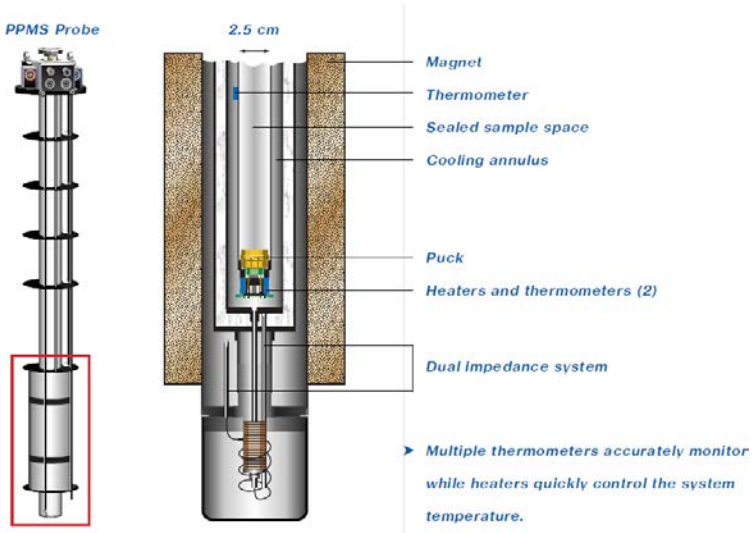

Figure 2.15: (a) PPMS probe. (b) PPMS probe which inserts into the sample chamber [86].

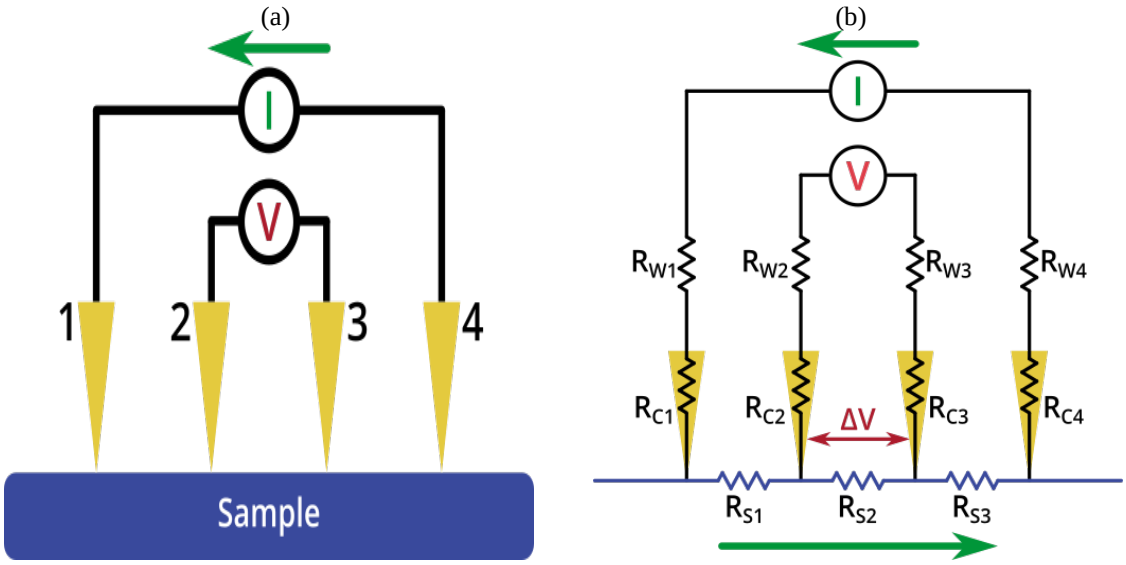

Figure 2.16: (a) Schematic diagram of a four-wire probe circuit [86].
(b) Equivalent circuit diagram of a four-wire probe, showing the wire resistances (R_W), contact resistances (R_C), and sample resistances (R_S). The green arrows represent current flow [86].

Using a four-wire method to connect a sample to the puck greatly reduces the contribution of leads and joints. The sample is then "mounted" on the puck and attached to the PPMS probe, which is inserted into the sample chamber, as shown in Fig. 2.15. In a four-wire resistance measurement, current is passed through the sample via two current leads, and two separate voltage leads measure the potential difference across the sample. Fig. 2.16 shows the schematic diagram of the four-wire method, and the equivalent circuit diagram.

2.4.5 X-ray Diffraction

X-ray diffraction (XRD) is the elastic scattering of x-ray photons by atoms in a periodic lattice, which is a rapid, non-destructive analytical technique to analyze materials properties, e.g. phase identification and structure. The main aims of X-ray diffraction are:

• Qualitative and quantitative phase analysis of pure substances and mixtures;
• Analysis of the influence of temperature and other non-ambient variables;
• Analysis of material micro-structures.

Miller indices (*hkl*) are used to identify different planes of atoms, which cut the axis lengths *a*, *b*, *c* or the axis intercepts in the reciprocal space $\frac{a}{h}$, $\frac{b}{k}$, and $\frac{c}{l}$, respectively. Observed diffraction peaks can be related to planes of atoms to assist in analyzing the atomic structure and microstructure. A powder X-ray diffractogram displays the scattered intensity versus the Bragg angle (2θ). It contains a few peaks, which are characterized by their position, intensity, and profile. Bragg's law describes the diffraction and interactions of X-rays in crystals as reflections from the atomic planes of the crystal lattice:

$$2d\sin\theta = n\lambda \tag{2.82}$$

where d is the interplanar spacing of lattice planes d_{hkl}, θ is the Bragg angle θ_B, 2θ is the angle between incident and reflected beam, n is the reflection order, and λ is the wavelength [87].

The intensity of peaks is mainly determined by the symmetry of crystals, the position of atoms in the unit cell, the number of electrons in atoms, the amount, and the absorption in materials. The shape of peaks is influenced by the diffractometer geometry, the X-ray components and their settings, the average crystal size, and defects in the crystal lattice [87]. The powder X-Ray diffractometer (GBC Scientific Equipment LLC, Hampshire, IL, USA) generates X-rays with Cu-Kα radiation (λ = 1.54 Å) working at the voltage and current of −40 kV and 25 mA, respectively. This setup permits peaks to be acquired throughout the range from 0 - 90 degrees. It uses the Bragg-Brentano reflection geometry, in which the diffraction vector is always normal to the surface of the sample [87].

Figure 2.17: The GBC Powder X-ray Diffractometer at the ISEM, UOW.

2.4.6 Scanning Electron Microscope

The JSM-7500FA (JEOL, Tokyo, Japan) is a 30-kV high resolution analytical field emission scanning electron microscope (FE-SEM) equipped with a high brightness conical field emission gun and a low aberration conical objective lens [88]. The gentle beam irradiation technique combination with the JSM-7500FA, and the improved overall stability of the JSM-7500FA makes it possible to observe specimen with resolution of 1 nm (Fig. 2.18).

Figure 2.18: The FESEM-JSM 7500FA at the UOW Electron Microscopy Centre.

2.4.7 Atomic Force Microscopy

Atomic force microscopy (AFM) is a type of high-resolution scanning probe microscopy, where a small probe with a sharp tip is scanned across a sample to measure the surface topography. The MFP-3D™ AFM (Asylum Research, Santa Barbara, CA, USA) that was used in this work is shown in Fig. 2.19. There is a head and an XY scanner to provide the cantilever position for accurate forces and topography measurements, measure exact position of each axis (X-Y). It holds

the cantilever chip, optical lever detection system, and vertical motion piezoelectric actuator and sensor, as well as the metal plate on which the head and scanner sit [89]. Its capabilities include the contact mode and tapping mode.

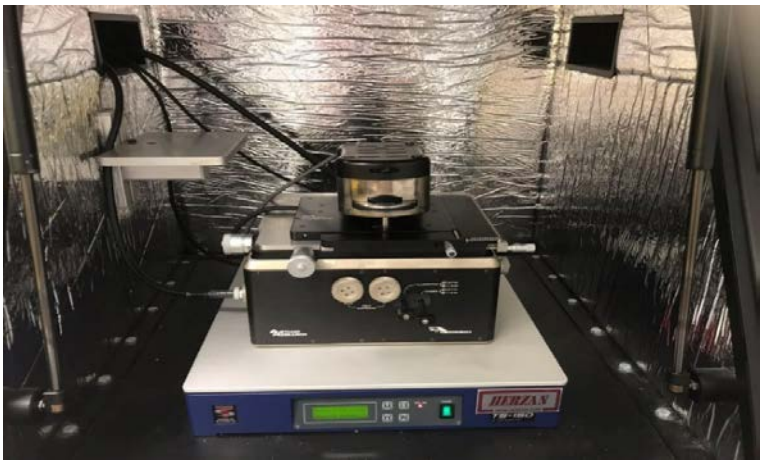

Figure 2.19: The MFP-3D™ AFM at the ISEM, UOW.

2.4.8 Dynamic Mechanical Analysis

The Dynamic Mechanical Analysis (DMA) is a powerful tool for determining viscoelastic properties and enable compression and tensile testing of soft materials [90].

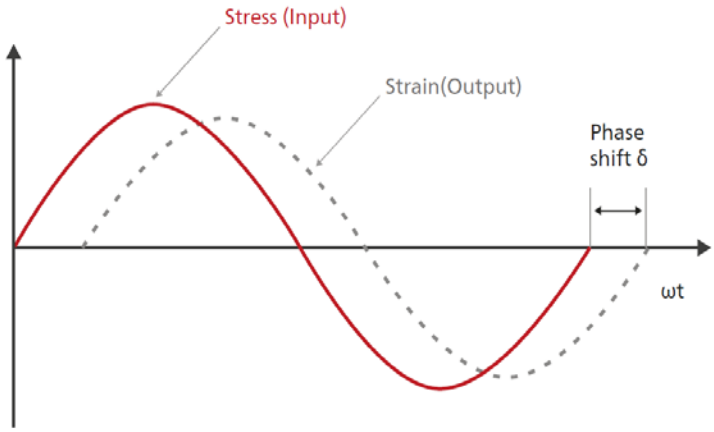

Figure 2.20: The physical principle of DMA measurement [90].

The viscos-elastic properties cause shifting of the corresponding stress and stain curves, with the phase shift δ (Fig. 2.20). The strain ε will be split into "in-phase" and "out-phase" parts via Fourier transformation. The real and imagery components of the complex modulus G^* (measure of resistance to deformation) are the storage modulus G' ("in-phase" response, or the ability to store energy) and the loss modulus G'' ("out-phase" response, or the ability to lose energy), respectively. The loss factor $\tan\delta$ is the ratio of the loss modulus G'' to the storage modulus G', which reflects the mechanical damping or internal friction of materials [90]:

$$G^* = G' + iG'' \tag{2.83}$$

$$\tan\delta = \frac{G''}{G'} \tag{2.84}$$

$$G' = \frac{Stress}{Strain} * \cos\delta \quad (2.85)$$

$$G'' = \frac{Stress}{Strain} * \sin\delta \quad (2.86)$$

The storage modulus G' (elastic response) refers to the stiffness and the loss modulus G'' (viscous response) is related to the oscillation energy transformed into heat. Fig. 2.21 is an image of the DMA 242 E Artemis (NETZSCH, Germany) at the Intelligent Polymer Research Institute (IPRI), UOW. This system can set the sweep frequency range from 0.01-100 Hz with the temperature range from -170 °C to 600 °C. The moduli range from 10^{-3} to 10^{6} MPa with damping rates from 0.005 to 100. This DMA operates in bending, shearing, tension, and compression modes.

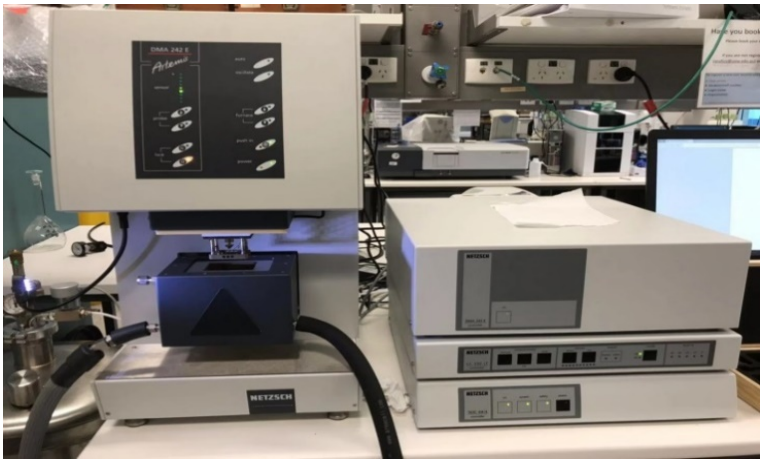

Figure 2.21: The NETZSCH DMA 242 E Artemis at the IPRI, UOW.

2.4.9 Uncertainty of Measurements

Measurement uncertainties can come from the measuring instruments, from the item being measured, the environment, the operator, and other sources. Such uncertainties can be estimated using statistical analysis of a set of measurements and using other kinds of information about the measurement process. Specifically,

• Measurement uncertainties in FTIR spectroscopy arise from several sources of random or symmetric errors, e.g. signal noise, sample alignment, and thickness measurement variation, etc. The Brüker IFS125HR FTIR spectrometer gives high quality spectra at a resolution of up to 0.0024 cm^{-1}. (However, such high resolution was not used for this thesis).

• Measurement uncertainties in Raman spectroscopy are mainly due to the calibration and the fitting error. Error comes from the pixel size of CCD detector, laser wavelength accuracy, and so on. When we record the Raman spectrum for some unknown sample, its peak position is extracted by fitting using a Lorentzian function, which also gives a fitting error. Optical repeatability of the inVia^{TM} confocal Raman microscope is smaller than 0.5 mm, and optical stability is smaller than 2 mm in 8 hours.

• Measurement uncertainties of the PPMS are produced by the accuracy of temperature controllers, bias, changes due to drift, poor readability, noise for electrical instruments.

• The source of measurement uncertainty of a DMA comes from computer error due to data processing. The data processing in the DMA is largely automated.

Chapter 3

Double Resonant Raman Scattering and Disorder-induced Band Dispersion for Aerographite and Graphitic Systems at Different Excitation Energies

3.1 Introduction

Carbon is a fantastically versatile element, owing to its three different hybridization states, sp^1, sp^2, and sp^3. Diverse carbon allotropes, such as carbene (sp^1 hybridization, linear), graphene/carbon nanotubes (sp^2 hybridization, plane trigonal), and diamond (sp^3 hybridization, tetrahedral) are formed from carbon atoms according to their different sp^n hybridizations. The focus in this chapter is on graphite and Aerographite. Graphite is a three-dimensional layered material formed by stacking single graphene sheets with honeycomb structures made up of carbon atoms in sp^2 hybridization, and features covalent σ and π bonds that are held together by weak interlayer van der Waals forces [47,61]. Aerographite is an ultralight weight porous graphite aerogel, which consists of an interconnected network of tubular carbon forms, resulting in an ultra-low density of 0.18 mg/cm^3 and a large specific surface area of 210 m^2/g. It has numerous potential applications in supercapacitors, lightweight batteries, water purification and so on [12,13].

Raman spectroscopy is a non-destructive experimental technique used to investigate lattice dynamics, structural, electronic, and vibrational properties, electron-phonon interactions, disorder, defects, and quantum confinement of sp^2 carbon materials. Raman sharp spectral lines exhibit a wide variety of features corresponding to carbon allotropes and reflect fine structural information [47,91-101]. Raman spectra of "plain" graphite and graphene are well understood from both theoretical and experimental aspects. Raman spectra of Aerographite at different excitation energies at the visible range have not been reported in detail, however. This results in an obstacle to our understanding and application of Aerographite. Systematic investigations of the Raman spectra of Aerographite and relatively new graphitic systems at different excitation energies are therefore highly desirable.

In this chapter, the Raman spectra of Aerographite and "plain" graphitic systems, i.e. graphite flakes, graphite oxide, and kish graphite, are investigated. The intensity ratio between the graphitic-feature (G) and the disorder-induced (D and 2D) bands are studied using different excitation energies. Single-peak fitting and deconvolution techniques are employed to interpret the properties of Aerographite and graphitic systems. Such study is important for further understanding the fine structures and physical properties of Aerographite using Raman scattering spectral studies and band assignments. The main question is: what makes Aerographite superior to "plain" graphite systems and how are its properties are related to its unique microstructure? In this chapter, I endeavor to reveal how disorder, defects, and symmetry breaking affect vibrational modes in sp^2 carbon systems and demonstrate the usefulness of Raman spectroscopy in identifying

various microstructures of these systems; how to relate specific defects to their corresponding disordering processes; and how to obtain quantitative information on the number of defects in the lattice.

3.2 Experimental Details

3.2.1 Sample Preparation

Aerographite was prepared and provided by the collaborator-Professor Yogendra K. Mishra (Keil University, Germany), which was synthesized by a single-step CVD method, as described in references [12,13]. Firstly, ZnO tetrapods were fabricated using an FTS approach. A mixture of Zn metal micro particles and PVB powder was rapidly heated in a muffle-type furnace to 900 °C under ambient air. Then, ZnO networks mixed with the metal micro particles were fabricated by homogenously mixing metal micro particles (Al, Bi, Cu, Fe, Sn) with the ZnO tetrapod powder before compressing and re-heating. The weight ratio between the ZnO tetrapod powder and the metal micro particles was 20:1. The volume and density of the ZnO networks were 1 cm^3 and 0.3 g/cm^3, respectively. Then Aerographite was fabricated by the direct conversion of ZnO networks in a CVD process. Graphitic carbon was grown at 760 °C on the top of the ZnO network while simultaneously removing the ZnO template. Toluene was used as the carbon source, and H_2 was used for ZnO reduction. The porous ZnO network acts as sacrificial template for Aerographite and its architecture is mainly decided by the structural morphology of the sacrificial ZnO template. The carbon-feeding rate is the key to adjusting the density of Aerographite.

Graphite flakes (with 99% carbon basis, and particle size of 300 μm) were purchased from Sigma-Aldrich (St. Louis, MO, USA). Graphite oxide powder (with a diameter of 0.5–5 μm, thickness of 1–3 nm) was supplied by ACS Material LLC (Pasadena, CA, USA). Kish graphite (Grade 200 with flake size: 0.7–2 mm, ultrapure: carbon > 99.2%, moisture < 0.35%) was supplied by Graphene Supermarket (Calverton, NY, USA). Graphite flakes, graphite oxide, and kish graphite were pressed into pellets using a laboratory press (International Crystal Laboratories, Garfield, NJ, USA) at the pressure of 4000 psi.

3.2.2 Sample Characterization Methods

Phase structures of samples were investigated using a powder X-ray diffractometer (GBC Scientific Equipment LLC, Hampshire, IL, USA), which generates X-rays with Cu-Kα radiation (λ=0.154 nm) working at an acceleration voltage and current of −40 kV and 25 mA, respectively. The diffraction patterns were collected at room temperature in the 2θ range from 10 to 80° with a step size of 0.02° and scan speed of 1°/min. Field emission scanning electron microscopy (FE-SEM, JEOL JSM-7500FA, Tokyo, Japan) was employed to study the morphology of the products.

Raman spectra were collected on a confocal Raman microscope (Renishaw plc, Gloucestershire, UK) in an ambient environment using a backscattering geometry with four different excitation

lasers: a 442 nm (excitation energy E_L = 2.80 eV, source power 19.5 mW) Hg-Cd laser with a 2400 1/nm grating; a 514 nm (E_L = 2.41 eV, source power 73.8 mW) Ar ion laser; a 532 nm (E_L = 2.33 eV, source power 33.6 mW) diode laser; and a 633 nm (E_L = 1.96 eV, source power 13.0 mW) He-Ne laser with a 1800 1/nm grating. The laser was focused on the sample via a Leica 50× magnification objective (Numerical aperture, N.A. = 0.75), using an exposure time of 10 s, and 1-10 accumulations in extended mode. Microscope optics were used to focus the laser beam onto the sample and to collect the backscattered light. The laser beam power was adjustable from 10% to 100% of the source power. The power was adjusted to prevent sample damage but to ensure the best SNR. Detection was achieved with an air-cooled charge-coupled device (CCD) camera. Raman shifts of the excitation frequency can be measured for visible wavelengths of 442 nm, 514 nm, 532 nm, and 633 nm with a spectral resolution of ~1 cm^{-1}. Spectra were recorded by spanning the regions 100-4000 cm^{-1} for the wavelengths of 442 and 514 nm and then 60-4000 cm^{-1} for the wavelengths of 532 and 633 nm. The calibration of this spectrometer was checked by using the line at 521 cm^{-1} of a silicon sample.

3.3 Results and Discussion

3.3.1 FE-SEM

FE-SEM images of Aerographite are shown in Fig. 3.1. Aerographite appears to have a random and disordered three-dimensional porous architecture. The open porous structure consists of an interconnected network of hollow, graphitic tubes of ~μm-sized diameter and ~nm-sized wall thicknesses (Fig. 3.1 (a)) [12,13]. They form a hollow network, which consists of a transition state between amorphous carbons and those ordered graphitic carbons with sp^2 hybridization in the hollow tube, as shown in the Fig. 3.1 (b).

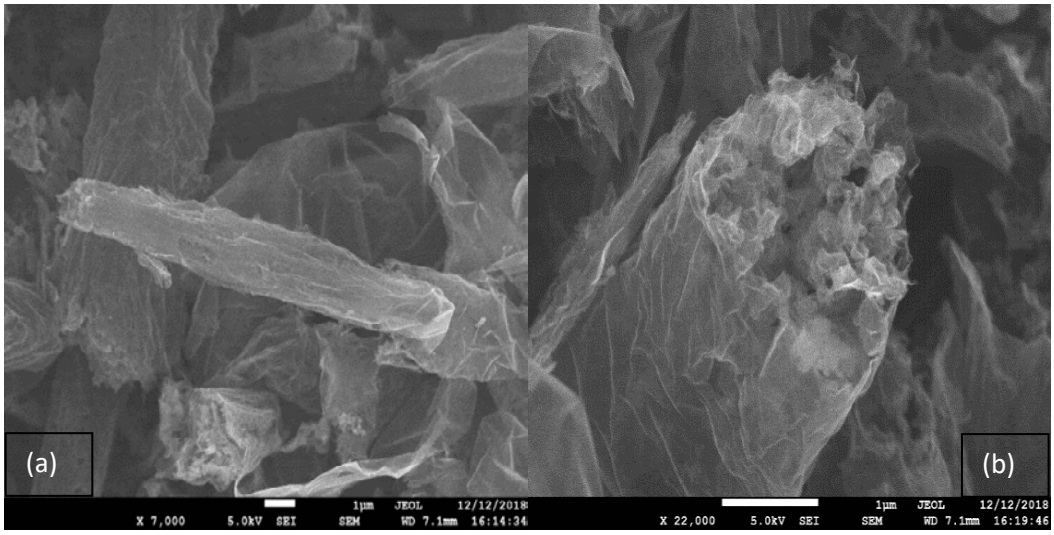

Figure 3.1: FE-SEM images of Aerographite.
(a) Shell-graphitic Aerographite. (b) Aerographite with porous graphite architectures. There are the scale bars (1 μm) in the SEM images.

3.3.2 X-ray Diffraction (XRD)

The powder XRD patterns of Aerographite and graphite oxide are shown in Fig. 3.2 (a). There are several sharp peaks for Aerographite sample in the 2θ range of 10 to 80°, which can be identified as peaks of residual ZnO at: 32.3° (100), 36.8° (002), 40.2° (101), 48.0° (102), 57.1° (110), 63.3° (103), 66.8° (200), 68.3° (112) and 69.5° (201) [131]. A broad peak is also observed at 18°. It is possible that the background of the XRD spectrometer and Kapton tape contributes to this peak [102].

There are three broad peaks in the XRD reflection of graphite oxide, i.e., 11.4° (001), 22.6° (002), and 43.1° (100) [128]. The diffraction intensity is known to be strongly modified by the thermal vibrations of carbon atoms, and the lattice spacing, d_{002}, increases from 0.20 nm (for graphite) to 0.25 nm (for graphite oxide produced by the Hummers method, which is used to oxidize graphite into graphite oxide) [102]. Only (00l) and (hk0) patterns are present in the XRD patterns of graphite oxide because its tubularly stacked structure [102].

The XRD patterns of graphite flakes and kish graphite are compared in Fig. 3.2 (b). These patterns feature sharp peaks, indicating that the samples have no significant structural disorder. Their XRD reflections are identical in the 2θ range of 10 to 80°, i.e. 27.5° (002), 49.9° (102), 55.5° (004), 60.6° (103), and 72.1° (104). This indicates that graphite flakes and kish graphite are *c*-axis aligned. It corresponds to the XRD pattern of graphite, which represents the perpendicular direction (*c*-axis) to the graphite hexagonal planes [102]. No impurity-related phases or inclusions were observed.

In summary, the XRD patterns show that Aerographite and graphite oxide are structurally highly disordered, showing only broad XRD features. Kish graphite and graphite flakes, on the other hand, give sharp XRD peaks corresponding to a graphitic structure. Therefore, they are structurally highly ordered. The difference in XRD patterns between these two groups of the samples will also be reflected in their Raman spectra.

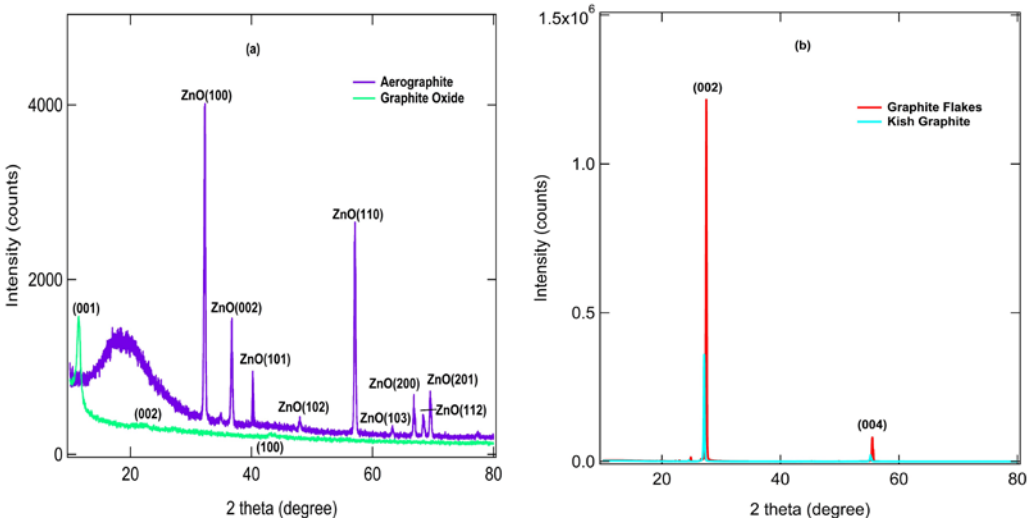

Figure 3.2: XRD spectra of Aerographite and Graphitic Materials.
(a) Aerographite and graphite oxide. (b) Graphite flakes and kish graphite.

3.3.3 Raman Scattering Spectra

Graphite has four carbon atoms in the unit cell, resulting in twelve phonon modes at the Γ point, and it belongs to the D_{6h}^4 point group ($P6_3/mmc$ space group). The phonon modes of graphite at the Γ point can be expressed as [47,61,92-100]:

$$\Gamma_{Graphite} = A_{2u}(IR) + 2B_{2g} + E_{1u}(IR) + 2E_{2g}(R) \quad (3.1)$$

where the A_{2u} and E_{1u} representations are the translations of the plane; the B_{2g} mode is an optical phonon for vibrations where carbon atoms move perpendicular to the plane; and E_{2g} is the in-plane optical mode. The phonon modes are thus: two double degenerate Raman active E_{2g} modes (1580 and 42 cm^{-1}); two IR active A_{2u} and E_{1u} modes (868 and 1588 cm^{-1}); and the other two are "silent" B_{2g} modes (neither Raman active nor IR active, one is at 127 cm^{-1} and another one occurs at 870 cm^{-1}).

The main features in the Raman spectra of graphitic materials are the G (~1580 cm^{-1}) and D (~1350 cm^{-1}) bands [47,61,92-100]. The G band (~1580 cm^{-1}, E_{2g} symmetry) corresponds to the double degenerate LO and TO phonon modes at the first Brillouin zone center, originating from the in-plane stretching vibrations of the C–C bonds. The G band is the only Raman active band due to a first-order Raman scattering process. It is sensitive to strain effects and external perturbations, which cause symmetry breaking of the hexagonal structure and modifications of the planar surface. The disorder induced D band (~1350 cm^{-1}) arises from a second-order double resonant Raman scattering process, which is due to the A_{1g} breathing mode of sp^2 rings. It involves an elastic scattering of the excited electrons by a defect followed by an inelastic scattering of electrons by TO phonons near the *K* point of the Brillouin zone. It requires a defect for its activation and is visible only with structural defects or at edges of the crystallites [47,92,93]. The activation process in the intervalley region involves: (1) a photon to produce an electron-hole pair; (2) electron-phonon scattering with a momentum exchange $q \sim k$; (3) defect scattering; and (4) electron-hole recombination [104]. Momentum conservation in the Raman scattering process will be satisfied where defects provide the missing momentum, and phonon will make a transition from the "silent" to the Raman active mode through symmetry breaking and a relaxation of wave-vector selection rule (due to finite crystal size effects), giving rise to the D band, which appears in the range from 1280 to 1350 cm^{-1}. This band exhibits dispersion behavior regarding the laser excitation energy (1.0 eV$< E_L <$ 4.5 eV) under resonant conditions [47,61,92,93,103,104].

Graphite with significant defects shows additional disorder related peaks, the D′ (~1620 cm^{-1}), 2D (also called G′, ~2710 cm^{-1}), and (D+D′) (~2970 cm^{-1}) peaks, originating from intravalley double resonance Raman scattering and a combination mode, respectively. The second-order Raman scattering process will generate the 2D (overtone of the D peak, arising from iTO phonons at the *K* point, ~2710 cm^{-1}) and 2D′ (overtone of the D′ peak, arising from LO phonons at the Γ point, ~3240 cm^{-1}) peaks due to the intravalley double resonance Raman scattering process [47,61,92,105]. These 2D and 2D′ bands are sensitive to small changes in both electronic and

vibrational structures, and act as a probe for electrons and phonons in sp^2 carbon systems. The inter-plane "shear" mode (C peak, E_{2g} symmetry) in graphitic materials is also observed at ~42 cm^{-1} due to the relative motion of the planes [106]. All the bands that are observed in the graphitic materials are due to in-plane vibrations of the graphitic layers, and the evolution of the spectra depends on the dimensions and structural perfection of the layers [60].

Raman spectra of graphite flakes, graphite oxide and kish graphite are displayed in the Fig. 3.3 for different excitation energies. Kish graphite and graphite flakes have very similar Raman spectra, with well-defined sharp peaks. Graphite oxide, however, gives broader Raman peaks which are not completely separated from each other. This is consistent with XRD data, where graphite oxide gave only broad features implying strong structural disorder, while kish graphite and graphite flakes gave sharp XRD peaks (see Fig. 3.2). Regardless of these differences, all three samples exhibit the G band, the disorder-induced D band, the overtone 2D band and other combination modes. Vibrational modes are assigned, and summarized band information is given in Table 3.1, based on the reports on graphitic structures [61]. All values are from Raman measurements in this work.

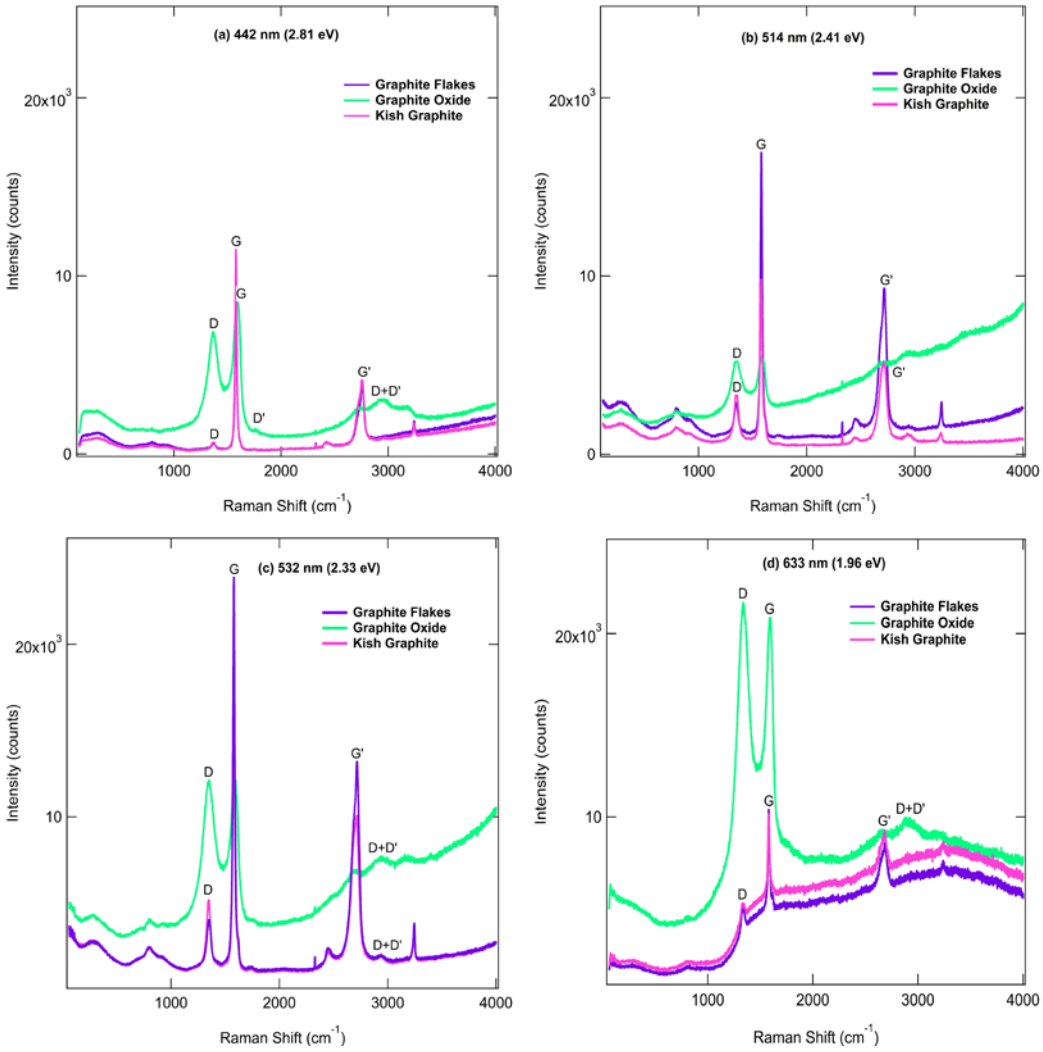

Figure 3.3: Raman spectra of graphitic materials excited by different photon energies from 1.96 eV to 2.81 eV.

TABLE 3.1. Raman band positions of graphitic materials by different photon energies from 1.96 eV to 2.81 eV.

Wavelength (nm)	Graphite Flakes	Graphite Oxide	Kish Graphite
442	1371 cm^{-1} D 1578 cm^{-1} G 2424 cm^{-1} T+D 2756 cm^{-1} G' (2D)	1351 cm^{-1} D 1580 cm^{-1} G 2452 cm^{-1} T+D 2719 cm^{-1} G' (2D)	1351 cm^{-1} D 1581 cm^{-1} G 2453 cm^{-1} T+D 2717 cm^{-1} G' (2D)
514	1365 cm^{-1} D 1596 cm^{-1} G 2715 cm^{-1} G' (2D) 2944 cm^{-1} D+G	1353 cm^{-1} D 1581 cm^{-1} G 2677 cm^{-1} G' (2D)	1346 cm^{-1} D 1580 cm^{-1} G 2680 cm^{-1} G' (2D) 2920 cm^{-1} D+G
532	1368 cm^{-1} D 1578 cm^{-1} G 2429 cm^{-1} T+D 2755 cm^{-1} G' (2D)	1352 cm^{-1} D 1582 cm^{-1} G 2464 cm^{-1} T+D 2727 cm^{-1} G' (2D) 2948 cm^{-1} D+G	1349 cm^{-1} D 1578 cm^{-1} G 2457 cm^{-1} T+D 2710 cm^{-1} G' (2D) 2941 cm^{-1} D+G
633	1325 cm^{-1} D 1581 cm^{-1} G 2687 cm^{-1} G' (2D)	1333 cm^{-1} D 1588 cm^{-1} G 2653 cm^{-1} G' (2D) 2887 cm^{-1} D+G	1336 cm^{-1} D 1580 cm^{-1} G 2677 cm^{-1} G' (2D)

[a] T means the phonon vibrational modes that is triply degenerate [61].

Raman spectra of Aerographite excited by four excitation energies in the visible range, namely 2.81 eV (442 nm), 2.41 eV (514 nm), 2.33 eV (532 nm) and 1.96 eV (633 nm) are shown in Fig. 3.4. Its Raman spectra exhibit typical spectral features of graphitic materials. The D and G peaks are the first-order Raman modes, which are located at 1366 and 1597 cm^{-1} when excited by the 442 nm laser, at 1342 and 1590 cm^{-1} when excited by the 514 nm laser, at 1339 and 1592 cm^{-1} when excited by the 532 nm laser, and at 1330 and 1594 cm^{-1} when excited by the 633 nm laser. The second-order Raman modes, the 2D and the (D+G) modes, are present at the positions of 2710 and 2922 cm^{-1} for 442 nm excitation, 2675 and 2917 cm^{-1} for 514 nm excitation, 2688 and 2890 cm^{-1} for 532 nm excitation, and 2728 and 2894 cm^{-1} for 633 nm excitation.

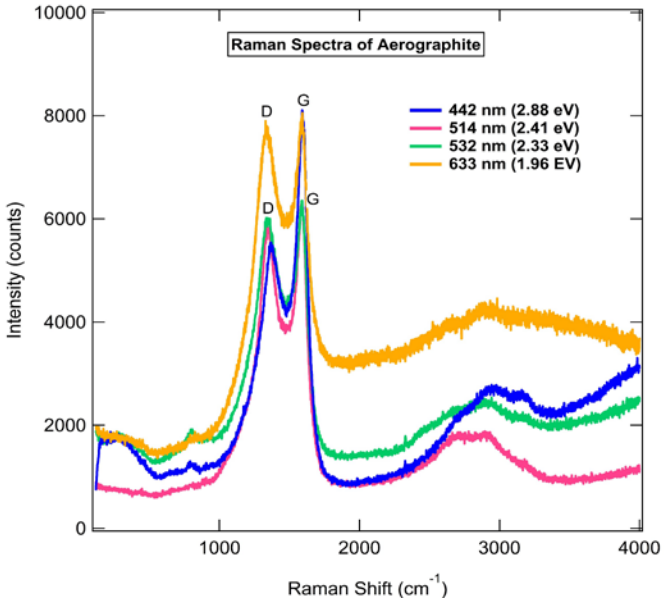

Figure 3. 4: Raman spectra of Aerographite excited by different photon energies from 1.96 eV to 2.81 eV.

The G band of Aerographite originates from a single resonance Raman scattering process associated with a doubly degenerate mode, which splits into LO and in-plane TO phonon modes at the Brillouin zone center [107,108]. It is due to the phonon softening and coupling with π electrons, which implies a softening of the Raman frequency near the Γ point. The presence of the G peak is related to the existence of structures similar to graphite in Aerographite, which contains sp^2 carbon networks. It also corresponds to the E_{2g} Raman active phonons at the Γ point in the Brillouin zone of graphite. The G mode is a zone-center optical mode ($k = 0$) in graphite materials, while the D and D′ modes are not zone-center optical modes ($k \neq 0$); they become Raman active due to double resonance scattering, as described later in this chapter [109,110]. The linewidth of the G mode in Aerographite is larger than that of graphite flakes and kish graphite, mainly due to the crystal disorder.

The D (A_{1g} symmetry) and D′ (E_{2g} symmetry) peaks in Aerographite are due to defect-induced Raman features and breathing modes of six-atom rings, which originate from a double resonance Raman process involving inter-valley scattering of TO phonons near the *K* point. The D′ peak is joined with the G peak; it appears at the right flank of G peak, as seen in Raman spectrum of graphite flakes (Fig. 3.7.b). These two peaks are strongly dispersive with excitation energies due to a Kohn anomaly at the *K* point [64,111]. This arises because of the existence of non-equivalent C-C bands, which is a consequence of the coupling of π-π^* electronic transitions with phonons near the *K* point in this disordered structure. Totally symmetric phonons at the *K* point are affected by interactions with π electrons, which leads to the selective and strong activation of D and D′ peaks in Raman spectra of Aerographite and graphitic materials containing structural and electronic modifications, i.e. disorder, defects (laser damage, or ion implantation), symmetry breaking and quantum confinement. Because of disorder effects in the FTS approach and the resulting unique shell structure of Aerographite, the degree of graphitization will be altered by amorphous sp^2 carbons generated by defects, which is reflected by different spectral profiles of Aerographite compared to those of other graphitic materials with their edge effects [96,112-114].

The 2D peak in Aerographite is the second-order mode of the D peak, which is associated with two-phonon inter-valley double resonance Raman scattering, with the two phonons having opposite momentum in the highest optical branch near the *K* point of the Brillouin zone. It splits into multiple peaks as the layer numbers increase, which reflects the evolution of electronic structures. The (D+G) combination mode in Aerographite is observed due to the disorder-induced scattering, edge functionalization, and defects formed during the FTS growth method of Aerographite. It is an optical response dominated by exciton effects, especially for excitation energies close to the optical gap [115,116]. There is a “blue-shift” (shift to higher frequency) with increasing laser excitation energy observed for the D and 2D bands, whereas the position of the G band is essentially invariant. The phonon energies (band positions) of the D and 2D bands are plotted against excitation energy in Fig. 3.5.

Both the D and the 2D bands show a down-shift in frequency with increasing wavelength (i.e. from ~1366 cm^{-1} at 442 nm (2.81 eV) to ~1330 cm^{-1} at 633 nm (1.96 eV) for D; and from ~2710 cm^{-1} at 442 nm (2.81 eV) to ~2728 cm^{-1} at 633 nm (1.96 eV) for 2D). The magnitude of the 2D shift (~98 cm^{-1}/eV) from 442 nm (2.81 eV) to 633 nm (1.96 eV) is approximately twice that of the D shift (~46 cm^{-1}/eV). This is assigned to the fact that the 2D band is the overtone of the D band. The variation in the D and 2D bands with excitation energy reflects the microstructure of Aerographite, since the variation in the extent of wave-vector leads to selection rule breakdown. This dispersion is attributed to the disorder-induced two-phonon scattering process, which involves the combination of an optical phonon at the *K* point in the Brillouin zone and an acoustic phonon with a momentum that is determined by the double resonant enhancement condition [101,103,117,118]. There is the data scatter in Fig. 3.5, reflecting the possible measurements uncertainities associated with instrumental, fitting and procedural errors. It is possible that the point on the sample at which laser is focused also changes when changing the laser (due to a slight misalignment of optics). The samples are inhomogeneous, resulting in data scatter for different E_L.

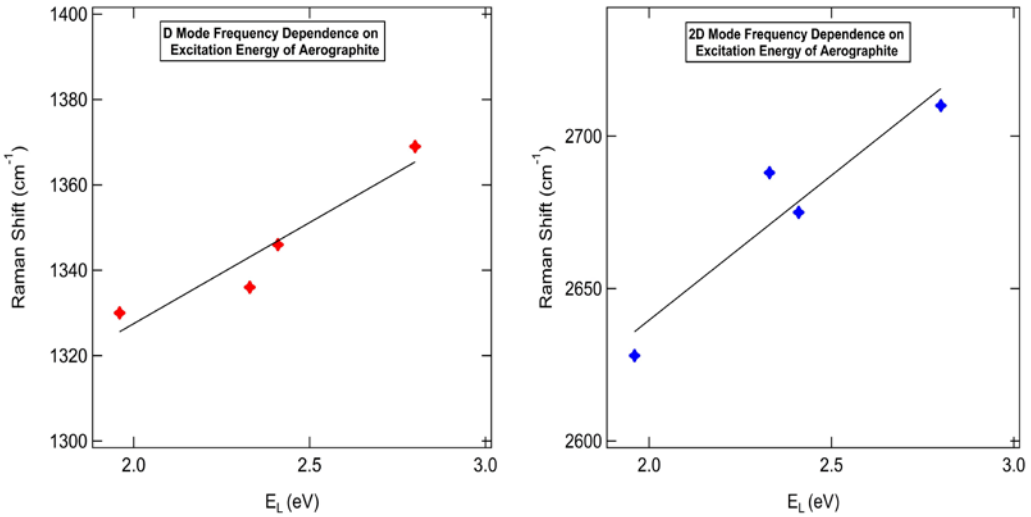

Figure 3. 5: Peak positions of the D and 2D bands as a function of laser excitation energies of Aerographite. Lines fit to the data.

A three-stage model based on Raman spectra was used to interpret the evolution of disorder for carbon atoms. This is dependent on the configuration of the sp^2 sites in sp^2-bonded clusters and the ratio of sp^2 and sp^3 hybridization, which control the positions, intensities, and widths of the G and D peaks for various forms of carbon from graphite to amorphous carbon [107,119]. In stage two (nano crystallite graphite to low sp^3 amorphous carbon), there are no more well-defined second-order Raman peaks, but a broad feature is present from ~2300 cm^{-1} to ~3200 cm^{-1} that is modulated by the 2D and 2D′ bands [107,119,120]. This is exactly as observed for Aerographite, indicating again a highly disordered structure. Therefore, there is good agreement between the results from XRD patterns, FE-SEM images and Raman scattering spectral studies.

3.3.4 Analysis of Raman Spectra by Peak Fitting and Deconvolution

To quantitatively interpret the Raman spectral features and distinguish the overlapping peaks, peak fitting analysis of the Aerographite data was carried out via the multi-peak fitting package of IGOR Pro (Wavemetrics Inc., Portland, OR, USA). By fitting the measured Raman peaks with appropriate profiles, precision in the peak position and intensity can be significantly improved. Fig. 3.6 shows peak fitting analysis of the Raman spectra of Aerographite at different excitation energies. The D and G peaks were fitted by Lorentzian functions, with a cubic baseline.

(a) Laser excitation energy 2.81 eV (442 nm) (b) Laser excitation energy 2.41 eV (514 nm)

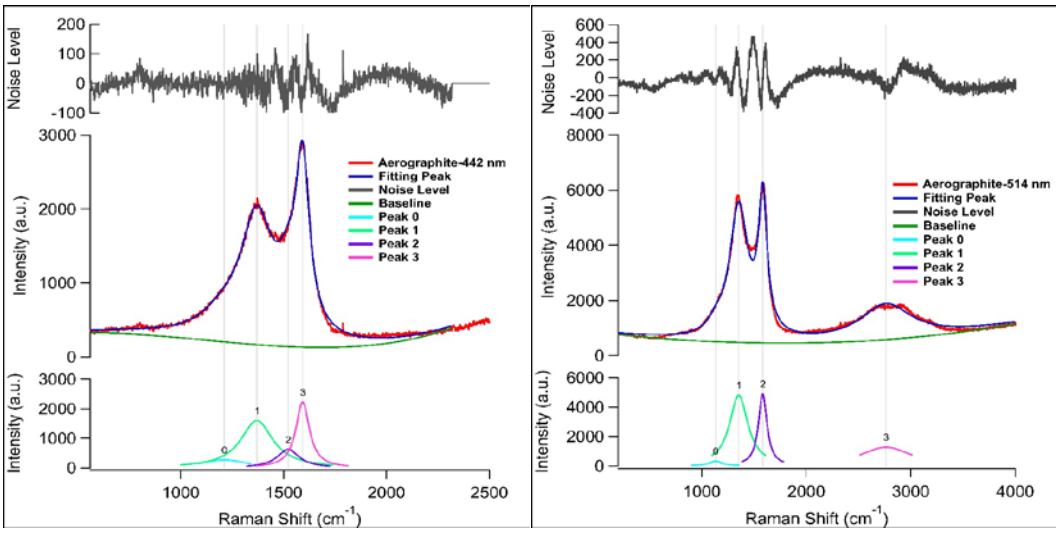

(c) Laser excitation energy 2.33 eV (532 nm) (d) Laser excitation energy 1.96 eV (633 nm)

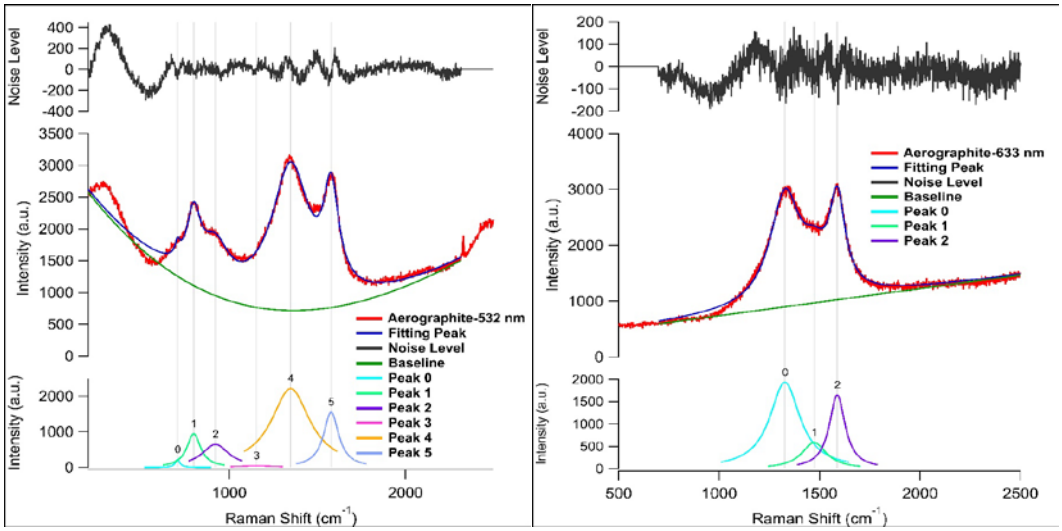

Figure 3.6: Peak fitting for Raman spectra of Aerographite by different photon energies from 1.96 eV to 2.81 eV. Noise level denotes difference between measured and fitted curves.

The Lorentzian curve used here is obtained as a resonance curve in a simple damped oscillator model. The Lorenzian function $I(P)$ is defined as:

$$I(P) = I_0 + A/[(P - P_0)^2 + B] \tag{3.2}$$

The best values of the coefficients are the ones that minimize the value of Chi-square,

$$\sum_i \left(\frac{I - I_i}{\sigma_i}\right)^2 \tag{3.3}$$

where I is a fitted intensity value for a given point, I_i is a measured intensity value for the point and σ_i is an estimate of the standard deviation for I_i. Regarding the quality of the fitting, it may be assessed by comparing it visually with the measured data-points.

Raman spectral parameters are summarized in Table 3.2. In the Table 3.2, the D band shows a down-shift in frequency with increasing wavelength, whereas the position of the G band is stable. For example, the position of the D band was shifted from ~1370 cm^{-1} at 442 nm (2.81 eV) to ~1354 cm^{-1} at 514 nm (2.41 eV) and ~1348 cm^{-1} at 532 nm (2.33 eV), and then to ~1327 cm^{-1} at 633 nm (1.96 eV). In contrast, the location of the G band was ~1593 cm^{-1} (442 nm, 2.81 eV), ~1583 cm^{-1} (514 nm, 2.41 eV), ~1578 cm^{-1} (532 nm, 2.33 eV), and ~1577 cm^{-1} (633 nm, 1.96 eV), respectively. In addition, because of the small crystal size of Aerographite, a higher frequency shift was observed to ~1593 cm^{-1} (Aerographite) from ~1580 cm^{-1} ("plain" graphite) in the G band, probably due to the overlap with the D′ band at ~1620 cm^{-1}. The fitted line widths (FWHM) of the D and G modes in the remnant spectrum are 191 and 80 cm^{-1} (442 nm, 2.81 eV), 214 and 99 cm^{-1} (514 nm, 2.41 eV), 267 and 105 cm^{-1} (532 nm, 1.96 eV), respectively. The FWHM of the D band tends to increase with decreasing excitation energy, indicating a decrease the disorder degree of graphitization as excitation energy reduces. This confirms that the first-order dispersive D mode originates from disorder and electron-phonon coupling with the same wave vector in the Brillouin zone.

TABLE 3.2. Spectral parameters obtained from the peak fitting of Raman spectra of Aerographite.

Wavelength (nm)	Position (cm^{-1})	Vibration Mode	Width (FWHM, cm^{-1})	Height (Intensity, Counts)
442	1370.1	D	190.81	1600
	1592.6	G	80.199	2222
514	1353.5	D	214.47	4808.2
	1583	G	98.925	4881
532	1348.1	D	266.71	2210.9
	1578	G	104.9	1547.9
633	1327.2	D	183.89	1933.5
	1577	G	95.929	1649.1

(a) Laser excitation energy 2.81 eV (442 nm)

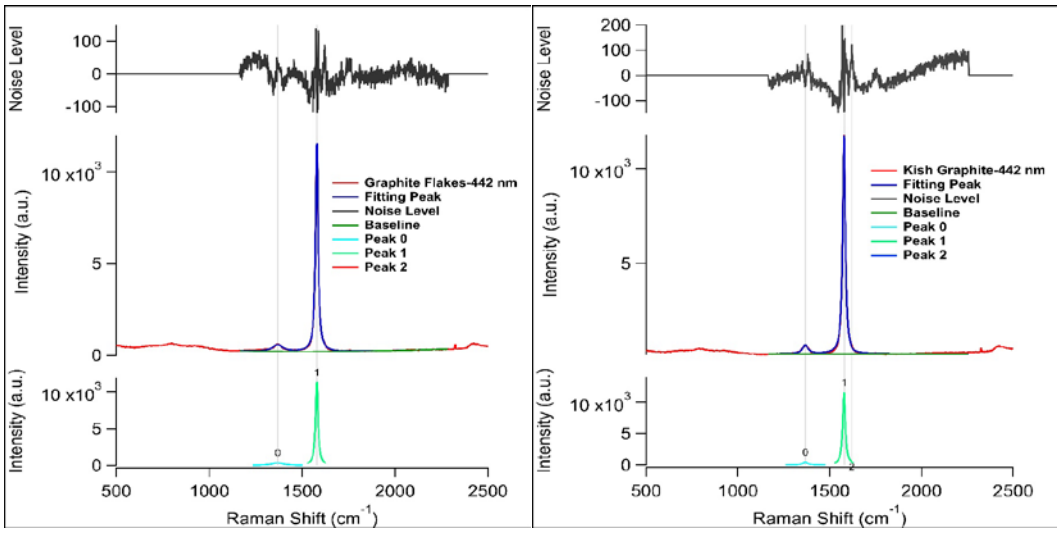

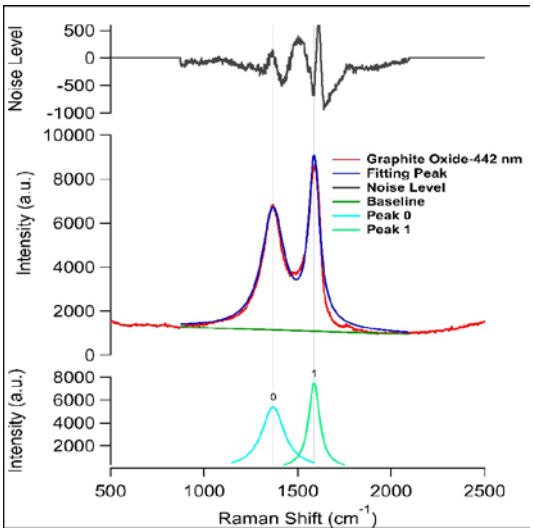

(b) Laser excitation energy 2.41 eV (514 nm)

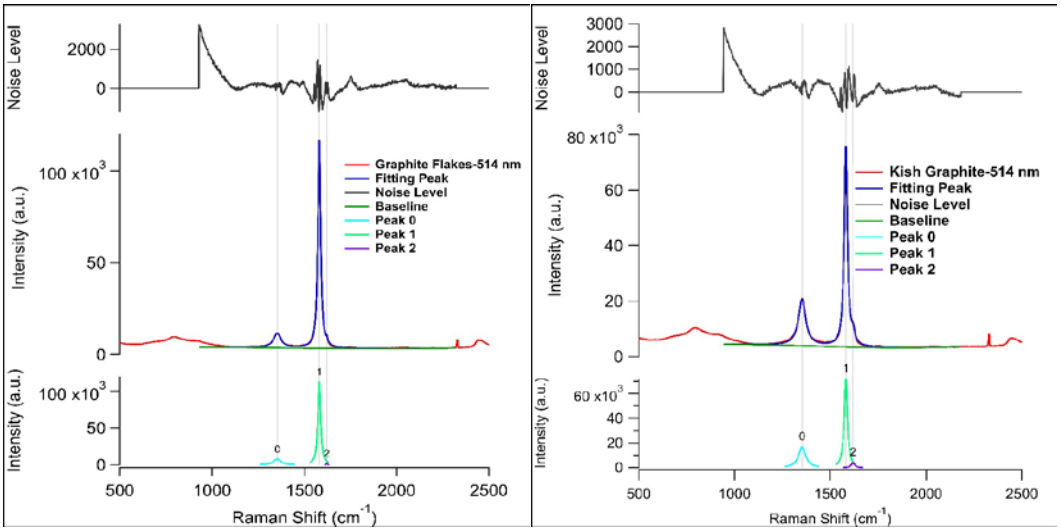

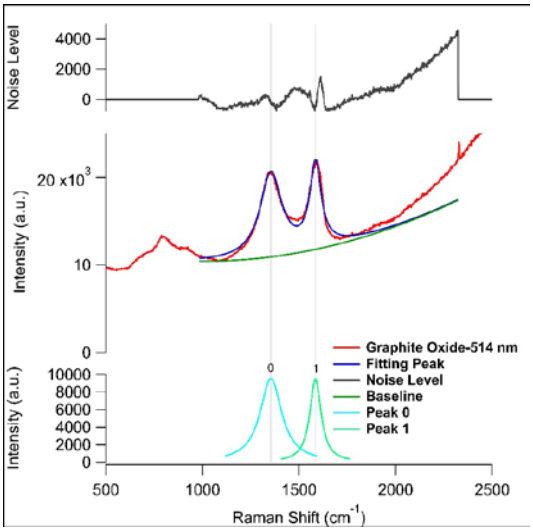

(c) Laser excitation energy 2.33 eV (532 nm)

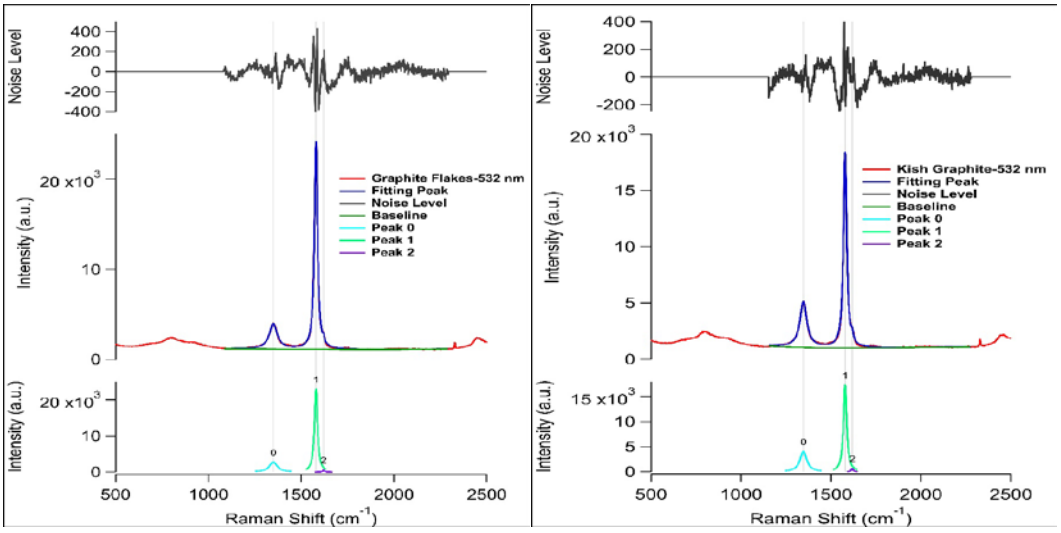

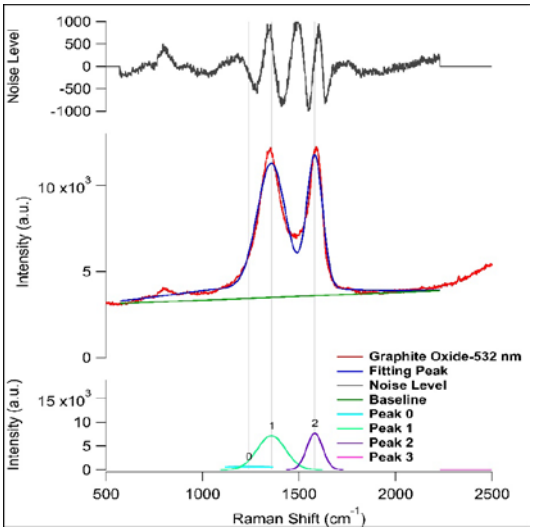

(d) Laser excitation energy 1.96 eV (633 nm)

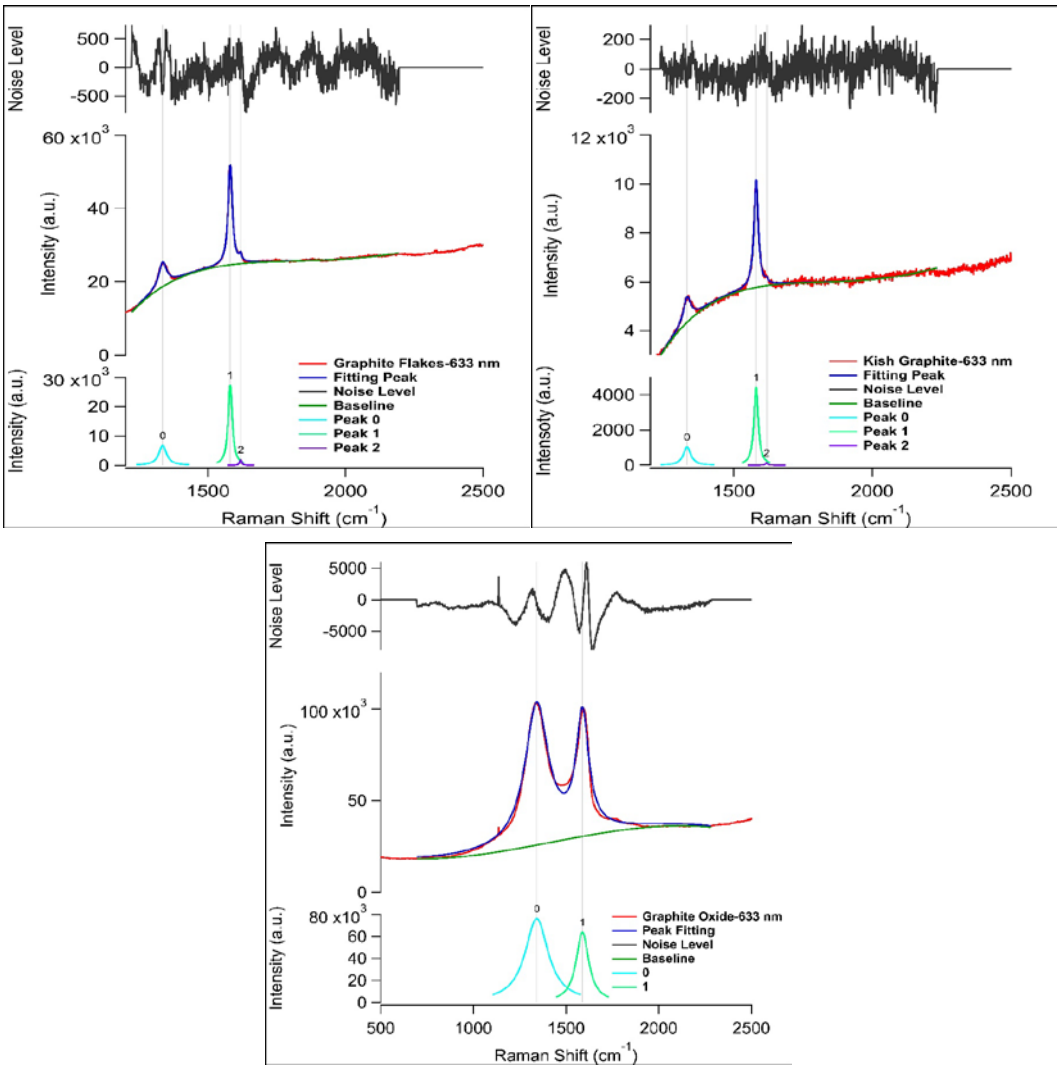

Figure 3.7: Peak fitting for Raman spectra of graphitic materials by different photon energies from 1.96 eV to 2.81 eV. Noise level denotes difference between measured and fitted curves.

Figs. 3.6 and 3.7 show peak fitting analysis of the Raman spectra of Aerographite and graphitic materials by different photon energies from 1.96 eV to 2.81 eV, respectively. The D and G peaks were fitted by Lorentzian functions, with a cubic baseline. Only intensities of the main peaks were considered in calculating intensities ratios between the D and G bands for each sample. The D′ band is not distinguishable for Aerographite and it could not be fitted. However, its contribution to the main Raman peaks is expected to be negligible as its intensity is much lower than the G band, as seen for the cases of graphite flakes and kish graphite. This is similar to the case of graphite oxide. It may be seen that the Lorentzian fit is not as good for Aerographite and disordered graphite as it is for kish graphite and for graphite flakes. This is expected, since Lorentzian function are appropriate where the resonance of simple harmonic oscillator is probed. In disordered systems such as Aerographite and graphite oxide, simple harmonic conditions are no longer expected. Instead, defects are likely to produce local changes of the resonant frequencies and introduce anharmonic effects. It would be difficult to obtain the exact distribution of these

effects of disorder and thus allow better fitting. Nevertheless, fitting of Raman peaks of Aerographite and graphite oxide with Lorentzian still provides good information on the intensities of the measured heights and energies of the peaks for the measured Raman D and G bands. The ratio of the intensities of these bands is commonly used in the literature to study the effects of defects in graphitic samples, as will be explored in the next section.

3.3.5 Quantifying Analysis of Defects and Disorder via Raman Spectra Reported for Ion Bombardment sp^2 Carbon Systems

Having established which Raman peaks occur in the samples studied in this project, further analysis will be performed of the Raman features that are shown to be associated with the structural disorder of graphitic systems. This section gives a brief overview of the methods used in such analysis, to help analyze the Raman data obtained for the samples investigated in this project (in Section 3.3.6).

To quantify the disorder in the sp^2 carbon-based systems, it is common to analyze the intensity ratio I_D/I_G between the D and G bands, which depends on both the degree of graphitization and the orientation of the graphitic planes [121]. A lattice-dynamical model has been reported to interpret the evolution of various carbon types ranging from highly graphitized to amorphous carbon in graphite [122]. For an increasing number of defects, the G band become smaller and the intensity of D band increases. The intensity ratio of the D to G bands varies inversely with the effective crystalline size of sp^2 clusters L_a (corresponding to the length of basal plane), which is quantified using the Tuinstra-Koenig relation [91,92,99]:

$$\frac{I_D}{I_G} = \frac{C(\lambda)}{L_a} \tag{3.4}$$

where I_D/I_G is the intensity ratio between the D and G bands and, the constant $C(\lambda)$ depends on the excitation wavelength λ.

Mernagh *et al.* found that the intensity ratio of I_D/I_G depends strongly on the excitation energy E_L [123]. Cançado *et al.* further reported a general formula that gave the crystalline size L_a of nanographite systems for any laser excitation energy in the visible range [124]:

$$L_a = \frac{560}{E_L^4}\left(\frac{I_D}{I_G}\right)^{-1} \tag{3.5}$$

$$\text{or} \quad L_a = 2.4 \times 10^{-10} \lambda_L^4 \left(\frac{I_D}{I_G}\right)^{-1} \tag{3.6}$$

The ratio I_D/I_G is inversely proportion to E_L^4 in their diamond like carbon films [124]. However, it is necessary to propose a new theory that considers the E_L dependence to explain the dependence of I_D/I_G on E_L^4.

Cançado *et al.* also studied the Raman spectra of Ar^+ bombarded graphene samples with increasing ion doses [125]. Their results show that the excitation energy dependence of the peaks areas and the intensity ratio of I_D/I_G is proportional to the defect density n_D (the average number of

defects in a unit cell) in the visible range of E_L. At the regime of low defects density (the average distance between defects $L_D \geq 10$ nm) [91,125]:

$$L_D^2 = \frac{4.3\times10^3}{E_L^4}\left(\frac{I_D}{I_G}\right)^{-1} \quad (3.7)$$

If the defect density n_D=$\frac{10^{14}}{(\pi L_D^2)}$, Eq. 3.7 becomes

$$n_D = 7.3 \times 10^9 E_L^4 \left(\frac{I_D}{I_G}\right) \quad (3.8)$$

In the high defects density region ($L_D < 3$ nm):

$$L_D^2 = 5.4 \times 10^{-2} E_L^4 \left(\frac{I_D}{I_G}\right) \quad (3.9)$$

$$n_D^2 = \frac{5.9\times10^{14}}{E_L^4}\left(\frac{I_D}{I_G}\right)^{-1} \quad (3.10)$$

These above analyses were made for graphene and other sp^2 carbon-based systems with well-defined defect structures. The relevance of this overview is in showing the expected E_L-dependence of I_D/I_G. These previous research show that I_D/I_G is proportional to λ_L^4. Electronic and geometrical structures between defects (due to the size effects), will result in a different intensity ratio dependence on the degree of disorder [104]. L_a and L_D are important structural parameters to identify the evolution of disorder in low dimensional carbon-based systems [125].

3.3.6 Analysis of Laser Excitation Energy Dependence of I_D/I_G for Aerographite

This section deals with the dependence of I_D/I_G on the laser excitation energy for Aerographite. Comparison with other forms of graphite will help pinpoint the origin of the surprising deviation of the expected I_D/I_G vs. E_L from the expected behaviour described by Eqs. 3.3-3.8. The importance of the PDOS will be singled out as the most likely reason for this deviation, which occurs in graphitic systems with very high degree of structural disorder. Intensities ratios between the D and G bands of Aerographite, I_D/I_G, were strongly dependent on the position on the sample at which the Raman spectrum was measured. Following to the peak fitting and analysis results, only intensities of the main peaks were considered to calculate I_D/I_G for each sample. For example, I_D/I_G at a particular spot on the sample was 0.68 (for the laser wavelength λ_L = 442 nm), 0.93 (λ_L = 514 nm), 0.96 (λ_L = 532 nm) and 0.98 (λ_L = 633 nm). Very large deviation in the values of I_D/I_G when measuring at different spots on the sample are obvious in Fig. 3.8. This is not surprising, considering that the XRD spectrum reveals that Aerographite is a highly disordered system. However, this result also implies that the disorder in the Aerographite is not homogeneously spread throughout the sample.

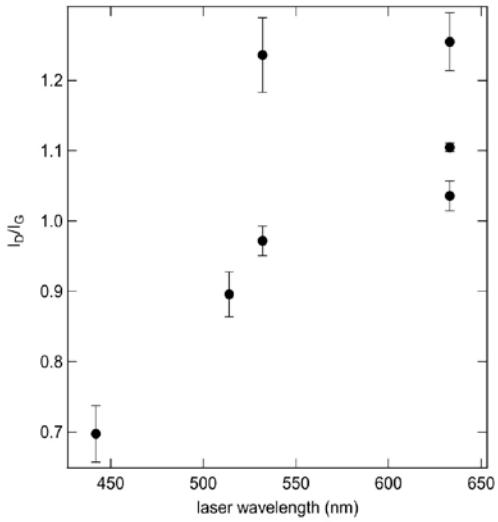

Figure 3.8: I_D/I_G of Aerographite as a function of laser wavelengths, as measured at different spots on the sample. The bars on the data points represent mean square deviation obtained for a particular spot on the sample.

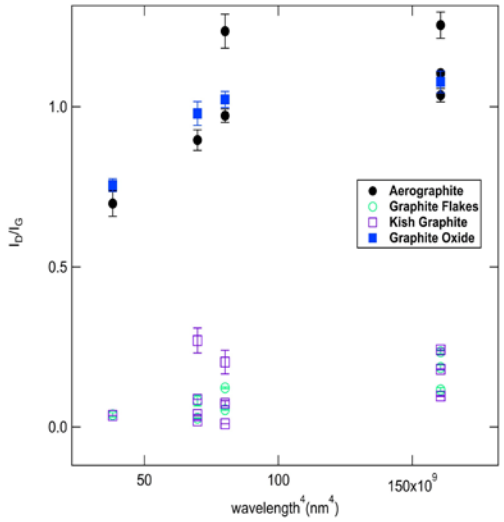

Figure 3.9 I_D/I_G of Aerographite and graphitic materials as a function of fourth power of laser excitation wavelengths.

To test if I_D/I_G gives the same dependence on the laser excitation wavelength as reported in the literature for graphene and common forms of graphite, I_D/I_G is plotted against λ_L^4 in Fig. 3.9 for all samples measured. Each point in Fig. 3.9 is average of several measurements taken on one point on the sample. The dependence of I_D/I_G on the position where Raman spectrum is measured seems to be a common feature. This gives large data scattering for highly ordered samples with low values of I_D/I_G, i.e. kish graphite and graphite flakes. To establish if I_D/I_G indeed gives the expected propotionality to λ_L^4, values of I_D/I_G were averaged over all measurements for each laser wavelength separately and plotted again. Error bars are mean square deviations from three measurements for each point.

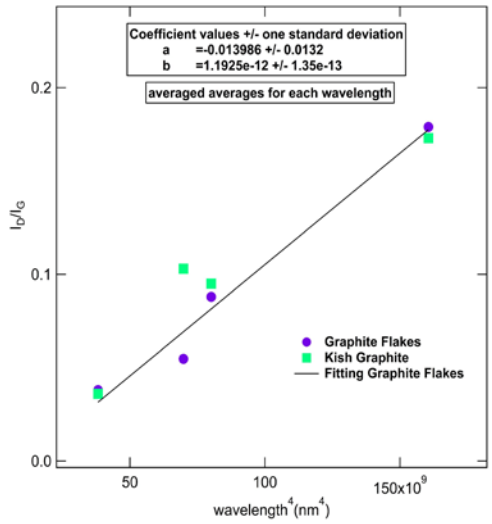

Figure 3.10 Dependence of I_D/I_G on laser wavelength for kish graphite (KG) and graphite flakes (GF), averaged over all measurements.

Fig. 3.10 shows dependence of the averaged I_D/I_G on laser wavelength, λ_L, for kish graphite and graphite flakes. It is seen that I_D/I_G scales linearly with λ_L^4, as expected for sp^2 graphite systems [61,91,123,125]. The gradient of I_D/I_G vs. λ_L^4, averaged over both samples, is 1.2 x 10^{-12} nm^{-4}.

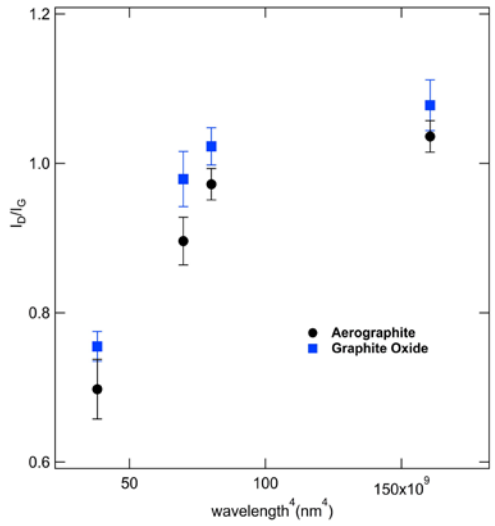

Figure 3.11: Dependence of I_D/I_G on laser wavelength for Aerographite and graphite oxide, taken at one point for each sample.

Fig. 3.11 shows the dependence of I_D/I_G on λ_L, at the same point of Aerographite. Here, only measurements at one spot ("spot 1") are shown, to eliminate uncertainty in overall behaviour of I_D/I_G associated with the choice of the spots on the sample that were measured. A linear relationship of I_D/I_G with λ_L^4 was obtained for the shorter laser wavelengths, λ_L = 442, 514 and 532 nm. This is as expected for sp^2 graphitic materials. The gradient in I_D/I_G vs. λ_L^4 was 8.9 x 10^{-12} nm^{-4}, larger than obtained for kish graphite and graphite flakes. However, this linear relationship no longer holds for λ_L = 633 nm. More specifically, I_D/I_G vs. λ_L^4 tends to saturate at the longest wavelengths. The same phenomenon was observed for graphite oxide sample (Fig. 3.11). The XRD results showed that both Aerographite and graphite oxide have highly disordered structure, giving no discernible XRD peaks (Fig. 3.1). On the other hand, kish graphite and graphite flakes

have highly ordered and orientated crystalline structure, giving sharp XRD peaks. This suggests that the unexpected saturation of I_D/I_G vs. λ_L^4 at high λ_L occurs because of strong structural disorder of Aerographite and graphite oxide.

This phenomenon is also reflected in the Raman peaks shapes. Aerographite and graphite oxide give broad D and G peaks that are merged. They do not display linear dependence of I_D/I_G with λ_L^4, contrary to what is expected from the literature on graphite Raman spectra [61,91,124,125]. It is tempting to ascribe this behavior to the D and G bands for these two samples being broad and merged, which may introduce artefacts into the band intensities. However, kish graphite and graphite flakes give sharp, well-separated D and G bands, and I_D/I_G for graphite flakes is linear with λ_L^4. On other hand, Aerographite displays linear I_D/I_G with λ_L^4 for three shortest wavelengths, and has well-separated D and G bands. Therefore, this nonlinearity cannot be an artefact of the merging of the bands for Aerographite, otherwise non-linearity would be also obtained for the shorter wavelengths. This lends support to treating the observed I_D/I_G versus λ_L^4 for Aerographite and graphite oxide as genuinely nonlinear if the long laser wavelengths are taken into account.

Additionally, literature has reported nonlinear I_D/I_G versus λ_L^4 for other samples which were studied as a function of ion radiation dose, introducing defects, and for different ion species and different ion energies [121,125]. Low-mass ions at low ion fluence introduce point defects, e.g. ion-bombarded highly ordered pyrolytic graphite (HOPG), graphene and Ar^+ bombarded graphene samples [61,91,121,125]. An increasing density of point defects and a larger damaged region of overlap were obtained with the ion dose increasing [121]. Point defects-induced lattice disorder and electron relaxation in the Raman scattering process should be responsible for this [125].

A local activation model was proposed by assuming that the single impact of an ion on the graphene sheet causes modifications on two length scales, namely, r_A (the radius of the area surrounding point defects in which the D band occurs) and r_s (the radius of the structurally disordered area caused by the impact of ion) (with $r_A > r_s$). These are the radii of two circular areas measured from the impact point [61,121,125]. With the shorter radius r_s, a structurally disordered *S*-region occurs relative to the point of impact [121,125]. At a distance larger than r_s but smaller than r_A, mixing of Bloch states near *K* and *K′* valleys occurs. The intensity of the D mode will be enhanced due to the selection rules being broken. This is the so-called activated *A*-region [121,125]. An electron-hole excitation will only be able to "see" the structural defect if the electron-hole excitation is close enough to the defect and the electron or hole lives long enough for the defective region to be probed by Raman spectroscopy [121,125]. Because these two disorder-induced mechanisms contribute to the D band, this phenomenological model yields the dependence between I_D/I_G and L_D [121,125]:

$$\frac{I_D}{I_G} = C_A f_A(L_D) + C_S f_S(L_D) \tag{3.11}$$

where f_A and f_S are the fractions of an activated (*A*-) area (weighted by a parameter C_A) and a structurally (*S*-) damaged area (weighted by a parameter C_S). The *A*- area will contribute more to

the D band, and the *S*- area will contribute less due to the breakdown of the lattice structure. Fig.3.12 plots C_A as a function of E_L: C_A=160E_L^{-4}. The I_D/I_G dependence on E_L will affected by the change on C_A, which is dependent on the interference effect [125].

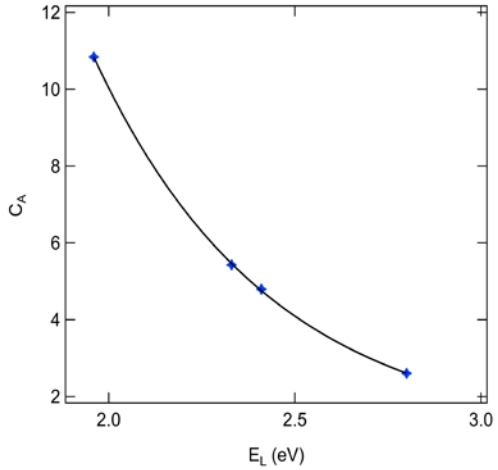

Figure 3.12: C_A as a function of E_L for Aerographite.

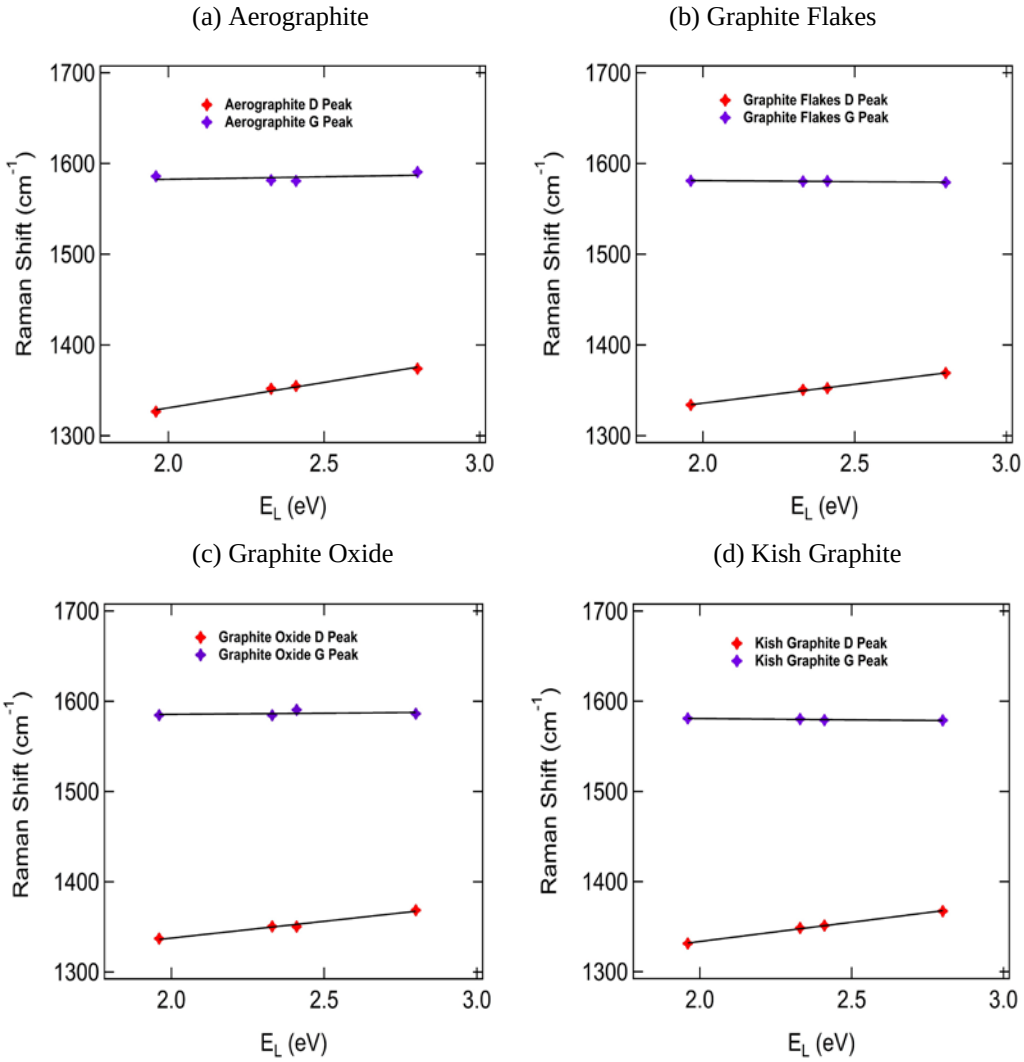

Figure 3.13: Peak positions of the G and D bands as a function of excitation energy for Aerographite, graphite flakes, graphite oxide and kish graphite. Lines fit to the data.

Further insight into these phenomena is obtained from dependence of peak positions of the D (E_D) and G peak (E_G) on the excitation laser energy (E_L). Fig. 3.13 shows the E_D and E_G vs. E_L for all samples measured. A linear relationship between E_D and E_L was obtained for all samples. The gradient of the E_D vs. E_L of Aerographite was ~54 cm^{-1}/eV, while the gradient of the E_G vs. E_L of Aerographite was ~6 cm^{-1}/eV. Similarly, the gradient of the E_D vs. E_L of graphite flakes, kish graphite and graphite oxide are ~42 cm^{-1}/eV, ~43 cm^{-1}/eV and ~36 cm^{-1}/eV, respectively. The E_G of graphitic materials is almost a constant with respect to E_L for all samples. Therefore, E_D has the same dependence on laser energy for high and for low values of E_L (or, equivalently, λ_L) for all samples. This behaviour is in agreement with the dependence of I_D/I_G on E_L for kish graphite and graphite flakes, where a single linear I_D/I_G vs. λ_L^4 is obtained for all measured λ_L. However, this differs from dependence of I_D/I_G on E_L for Aerographite and graphite oxide, for which I_D/I_G is linear at small λ_L, but it saturates for larger λ_L.

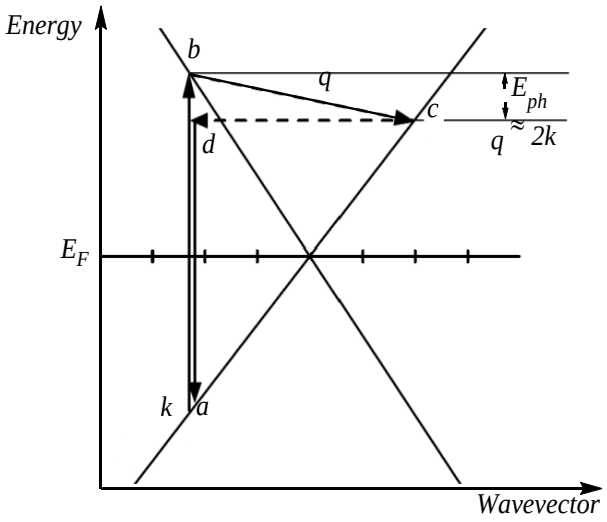

Figure 3.14: Schematic diagram of double resonant Raman scattering. The relative size of E_{ph} is exaggerated.

The occurrence of peak D has been successfully described by a model utilizing double resonance Raman scattering process, in which elastic scattering of an electron on crystal defects plays a key role [61,62]. In this double resonant Raman scattering model, electron dispersion relation for electrons in graphite near the Fermi level is approximately linear (Fig. 3.14). An electron in graphite is excited by a photon of energy E_L to the next higher available energy level at the same value of the electron wavevector, k (*a*-*b* in Fig. 3.14). The value of k is determined by the electron dispersion relation and E_L. A larger value of E_L results in excitation of an electron at a higher value of k. Thus, the excited electron can exchange energy with a phonon of non-zero phonon momentum, q. The energy of this phonon (E_{ph}) is such that the electron takes a real electron state at point *c* in Fig. 3.14, defined by electron dispersion relation for these values of q and E_L. After that the electron is elastically scattered by crystal defects into a virtual electron state (*c*-*d* in Fig. 3.14), keeping the same energy but reversing its momentum. At this point, electron can recombine with the hole, emitting a photon of energy E_L-E_{ph}, which is then detected in Raman spectroscopy. Other options are possible [61,62], in which two excited states of the electron are real states and

one is a virtual state (i.e. point *d* in Fig. 3.14). Further, D bands occur through an inter-valley double resonance Raman process, rather than the intra-valley one described in Fig. 3.14. However, the intra-valley process in Fig. 3.14 captures all the essential processes needed for our discussion and the other processes will not be considered here for simplicity. The probability of this double resonant Raman process was reported to be proportional to the squares of the transition matrix elements for each of the transitions *a*-*b*, *b*-*c*, *c*-*d* and *d*-*a* in Fig. 3.14. It has been shown that the D band scattering is mediated by phonons with $q \approx 2k$ [47,61,62]. In this model, increasing E_L leads to a linear increase of *k*, which in turn leads to a linear increase of *q*. The phonon responsible for the transition *b*-*c* in Fig. 3.14 was shown to be a iTO phonon in the vicinity of *K* point of symmetry [47,61,62]. As E_{ph} increases approximately linearly with *q* for this phonon at the *K* point [47,61,62], it follows that the energy of the Raman D peak (E_D) increases linearly with E_L. The linear relationship in E_D vs. E_L is exactly what is obtained experimentally. This could not be reproduced by any other models describing the occurrence of D peak.

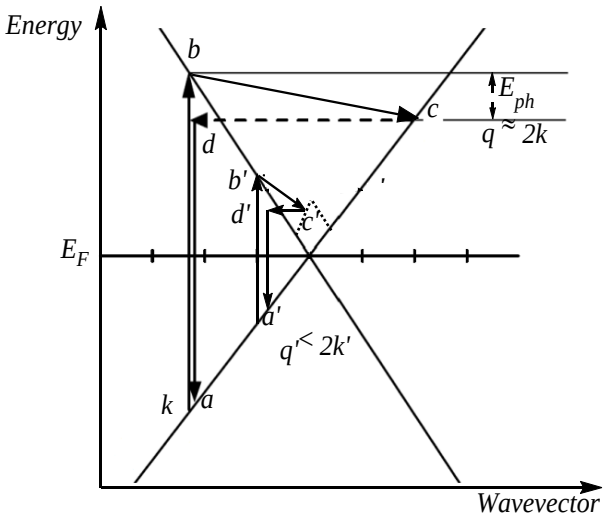

Figure 3.15: Schematic diagram of double resonant Raman scattering with electron defect states (dotted lines).

A physical explanation for the saturation of I_D/I_G vs. λ_L^4 for Aerographite and graphite oxide (Fig. 3.11) might be sought within the framework of the defect-induced double resonance Raman scattering model, because measurements in this thesis give a linear E_D vs. E_L for the entire range of E_L (i.e. λ_L) used (Fig. 3.13). A distinct difference between the samples showing the saturation in I_D/I_G vs. λ_L^4 (Fig. 3.11) and samples showing linear I_D/I_G vs. λ_L^4 in the entire range of λ_L (Fig. 3.10) is that the former are highly structurally disordered. Therefore, disorder-induced localized electron states may play a role. A study of electron density of states near the Fermi level introduced by strong point-defects for graphene showed enhanced density of states near the Fermi level [129,130]. The dispersion relation for these states was not given. What was important, however, is that the finite defect-related electron DOS was obtained only close to the Fermi level. A schematic diagram of the dispersion relation for the electron DOS is given in Fig. 3.15 by dashed lines, assuming arbitrarily a linear form for simplicity. In a Raman experiment with high E_L, i.e. small λ_L,

the electron will be excited to an energy above the disorder-induced electron states (*a*-*b* in Fig. 3.15). Subsequent interaction with a phonon will then result in the same double resonance Raman effect as without defect-induced electron states (*b*-*c*-*d*-*a*). If E_L is low enough, the electron will be excited to energies at which electron defect states exist close to the Fermi level. A possible double resonant scattering can then be described by transitions *a'*-*b'*-*c'*-*d'*-*a'* in Fig. 3.15. This is a different process than for high E_L and it is a good candidate for explaining the saturation in I_D/I_G vs. λ_L^4 for Aerographite and graphite oxide. However, because *k* and *q* are now lower than for what would occur without the electron defect states, this should result in a different E_D vs. E_L dependence than for high E_L. In other words, the linear behavior of E_D vs. E_L occurs through linearity in the electron dispersion relation and with the involvement of the electron defect states. The same relation would no longer hold for low and high values of E_L. Experiments do not show such a transition in E_D vs. E_L (Fig. 3.13). Therefore, disorder-induced local electron states cannot be the mechanism for the observed saturation in I_D/I_G vs. λ_L^4 for Aerographite and graphite oxide.

The linearity of the electron dispersion relation near the Fermi energy (E_F) for non-local states would also be affected by the structural disorder, which would in turn affect the intensity of the D band. However, this would affect the phonon momentum and energy of the step *b*-*c* in the double resonant Raman scattering (Fig. 3.14). Consequently, E_D vs. E_L would also have to be different for low and high values of E_L, reflecting the non-linearity of the electron dispersion relation near the Fermi level. Since the experiment shows otherwise, the effect of disorder on the non-local electron states can be ruled out as a mechanism for the observed saturation in I_D/I_G vs. E_L at low E_L.

In addition to the electron states, a high degree of structural disorder will also affect the phonon states. The dispersion of the iTO phonon near the *K* point was approximated to be linear in the double resonant scattering model. A high degree of structural disorder can affect this linearity, which in turn could affect I_D/I_G vs. E_L. However, this would again have to be reflected in E_D vs. E_L relationship, because phonons energies would then no longer change linearly with E_L. As the experiment gives a linear E_D vs. E_L relationship for all experimental values of E_L, the effect of structural disorder on the iTO phonon dispersion near the *K* point can be also excluded as a possible cause of saturation in I_D/I_G at small E_L.

Structural disorder can also affect the phonon density of states, PDOS, which exhibits a peak at the energy of D band [60,91,105]. The larger the magnitude of this peak, the greater is the probability for an electron-phonon interaction corresponding to step *b*-*c* in Fig. 3.14. Therefore, the probability of the double resonant Raman process leading to the occurrence of D peak in Raman spectrum increases with the increase of the PDOS function at the phonon energy corresponding to Raman shift at a point within the experimental D peak. This peak in the PDOS associated with the D band is expected to broaden and become lower in magnitude with the introduction of strong structural disorder. As E_L increases, phonons with higher energies contribute to the Raman shift (*b*-*c* in Fig. 3.14). If the PDOS increases with phonon energy more

gradually (as in the case of strong structural disorder), the intensity of the D band will change with E_L more gradually, too. It should be stressed that the energy of phonons contributing to the D band will not be affected by the disorder induced change of the PDOS; only the probability of the Raman scattering will be affected. Thus, a linear E_D vs. E_L is still expected, in agreement with the experiment. The energy of the Raman band G does not depend on E_L and consequently its intensity does not depend on E_L, either. Therefore, change in the PDOS by structural disorder is a viable mechanism that can lead to the observed saturation on I_D/I_G vs. E_L.

First-principles calculation were performed using Quantum ESPRESSO to model the PDOS for graphite and point defects in graphite. The PDOS spectra of ideal graphite and point defects in graphite from 1200-1650 cm^{-1} are shown in Fig. 3.16 [47,126-128]. The main features of the PDOS spectrum of ideal graphite correspond to peaks at 1226, 1427, 1600 (G) and 1634 (D′) cm^{-1}. For graphite with point defects, the peak at 1490 cm^{-1} is assigned to the disorder-induced D peak in this modelling, which corresponds to emission of an optical phonon with wavevector near the *K* points in the Brillouin zone [126,127]. The PDOS for the D peak increases more gradually for the graphite with defects, supporting the above proposition.

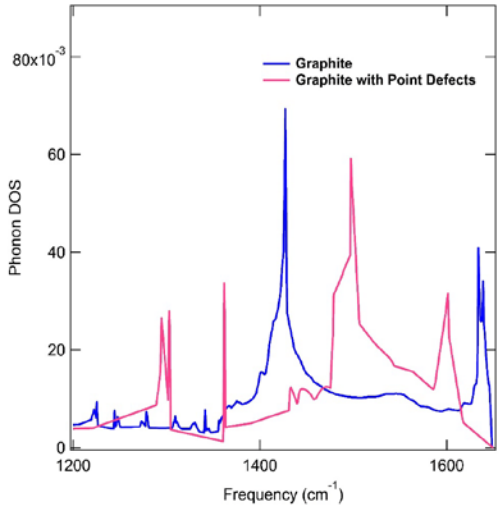

Figure 3.16: PDOS of ideal graphite and graphite with point defects from 1200-1650 cm^{-1}.

The influence of point defects on the graphite phonon spectra has shown that point defects (carbon isotopes, substitution atoms, vacancies) can cause additional Van Hove singularities in the PDOS at the *K* and *M* points of optical branches, and further induce additional Raman peaks [126,127]. Compared with the ideal graphite phonon spectra, the PDOS of graphite with point defects shows a broadening trend at high frequencies because there is a defect-induced double resonant Raman scattering in non-ideal graphite [126,127]. The PDOS of graphite with point defects decreases more gradually with energy than that for crystalline graphite. It is for this reason that I_D/I_G vs. E_L of the defected graphite changes more grdually with E_L than for the crystalline graphite. This leaves the change of the PDOS by defects as the most likely explanation for the observed behavior.

3.4 Conclusion

In this chapter, I investigated the Raman spectra of Aerographite in comparison to graphite oxide, kish graphite and graphite flakes using different laser excitation energies in the visible range and quantitatively analyzed their respective intensities ratios, depending on the excitation energy. XRD measurements showed that Aerographite and graphite oxide are structurally highly disordered, while kish graphite and graphite flakes are structurally ordered. All samples give Raman bands characteristic for graphitic systems, but the bands for the disordered samples are broadened. The results reveal that the Raman spectrum of Aerographite is composed of two parts: one is typical spectral peaks of graphitic materials with G, D, and 2D bands. It also has special spectral features due to its 3D interconnected carbon foam with a hollow tetrapodal structure. The D and 2D bands of Aerographite show the “blue-shift” effect as excitation energy increases, but in contrast, positions of the G band do not obviously shift. This dispersion behavior supports the vibrational mode assignments of Aerographite. Structural and electronic modifications, i.e. disorder, defects, curvature, and edge functionalization, are likely to responsible for the presence of D and 2D bands in the Raman spectra of Aerographite. The amount of amorphous sp^2 carbons in Aerographite reflects its a hollow nano- and micro-tubular interconnected tetrapod structure, which is the main reason for different Raman spectral profile of Aerographite compared to those of other graphitic materials.

In addition, a saturation in the intensity ratio between D and G bands (I_D/I_G) was observed, for which a new physical model was proposed. This model involves is based on double resonant Raman scattering, but invokes also change of PDOS by structural disorder, making it possible to obtain the saturation of I_D/I_G vs. E_L and, at the same time, maintaining the linear E_D vs. E_L through whole range of E_L measured.

Chapter 4

Temperature Dependent Synchrotron Terahertz/Far-Infrared and Raman Scattering Spectral Studies of Aerographite and Single-walled Carbon Nanotube Aerogel

4.1 Introduction

Carbon aerogels exhibit a unique combination of properties, including ultra-low density, a large specific surface area (SSA), high electrical conductivity, thermal and chemical robustness, and excellent mechanical properties [9,10,129]. These properties arise directly from assembling amorphous sp^2 carbons into a highly porous, low-density aerogel. THz/Far-IR reflectance and scattering properties of carbon aerogels have not been adequately reported due to their highly porous structures on nanoscale. THz/Far-IR transmission measurements are very difficult to perform because of very low transmissivity of these materials. This will impede the potential applications in THz and Far-IR areas, especially in space-borne optical systems [130].

Vibrational spectroscopy, embracing both IR absorption spectroscopy and Raman scattering spectroscopy, represents a powerful tool to investigate phonon properties, phonon anharmonicity and electron-phonon coupling of carbon-based materials. IR absorption spectroscopy probes IR active phonon modes of small wave vector because the wave vector of the incident photons is small in comparison with the Brillouin zone [96]. Raman scattering spectroscopy is widely used to identify defects, disorders, layer numbers, diameters, and chirality [47,131-133]. The basic difference between the IR and Raman spectroscopy is associated with the symmetry difference which is described by a dipole moment for the absorption process and by a symmetrical tensor for the scattering process [45,82]. Being sensitive to odd-parity phonon modes, IR absorption spectroscopy provides a complementary method to Raman scattering spectroscopy, which is sensitive to even-parity phonon modes and mutually exclusive character resulting from the quantum mechanical selection rules [134]. Temperature dependent Raman line width and peak shift of a Raman or IR mode can further provide important information on anharmonic terms in the lattice potential energy and electron-phonon coupling [135,136].

Synchrotron light source emits a wide frequency range, from microwaves to X-rays, with several advantages over conventional light source in the area of low-noise, high brightness, high collimation, and high polarization. Thus, synchrotrons provide the ideal source to study thin samples in transmission or reflection in THz/Far-IR region. Optically active vibrational modes corresponding to long-range interactions may be detected in large molecular systems in this spectral region [134]. In addition, as the synchrotron beam displays a high level of polarization, it is also excellent for the study of samples with oriented IR absorbing bonds [137].

In this chapter, I present complementary synchrotron THz/Far-IR and Raman spectral investigation

of temperature dependent measurements of Aerographite and SWCNT aerogel. Synchrotron THz/Far-IR spectra acquired from the THz/Far-IR Beamline at the Australian Synchrotron were measured in the frequency range of 7-1000 cm^{-1} and temperature from 6–300 K. Variable temperature Raman spectra were excited by a 514 nm laser at temperatures from 80–300 K in the frequency range of 100–4000 cm^{-1}. THz Raman spectra were measured from 10–220 cm^{-1} for comparison with the synchrotron IR spectra; but only room temperature measurements were available. All possible IR and Raman peaks are assigned. Room temperature THz Raman spectra of graphite flakes and SWCNT aerogel were also studied.

4.2 Experimental Details

4.2.1 Materials Preparation

The sample preparation details of Aerographite were have already been given in Chapter 3.

SWCNT aerogel was produced at University of Pennsylvania, under the joint supervision of Professor Arjun G. Yodh and Professor Mohammad F. Islam (Carnegie Mellon University). The SWCNT aerogel was created from SWCNT hydrogel (aqueous gel) precursors by critical point drying and freeze drying [17,131]. Specifically, SWCNT powder (CG 300 conductive SWCNTs 0.03 g, average diameter: 0.84 nm, median length: 1 μm, carbon purity: ≥ 95wt%, specific surface area: ≥ 700 m^2/g, CHASM Advanced Materials, Inc., Canton, MA, USA) was suspended in deionized water (30 mL) using sodium dodecylbenzene sulfonate (SDBS) surfactant (0.3 g, Acros Organics) at a SWCNT dispersion concentration of 1 mg/mL; the mass ratio of SWCNT with SDBS was 1:10. The solution was magnetically stirred (IKA@RET basic, Staufen, Germany) with 750 rpm for one hour, then tip-sonicated (VC 505, Sonics & Materials, Inc., Newtown, CT, USA) for 2 h operating at 90 W (20% amplitude) with “on” and “off” cycles, equal to 10 and 5 s, respectively. During the sonication process, the dispersion was maintained at room temperature using a water bath. Then the SWCNT dispersion was centrifuged at 1500 rpm for 30 min (Fisher Scientific Marathon 21000R, Hampton, NH, USA). After centrifugation, the SWCNT suspensions were concentrated by evaporating in a forced air oven (VWR Scientific 1330 FM, Radnor, PA, USA) at 60 ℃ for 6 h and were then poured into circular molds covered with parafilm and left for 24 h in a humid ambient condition. After the gelation of the solution, the surfactant was removed by soaking in deionized water for 20 min, then in 1 M nitric acid for 20 min. Different concentrations (20%, 40%, 60%, 80% and 100%) ethanol solutions were used to exchange the water in the samples. The SWCNT hydrogel was finally dried by an automated critical point dryer (CPD, Leica EM CPD030, Wetzler, Germany) and the SWCNT aerogel was thus obtained.

Fig. 4.1 shows an optical image obtained using an inVia™ confocal Raman microscope of the samples of Aerographite and SWCNT aerogel studied, showing the overall sample structures. In Fig. 4.1 (a), Aerographite manifests its hollow tetrapod morphology with a random and disordered

three-dimensional porous architecture. The optical image of the SWCNT aerogel cross-section given in Fig. 4.1 (b), reveals a porous, isotropic SWCNT network.

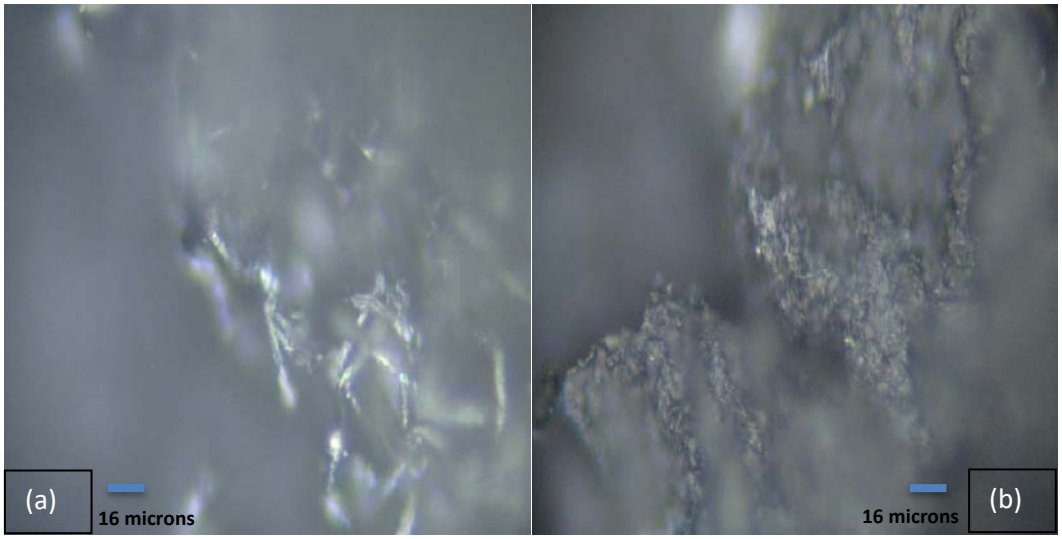

(a) Aerographite (b) SWCNT Aerogel

Figure 4.1: Optical images of Aerographite and SWCNT aerogel.

4.2.2 Measurements of Spectra

Synchrotron THz/Far-IR Fourier transform IR (FTIR) spectra were acquired at the THz/Far-IR beamline of the Australian Synchrotron (Clayton, Victoria, Australia) and using a Brüker IFS125HR FTIR spectrometer (Brüker Optics, Ettlingen, Germany) which offers a used spectral resolution of 1 cm^{-1}. Temperature dependent THz/Far-IR spectra from 6–300 K with steps of 10 K were obtained using a cryogen-free closed-loop cryostat with variable temperature insert (Cryo Industries of America, Inc., Manchester, NH, USA), equipped with diamond windows. The temperature was maintained and recorded using a PID temperature controller (Lake Shore Cryotronics, Westerville, OH, USA). IR transmission spectra from 7–1000 cm^{-1} (0.2–33 THz) were obtained using a 6-μm multilayer Mylar beam splitter. A liquid helium cooled silicon-based bolometer (HDL-5, Infrared Laboratories, Tucson, AZ, USA) was employed to detect signals in the 7–350 cm^{-1} region. A Si: B photodetector was used in the 300–1000 cm^{-1} region. Samples were mounted in a transmission geometry, allowing one to acquire transmittance by taking the ratio of intensity of passing through the sample and a reference without the sample. The spectrometer is remotely controlled and the data was analyzed using OPUS^{TM} software version 6.5. Paraffin wax is an ideal solvent for low-temperature THz/Far-IR measurements. The use of paraffin wax has a key advantage that a self-supporting disc can be prepared at room temperature, suitable for mounting samples [138]. With this configuration, I acquired spectra from dilute Aerographite and SWCNT aerogel dispersed in paraffin wax at ratios of 1% and 0.1%. Multiple measurements (repeated three times at each temperature) were employed to confirm the reliability of resulting spectra.

Raman spectra were measured on an inVia^{TM} confocal Raman microscope (Renishaw plc, Gloucestershire, UK) using a 514 nm Ar^{+} laser (excitation energy 2.41 eV) with 1800 l/mm grating.

Samples were loaded onto a glass slide into a flowing nitrogen atmosphere and cooled using a variable temperature stage and then measured in 10 K within +/-1 K steps from 80 K up to 300 K; optical access was via a quartz window (Linkham Scientific Instruments, Epsom, UK). The laser was focused on the sample via a Leica 50× long-working-distance objective (N.A. = 0.75). These optical components were used to focus the laser beam onto sample and to collect the backscattering light. The laser beam power was adjustable from 10%–100% of the laser maximum power. The power was adjusted in order to prevent laser-induced heating but still ensure a high SNR. Detection was achieved with an air-cooled CCD detector. Variable temperature Raman spectra were collected using an exposure time 20 s, and 5 accumulations in an extended mode from 100–4000 cm^{-1}. The calibration of the Raman spectrometer was checked by using the line at 521 cm^{-1} of a silicon sample.

4.3 Results and Analysis

4.3.1 IR and Raman Phonon Activity Overview for Graphite and SWCNTs

Graphite is a hexagonal crystal with four carbon atoms per unit cell and twelve zone center lattice modes. According to group theory, the zone-center optical phonon modes of graphite are [45,47,139]

$$\Gamma_{\text{Graphite}} = A_{2u}(IR) + 2B_{2g} + E_{1u}(IR) + 2E_{2g}(R) \quad (4.1)$$

There are two additional phonon modes, A_{2u} and E_{1u}, for the acoustic modes. There are only two IR active modes for graphite: one A_{2u} and one E_{1u}. Two first-order IR active vibrational modes are observed in the mid-IR range, one at 868 cm^{-1} ("out-of-plane" vibration, A_{2u} symmetry, nondegenerate) and one at 1588 cm^{-1} ("in-plane" vibration, E_{1u} symmetry, doubly degenerate) [47,139]. Jeon *et al*. reported that the origin of the IR activity in graphite is the interlayer Coulomb interactions involving the electronic charge in the π-bonds [139].

Due to the energy-momentum conversation requirements, it is only necessary to consider the symmetry of the SWCNT zone-center vibration at the Γ point (k = 0). The number of the Raman active (A_{1g}, E_{1g} and E_{2g} symmetries) and IR active (A_{2u} and E_{1u} symmetries) modes for SWCNT is related to the lattice structure and its symmetry. The phonon modes of SWCNTs are [51]:

$$\Gamma_{\text{SWCNTs}} = A_{2M}(IR) + 2B_{2g} + 2E_{1M}(IR) + 2E_{2g}(R) \quad (4.2)$$

Selection rules indicate that there are 15-16 Raman active and 6-9 IR active modes for SWCNT, depending on their symmetry (i.e. armchair, chiral, or zigzag) [51]. However, a Raman active mode allowed by group theory may nevertheless only have a small Raman cross-section [51]. Only 6-7 Raman intense Raman active modes are observed by the Raman scattering measurements for any SWCNT chirality. IR active vibrational modes of SWCNT samples are difficult to detect because SWCNTs do not support a static dipole moment, and IR activity related to the dynamic dipole moment is very weak [140,141]. IR transmission and reflectance spectra show that phonon

modes around 860 and 1590 cm^{-1} appear in all symmetries, independently of the diameter of SWCNTs. The low frequency modes of the SWCNT (below 400 cm^{-1}) depend strongly on the diameter, i.e. they soften with increasing diameter. Modes above 1100 cm^{-1} exhibit primarily tangential *C*-atom displacement [51,140].

Bantignies *et al.* studied the IR transmission spectra of carbon aerogel, SWCNT and graphite in the wavenumber range 450–4000 cm^{-1} [141]. They found that there are only small features at 860 (IR active radial mode, A_{2u} symmetry) and 1590 cm^{-1} (IR active tangential mode, E_{1u} symmetry) in the graphite and SWCNT spectra, and one additional band located around 1190 cm^{-1} in the SWCNT spectrum. Due to the amorphous carbon present in carbon aerogel, a very broad and complex feature was observed in carbon aerogel around 1250 cm^{-1} along with other bands located in 880 and 1590 cm^{-1}. Further bands around 1127, 1168 and 1190 cm^{-1} (due to the overlap between an IR active mode and the D mode) have also been reported for carbon aerogel [141]. Alon reported that all achiral SWCNTs have only 8 Raman active and 3 IR active phonon modes [142]. The symmetries and numbers of Raman active and IR active phonon modes in SWCNTs (after subtracting the acoustic modes) are [49,142]:

$$\Gamma_{Zagzig}^{Raman} = 2A_{1g} \oplus 3E_{1g} \oplus 3E_{2g} \rightarrow n_{Zagzig}^{Raman} = 8 \text{ modes;} \quad (4.3)$$

$$\Gamma_{Zagzig}^{IR} = A_{2u} \oplus 2E_{1u} \rightarrow n_{Zagzig}^{IR} = 3 \text{ modes;} \quad (4.4)$$

$$\Gamma_{armchair}^{Raman} = 2A_{1g} \oplus 2E_{1g} \oplus 4E_{2g} \rightarrow n_{armchair}^{Raman} = 8 \text{ modes;} \quad (4.5)$$

$$\Gamma_{armchair}^{IR} = 3E_{1u} \rightarrow n_{armchair}^{IR} = 3 \text{ modes;} \quad (4.6)$$

$$\Gamma_{chiral}^{Raman} = 3A_1 \oplus 5E_1 \oplus 6E_2 \rightarrow n_{chiral}^{Raman} = 14 \text{ modes;} \quad (4.7)$$

$$\Gamma_{chiral}^{IR} = A_2 \oplus 5E_1 \rightarrow n_{chiral}^{IR} = 6 \text{ modes.} \quad (4.8)$$

4.3.2 THz/Far-IR Spectra

Figs. 4.2 and 4.3 display raw measurements of IR transmission for Aerographite and SWCNT aerogel in the log-scale. The raw measurements show several obvious absorption features. However, these features are produced by the experimental setup, and they disappear when the raw spectrum is divided by the spectrum measured without the sample and the transmittance is obtained. The features belonging to samples are much more subtle and they are only obvious when zooming into a narrow spectral range. The large sharp features in the transmittance curves above 650 cm^{-1} are not sample features either. These are an artefact of the small signal values in the raw spectra above 650 cm^{-1} and division by small numbers in the reference spectrum when calculating the transmittance.

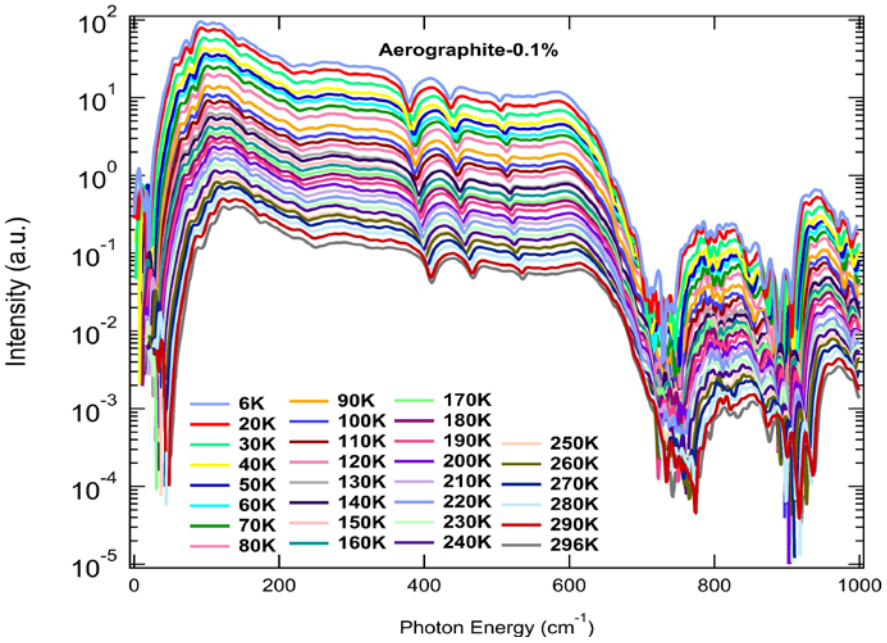

Figure 4.2: Synchrotron THz/Far-IR raw spectra of Aerographite on a log-scale at various temperatures, from 6 K to 300 K.

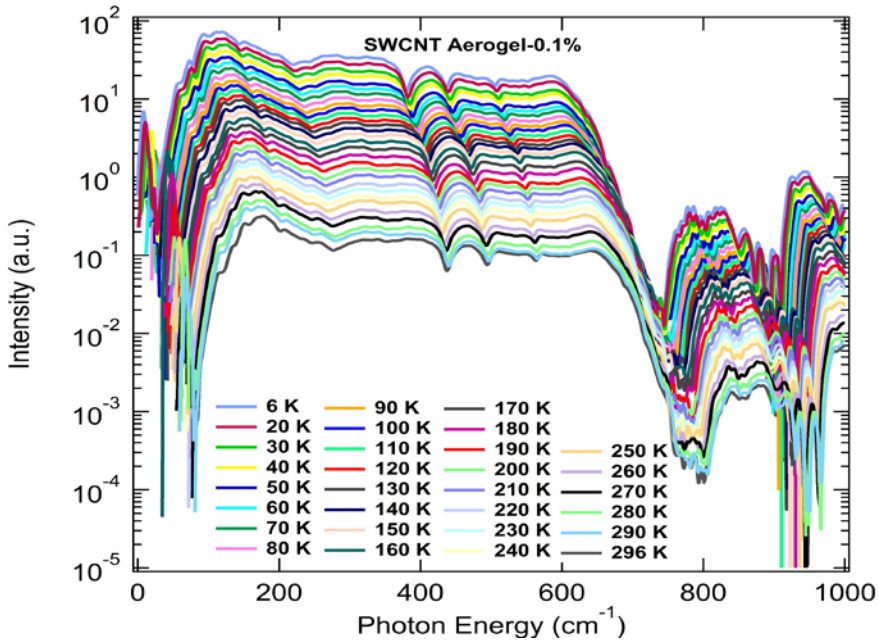

Figure 4.3: Synchrotron THz/Far-IR raw spectra of SWCNT aerogel on a log-scale at various temperatures, from 6 K to 300 K.

The observed IR bands for the Aerographite and SWCNT aerogel are at 40, 79, 115, 152, 250 and 660 cm^{-1}. There are others that are more difficult to distinguish. In addition, there are probably other common bands as well; but it is difficult to be certain because the bands are small and broad. The 660 cm^{-1} band seems to be common, but that band is complicated because it is close to the noisy area (the band itself might be an artefact). Only one observed band has a straightforward explanation: 867 cm^{-1} is A_{2u} out-of-plane vibration mode, which is expected to be IR active.

IR spectroscopy on graphite and CNTs below 1000 cm^{-1} is difficult, because the signal is very weak due to the high IR absorption and reflection of carbon-based materials generally [50]. Furthermore, the IR active modes around 867 cm^{-1} and 1588 cm^{-1} are close to those of other carbon-based materials [50]. IR active modes in the SWCNT exhibit an upshift by some wavenumbers with respect to the corresponding graphite mode [50]. Zhang *et al.* used first-principles modelling (Quantum ESPERSSO) to calculate the IR spectra of graphite oxide in the frequency range 1000–4000 cm^{-1} [143]. Xing *et al.* ball-milled crystalline graphite powder at Argon gas atmosphere up to 100 hours and diluted this to obtain Raman spectra from 200 to 3500 cm^{-1} [143]. However, milling probably affects the graphite fine structure, as it produces very small particles. From a few Raman spectra, it appears the SWCNT exhibit the RBM around 200 cm^{-1}. This may be related to what we observe for SWCNT aerogel (wide bands in this area). However, Aerographite also has wide bands there-which is confusing, because Aerographite cannot have the RBM (unless this is because Aerographite follows the round shapes of the underlying ZnO tetrapods).

To reveal the spectral features of Aerographite more clearly, parts of the IR spectra are shown separately in Figs. 4.4–4.7. Arbitrary units are different for each graph, but they are the same within each of the graphs. In the frequency range of 30–300 cm^{-1} (the low frequency region), IR absorption bands at 40, 79, 114, 152 and 248 cm^{-1} are seen to occur in Aerographite (Figs. 4.4 and 4.5). The low frequency IR spectra exhibit distinct features because resonant scattering from quasi-acoustic phonons with a shearing and breathing atomic motion of the adjacent layers, the so-called shearing modes and breathing modes [106].

The IR absorption band at 40 cm^{-1} is a shear mode that shows a “red-shift” as the temperature increases up to 296 K (the band moves to 36 cm^{-1}). This frequency shift is accompanied by a thermal evolution from a sharp band profile at low temperatures to a broad band profile at high temperatures. The E_{2g} shear phonon mode occurs at this energy in graphite, but it is not expected to be IR active, only Raman active.

The band at 79 cm^{-1} is mainly due to vibration of graphite planes parallel to each other [144]. Resonance and overtone/combination modes cannot be predicted by symmetry since these vibration modes are caused by interactions among the fundamental modes [44,61-65]. The role of phonon interactions will be implicated in the measurable widths of peaks, while non-interacting vibrational modes would be manifested as a δ function in the dielectric constant [44].

The IR absorption band at 114 cm^{-1} is identified as a low-wavenumber out-of-plane (ZO′) optical phonon mode in graphite [139]. This phonon mode represents relative motions between rigid monolayer planes when assembled in *N*-layer stacking. It shows an asymmetric shape, a consequence of Breit-Wigner-Fano resonance, resulting from the coupling between the low-wavenumber phonon and electron transitions around the touching region of conduction and

valence band continuum [144]. The IR absorption band at 152 cm^{-1} is assigned to the low frequency A_{1g} mode, which is strongly dependent on the van der Waals interaction potential in graphite [51,144].

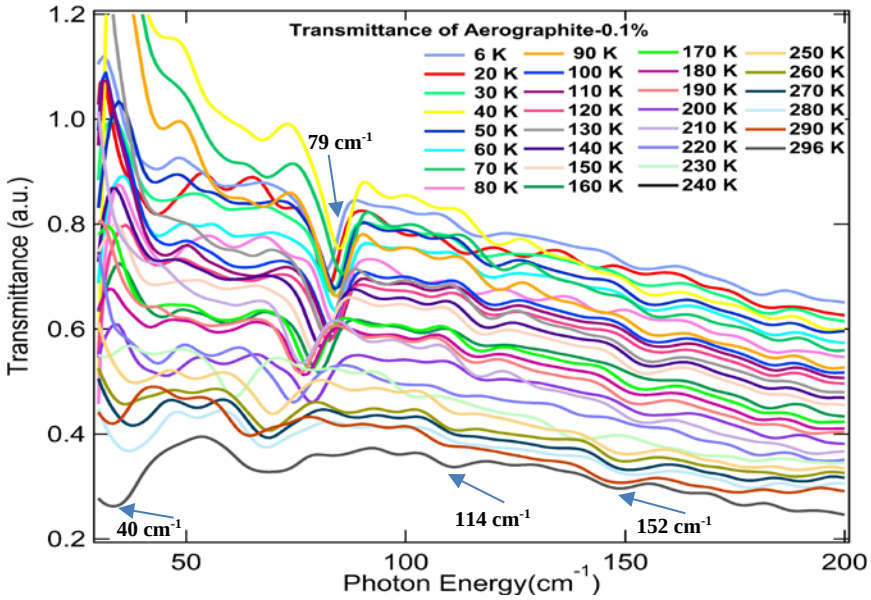

Figure 4.4: THz/Far-IR transmittance spectra of Aerographite from 30–200 cm^{-1} at various temperatures, from 6 K to 300 K.

The band at 248 cm^{-1} (Fig. 4.5) is tentatively attributed to the radial breathing-like (RBLM) mode, which appears due to the curvature effect in corrugated graphite sheets comprising 1–3 graphene layers and graphene nanoribbons [136,145].

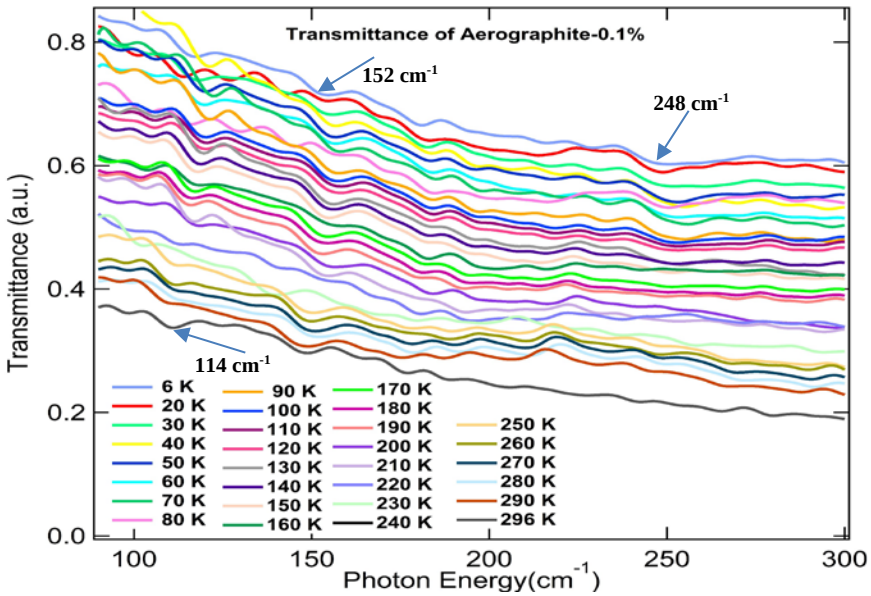

Figure 4.5: THz/Far-IR transmittance spectra of Aerographite from 90–300 cm^{-1} at various temperatures, from 6 K to 300 K.

In the frequency range 400–700 cm^{-1} (Fig. 4.6), the IR absorption band of Aerographite at 660 cm^{-1} was assigned to a first order IR vibration mode A_2 arising from a C-H out-of-plane deformation

band. This has been shown earlier to occur in Aerographite [82]. The origin is the Fermi resonance between the C-H stretching vibration and the first overtone of the C-H deformation vibration [82].

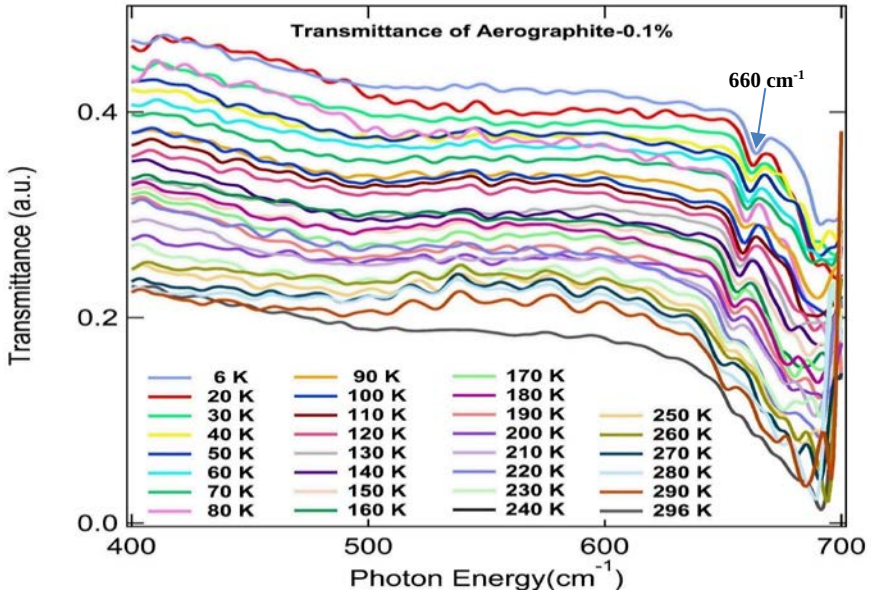

Figure 4.6: THz/Far-IR transmittance spectra of Aerographite from 400–700 cm^{-1} at various temperatures, from 6 K to 300 K.

In the frequency range of 800–1000 cm^{-1}, the obvious IR active bands of Aerographite at 889 cm^{-1} were assigned to the A_{2u} symmetry out-of-plane vibration [139] (Fig. 4.7). It also reported that there is an IR active A_{2u} mode (868 cm^{-1}) in graphite. The peak at 889 cm^{-1} has anomalous intensity vs. temperature. It is the strongest at 180 K and it is split between 110 and 130 K and then again at 190 and 200 K. As temperature increases, the IR spectra lines increase, and the peaks shift. Couples of vibrational transitions overlap in the absorption bands at higher temperature due to the broadening of the linewidths.

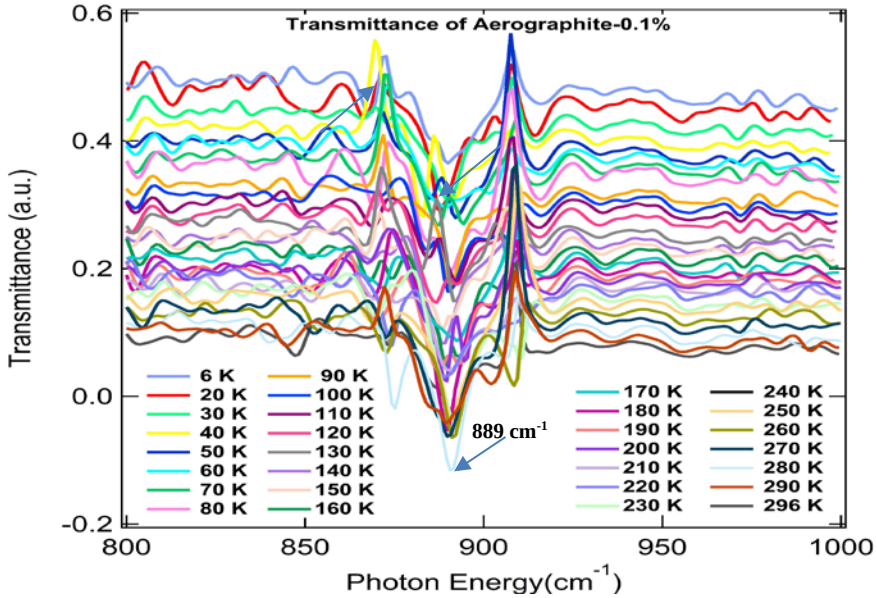

Figure 4.7: THz/Far-IR transmittance spectra of Aerographite from 800–1000 cm^{-1} at various temperatures, from 6 K to 300 K.

In the 30–300 cm^{-1} spectral region, the IR absorption bands of SWCNT aerogel at 40, 79, 115 and 252 cm^{-1} are presented in Fig. 4.8. Only the peak position at 79 cm^{-1} shows a "red-shift" effect as temperature increases. The sharp absorption band profiles at low temperatures became broad at high temperatures due to the amorphous and disordered structures in the SWCNT aerogel. The 79 cm^{-1} is ascribed to sliding of graphite planes parallel to each other. This raises the question as to whether SWCNTs have such mode (which will be possible if their diameters are very large), or perhaps some SWCNTs changed into graphite when making the SWCNT aerogel. This is normally a Raman active mode, yet it appears in the IR spectrum. The IR absorption band at 115 cm^{-1}, is attributed to the E_{1g} active mode. Rao *et al.* reported diameter selective coupling of the SWCNTs to the exciting radiation field that stems from the diameter dependence of the electronic density of states induced by quantum confinement [49]. The band at 252 cm^{-1} in Fig. 4.9 is tentatively, attributed to the RBM mode in SWCNT aerogel [145]. It appears in the low temperature range from 6–160 K, and becomes indistinguishable obvious above 160 K.

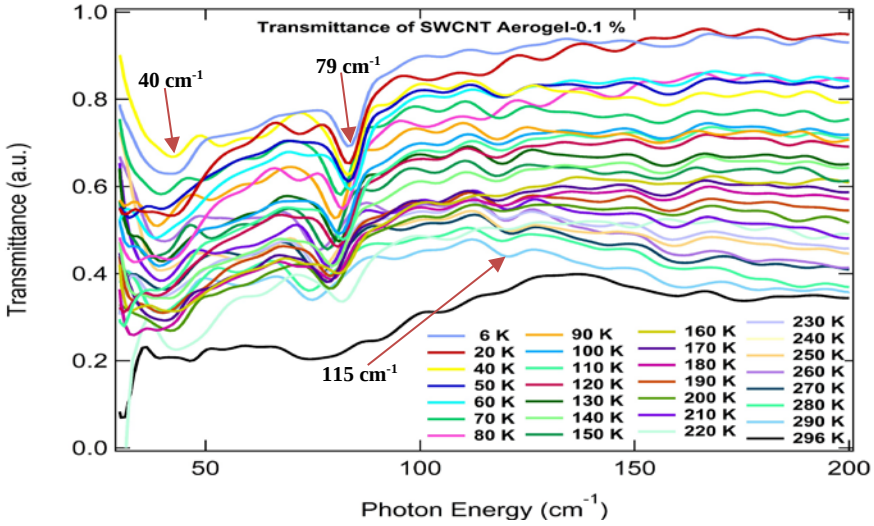

Figure 4.8: THz/Far-IR transmittance spectra of SWCNT aerogel from 30–200 cm^{-1} at various temperatures, from 6 K to 300 K.

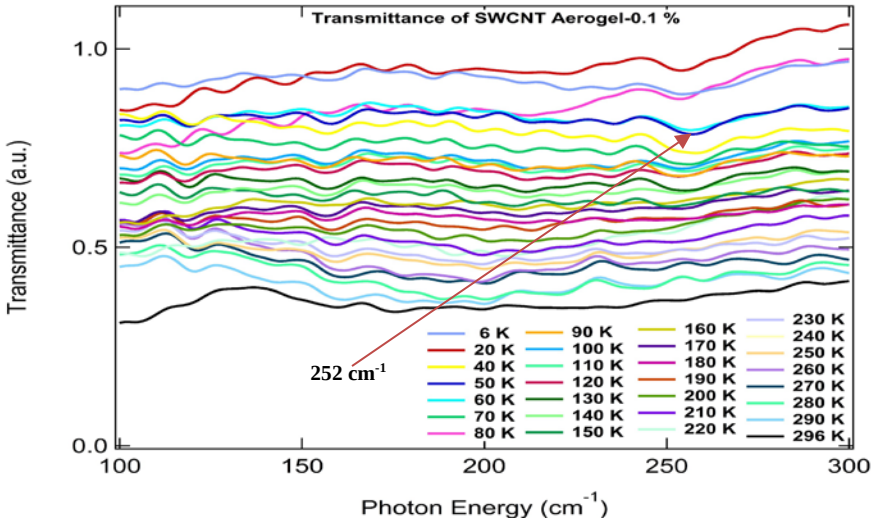

Figure 4.9: THz/Far-IR transmittance spectra of SWCNT aerogel from 90–300 cm^{-1} at various temperatures, from 6 K to 300 K.

In the 500–750 cm^{-1} spectral region, there is an IR absorption band of SWCNT aerogel located at 685 cm^{-1} (Fig. 4.10), which was attributed to the first order IR vibration mode (A_2) because of the C-H out-of-plane deformation bands. This arises from a Fermi resonance effect between the C-H stretching vibration and the first overtone of the C-H deformation vibration [82,141].

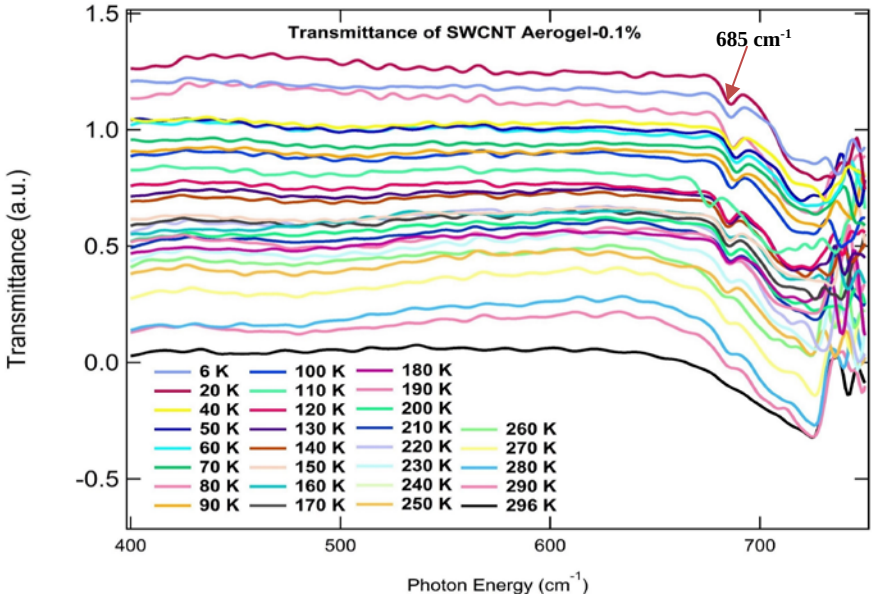

Figure 4.10: THz/Far-IR transmittance spectra of SWCNT aerogel from 400–750 cm^{-1} at various temperatures, from 6 K to 300 K.

In the 800–1000 cm^{-1} spectral region, the obvious IR absorption bands of SWCNT aerogel appear, at different temperatures, at 832, 902, 923, and 968 cm^{-1} (Fig. 4.11). The observed band at 832 cm^{-1} was possibly due to the oscillations or multiple reflections in the spectrometer and samples. Other IR absorption bands at 902, 923, and 968 cm^{-1} are attributed to the second order IR vibrations [141].

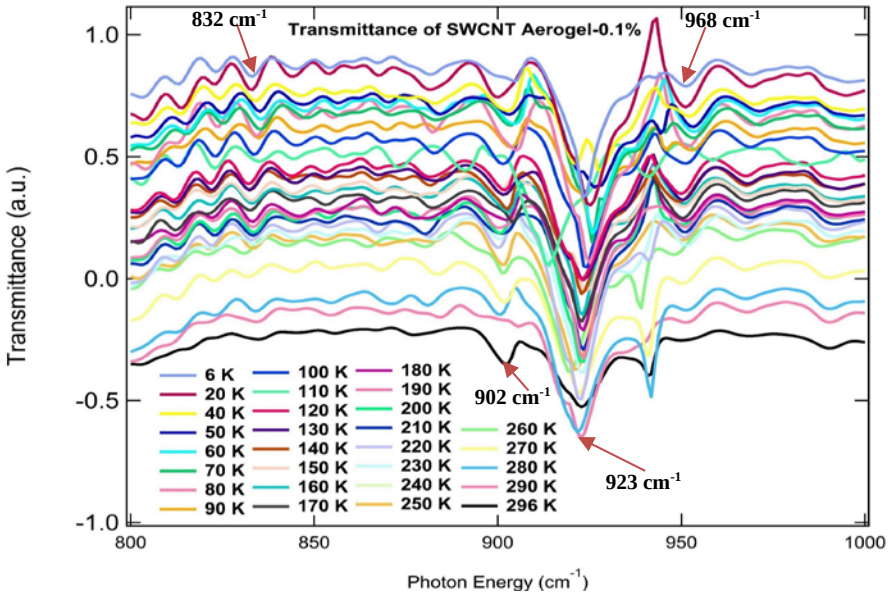

Figure 4.11: THz/Far-IR transmittance spectra of SWCNT aerogel from 800–1000 cm^{-1} at various temperatures, from 6 K to 300 K.

There are some factors, such as the Fabry–Pérot interference effects, parallelism of the sample surfaces and the inhomogeneity of and scattering by the sample, that will affect the background oscillations [25,30]. All the contributing background oscillations, affecting the optical constants, are combined to give the total uncertainty in the measurement.

4.3.3 Raman Spectra

Section 4.3.2 reports some IR absorption bands that are not expected from group theory. For example, the observed 40 cm^{-1} band of Aerographite (Fig. 4.4) is expected to be Raman active, but not IR active. Raman spectroscopy of Aerographite and SWCNT aerogels is presented in the following sections going down to energies as low as 10 cm^{-1}, to check if the observed IR bands indeed correspond to the expected vibrational modes that are predicted for the Raman spectra. After introducing the spectra in Section 4.3.3.1 and Section 4.3.3.2, the temperature dependence of the Raman bands is presented in Section 4.3.4.1. This will be compared to the temperature dependence of the corresponding IR absorption bands, which will give further clues on the occurrence of the unexpected IR absorption bands in the synchrotron measurements.

4.3.3.1 Aerographite

The room temperature Raman spectrum of Aerographite excited by a 514 nm laser is shown in Fig. 4.12. The Raman spectrum exhibits the typical spectral features of graphitic materials. Raman peaks at ~1588 cm^{-1} and ~1346 cm^{-1} are the first order Raman modes and known as the G and D modes, and the Raman peak at about 2600–2900 cm^{-1} is the overtone of the D mode (G′/2D), which has its origin in the breathing modes of six atom rings [47,52,57]. The strong D band indicates that armchair edges are present in Aerographite [121]. Because of its highly disordered structure, the Raman modes of Aerographite associated with disorder or defects are activated either as a higher-order (combination and overtones modes) or as a defect-induced process. These details have been discussed already under the double resonant Raman scattering theory in Chapter 3.

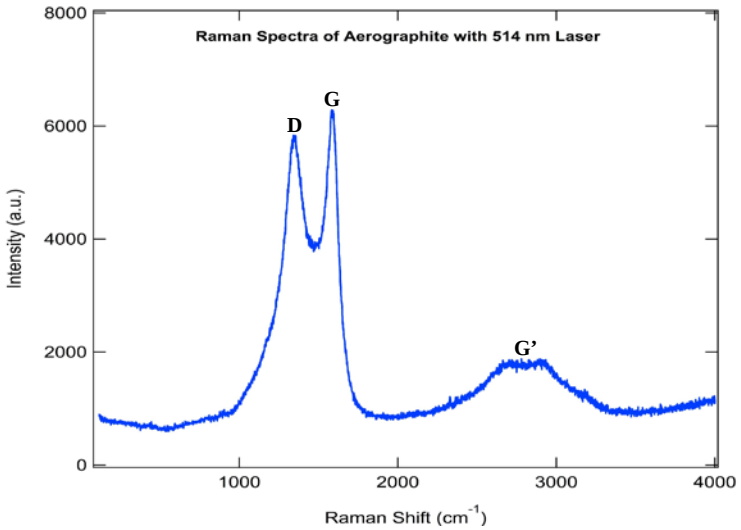

Figure 4.12: Raman spectrum of Aerographite at 514 nm laser excitation.

Combining the IR and Raman results, there are two Raman active E_{2g} modes as fundamentals (1585 and 40 cm^{-1}); two IR active A_{2u} modes (1588 and 867 cm^{-1}); one IR active A_{1g} mode (152 cm^{-1}); the other two are "silent" modes.

4.3.3.2 SWCNT Aerogel

The room temperature Raman spectrum of SWCNT aerogel excited by a 514 nm laser is shown in Fig. 4.13. It may be divided into four main regions: the low frequency region from 100–500 cm^{-1}, the intermediate region from 500–1000 cm^{-1}, the high frequency region from 1000–2000 cm^{-1}, and the second order region from 2000–4000 cm^{-1}.

There features which distinguish this from the Raman spectra of Aerographite: (1) the low frequency RBM appears in the range 50–760 cm^{-1}, which is unique to each SWCNT structure with a particular (*n*, *m*), assigned to a bond-stretching out-of-plane phonon mode; and (2) two in-plane optical-phonon modes in SWCNT aerogel, i.e. the LO and TO phonon modes at the Γ point in the Brioullin zone [53,61]. These modes are degenerate in other sp^2 carbon materials. However, they split into two peaks, G^+ (~1571cm^{-1}, LO phonon, high frequency part) and G^- (~1520 cm^{-1}, iTO phonon, low frequency part) peaks in the semiconducting SWCNT. This spliting is inversely proportional to the square of diameter of the SWCNT due to the curvature effect and electron-phonon interaction [55,61,133]. The peaks in the Raman spectra for SWCNT aerogel (Fig. 4.13) can be assigned to one-phonon or two-phonon, first order or second order double resonance Raman scattering processes. These are summarized in Table 4.1.

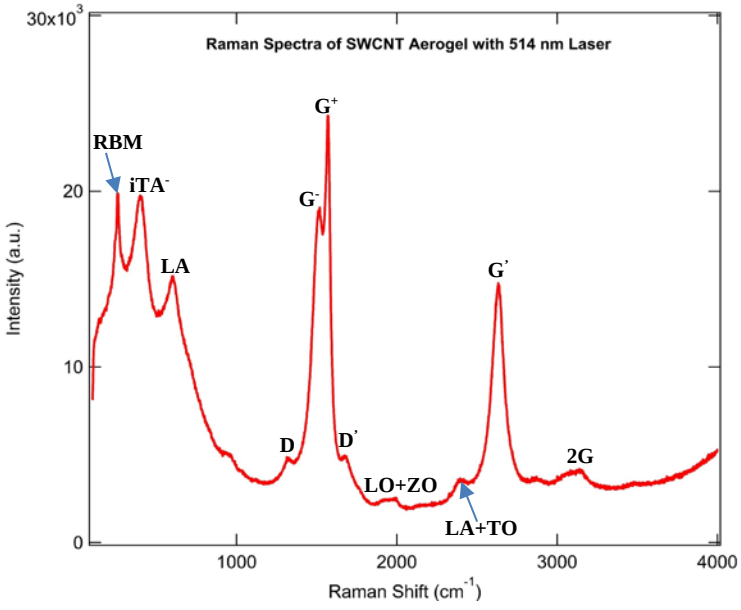

Figure 4.13: Raman spectrum of SWCNT aerogel at 514 nm laser excitation.

The RBM is the characteristic phonon mode of SWCNTs, which has A_{1g} (IR) symmetry [140]. All carbon atoms move in phase in the radial direction creating a breathing-like vibration of the tube [50]. The RBM frequency ω_{RBM} is proportional to the inverse of SWCNT diameter, *d*, [61,140],

$$\omega_{\mathrm{RBM}} = \frac{227}{d}\sqrt{1 + C_{\mathrm{e}} d^2} \approx \frac{227}{d} \quad (4.9)$$

$$d = a_0\sqrt{n^2 + nm + m^2} \,/\, \pi \quad (4.10)$$

where C_e (nm^{-2}) probes the enviornment effect on ω_{RBM}, such as contact with a substrate, water, oxygen, or charged molecular species; a_0= 0.2461 nm, and (*n*, *m*) is the chiral index [61,140]. The most abundant (*n*, *m*) species for the CG 300 semiconducting SWCNTs are (6, 5), (7, 5) and (7, 6). From this we can deduce that the diameters of the SWCNT are 0.75 nm, 0.86 nm and 0.88 nm, and the frequencies of the RBM are ω_{RBM} = 303 cm^{-1}, 264 cm^{-1} and 258 cm^{-1}, respectively.

TABLE 4.1 Assignments and frequency behavior for Raman modes of SWCNT aerogel.

Name	Pos. (cm^{-1})	Origin	Details
RBM	262	first order	SWCNT vibration of radius
iTA	403	one-phonon DR Raman	iTA mode, intravalley scattering (*q=2k*)
LA	604	one-phonon DR Raman	LA mode, intravalley scattering (*q=2k*)
D	1323	one-phonon DR Raman	iTO mode, intervalley scattering (*q=2k*)
G$^-$	1520	first order Raman	in-plane vibrations, Raman active mode
G$^+$	1573	first order Raman	in-plane vibration, Raman active mode
D′	1686	one-phonon DR Raman	LO mode, intravalley scattering (*q=2k*)
LO+ZO	1998	two-phonons DR Raman	Combination mode of LO and LA
LA+TO	2396	two-phonons DR Raman	Combination mode of LA and TO
G′ (2D)	2634	two-phonons DR Raman	Overtone of D mode
2G	3150	two-phonons DR Raman	Overtone of G mode

[a] Mode frequencies for dispersive modes are given at E_L= 2.41 eV.
[b] ZO is the out-of-plane optical phonon mode [143].
[c] DR is the double resonance Raman scattering process.

Thus, Raman spectroscopy of SWCNT aerogel yields important information on the structural properties of the SWCNT aerogel, as well as on the physical properties of SWCNTs. These Raman results confirm that the SWCNT in the SWCNT aerogel gave all Raman features as expected for "free" SWCNTs. Therefore, the procedure of making the SWCNT aerogels did not affect the Raman properties of SWCNT's.

4.3.4 Temperature Dependence of Raman and Synchrotron THz/Far-IR Spectra

Temperature dependent vibrational spectroscopy can provide valuable information on physical and chemical properties, phonon anharmonicity and electron-phonon coupling of sp^2 carbon-based materials [135]. It is important in determining the intrinsic values of related parameters, which may have consequences for the further applications of materials.

Bononi *et al.* reported the finite-temperature dependent properties of graphite and graphene by first-principles considerations, i.e. linewidths, line shifts and lifetimes [146]. In graphite, the phonon linewidth of the Raman active E_{2g} mode anomalously decreased with temperature. This is driven by the electron-phonon coupling and does not appear in the nearly degenerate IR active E_{1u}

modes [146]. Ugawa *et al.* reported temperature dependent IR properties of SWCNT in the frequency range of 15–5000 cm^{-1} and temperature range 7.8–298 K [147]. The temperature dependence of reflectance is small, and no temperature dependence of vibrational structures was observed at the measured temperatures. A low frequency absorption band was observed in the optical conductivity at 135 cm^{-1} due to a pseudo- and small gap in SWCNTs [147]. Giura *et al.* performed a comparative experimental and theoretical investigation of the temperature dependence of the frequency and linewidth of IR active optical phonons modes (E_{1u} and E_{2g}) in highly oriented pyrolytic graphite (HOPG) from 300–700 K [148].

4.3.4.1 Temperature Dependence of Raman Spectra

Temperature dependent Raman spectra provide a method to further understand the fine structural information and intrinsic physical properties of the materials under study, such as atomic bond structure, electron-phonon coupling and thermal stability. The change in phonon frequency with temperature can be attributed to a thermal effect $\left(\frac{\partial\omega}{\partial T}\right)_V$ and to a volume-related effect $\left(\frac{\partial\omega}{\partial v}\right)_T \left(\frac{\partial v}{\partial T}\right)_p$ through lattice expansion according to [51]:

$$\Delta\omega = \left(\frac{\partial\omega}{\partial T}\right)_V \Delta T + \left(\frac{\partial\omega}{\partial v}\right)_T \left(\frac{\partial v}{\partial T}\right)_p \Delta T \tag{4.11}$$

The intrinsic temperature dependence of the Raman spectra of graphite and carbon nanotubes have been reported by [135,147,148] and [126,149], respectively. Chatzakis *et al.* studied the temperature dependence of the anharmonicity decay rate of zone-center (G mode) optical phonons in both SWCNs and graphite using time-resolved anti-Stokes Raman spectroscopy [149]. For SWCNTs, little temperature dependence of the decay rate was observed below 300 K. Above 300 K, the decay rate increased from 0.8–1.7 ps^{-1}. The decay rate of graphite was observed to increase from 0.5 to 0.8 ps^{-1} over the temperature range of 300–700 K [149].

In order to distinguish the intrinsic contributions of phonon anharmonicity to the positions of the G and 2D peaks, temperature dependent Raman spectra of Aerographite and SWCNT aerogel were investigated in this project in back-scattering geometry using a Renishaw inVia™ confocal Raman microscope equipped with a liquid nitrogen cooled CCD over the temperature range 80–300 K. Figs. 4.14 and 4.15 show the Raman spectra for Aerographite under a laser excitation at 514 nm at various temperatures, from 80 K to 300K, respectively.

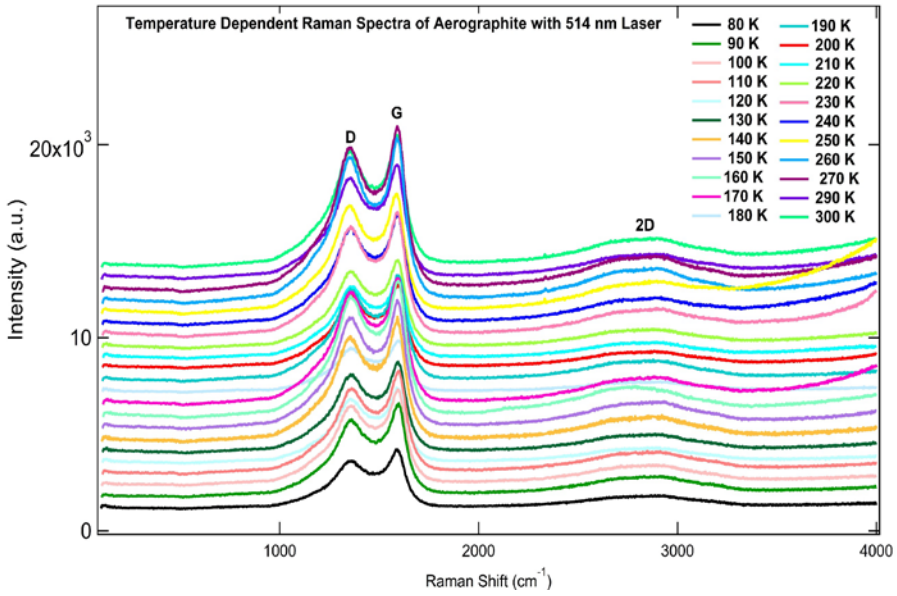

Figure 4.14: Raman spectra for Aerographite under a laser excitation at 514 nm at various temperatures, from 80 K to 300 K.

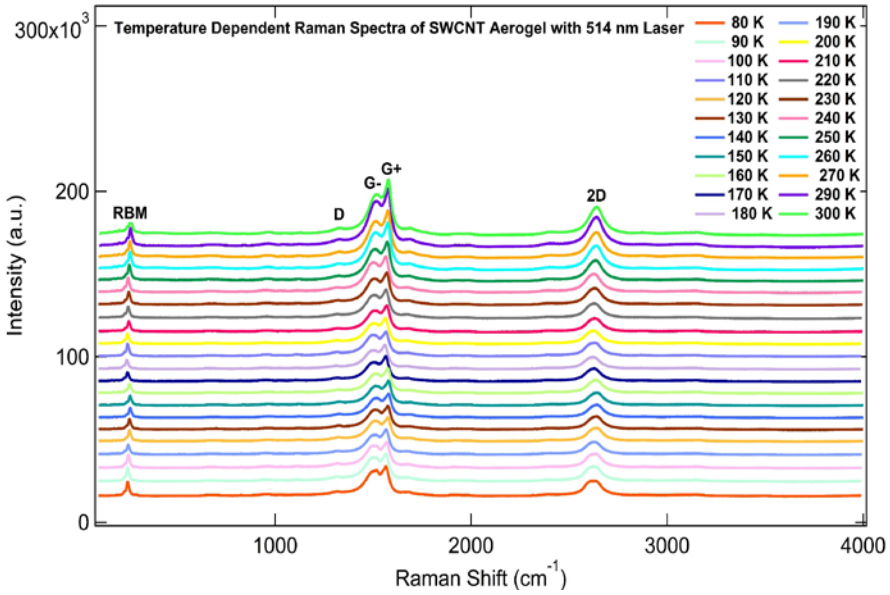

Figure 4.15: Raman spectra for SWCNT aerogel under a laser excitation at 514 nm at various temperatures, from 80 K to 300 K.

In Fig. 4.14, the temperature dependent Raman spectra of Aerographite may be seen to be composed of three major spectral features of graphitic materials, namely the D, G and 2D bands. Raman spectra of SWCNT aerogel (Fig. 4.15) at different temperatures also show typical Raman peaks of SWCNTs, namely, the RBM, D, G^-, G^+ and 2D peaks. Figs. 4.16 and 4.17 present the temperature dependent evolutions of Raman peak energies of Aerographite and SWCNT aerogel across the measured temperature range. The oscillations appear in the data in Figure 4.17 are artefacts of fitting; temperature oscillations would not be this large.

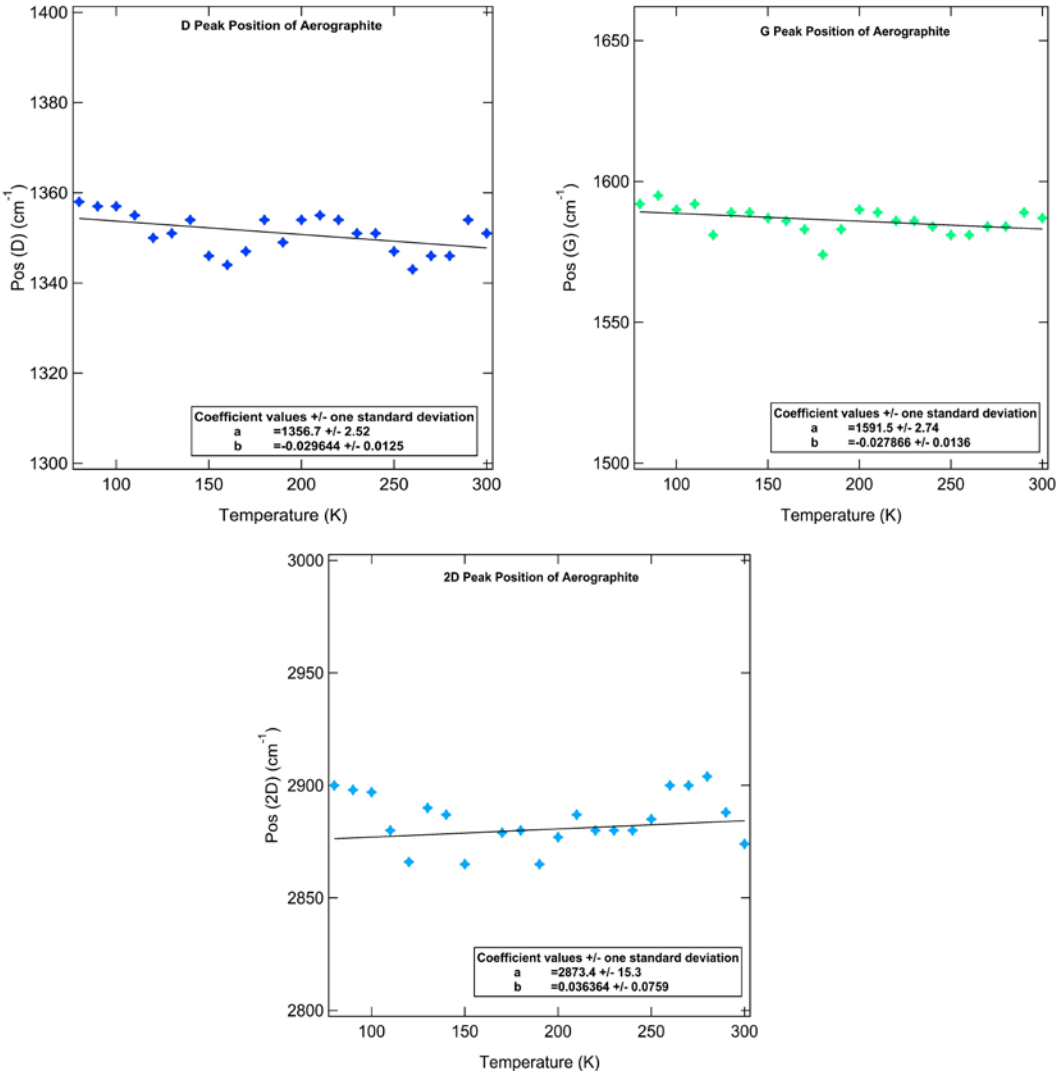

Figure 4.16: Temperature dependent evolutions of Raman peak positions of Aerographite from 80–300 K.

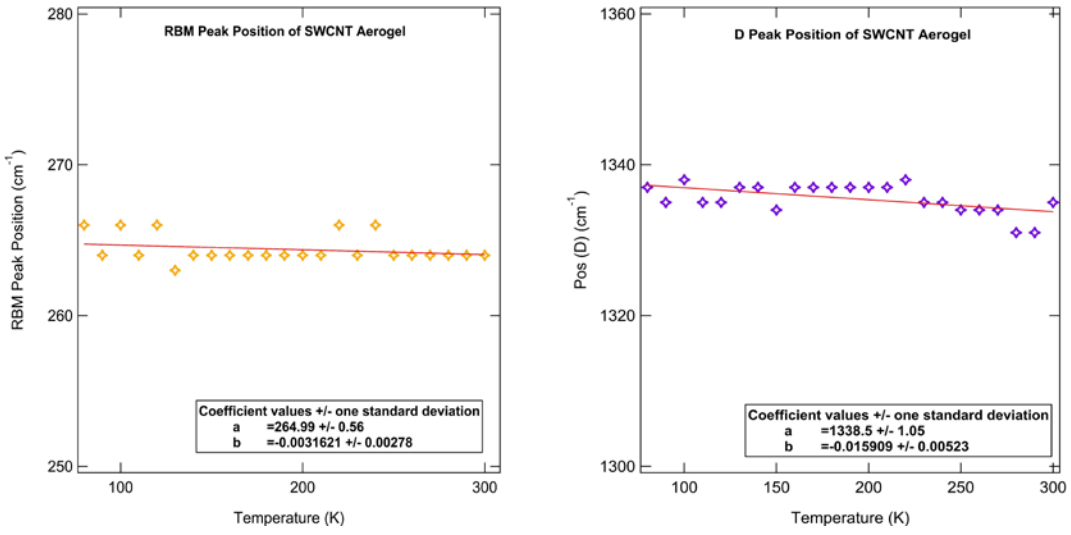

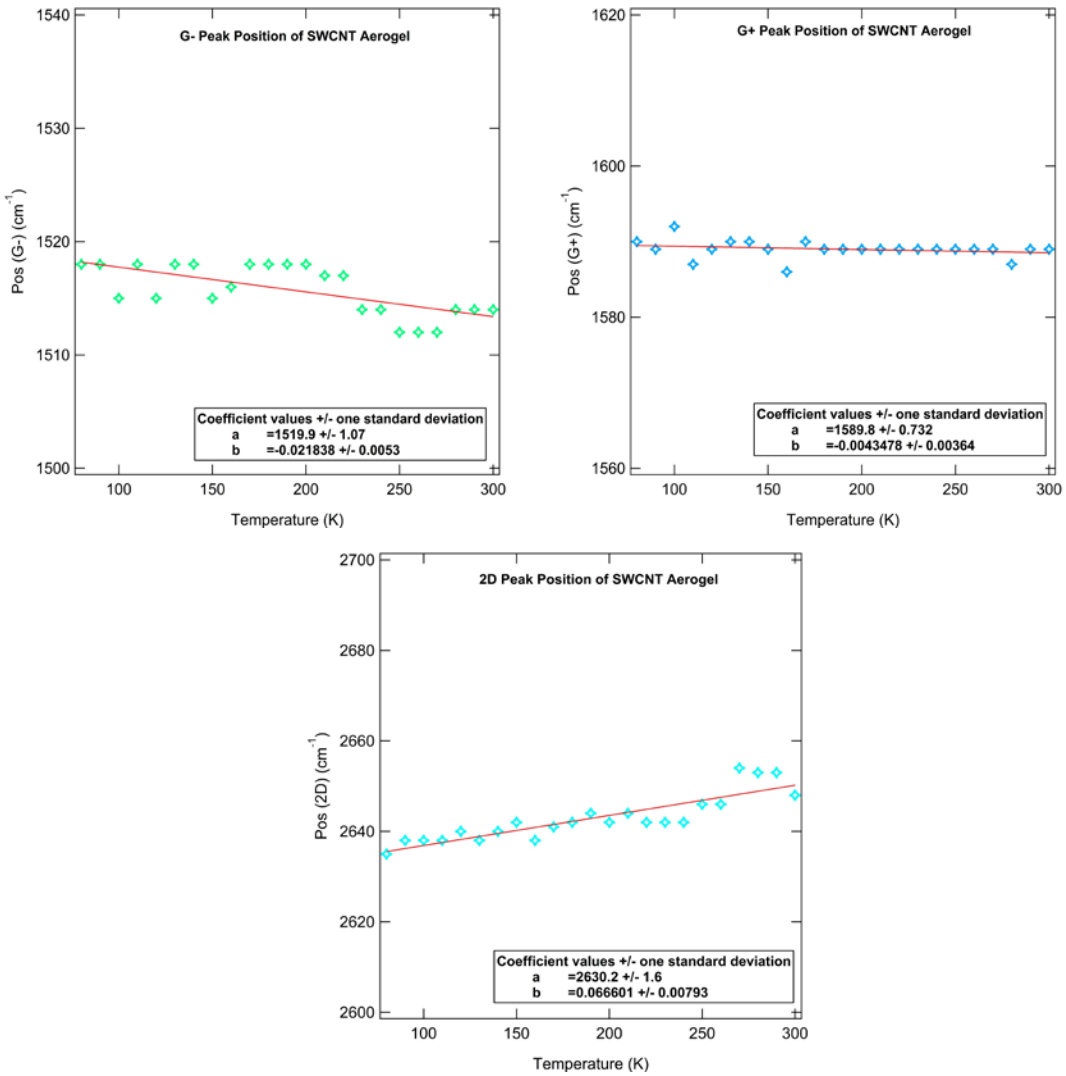

Figure 4.17: Temperature dependent evolutions of Raman peak positions of SWCNT aerogel from 80–300 K.

Increasing temperature leads to the "red-shift" of Raman peaks D and G bands in Aerographite and of the D and G^+ peaks in SWCNT aerogel with temperature over the range 80–300 K. The measured temperature dependence of the frequency shift of the Raman modes in Aerographite may be fitted by a linear equation:

$$\omega = \omega(0) + \chi T \tag{4.12}$$

where $\omega(0)$ is the mode frequency at 0 K and the first-order thermal coefficient $\chi = \frac{d\omega}{dT}$ is defined as the frequency shift when the temperature of the sample increases by 1 K, which is the slope of the fitted straight line [148,150]. By fitting the extracted peaks positions of temperature dependent Raman spectra, the χ values for D and G modes in Aerographite are found to be (-0.03+/-0.01) cm^{-1}/K and (-0.03+/-0.01) cm^{-1}/K, shown as the fitting parameter *b* indicated in Fig. 4.16, while the χ value for the 2D mode in Aerographite is (0.04+/-0.07) cm^{-1}/K, that is, negligible (Fig. 4.16). In Fig. 4.17, the position of the RBM peak in SWCNT aerogel (264 cm^{-1}) is a constant within experimental uncertainty. This occurs because the RBM, a unique Raman feature of SWCNTs, only depends on both diameter and chirality [148]. The χ values for the D, G^- and G^+ modes in

SWCNT aerogel are (-0.016+/-0.005) cm^{-1}/K, (-0.022+/-0.005) cm^{-1}/K and (-0.004+/-0.004) cm^{-1}/K, respectively. The χ value for the 2D mode in SWCNT aerogel is (0.067+/-0.008) cm^{-1}/K.

Comparing the Aerographite and SWCNT aerogel results, the χ value for the D mode for Aerographite (-0.03+/-0.01 cm^{-1}/K) is twice the χ value for the D mode in SWCNT aerogel (-0.016+/-0.005 cm^{-1}/K) whereas the χ value for the G^+ mode in Aerographite (-0.03+/-0.01 cm^{-1}/K) is similar to the corresponding χ value of the G^- mode in SWCNT aerogel (-0.022+/-0.005 cm^{-1}/K). This relatively strong temperature dependence in Aerographite may be due to the enhanced increase in the C-C distance, reflecting that Aerographite is a highly disordered graphite system containing many defects [135,136]. The χ value of the G^+ mode in SWCNT aerogel is (-0.004+/-0.004) cm^{-1}/K, which reflects the softening of the C-C (intratubular) bonds with temperature, and the softening of the van der Waals inter-tubular interactions between SWCNTs in SWCNT aerogel [136,150]. The χ value of the 2D modes in Aerographite and SWCNT aerogel are all positive. This value in Aerographite (0.04+/-0.07 cm^{-1}/K) is around half of that in SWCNT aerogel (0.067+/-0.008 cm^{-1}/K). This is attributed to the structural characteristic of the SWCNT, being a single tubular carbon sheet, having a smaller diameter and thus relatively larger curvature effect than occurs in Aerographite [135,136].

The changes in Raman frequency with temperature are mainly attributed to anharmonic effects in the lattice vibrational energy, which are related to the anharmonic potential constant and the thermal expansion of the crystal [146,151]. As the temperature increases, there is a shift in the frequency to the low-wavenumber region because of the phonons softening [135,136,152]. The changes in the frequency of SWCNT with temperature is attributed to the C-C bond stretching, due to thermal expansion in the lattice or anharmonic couplings of phonon modes [150,153]. The behavior of the 2D peak of SWCNT aerogel is the opposite to what is expected from anharmonic effects, “blue-shifting” instead of “red-shifting” with temperature. A “blue-shift” of phonon energies with temperature has been also reported for some molecular crystals, where hydrogen and van der Waals bonds play an important role [154]. The interplay between the thermal expansion determined mainly by van der Waals bonds with intra- and inter-molecular hydrogen bonds was shown to result in the “blue-shift” for phonon modes in which the inter-and intra-molecular hydrogen bonds play the decisive role. However, it is difficult to see how this explanation would apply for SWCNTs as there are only carbon atoms in SWCNT.

4.3.4.2 Temperature Dependence of Synchrotron THz/Far-IR Spectra

Synchrotron THz/Far-IR peak positions of Aerographite and SWCNT aerogel vs. temperature from 6–300 K as obtained in this project are shown in Fig. 4.18. The IR peak positions are given for both samples of Aerographite and SWCNT aerogel at 40 (E_{2g}), 78 (E_{1u}), 114 (ZO′), 660 (A_2) and 867 (A_{2u}) cm^{-1}, respectively. Only the positions of E_{1u} mode (78 cm^{-1}) of Aerographite and SWCNT aerogel show an obvious linear behavior, decreasing with temperature increase in the measured temperature range. All other peak positions are nearly constant and do not show

measurable change with temperature for either Aerographite or SWCNT aerogel.

(a) Aerographite (b) SWCNT Aerogel

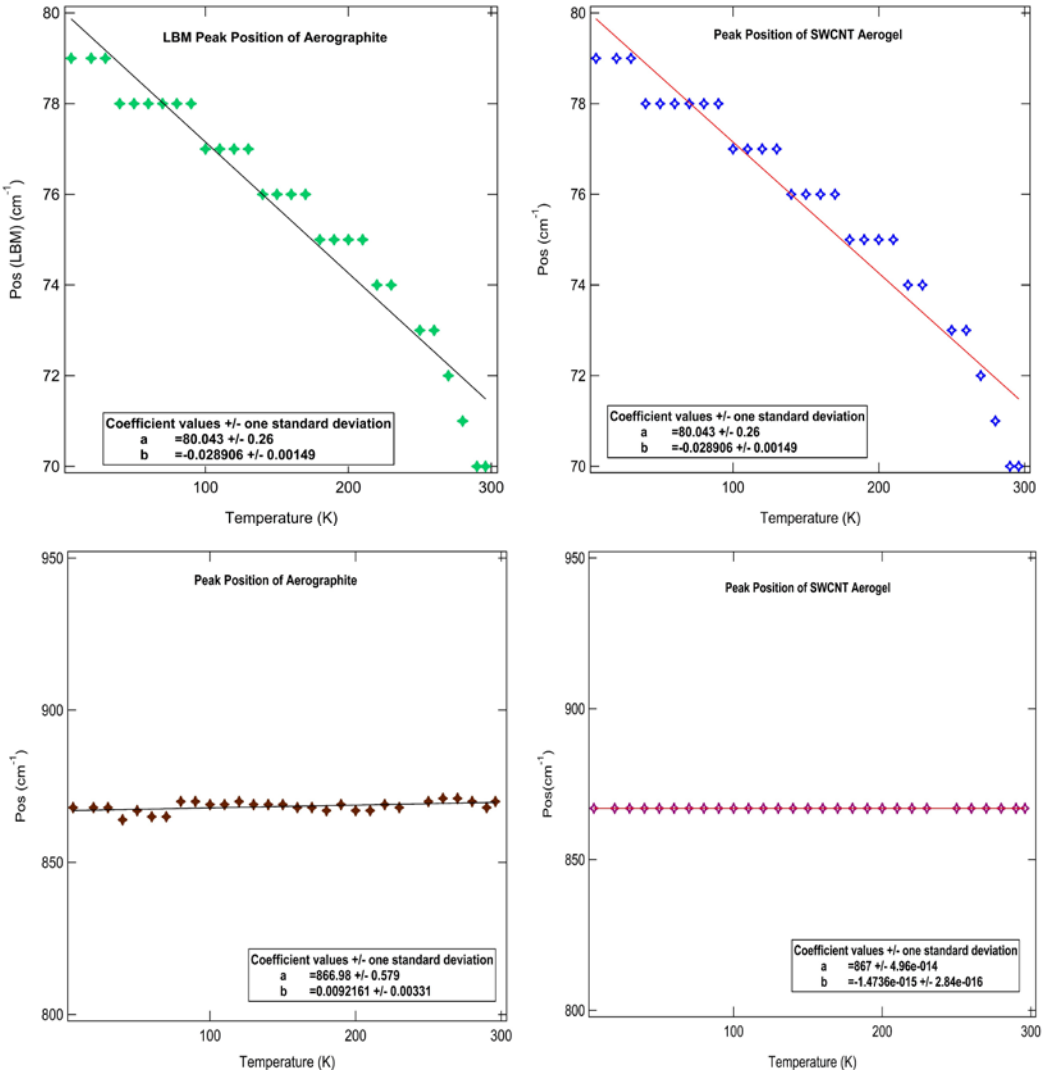

Figure 4.18: Synchrotron THz/Far-IR peak positions of Aerographite and SWCNT aerogel vs. temperature from 6–300 K.

For Aerographite and SWCNT aerogel, the position of the IR active E_{1u} mode is constant around 79 cm^{-1} in the low temperature range (6–30 K). As the temperature increases from 40 K to 275 K, the position of the IR active E_{1u} mode decreases to 72 cm^{-1}. The rate of shift is (-0.03+/-0.0015) cm^{-1}/K, which is nearly equal to the χ values of the D and G^{+} modes of Aerographite. The shift accelerates above 275 K, becoming ~70 cm^{-1} at 300 K. There is a "red-shift" trend in that the peak position of IR active E_{1u} mode shifts to lower frequencies, linearly decreasing with increasing temperature from 6 K to 300 K.

4.4 Discussion on Synchrotron THz/Far-IR and Raman Spectra

4.4.1 Activation of New IR Bands by Disorder and Defects in Aerographite and SWCNT Aerogel

Synchrotron THz/Far-IR spectra measurements of Aerographite and SWCNT aerogel indicate several new IR absorption bands over the measured temperature ranges, which is useful in understanding the structure and interactions in these materials. For Aerographite, all observed IR absorption bands, namely those at 40, 79, 114, 152, 248, 660, 867 and 889 cm^{-1}, are presented in Section 4.3.1. For SWCNT aerogel, all expected IR absorption bands were observed, at 40, 79, 115, 252, 685, 832, 853, 867, 902, 923, 968 and 992 cm^{-1}, respectively. These IR absorption bands, appearing in the far- or mid-IR region, correspond to phonon or intermolecular vibrations. A previously reported IR active absorption band at 867 cm^{-1} was confirmed in both Aerographite and SWCNT aerogel.

According to group theory and symmetry, graphite contains two double degenerate Raman active E_{2g} modes (1580 and 42 cm^{-1}); two IR active A_{2u} and E_{1u} modes (868 and 1588 cm^{-1}); and two are "silent" B_{2g} modes (one is at 127 cm^{-1} and another at 870 cm^{-1}) [47,139]. For SWCNTs, the selection rules indicate there are 15-16 Raman active and 6-9 IR active modes for SWCNT, depending on their symmetries [50,141,142]. Phonon modes around 868 and 1588 cm^{-1} appear in all symmetries and independently of the diameter. Typically, SWCNTs exist the low frequency RBM (~262 cm^{-1}), G^+ (~1573 cm^{-1}, LO phonon), G^- (~1520 cm^{-1}, iTO phonon), D (~1573 cm^{-1}), G′ (~2634 cm^{-1}) and other weak Raman features [49,156]. SWCNTs also exist the IR radial mode and tangential modes are identified around 860 and 1587 cm^{-1}, and additional peaks (i.e. 682, 820, 854, 860, 868, 873 and 880 cm^{-1}) [141].

The possible explanation for these unpredicted bands occurring in the synchrotron IR spectra of Aerographite is the high structural disorder and numerous defects in Aerographite disrupting the lattice symmetry of the sp^2 carbon-based system. Using symmetry considerations to assign IR and Raman activities to each of the bands is no longer valid when the symmetry is disrupted by the extensive defects in Aerographite. The crystalline selection rules are relaxed in this amorphous sp^2 carbon structure [119,121,141]. New IR modes are activated by disorder-induced symmetry breaking effects in Aerographite [141]. The most common reason for symmetry breaking is vacancies and interstitial or substitutional atoms which may be introduced intentionally, or by inducing interfaces at the boundary of crystallite areas. The defect-induced double-resonant model in chapter 3 may be used to account for this IR activation behavior [61-65,122].

In Aerographite, defects break the momentum conservation requirement for the first order q=0 IR allowed phonons. In principle, any resonance involving phonons in the interior of the Brillouin zone ($q \neq 0$) would be allowed [61,121]. On the other hand, the edge structures of Aerographite, i.e. the armchair and zigzag edges, are also the source of defect-induced IR active modes. Since the edge states are particularly occupied by π electrons, the IR intensity depends on the sp^2 fraction and π electrons delocalization [141]. In the disordered structure in Aerographite, with small crystallite sizes, the boundaries of crystallites form defects with random orientation. The defect

wave vectors then exhibit all possible directions and values. In this way, it is possible to activate new IR bands in Aerographite by such edge effects.

Similarly, the curvature effect on the structure and quantum confinements in SWCNT aerogel will break the inversion symmetry, leading to activation of new IR bands, which depend on defect density and tube lengths [121,136,141,145]. The temperature-induced softening of the intra-and inter-tubular bonds then contribute to the temperature-dependent vibrational mode shift in SWCNTs [136].

4.4.2 van der Waals Force for Thermal Expansion of Aerographite and SWCNT Aerogel

Temperature dependent vibrational spectra of Aerographite and SWCNT aerogel revealed major Raman features–D, G and 2D bands for Aerographite, and RBM, D, G^-, G^+ and 2D bands for SWCNT aerogel. The "red-shift" phenomenon of the Raman D and G bands was observed in Aerographite and for the D and G^+ peaks in SWCNT aerogel over the temperature range 80–300 K. In contrast, the 2D peak of SWCNT aerogel showed a "blue-shift" effect with temperature over the same temperature range. This is mainly driven by the van der Waals force, which reflects the anisotropic nature in graphite: the in-plane thermal conductivity is much higher than cross-plane [155]. This increases the distance between the SWCNTs and conceivably results in a small charge re-distribution between the C-atoms. This in turn may result in a "blue-shift", similar to the one observed in 2,4-dinitrotoluene (DNT) [154].

The variation of the Raman spectral peak position with temperature possibly arises from anharmonicity in the bonding between different atoms [156,157]. Thermal expansion of Aerographite and SWCNT aerogel results in lengthening of the intermolecular bonds. These are the van der Waals bonds, which are much weaker than intramolecular covalent bonds [136,154,156]. The lengthening will cause the force constants to increase or decrease, which will eventually result in a shift of Raman spectra peak position for those vibrational modes which are determined by the inter-molecular vibrations [156,157]. It is confirmed in the results presented that Aerographite and SWCNT aerogel have red-shifting spectral lines at energies around ~ 79 cm^{-1}. These modes are therefore deduced to be associated with inter-molecular vibrations between different CNTs (in SWCNT aerogel), or between different graphite layers in Aerographite. Indeed, symmetry considerations predict that 79 cm^{-1} modes correspond to the vibration of graphite planes parallel to each other [144]. Resonance and overtone/combination modes cannot be predicted by symmetry because these vibration modes are caused by interactions among the fundamental modes [44,61-65]. The role of phonon interactions will be implicated in the measurable widths of peaks, while non-interacting vibrational modes would be manifested as a δ function in the dielectric constant [44].

The peaks around 40 cm^{-1} constitute a low frequency E_{2g} shear Raman mode (C peak) involving sliding of graphite layers [158-160]. Therefore, van der Waals bonds between the layers determine the energy of these vibrations and the anharmonic effects associated with these vibrations are determined purely by such van der Waals forces. The intra-molecule covalent bonds do not distort this vibration and the anharmonicities associated with the covalent bonds do not contribute to the "red-shift" observed here.

Vibrational modes responsible for the "blue-shift" with temperature should also be affected by the thermal lengthening of van der Waals interaction distances. An explanation of "blue-shift" in DNT was given through an interplay between van der Waals and hydrogen bonds and associated charge transfer within the hydrogen bonds arising from thermal expansion of this molecular crystal [180]. Similar explanation could be sought for the blue shift observed for 2D band of SWCNT (Fig. 4.17). However, there are no hydrogen bonds in SWCNT. Instead, explanation for the "blue-shift" could be sought in terms of the charge transfer between covalently bonded C atoms in SWCNT, induced by lengthening of van der Waals bonds as temperature increases [156]. This explanation would require interaction electrostatic interactions between neighboring SWCNT's affecting the local charge density within each of the SWCNTs. An alternative explanation may be sought within the double resonant Raman scattering model, which describes the occurrence of D bands. Then, thermal expansion could affect the electron dispersion relation of SWCNT's through a change of electrostatic interactions between SWCNTs as the distance between them increases. This would in turn result in change of the energy of the phonon participating in the double resonant Raman scattering. These are two hypotheses that require a more rigorous theoretical verification for their ability to explain the observed "blue-shift" with temperature.

4.5 THz Raman Spectra of Graphite Flakes and SWCNT Aerogel

Raman spectroscopy is a "scattering" method to analyze molecular vibrations usually in the frequency from 200 cm^{-1} (6 THz) to 4000 cm^{-1} (120 THz). It is possible to identify chemical information ("fingerprint") of a substance in this range. However, the Raman signal is intrinsically weak due to its inelastic scattering nature, which measures the transfer of energy between phonons and excited electrons. In addition, there is rich structural information on vibrational energies associated with molecular and intermolecular features in the low-wavenumber region (5 cm^{-1} to 200 cm^{-1}, or 150 GHz–6 THz). However, the Raman shift below 200 cm^{-1} (6 THz) is difficult to access because the edge or notch filter usually blocks a relatively large spectral region [161]. Recent advances in volume holographic grating filters have enabled the manufacture of narrow bandwidth notch filters with high throughput to access the THz region [161]. THz Raman spectroscopy gives access to both the THz "new structural fingerprint" and the traditional Raman "chemical fingerprint" region, including anti-Stokes signals.

Room temperature THz Raman spectra were obtained using a NTEGRA Spectra AFM-Confocal Raman-SNOM-TERS integration system (NT-MDT Spectrum Instruments, Moscow, Russia) in

ambient environment using a 532 nm laser (laser power 100 mW) with 75/mm Echelle grating with ultrahigh dispersion. These measurements were performed at the Singh Center for Nanotechnology, University of Pennsylvania.

The laser was focused onto the sample via a 100× magnification objective, using an exposure time from 20–220 s, to ensure a high SNR. Detection was achieved with a thermoelectric-cooled CCD camera. This setup offers access to frequencies down to 10 cm^{-1} and spectral resolution of ~ 0.1 cm^{-1}. Spectra were recorded by spanning the regions of 10–220 cm^{-1} for graphite flakes and 20–400 cm^{-1} for SWCNT aerogel, respectively. The calibration of the spectrometer was checked by using the line at 521 cm^{-1} of the silicon sample. Fig. 4.19 shows the peaks features are more pronounced as the acquisition time increases. This means that these features are real properties of the sample and not instrumental noise, since the noise diminishes with longer acquisition times.

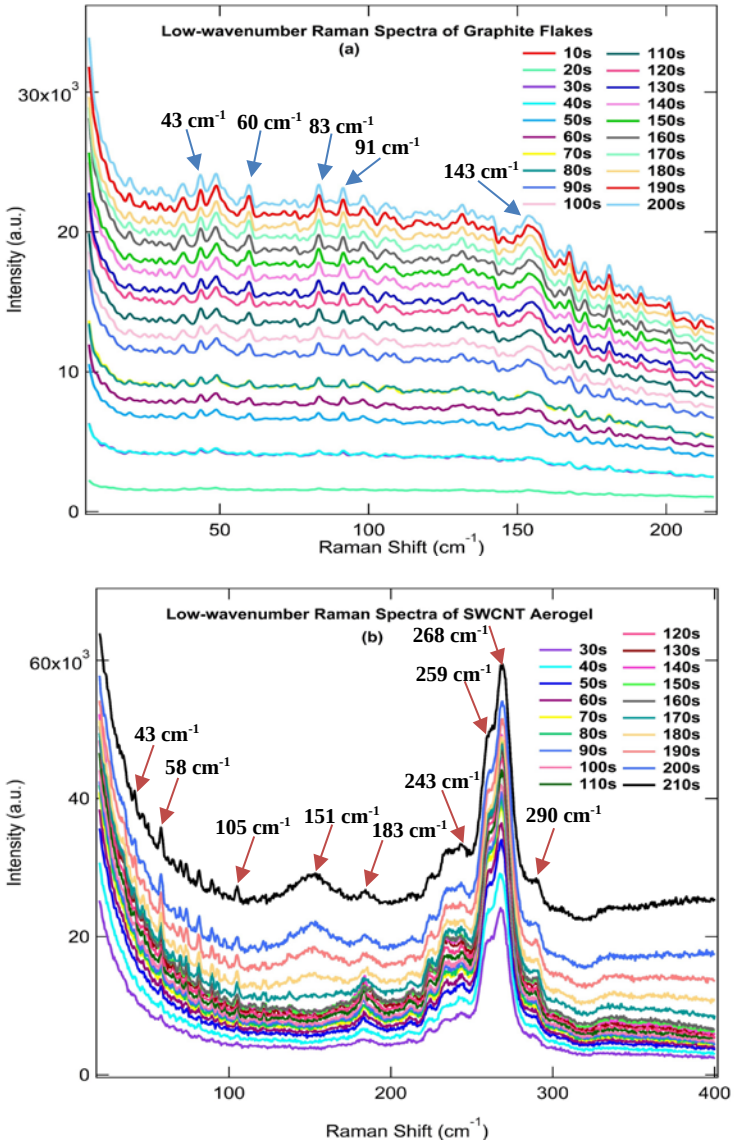

Figure 4.19: THz Raman spectra of graphite flakes and SWCNT aerogel. Each trace is for a different measurement time as indicated.

In Fig. 4.19 (a), the graphite flakes exhibit THz Raman peaks at 37 cm^{-1}, 43 cm^{-1}, 49 cm^{-1}, 60 cm^{-1},

83 cm^{-1}, 91 cm^{-1}, 98 cm^{-1}, 154 cm^{-1}, 167 cm^{-1}, 173 cm^{-1} and 181 cm^{-1}. The Raman peak at 37 cm^{-1} is assigned to the low-energy longitudinal optical mode E_g (E′) (LELOM), which is not detectable unless a broken symmetry is introduced [162-164].

The peaks at 43 cm^{-1} (and 49 cm^{-1}) correspond to a low frequency E_{2g} shear Raman mode (C peak) in graphite [158-160]. This is a doubly degenerate rigid layer shear mode, involving the relative displacement of atoms in adjacent planes [106]. It provides a direct measurement of the interlayer coupling [159,160]. Once the excitation energy is resonant with the transition gaps between the conduction and valence bands, the C mode intensity will be resonantly enhanced. The resonance condition of the C modes will be dependent on the excitation energy and measured positions [106].

The Raman peak at 60 cm^{-1} is assigned to torsion (X) mode, which is due to a torsional motion in the top and bottom graphite layers executing out-of-phase rotations [165,166]. It is mainly influenced by the electron-phonon coupling and might be linked to restoring force that tends to rotate the graphite layers relative to their stacking structures [166].

The peak at 83 cm^{-1} (low frequency) correlates with a peak around 91 cm^{-1} (high frequency) when using 514 nm laser excitation for graphite flakes. This is a Raman active mode as well. It is possible to assign these to the layer breathing mode (LBM) or to the ZO′ mode with perpendicular displacement of the graphite layers. This mode is sensitive to the external perturbations. The coexistence of two fundamental ZO′ Raman bands originates from phonons in different parts of the Brillouin zone (with different phonon wave vectors) [159]. Direct observation of the LBM is difficult because it is an optically silent mode for graphite [94,159,160,165]. It may be observed indirectly by means of the double resonant low frequency combination (E_g+ZO′) and overtone (2ZO′) Raman modes, respectively [167-169]. Laser heating is crucial to activate the LBM modes. This is reversible when the laser power decreases from high to low values [167]. However, as an equivalent mode is expected to appear at higher energy for graphite. Mode coupling may possibly explain the observations for Aerographite and SWCNT aerogel.

The Raman peak at ~154 cm^{-1} is the low frequency combination (E_g+ ZO′) mode in which two phonon modes (E_g and ZO′) couple with each other as a combination mode; in other words, one phonon mode excites another phonon mode. There are double peak features at ~167 and 173 cm^{-1} related to the 2ZO′ overtone mode in the range of 150-200 cm^{-1}. Although the intensity of this feature is less than that of the G mode response of the intraplane vibration, these low frequency peaks are clearly observable [168]. They arise from the emission of two LBM phonons with two opposite finite momenta through an intravalley double resonance Raman process [168,169].

For SWCNT aerogel, the THz Raman bands at 42 cm^{-1}, 58 cm^{-1}, 81 cm^{-1}, 105 cm^{-1}, 151 cm^{-1}, 183 cm^{-1}, 243 cm^{-1}, 259 cm^{-1}, 268 cm^{-1}, 290 cm^{-1}, 394 cm^{-1} and 607 cm^{-1} were shown to occur in SWCNT aerogel (Fig. 4.19 (b)). The assignments of the THz Raman bands of SWCNT aerogel are

listed in Table 4.2 together with the frequencies, symmetries, and physical processes.

TABLE 4.2 Assignments for the THz Raman modes of SWCNT aerogel.

Symmetry	Frequency (cm^{-1})	Note
E_{2g}	42	
	58	
	81	
E_{1g}	105	
	151	
	183	RBM
A_{1g}	243	first-order Raman allowed
	259	
	268	
E_{2g}	394	iTA mode, one-phonon DR
A_{1g}/E_{2g}	607	LA mode, one-phonon DR

[a] Mode frequencies for dispersive modes are given at E_L= 2.33 eV.
[b] The RBM is a totally symmetric A_{1g} mode, but it is not the only one [51].

The RBM Raman spectra for SWCNT aerogel contains the RBM contributions from different SWCNTs in resonance with the excitation laser energy [50]. The Raman intensity will be enhanced by the resonant effect, which occurs in the Raman scattering when the energy of the incident or scattered light matches an optical transition energy E_{ij} from the i^{th} valence band state to the j^{th} conduction band state [50,61]. The energy E_{ij} depends on (n, m), e.g. the second transition semiconducting SWCNT E_{22} (S) for (7, 5) is 1.915 eV, and for (7, 6) is 1.909 eV [75]. E_{ij} is sensitive to excitonic effects and electron-electron interactions [61].

From the low frequency Raman spectra of SWCNT aerogel, it appears that SWCNT will have low frequency RBM between 120 and 300 cm^{-1} for tube diameter in the range 0.65 nm < d_t < 1.1 nm. This is related to what is observed here for SWCNT aerogel (wide bands in this area). Aerographite may have similar modes. Lee *et al.* reported radial modes observed on multi-layered graphene between 150 and 300 cm^{-1} due to buckling of the graphene layers [145]. Such modes may also occur in Aerographite. In the present case, Aerographite was grown on a series of round, tubular shapes of ZnO tetrapods that acted as sacrificial template. It is structurally highly disordered (Chapter 3). Strain-induced deformation causes buckling of the carbon sheets. This buckling is similar to the buckling of graphene sheets reported [145]. Therefore, the observed peaks of Aerographite at 248 cm^{-1} are most likely due to the radial modes arising from strain-introduced buckling in Aerographite. A similar behavior is illustrated by the synchrotron THz/Far-IR results in Section 4.3.2.

4.6 Conclusion

In this chapter, a complementary synchrotron THz/Far-IR and Raman spectral investigation of

temperature dependent measurements of Aerographite and SWCNT aerogel is presented. New IR absorption bands of Aerographite and SWCNT aerogel were observed in the temperature range from 6–300 K. Some low frequency IR absorption bands show a “red-shift” effect. Variable temperature Raman results reveal frequency shifts of phonon modes with the change of temperature. Raman peak positions of Aerographite and SWCNT aerogel also show a behavior of “red-shift” with increasing temperature. This is attributed to C-C bond stretching, which in turn is due to the thermal expansion in the lattice and anharmonic coupling of phonon modes. The 2D peaks of Aerographite and SWCNT aerogel both show a “blue-shift” effect with temperature. The explanation of this is proposed to be either through the increase of the distance between covalently bonded C structures and a possible charge redistribution within the covalent bonds, or through the double resonant Raman scattering mechanism. Measurements of both “red-shift” and “blue-shift” serve as a tool to reveal the intricacies of inter- and intra-molecular bonds for a range of different molecular solids.

In addition, multiple low frequency Raman features are assigned in the THz region. There could be used to identify and discriminate subtly low frequency Raman modes in low-dimensional sp^2 carbon systems and specific chemical bonds and roles in the THz region in future.

Chapter 5

Temperature Dependent Electrical Transport Properties of Aerographite and Single-Walled Carbon Nanotube Aerogel

5.1 Introduction

Carbon aerogels are highly porous amorphous carbon materials consisting of interconnected clusters of carbon nanoparticles. They are specifically promising candidates for practical applications in that they possess a three-dimensional hierarchical morphology with ultrafine cell size and an electrically conductive framework [9,10]. They have customizable performance for specific applications based on their excellent electrical, thermal, and mechanical properties; for example, a thermal insulator or an electric double-layer supercapacitor. Both graphite [99] and carbon nanotubes (CNTs) [170] are important allotropes of sp^2 carbon-based materials having a low electronic density of states with desirable mechanical, thermal, and electrical properties.

The electrical conduction mechanism of carbon aerogel is found to be affected by several factors, including the type of associated CNTs, the network density, interactions between tubes or bundles, the bundle length, and doping [9]. The fluctuation-induced tunneling conduction (FITC) [171] and variable-range hopping (VRH) [172-176] approaches are widely used to model electrical transport properties of sp^2 carbon-based materials and composites [177-186], carbon aerogels [9,187-189] and other porous nanomaterials [190-195].

Marx *et al.* reported that the electrical conductivity of Aerographite is strongly dependent on its wall thickness, the degree of graphitization and the ambient temperature [196]. Decreasing the wall thickness leads to a reduced electrical conductivity [196]. The dependence of the electrical conductivity on the temperature shows that Aerographite generally exhibits a metallic conductive behavior, which can be changed to semiconducting behavior by high temperature treatment [196]. Zhang *et al.* studied the temperature dependent thermal, electrical, and thermoelectric properties of SWCNT aerogels with ultralow density over the temperature range 100–300 K [188]. Their results indicated that the thermal and electrical conductance of the constituent junctions were much higher than the values for isolated SWCNT junctions [188]. However, the electrical conduction mechanisms in the low temperature range responsible for electrons or charges transport through the Aerographite and SWCNT aerogel remain only partially understood, even though these mechanisms often determine the limits of device performance and application.

In this Chapter, I investigate the temperature dependent electrical transport properties of Aerographite and SWCNT aerogel. A Quantum Design Physical Property Measurement System (PPMS) was employed in the temperature range of 2 K to 300 K and a magnetic field range of zero to 9 T, in 2 T steps. The experimental results were fitted based on the FITC and VRH models, respectively. The statistical length and diameter distributions of the SWCNTs were quantitively

determined according to the Burr distribution and the logistic distribution using atomic force microscopy (AFM). The characteristic parameters (T_0, T_1 and R_0) in the FITC and VRH models have been estimated from the morphology and the uncertainty principle for Aerographite and from percolation theory for the SWCNT aerogel. A good agreement between the experimental data and theoretical models is observed. While the FITC mechanism accounts for a wide temperature range of data for Aerographite, the VRH model serves as an excellent explanation for the SWCNT aerogel data.

5.2 Physical Models

There are several different electrical transport models that might be used to explain electrical conduction in nanoscale clusters. The fluctuation-induced tunneling conduction (FITC) model and the variable range hopping (VRH) model are two ways of modelling parallel conduction mechanisms that are widely used to explain the electrical transport properties of disordered systems. The FITC model is based on the tunneling of electrons across a potential barrier affected by thermal fluctuations [171]. On the other hand, the VRH model (following Mott's and Efros-Shklovskii's laws) is based on the thermal phonons-assisted hopping of charge carrier between localized states near the Fermi level [197].

5.2.1 Fluctuation-induced Tunneling Conduction Model

The FITC model describes a quantum tunneling mechanism with potential-barrier modulation by thermal fluctuation. It has been applied to a variety of disordered systems with heterogeneous microstructures, such as carbon-polyvinylchloride composites [171], SWCNT bundles [181], K_xC_{70} [190], polymer composite [191], RuO_2 nanowires [192], polycrystalline CrO_2 [193], TiO_2 film [194] and iodine-doped bilayer-graphene [195]. The FITC model assumes that the sample is heterogeneous, consisting of large metallic regions separated by thin insulating layers forming mesoscopic junctions. The charge-carriers tunnel through such junctions. The tunneling conduction mechanism with potential-barrier modulation by thermal fluctuation (the local temperature fluctuations) thus describes the tunneling of electrons through a barrier of variable height resulting in voltage fluctuation at the junction [171]. A constraint is that the charging energy $E_c \sim \frac{e^2}{d}$ (where d is the dimension of metal grain) is smaller than the thermal energy k_BT (k_B is the Boltzmann constant and T is the temperature). The charge transport is limited by the tunneling across these barriers. The tunneling probability and the electrical conductivity mainly depend on the fluctuation of thermal voltage across the barriers [171]. The tunnel junction especially consists of a dielectric sandwiched between two conductors. This is equivalent to a parallel plate capacitor with a small effective capacitance associated with the small effective junction area [191].

The FITC model then gives an expression for the temperature dependent resistance as shown below:

$$R = R_0 \exp\left(\frac{T_1}{T_0 + T}\right) \tag{5.1}$$

where T_0 is the temperature above which the thermally activated conduction over the barrier begins to occur; T_1 represents the temperature at which the thermal voltage fluctuations across the tunneling junction become large enough to raise the energy of electronic states to the top of the barrier, or the energy required for an electron to overcome the energy barrier between conductive clusters [192]. The ratio T_1/T_0 determines the tunneling in the absence of fluctuation [197].

$$T_0 = \frac{16\varepsilon_0 \hbar}{\pi (2m_e)^{\frac{1}{2}} e^2 k_B} \left(\frac{AV_0^{\frac{3}{2}}}{w^2}\right) \tag{5.2}$$

$$T_1 = \frac{8\varepsilon_0}{e^2 k_B} \left(\frac{AV_0^2}{w}\right) \tag{5.3}$$

where ε_0 is the permittivity of vacuum, $\hbar$ is the reduced Planck constant, A is the junction area, w is the potential barrier width, V_0 is the potential height and m_e is the electron mass.

5.2.2 Variable Range Hopping Model

The VRH model describes electrical resistance in strongly disordered systems with local electron states [172-176]. It is based on the principle that at the low temperature an electron does not necessarily hop between neighboring sites, the hopping distance might be adjusted in order to minimize the energy difference between the two sites involved [174,175]. It is widely used to explain the temperature dependent resistance behaviors in amorphous materials, e.g. CNTs [183], SWCNT-polymer composite films [199], conducting polymers [200] and black phosphorus [201].

The model invokes a quantum tunneling process of electrons across an energetic barrier involving lattice phonons whose energy promote the process. Phonon-assisted hopping of electrons or holes results in a temperature dependence of the tunneling process. There is an optimum hopping distance, which maximizes the hopping probability. The possibility of hopping is proportional to phonon number and wave function overlap between two different energy states. The VRH model assumes a constant density of localized states around the Fermi level to give an equation for the temperature dependence resistance as shown below:

$$R = R_0 \exp\left[\left(\frac{T_c}{T}\right)\right]^p \tag{5.4}$$

where R_0 is a temperature independence pre-factor; and Tc is a characteristic temperature. The parameter p is a characteristic exponent, the value of which distinguishes different conduction mechanisms and varies with disorder, dimensionality, morphology, and the interactions between charge carriers.

$$p = \frac{1}{1+d} \tag{5.5}$$

where d is the system dimensionality with p=1/4 for a 3D system (d = 3), p = 1/3 for 2D system (d = 2) and p = 1/2 for 1D system (d = 1).

T_c is a characteristic temperature determining thermally activated hopping among localized states at different energies.

$$T_c = \frac{\beta}{k_B N(E_F) L_c^3} \tag{5.6}$$

where $N(E_F)$ is the density of states at the Fermi level, L_c is the localization length of states near the Fermi level, and β is a numerical coefficient.

Mott's theory of VRH between localized carrier states near the Fermi level is described by

$$R = R_0 \exp\left[\left(\frac{T_c}{T}\right)\right]^{1/4} \tag{5.7}$$

$$T_c = T_{Mott} = \frac{18.1}{k_B N(E_F) L_c^3} \tag{5.8}$$

where T_{Mott} is a characteristic temperature referred as the Mott temperature [178,202].

The Efros-Shklovskii (E-S) version of VRH takes into account the effects of long-range Coulomb (electron-electron) interactions between localized states. There is a Coulomb gap in the density of states near the Fermi level [176]:

$$R = R_0 \exp\left[\left(\frac{T_c}{T}\right)\right]^{1/2} \tag{5.9}$$

$$T_c = T_{ES} = \frac{\beta e^2}{k_B L_c \kappa} \tag{5.10}$$

where T_{ES} is the characteristic temperature known as the ES temperature, β is numerical coefficient equal to 2.8 to 3D system and 6.2 to 2D system, e is the electron charge and κ is the dielectric constant [178,202].

5.2.3 Percolation Theory

Fischer *et al*. reported that the electrical resistivity of SWCNT bundles decreased with decreasing temperature from 350 K to 35 K, and then reversed to increase as the temperature decreased down to 10 K [197]. There is similar turning point at 200 K for bulk samples [184,197]. Kane *et al.* investigated the coupling of the conduction electrons to thermally excited long-wavelength torsional shape fluctuations [203]. When CNTs are dispersed in an insulating matrix, the CNTs form an electrical percolating network (provided that their content in the matrix exceeds the electrical percolation threshold) [204]. There will be an insulting layer formed between contact points of the CNTs junction, which increases the contact resistance [204-207]. Electrical conduction is then determined by two interacting physical mechanisms: percolation in a continuum conducting network [207,208] and tunneling between isolated conducting particles [207,209,210].

In the percolation theory, the hopping process is mapped onto a random-resistor network [211-214]. The resistors are moved randomly in a percolation network. The connections consist of electrical resistors that are present with probability q and absent with probability $1-q$ [215-219]. The diverse effects of CNT agglomeration (mainly due to the van der Wales force and Coulomb interactions), CNT dispersion rate, CNT aspect ratios (length to diameter ratio), the tunneling effect, loading and morphology are then related to the electrical percolation thresholds in the crossed CNT junction [220,221] and of the percolation network [222-228].

To determine the electrical conductivity percolation, the scaling law is used

$$\sigma = \sigma_0 (q - q_c)^{\gamma} \tag{5.11}$$

where σ_0 the fitting constant, q is the CNT content, q_c is the percolation threshold, and γ is the critical exponent.

In a CNT percolation resistor network, there are two types of resistances: the intrinsic resistance R_{ij} along one undeformed CNT between two nearest contacts *i* and *j* with the neighboring CNTs and the CNT contact resistance $R_{contact}$ [206,222,223]:

$$R_{CNT} = R_{ij} + R_{contact} \tag{5.12}$$

The intrinsic resistance R_{ij} is given by

$$R_{ij} = \frac{4 l_{ij}}{\sigma_{CNT} \pi D^2} \tag{5.13}$$

where l_{ij} is the length of the CNT segment between the points *i* and *j*, *D* is the CNT diameter, σ_{CNT} is the CNT intrinsic electrical conductivity, which depends on the CNT diameter and chirality [206,222,223].

The contact or tunneling resistance $R_{contact}$ depends on the distance between adjacent CNTs, geometry and chirality, and the contact area. It results in electron ballistic tunneling through the contact junction. This can be approximately calculated by the tunneling current-voltage (*I-V*) relationship [203-205] and the Landauer–Büttiker formula [75,228-231]:

$$I = \frac{2e}{h} \int_0^{+\infty} \eta(E) M(E) \left[\frac{1}{e^{\frac{E-\mu-eV}{k_B T}} + 1} - \frac{1}{e^{\frac{E-\mu}{k_B T}} + 1} \right] dE \tag{5.14}$$

$$R_{contact} = \frac{V}{I} = \frac{h}{2e^2} \frac{1}{M\left[\eta(E) + \frac{\pi^2}{6} (k_B T)^2 \frac{d^2 \eta(E)}{dE^2}\right]} \approx \frac{h}{2e^2} \frac{1}{M \eta(E)} \tag{5.15}$$

where *M(E)* is the total number of conduction channels and $\frac{h}{2e^2} \approx 12.91\ \text{k}\Omega$ is the quantized resistance. *T* and μ represent respectively the temperature and the chemical potential of the CNT.

The transmission probability *Ƞ(E)* is the probability of an electron tunneling through the potential barrier between CNTs. This probability may be estimated by solving the Schrödinger equation with a rectangular potential barrier or from the Wentzel–Kramers–Brillouin (WKB) approximation [206]:

$$\eta(E) = \begin{cases} exp\left(-\frac{d_{VdW}}{d_{tunnel}}\right), 0 \le d \le D + d_{VdW} \\ exp\left(-\frac{d-D}{d_{tunnel}}\right), D + d_{VdW} < d \le D + d_{cutoff} \end{cases} \quad (5.16)$$

$$d_{tunnel} = \frac{\hbar}{\sqrt{8m_e\Delta E}} \quad (5.17)$$

where d is the minimum distance between the axes of two neighboring CNTs, through which electron tunneling is most likely to occur. According to the Pauli Exclusion Principle [206], the separation distance between two CNT surfaces should be no less than van der Waals separation distance d_{VdW}. Now d_{cutoff} is the maximum effective distance of tunneling effects, d_{tunnel} is the tunneling characteristic length, m_e is the electron mass and ΔE is the height of potential barrier.

5.3 Experimental Details

5.3.1 Sample Preparation

Aerographite was synthesized by a single-step chemical vapour deposition (CVD) method by collaborators [12,13]. Its preparation details were given in Chapter 3. SWCNT aerogel was produced at University of Pennsylvania, under the supervision of Professor Arjun G. Yodh and Professor Mohammad F. Islam (Carnegie Mellon University). The details were given in Chapter 4 [17,134].

5.3.2 Structural and Morphological Characterization

In order to understand the relationship between morphological structures and electrical conduction mechanisms in Aerographite and SWCNT aerogel, it is essential to know how graphite surface wrinkled into shell micro-tubes and SWCNT organized into interconnected networks, respectively. Fig. 5.1 shows analytical field emission scanning electron microscope (FE-SEM; JEOL JSM-7500FA, Tokyo, Japan) images of a porous interconnected network structure of Aerographite. It comprises a seamless interconnected network of CNTs that have micron-scale tube diameters and a wall thickness of about 15 nm [12]. The ultralow density of Aerographite is 0.18 mg/cm^3, which is around six times lighter than air (1.125 mg/cm^3).

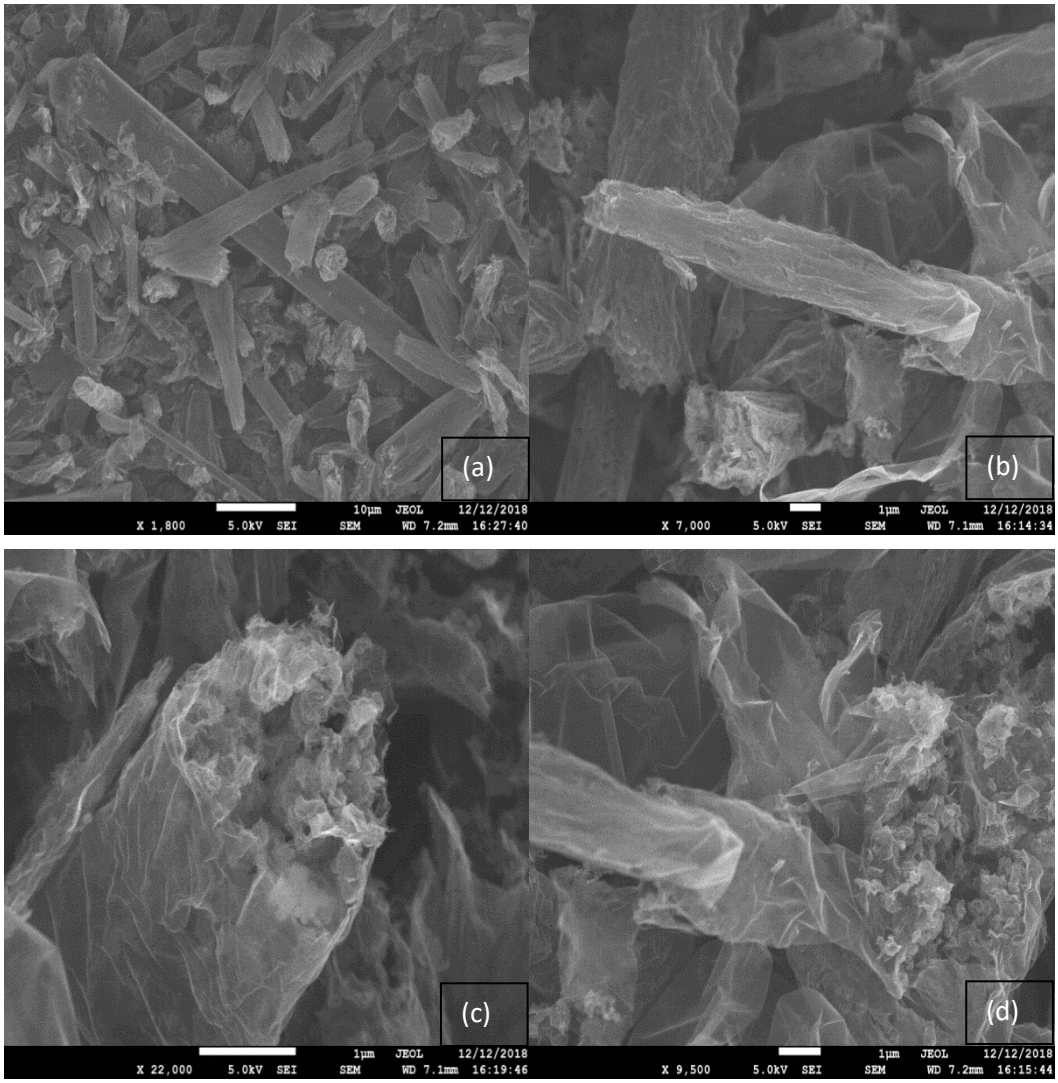

Figure 5.1: FE-SEM images of Aerographite.
(a-b) 3D interconnected structures of shell-graphitic Aerographite.
(c-d) Aerographite with porous graphite fillings.

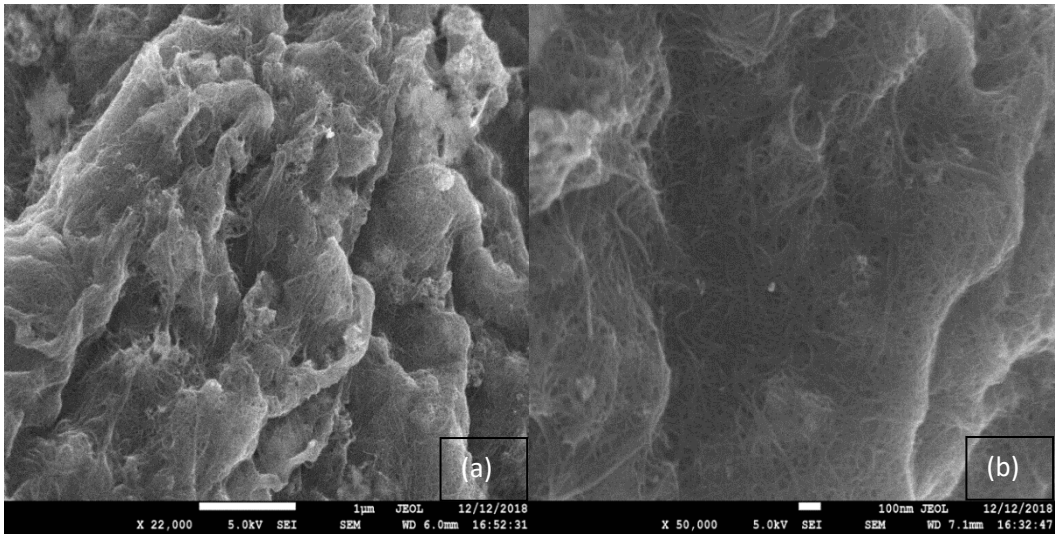

Figure 5.2: FE-SEM images of SWCNT aerogel.
(a) An open-cell, porous structure of SWCNT aerogel.
(b) SWCNTs in the aerogel form an aligned and random porous network with little binding.

The high-resolution FE-SEM images of SWCNT aerogel (Fig. 5.2) show that individual SWCNTs in the SWCNT aerogel are entangled in a random porous network with an open-cell structure and having van deer Waals interactions between the SWCNT at discrete CNTs cross-link points [17,132,189]. The low density of the SWCNT aerogel is 2.3 mg/cm^3, which was calculated from the measured final mass and dimensions of the SWCNT aerogel.

5.3.3 Temperature Dependent Resistance Measurements

To measure the temperature dependent resistances and electrical transport properties, each sample was mounted on a sample puck using the standard four-probe resistivity measurement arrangement. The arrangement of the contacts was one positive and one negative for current and one positive and one negative voltage. The sample was wired to the bridge with gold wires (0.5 mm diameter). Contacts were made to the electrodes using conductive silver paint. The contact resistance between the electrodes and samples was checked to be very small. The temperature dependence resistances of the Aerographite (Fig. 5.3) and the SWCNT aerogel (Fig. 5.4) with different magnetic field strengths (0 T, 3T, 5 T, 7 T and 9 T) applied to the samples were measured from 2 K to 300 K using the resistivity option integrated with the PPMS DynaCool (Quantum Design, Inc., San Diego, CA, USA) in the "No Overshoot" temperature approach. These measurements were carried out using the standard procedures with the different temperature ramp rates of 1 K/min (from 2 K to 5 K), 2 K/min (from 15 K to 50 K) and 5 K/min (from 50 K to 300 K), respectively. The set temperature was stabilized for 10 seconds before the measurements were taken.

Subsequent to data collection, the FITC and the VRH models were used to fit to Aerographite and SWCNT aerogel according to the least square method using the MATLAB code (Appendix 2: MATLAB Code for FTIC and VRH fittings).

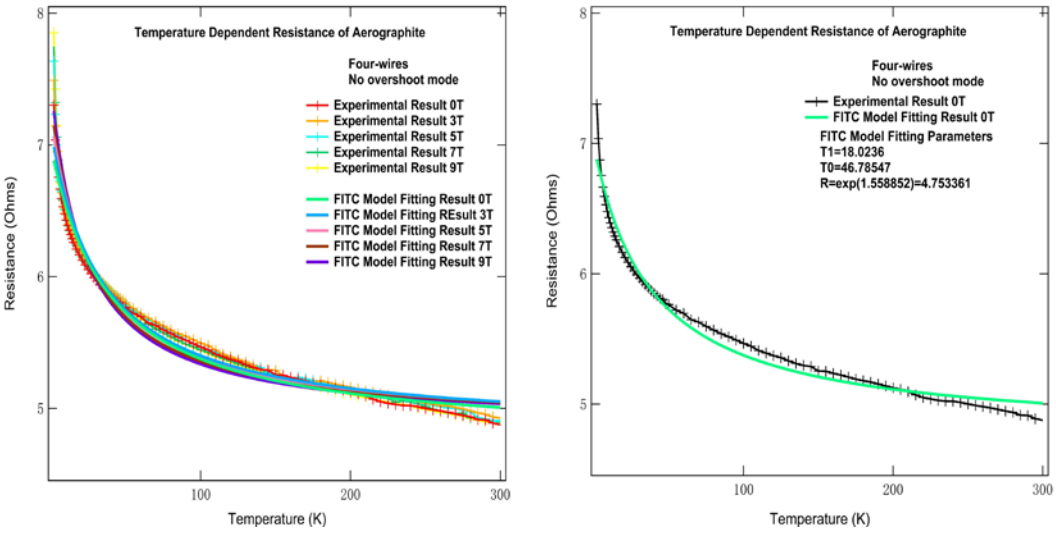

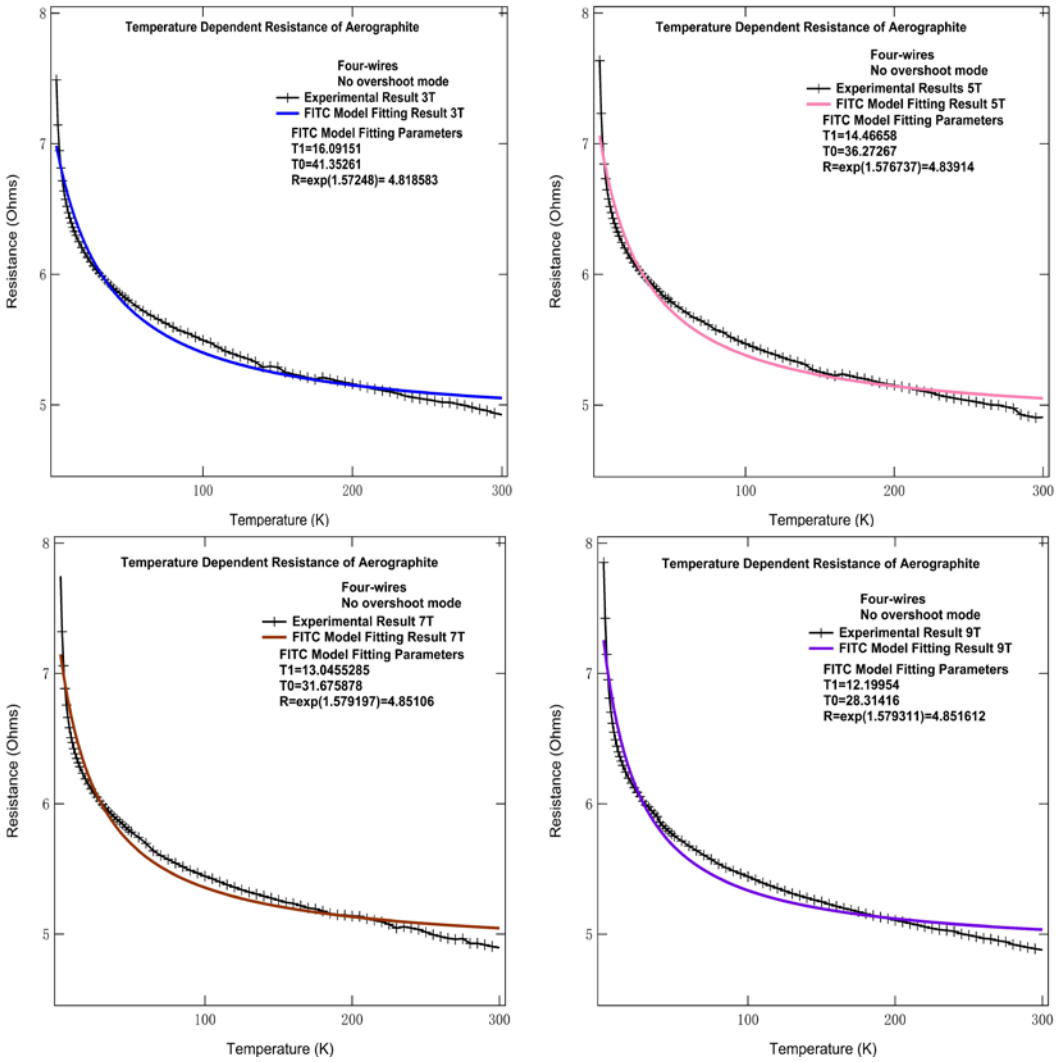

Figure 5.3: Temperature dependent resistance of Aerographite with different magnetic field strengths from 2–300 K in the "No Overshoot" temperature approach mode.
The lines and markers are experimental results.
The solid lines are obtained using the FIT model.

TABLE 5.1. Values of fitting parameters obtained from applying the FITC model to Aerographite.

Magnetic Field Strength (T)	**0**	**3**	**5**	**7**	**9**
T_1 **(K)**	18.02	16.09	14.47	13.05	12.20
T_0 **(K)**	46.79	41.35	36.27	31.68	28.31
R_0 **(Ω)**	4.75	4.82	4.84	4.85	4.85
T_1/T_0	0.39	0.39	0.40	0.41	0.43

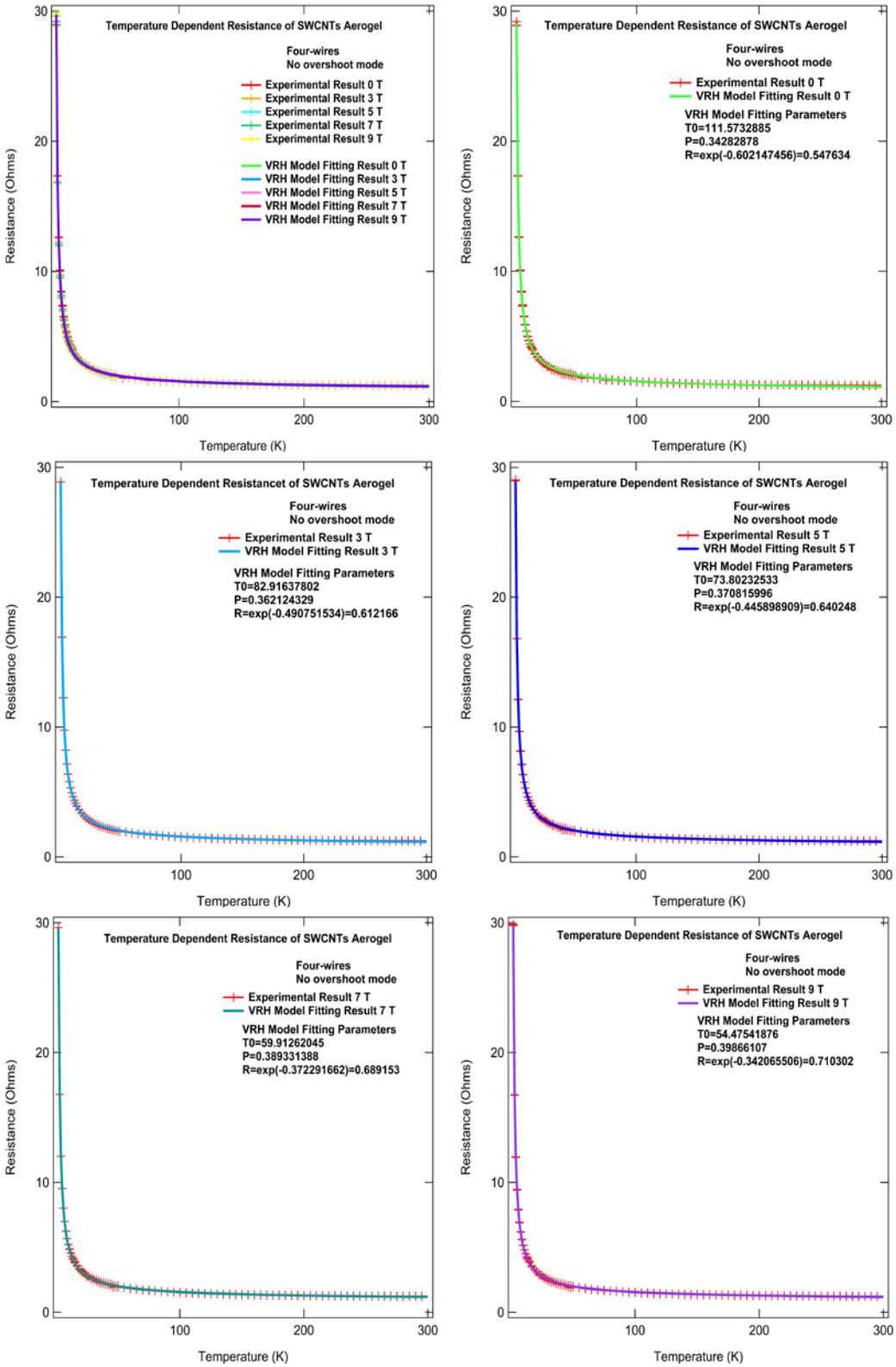

Figure 5.4: Temperature dependent resistance of the SWCNT aerogel with different magnetic field strengths from 2–300 K in the "No Overshoot" temperature approach mode. The lines and markers are experimental results. The solid lines are obtained using the VRH model.

TABLE 5.2. Values of fitting parameters obtained from applying the VRH model to SWCNT Aerogel.

Magnetic Field Strength (T)	**0**	**3**	**5**	**7**	**9**
T_1 **(K)**	111.57	82.92	73.80	59.91	54.48
p	0.34	0.36	0.37	0.39	0.40
R_0 **(Ω)**	0.55	0.61	0.64	0.69	0.71

Figs. 5.3 and 5.4 show the temperature dependent experimental data (lines and markers) and the fit (solid line) to the experimental curves using the FITC model (Eq. 5.1) and the VRH model (Eq. 5.4) for Aerographite and SWCNT aerogel, respectively. The corresponding fitting parameters obtained from the FITC model of Aerographite and the VRH model of SWCNT aerogel are listed in Tables 5.1 and 5.2. In Fig. 5.3, the electrical resistance of Aerographite decreases from 7.6 Ω at 2 K to 4.9 Ω at 300 K. The FITC characteristic parameters (T_1, T_0 and R_0) show different variable trends with magnetic field strength increases in this temperature range. Characteristic temperatures T_1 and T_0 decrease with increasing magnetic field strength, while R_0 increases with increasing magnetic field strength. According to Table 5.1, the ratio of T_1/T_0 were 0.39, 0.39, 0.40, 0.41, 0.43 at the magnetic field strengths of 0, 3, 5, 7 and 9 T, respectively. Thus, this ratio steadily increases with magnetic field strength. The ratio T_1/T_0 is proportional to the potential barrier width w [229]. A larger ratio T_1/T_0 means that there is a lower electron tunneling probability, corresponding to a stronger temperature dependent behavior [189]. The electrical resistance of SWCNT aerogel also decreases from 29.6 Ω at 2 K to 1.2 Ω at 300 K (Fig. 5.4). The VRH characteristic parameters (T_0, R_0 and p) also show different trends with magnetic field strength increase in the temperature range 2–300 K. More specifically, T_0 decreases with increasing magnetic field strength, while R_0 and p increase with increasing magnetic field strength. The dimensional characteristic parameter p is around 0.4 for SWCNT aerogel, locating it between a 1D system (p = 0.5) and a 2D system (p = 0.3).

The current-voltage (I–V) characteristics of the samples were measured under conditions of 100 mA current amplitude and 1 Hz current frequency at the different magnetic field strengths (0 T, 3 T, 5 T, 7 T and 9 T) at different temperatures (5 K, 50 K, 100K, 150 K, 200K, 250 K and 300 K), using the electrical transport option (ETO) integrated with the PPMS DynaCool instrument. The I−V curves of Aerographite and the SWCNT aerogel shown in Fig. 5.5 are linear and symmetric about zero bias voltage, indicating ohmic behavior down to a very low temperature (5 K). The reciprocal of the slope of the I-V curves around zero bias voltage, that is, the resistance R, changes continuously with temperature. In particular, the I-V curves of the SWCNT aerogel exhibit slightly nonlinear behavior at 5 K with different magnetic field strengths. This behavior can be attributed to the formation of non-ohmic contacts in the SWCNT aerogel and a Luttinger-liquid behavior in the SWCNT networks that depends on both temperature and bias voltage [198].

(a) (b)

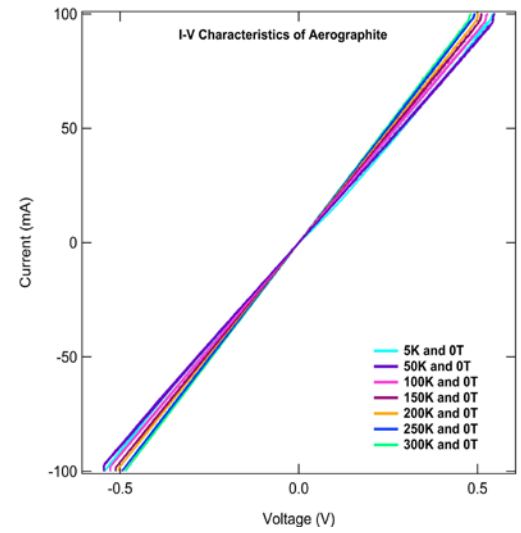
I-V Characteristics of Aerographite
Current (mA)
Voltage (V)
5K and 0T
50K and 0T
100K and 0T
150K and 0T
200K and 0T
250K and 0T
300K and 0T

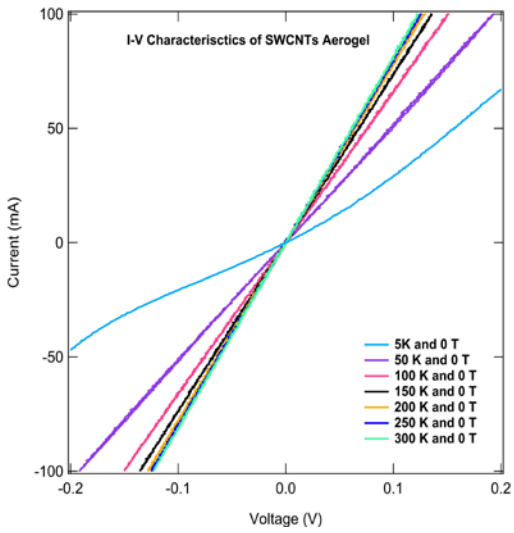
I-V Characterisctics of SWCNTs Aerogel
Current (mA)
Voltage (V)
5K and 0 T
50 K and 0 T
100 K and 0 T
150 K and 0 T
200 K and 0 T
250 K and 0 T
300 K and 0 T

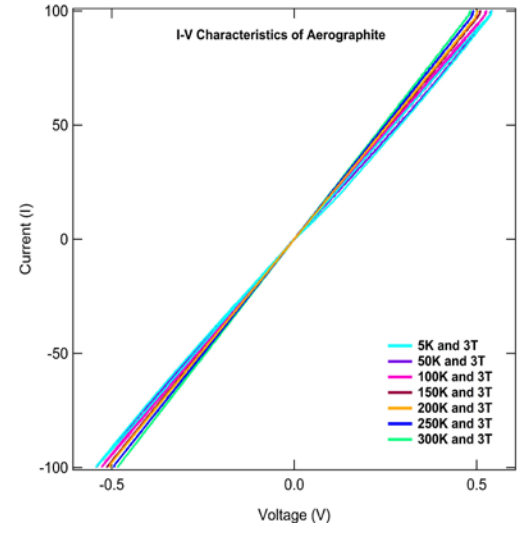
I-V Characteristics of Aerographite
Current (I)
Voltage (V)
5K and 3T
50K and 3T
100K and 3T
150K and 3T
200K and 3T
250K and 3T
300K and 3T

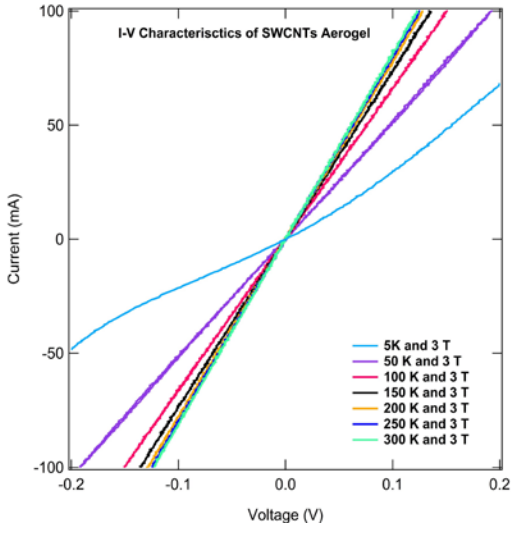
I-V Characterisctics of SWCNTs Aerogel
Current (mA)
Voltage (V)
5K and 3 T
50 K and 3 T
100 K and 3 T
150 K and 3 T
200 K and 3 T
250 K and 3 T
300 K and 3 T

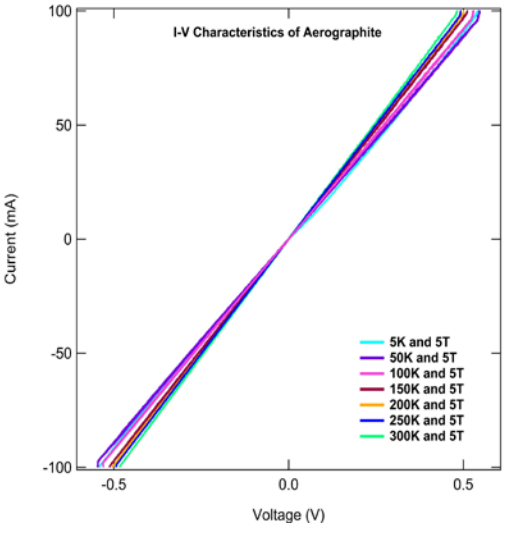
I-V Characteristics of Aerographite
Current (mA)
Voltage (V)
5K and 5T
50K and 5T
100K and 5T
150K and 5T
200K and 5T
250K and 5T
300K and 5T

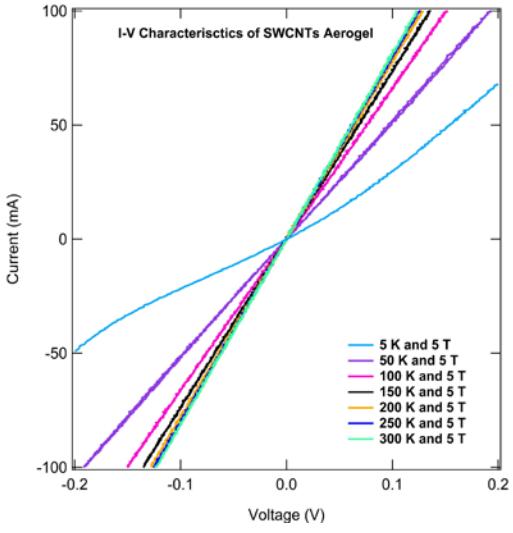
I-V Characterisctics of SWCNTs Aerogel
Current (mA)
Voltage (V)
5 K and 5 T
50 K and 5 T
100 K and 5 T
150 K and 5 T
200 K and 5 T
250 K and 5 T
300 K and 5 T

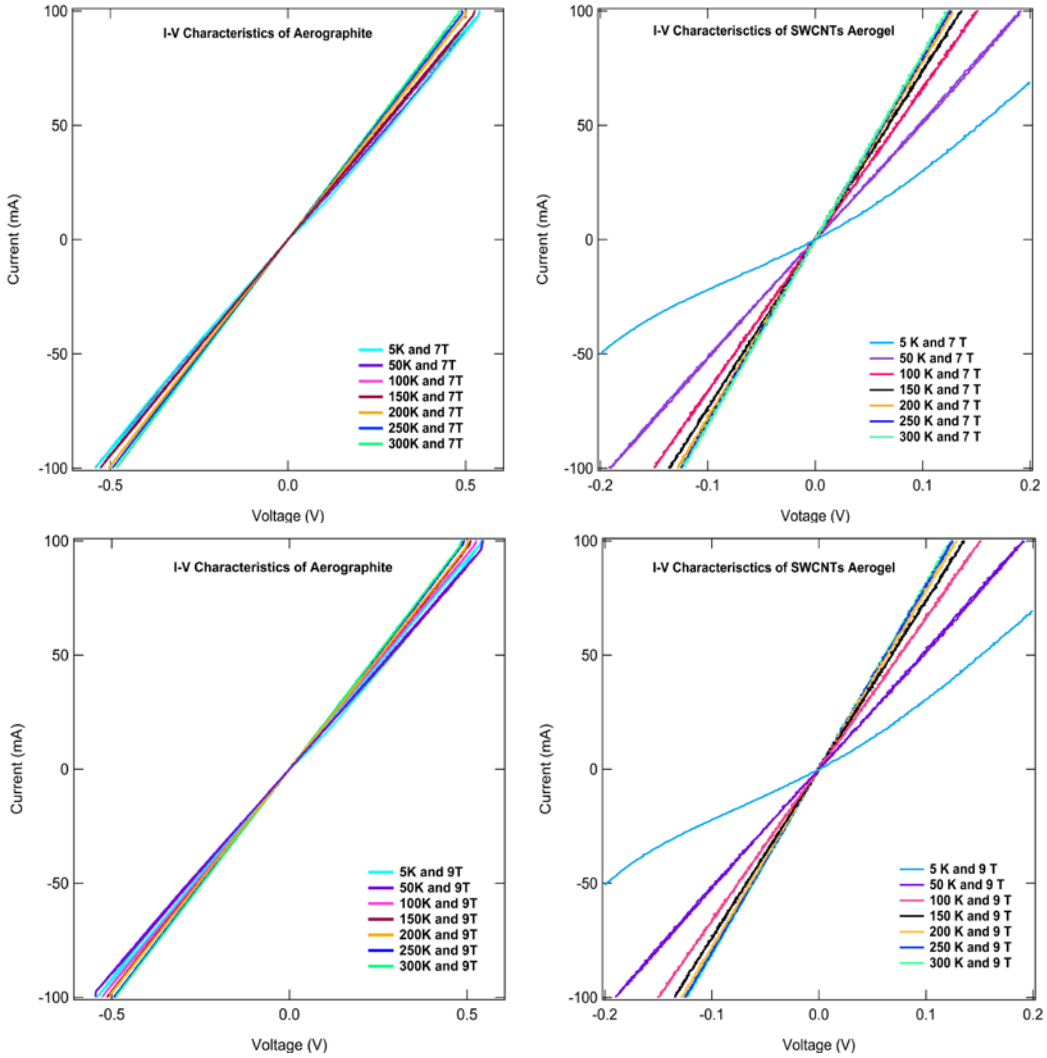

Figure 5.5: (a) The *I-V* characteristics curve of Aerographite with different magnetic field strengths at different temperatures. (b) The *I-V* characteristics of SWCNT aerogel with different magnetic field strengths at different temperatures.

5.4 Discussion of Results

The electrical transport measurements presented indicate that the temperature dependence of electrical resistance is a sensitive probe when applied to carbon aerogels. The data suggests a close relationship between structural defects and disorder in amorphous carbons and electrical conduction mechanisms. The temperature dependent electrical transport properties of Aerographite can be explained well in terms of the FITC model. On the other hand, the electrical transport mechanism inherent in the SWCNT aerogel at low temperature is found to exhibit to a $(1/T)^{1/2}$ dependence, indicative of a variable hopping around a Coulomb gap in the density of states due to carrier-carrier interactions [230]. It further indicates that structural perfection plays an important role in determining the electrical transport mechanism of carbon aerogels [230] and thus leads to a better understanding of which electrical transport mechanism is effective in the investigated structures. In general, the resistance of Aerographite and SWCNT aerogel should depend on two physical factors: the structure (defects, disorder, vacancies, dopant, and functional

groups) and the morphology (porosity and average bundle diameter) [231-236]. A sparser (more porous) network will have lower conductivity, and the conductivity decreases as the bundle diameter increases.

5.4.1 Fluctuation-induced Tunneling Conduction Model for Aerographite

For Aerographite, the cross-sectional shape of the underlying ZnO is transferred onto the final structure. Aerographite is a nanoscale porous graphite, with metallic-type conductivity [12,13,196]. Since the XRD pattern of Aerographite shows the presence of some residual ZnO that did not get removed completely during the growth (Fig. 3.1), it is reasonable to deduce that ZnO layers will form insulating barriers between graphite grains in this Aerographite sample. Metallic-type Aerographite grains are then separated by insulating Schottky barriers and the contact gap potential between two grains can form a tunneling potential barrier with an effective capacitance as shown in Fig. 5.6.

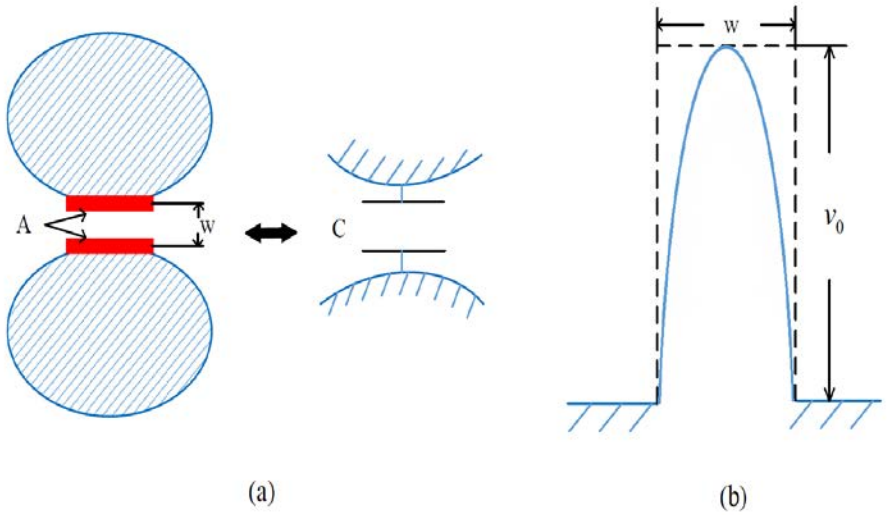

Figure 5.6: (a) Schematic illustration for the insulating junction between two conducting segments (shaded areas) with the effective area *A* for the tunnel process and separation *w*, which may be regarded as a parallel-plate capacitor. (b) Schematic representation of the parabolic potential barrier of height V_0 and width *w* between two conducting segments. The dashed lines denote the corresponding rectangular barrier.

The contact position at interface between two different materials can be described by an effective capacitance,

$$E = \frac{1}{2} C V_T^2 \tag{5.18}$$

According to the uncertainty principle, it is required that the transport electrons between two different materials pass through two different surfaces. It is possible then to obtain that their work function is equivalent to the charging energy of an effective capacitance:

$$\frac{1}{2}\varepsilon_r C V^2 = 2\frac{(\hbar/2\Delta x)^2}{2m} = \frac{\hbar^2}{4m\Delta x^2} \tag{5.19}$$

Here we assume the microscopic tunneling energy is equal to the energy estimated by the uncertainty principle:

$$E = \frac{1}{2} C V_T^2 = \frac{\hbar^2}{4m\varepsilon_r \Delta x^2} \tag{5.20}$$

where C is the micro-capacitance, V_T is the fluctuation voltage, ε_r is the relative dielectric constant of ZnO, and Δx is the surface barrier width of ZnO. Here, it is replaced by the ZnO depletion layer [237,238]:

$$\Delta x^2 = \frac{2\emptyset\varepsilon_r\varepsilon_0}{e^2 N_d} \tag{5.21}$$

where φ is the barrier height. In this sample, this is given by the differences of work function between reduced graphite oxide and ZnO. N_d is the donor concentration [239-241]. We get

$$\Delta x \approx 1.65 \times 10^{-9}\, m,$$

$$E \approx 0.827 \times 10^{-3} eV = 0.83\, meV.$$

As the surface of the ZnO crystal is in contact with the nanoscale porous graphite, it is possible to replace the barrier area by the ZnO crystal surface. The surface diameter of ZnO crystal, which is prepared by the vacuum thermal reduction method [240,241], is about 130 nm. So, the barrier effective area A is then:

$$A = \frac{\pi r^2}{4} = 1.33 \times 10^{-14}\, m^2.$$

Using the above parameters with the FITC model, we may calculate the characteristic temperatures T_0 and T_1 [192,195]. The calculation results show that:

$$T_1 = 18.36 \text{ K}, T_0 = 46.91 \text{ K}.$$

For the experimental fitting results without magnetic field (Fig. 5.3 and Tab. 5.1), we get:

$$T_1 = 18.02 \text{ K}, T_0 = 46.79 \text{ K}.$$

Temperature dependent electrical transport behavior of Aerographite is closely related with its preparation methods (e.g. thermal treated or not), and its structural factors (e.g. defects and wall thickness) [196]. Different treatments and different wall thickness will lead the different electrical transport behavior. The highly disordered structure of Aerographite, including surface defects and charge carrier, will assist the thermally induced fluctuation voltages across the insulating gap. It will result in the tunneling takes place in and thereby impart a characteristic temperature dependence on the electrical resistance. It may be the main reason that the FITC model is well used to this temperature-dependent electrical transport behavior in Aerographite.

5.4.2 Variable Range Hopping Model for SWCNT Aerogel

The Landauer-Büttiker formula is employed to study the tunneling effect on the temperature dependent resistance of the semiconducting SWCNT aerogel. Two main aspects of resistance have been considered in this percolation network: (a) the intrinsic resistance between two adjacent points in the SWCNT ($R_{intrinsic}$), that is, the one-dimensional resistance of the SWCNT; and (b) the contact resistances at SWCNT junctions ($R_{contact}$) resulting from the electron tunneling effect at the crossed SWCNT-SWCNT junctions [223].

A uniform random distribution of SWCNTs is considered in a representative rectangle of dimensions L_x (25 mm, length) × L_y (10 mm, width) × L_z (10 mm, thickness). The boundary condition is

$$U = \begin{cases} 0.095\ mV, & x = 0 \\ 0, & x = 25\ mm \end{cases} \tag{5.22}$$

In order to obtain the distribution in SWCNT lengths, I prepared a surfactant stabilized SWCNT suspension, which was measured by the MFP-3D AFM (Asylum Research, Santa Barbara, CA, USA). The CNTs were dispersed with SDBS surfactant and then the SDBS was removed using gentle acetic acid washing for around 8 min after SWCNTs deposition on a silicon chip for AFM images [242]. The AFM has the capability of analyzing multiple AFM images to achieve precise length and diameter measurements of SWNT dispersed in samples [243].

Fig. 5.7 shows the AFM images of SWCNT on a silicon surface. Each SWCNT is assumed to consist of a set of straight-line segments, and the head point (x_i, y_i, z_i) of a line segment of the i^{th} SWCNT is generated by

$$\xi_i = L_h \times random,\ \ h = (x, y, z) \tag{5.23}$$

where i is the index of the i^{th} SWCNT, and the "random" denotes uniformly distributed random numbers in the interval (0,1).

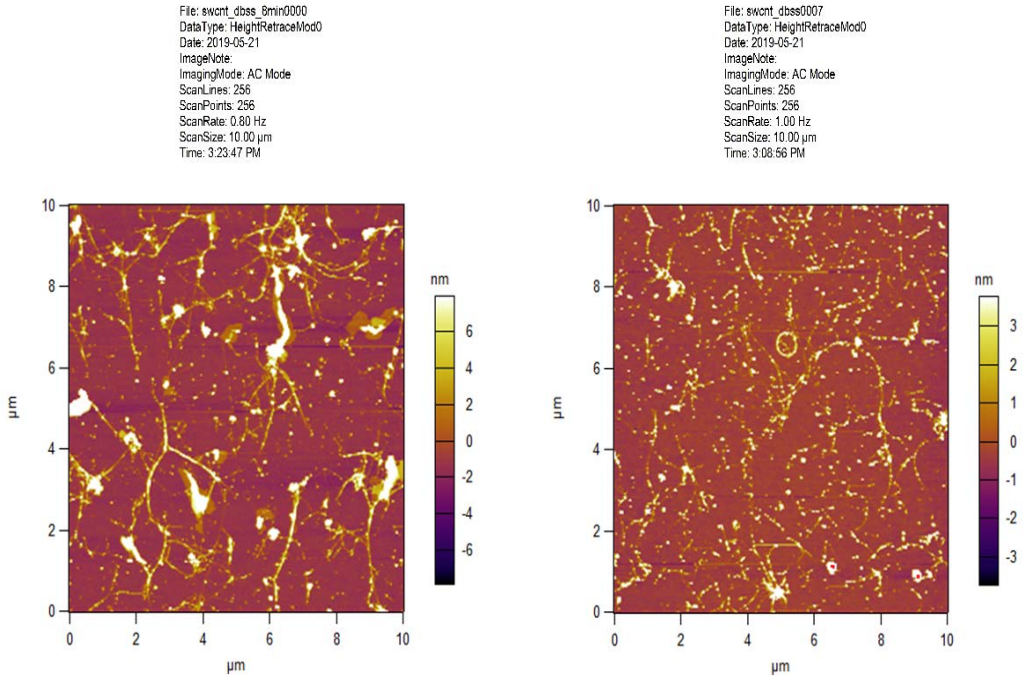

Figure 5.7: Tapping mode AFM image of SWCNT on a silicon surface.
The SWCNTs suspension was prepared at 0.1 mg/mL by the tip sonicator.

It is assumed that the length of each SWCNT varies and obeys the Burr distribution, such that its cumulative distribution function (CDF) $F(x)$ is given according to:

$$l_i = F^{-1}(random) \tag{5.24}$$

$$F(x) = \{x \geq l_i\} = 1 - \left[1 + \left(\frac{x}{\lambda}\right)^c\right]^{-K}, x > 0 \quad (5.25)$$

where λ, K and c are the parameters of the Burr distribution. According to the fitting data of the lengths of the SWCNT, the values of the Burr distribution parameters are λ = 3.48965, K = 5.02701, c = 3.5835, respectively. The length CDF $F(x)$ for the SWCNTs are used to prepare SWCNT aerogel is:

$$F(x) = 1 - \left[1 + \left(\frac{x}{3.48965}\right)^{3.5835}\right]^{-5.02701}, x > 0$$

Similarly, the diameter of each SWCNT varies and obeys the logistic distribution, such that its CDF $F(x)$ is given by:

$$F(x) = \frac{1}{1+exp\,(\frac{x-\mu}{s})} \quad (5.26)$$

where μ and s are the parameters of the logistic distribution. According to the diameter fitting data of the SWCNTs, the values of the logistic distribution parameters are μ = 0.835042, s = 0.0504149. The diameter CDF $F(x)$ for the SWCNTs are used to prepare SWCNT aerogel is given by:

$$F(x) = \frac{1}{1+exp\,(\frac{x-0.835042}{0.0504149})}$$

The azimuthal and the polar angles are generated randomly by

$$\varphi_i = 2\pi \times random \quad (5.27)$$

$$\theta_i = cos^{-1}\,(2\pi \times random - 1) \quad (5.28)$$

where $\varphi_i \in [0,2\pi]$ and $\theta_i \in [-\frac{\pi}{2}, \frac{\pi}{2}]$.

The coordinate (x_i', y_i', z_i') of the end point of the CNT is then:

$$(x_i', y_i', z_i') = (x_i + l_i sin\theta_i cos\varphi_i, y_i + l_i sin\theta_i sin\varphi_i, z_i + l_i cos\theta_i) \quad (5.29)$$

According to reports on the temperature dependent electrical resistance of SWCNT [203,244], the relationship of the intrinsic resistance between two adjacent points in the SWCNT ($R_{intrinsic}$) with temperature and SWCNT diameter based on the experimental data is [245]:

$$R_{intrinsic} = R_0 \exp\,[aD^b(\frac{1}{T} - \frac{1}{300})] \quad (5.30)$$

$$R_0 = \frac{4l_{ij}}{\sigma_{300}\pi D^2} \quad (5.31)$$

where a = 0.003708763 and b = -1.963154565 are the fitting parameters; D is the diameter, l is the length, and σ_{300} is the electrical conductivity at 300 K.

The electrical resistance behavior of an individual SWCNT is inversely proportional to the cross-section and is proportional to the length [245,246]. The contact resistances at SWCNT junctions ($R_{contact}$) is proportional to the SWCNT length or the length of the contact between SWCNTs [234]. The contact region between two SWCNTs is on the nano scale, the dimension of which can be less than the momentum relaxation length and the Fermi wavelength λ_F [206]. Electron tunneling through the contact junction in the ballistic transport range, and the contact resistance $R_{contact}$ is caused by the electron ballistic tunneling [206,223]. The Landauer-Büttiker formula (5.14) may be also expressed as the following form [76,206,222,234-236]:

$$I = \frac{2e}{h}\int_0^{+\infty} T_{ij}[f_i(E-\mu_1) - f_j(E-\mu_2)]dE \tag{5.32}$$

where E and μ represent the electron energy and the chemical potential of the SWCNT. T_{ij} denotes a transmission probability of the electron to tunnel through the potential barrier between SWCNTs.

If the chemical potential difference between two contacting semiconducting SWCNTs is

$$\mu_1 - \mu_2 = eV \tag{5.33}$$

then net current flowing between the two SWCNTs is given by

$$I = \frac{2e}{h}\int_0^{+\infty} T_{ij}\frac{f(E-\mu_1)-f(E-\mu_2)}{\mu_1-\mu_2}(\mu_1-\mu_2)dE \tag{5.34}$$

The derivative of the equilibrium Fermi distribution $f(E-E_F)$ is [76]

$$-\frac{df}{dE} \approx \frac{f(E-\mu_1)-f(E-\mu_2)}{\mu_1-\mu_2} = \frac{f(E-\mu_1)-f(E-\mu_2)}{eV} \tag{5.35}$$

Now, according to the two-points central difference formula,

$$-\frac{df}{dE} = \frac{f\left(E-\frac{\mu_1+\mu_2}{2}+\frac{eV}{2}\right)-f\left(E-\frac{\mu_1+\mu_2}{2}-\frac{eV}{2}\right)}{eV} = \frac{-d(E-\frac{\mu_1+\mu_2}{2})}{dE} \tag{5.36}$$

$$I = \frac{2e}{h}\int_0^{+\infty} T_{ij}\frac{-df\left(E-\frac{\mu_1+\mu_2}{2}\right)}{dE}dE = \frac{2e}{h}\int_0^{+\infty} T_{ij}\frac{-df(E)}{dE}dE = \frac{2e^2VT_{ij}}{h}\frac{1}{1+\exp\left(-\frac{\mu_1+\mu_2}{2k_BT}\right)} \tag{5.37}$$

$$R = \frac{U}{I} = \frac{h}{2e^2T_{ij}}\left[1+exp\left(-\frac{\mu_1+\mu_2}{2k_BT}\right)\right] \tag{5.38}$$

Assuming the Fermi energy is in the energy gap center of semiconducting SWCNT, the Fermi energy at 0 K is equal to the chemical potential at 0 K,

$$\mu_i = E_F(0K) = \frac{0.7668}{2d_i} \tag{5.39}$$

$$R = \frac{R_0}{T_{ij}}\left[1+exp\left(-\frac{\frac{1}{d_1}+\frac{1}{d_2}}{4k_BT}\times 0.7668\right)\right] \tag{5.40}$$

where $R_0 = \frac{h}{2e^2}$ is the quantum resistance.

Temperature dependent electrical transport behavior of SWCNT aerogel reflects its three-dimensional interconnected, porous structure. Temperature active hopping (with electrical field assistance as the applied voltage increasing) will take place in the percolation paths in SWCNT aerogel, which consists of randomly oriented electrical resistor network. As temperature increases, the probability of hopping also increases with temperature. In addition, the softening of the van der Waals inter-tubular interactions leads to a reduction in inter-tube transfer of carriers. These are a systematic change in the shape of the overall temperature dependence in this percolation network, which is consistent with hopping conduction.

5.5 Conclusion

In this chapter, temperature dependent electrical transport properties of Aerographite and SWCNT aerogel were studied in the temperature range 2–300 K with the magnetic field effects, and fitted by the FITC and VRH models, respectively. It is found that structural disorder and the charge carrier density of electrons, which are modified by their structural symmetries and electronic band

structures, both play important roles in the temperature dependent electrical transport properties of Aerographite and SWCNT aerogel.

Based on the temperature dependent electrical transport analysis, Aerographite shows a semi-metallic conductive behavior down to low temperature because its resistance will decrease with increasing temperature. While SWCNT aerogel hold a semiconducting behavior in very low temperature (5 K). Structural disorder and charge carrier density of electrons are analyzed as a important reason for the resulting temperature dependent electrical transport properties of Aerographite and SWCNT aerogel, which plays as a pertubation of their structure symmetries and band structures.

Chapter 6

Self-healing and Piezoresistive Properties of Polydopamine-based Single-Walled Carbon Nanotube Hydrogel Hybrid Network

6.1 Introduction

In recent years, self-healing hydrogels have gained great attention in light of their tunable structures, mechanical robustness, and rheological properties. The property of rapid self-repair of structural damage and the recovery the original functions open up opportunities for wide applications in biomaterials, biomedical science, soft electronics, soft robotics, and tissue engineering [247-251]. Carbon nanotubes and their nanocomposite hydrogels have been widely deployed into diverse applications, such as drug delivery, actuators and sensors, biofuel and solar cells, nanomedicine, and conducting polymeric material [252-261].

Polydopamine (PDOPA) has high adhesivity to various surfaces and excellent surface affinity. This may be attributed to its similar structure to the adhesive protein found in mussels and the highly reactive catechol groups. These properties open up the possibility of preparing self-healing hydrogels [262]. Most previously reported polydopamine-based hydrogels were formed through metal chelation, but the toxicity of metals is a concern for biomedical applications [262,263]. Han *et al.* prepared a mussel mimicking, very tough polydopamine–polyacrylamide (PDOPA–PAM) hydrogel with self-healing ability, excellent cell affinity and strong tissue adhesiveness [264]. They further reported that a mussel-inspired glycerol-water hydrogel with polydopamine-decorated CNTs as conducting nanofillers exhibited long-term stability, good conductivity, and superior mechanical properties [265].

This collaborative project with University of Pennsylvania and Carnegie Mellon University took a similar approach in order to develop a novel functional hydrogel combining the advantages of carbon nanotube hydrogels and polydopamine which would be expected to lead to a material with elevated toughness and a superior self-healing ability. SWCNT hydrogel precursors were thus embedded into the catecholic amino acid, 3,4-Dihydroxy-L-phenylalanine-polyacrylamide (L-DOPA-PAM) hydrogel to form an L-DOPA-PAM-SWCNT hydrogel hybrid network. This hybrid network as formed was soft but became a hard gel at room temperature. An advantage of this material design is the prevention of overoxidation of L-DOPA to maintain enough free catechol groups to endow the desired properties [264]. Several characterization methods, including optical microscopy, Raman spectroscopy, and dynamic mechanical analysis (DMA) were utilized to characterize the L-DOPA-PAM-SWCNT hydrogel hybrid network. The piezoresistive properties of the hydrogel hybrid network were also investigated. The resistance dependence of L-DOPA-PAM hydrogel was measured under different pressures and at different times after the application of pressure started.

6.1.1 Sol-Gel Transition

The sol-gel transition (gelation) is a phase transition from a liquid state to a solid state. A gel is a material composed of subunits that can bond with each other so that one obtains a network of macroscopic dimensions, in which all the subunits are connected by bonds [266]. If one starts out with isolated subunits, and adds bonds, one transfers from a liquid state (a sol) to a material with a non-zero shear modulus (a gel) [265]. In the gelation process, a sol-gel transition takes place: from the sol state, to a gel, by the process of increasing the number of bonds between the subunits until a macroscopic network of subunits are connected [266].

6.1.2 Classes of Gel

Gels may be divided into two classes, depending on the nature of the bonds that link the subunits.

Chemical gels (“strong gels”): the bond linking the subunits are covalent chemical bonds or dynamic covalent reactions [266]. The strength of these bonds means that the network cannot be rearranged by heating thermally breaking the crosslinking [267].

Physical gels (“weak gels”): the bonds linking the subunits are physical interactions and exhibit thermo-reversible properties as a function of temperature [266]. Physical crosslinking involves ionic bonding, hydrogen-bonding, supramolecular interactions, hydrophobic bonding, molecular diffusion, and chain entanglement, either separately or in combination [264].

6.1.3 Hydrogels

Hydrogels are 3D cross-linked viscoelastic polymeric matrix networks which can absorb and retain large amounts of water. In an aqueous environment, hydrogels may be regarded as molecular scale porous materials in which the pore space is occupied by water [249]. These structures are often described by their swelling behavior [249,250]. Due to their biocompatibility and high thermo-dynamical affinity, hydrogels have recently drawn interest for biomedical applications, microelectromechanical systems (MEMS) and as bioelectronics interfaces [251,268].

As a result of the inhomogeneous distribution of the network and cross-links, conventional hydrogels are soft, weak, brittle, and fragile upon mechanical loading. Double network hydrogels (DN gels), such as poly (2-acrylamido, 2-methyl, 1-propanesulfonic acid) (PAMPS) polyelectrolyte and polyacrylamide (PAM) DN gels, were firstly proposed by J.-P. Gong *et al.* and manufactured using a two-step free-radical polymerization method [269]. In DN gels, a high relative molecular mass neutral polymer network is embedded within a swollen heterogeneous polyelectrolyte network [269,270]. The reported DN gel structure achieved extremely high mechanical strength (fracture compressive stress of 17.2 MPa and strain of 92%, fracture tensile stress of 1 – 10 MPa and strain of 1000 – 2000%) and high mechanical toughness (tearing fracture

energy of $10^2 – 10^3$ J m^{-2}), comparable to the strength and toughness of cartilages and rubbers [269,270].

Self-healing hydrogels, which autonomously recover their strength after being forced to fracture, are being developed as the self-healing ability in response to external stimuli, e.g. temperature, light, and pH, allows for the formation of adaptive smart materials [249]. The underlying principle is the re-establishment of bonds or structures after damage [249,250]. Reversible bonds, such as hydrogen bonds, host-guest interactions, hydrophobic associations, and dynamic bonds, have been developed successfully into self-healing hydrogels [249,250]. It is preferable if the self-healing hydrogel is produced from inexpensive and nontoxic materials and does not degrade prematurely in respect to the planned application [249,250]. In addition, it is desirable that self-healing hydrogels must: (a) respond to damage autonomously (without external stimuli), rapidly and repeatedly; (b) respond to damage (self-heal) from the micro- to macroscale; (c) possess electrical, mechanical, and rheological properties appropriate for the intended application; and (d) retain their original physical and rheological properties after self-healing [250].

6.1.4 Mussel-inspired Hydrogels: Cross-linked Network Precursor

Mussel-inspired hydrogels, held together by reversible catechol–metal coordination bonds, have been reported to exhibit attractive self-healing, viscoelastic and adhesive properties [268]. Based on polymer functionality and the use of other substances, mussel-inspired hydrogels may be classified into non-functional, nanocomposite, thermo-responsive and pH-responsive hydrogels [268,271]. They are widely used in tissue engineering, cell therapeutics and wound healing. A catechol amino acid called 3,4-dihydroxyphenyl-L-alanine (L-DOPA, Fig. 6.1) and lysine amino acids are present and involved in various types of interactions, i.e. hydrogen bonding, coordination between metal–catechol ligands, electrostatic interaction, cation-π interaction and π-π aromatic interaction. These make up a major component of the mussel foot proteins which have the property of moisture-resistant adhesion [272-275].

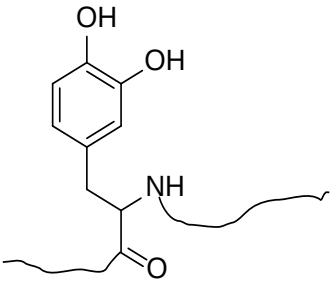

Figure 6.1: The chemical structure of protein bound L-DOPA containing the catechol side chain.

Catechol is a unique and versatile adhesive molecule capable of forming reversible physical bonds and irreversible covalent bonds [271,272]. A major challenge in catechol systems is to orchestrate the degree of catechol oxidation that occurs under alkaline conditions in air and has a great impact on the properties because it introduces irreversible covalent cross-links to the system. The cross-linking stiffens the hydrogels but consumes catechol groups needed for self-healing

[268]. Additionally, the exposed part of the byssus thread is coated by a self-healing layer, rich in DOPA and metal ions, such as Ti^{4+}, Fe^{3+}, Al^{3+}, Ca^{2+}, Cu^{2+} and Zn^{2+} [276-280]. The catechol side chain of DOPA is capable of various catechol-catechol and catechol-surface interactions, leading to the curing of the catechol-containing adhesive and strong interfacial binding [268]. Polydopamine (PDOPA) is a good candidate for preparing self-healing hydrogels because it has a similar chemical structure to DOPA and a highly catecholic group, which is able to release electrons when oxidized into the corresponding functional group and trigger reduction process in metallic cations [281-283]. It is important that over oxidation of PDOPA is prevented during hydrogel synthesis to maintain enough free catechol groups in the hydrogel [264].

6.2 Principle and Methodology

Self-healing can be defined as the ability of materials to recover or repair damages automatically and autonomously without any external intervention [284]. There are two types healing behaviors:

i. Automatic (without any intervention);
ii. No automatic (needing external triggering).

Self-healing and stimuli-response polymeric materials aim to generate a cross-linked network, either by dynamic covalent bonding interactions (such as chain exchange reactions, cycloaddition, and free radical intermediates), supramolecular interactions (such as hydrogen bonding, π-π stacking interactions and ionic interactions), or by physical cross-linking via chain entanglements. There are many different design strategies for self-healing materials, such as release of a healing agent, reversible cross-links, and miscellaneous technologies (electrohydrodynamic, conductivity, shape memory effect, nanoparticle migration, and co-deposition) [310]. Based on the principle of self-healing hydrogels, two approaches were proposed to develop self-healing hydrogels based on SWCNT hydrogel:

i. Metal-catecholate complexes with SWCNT hydrogel;
ii. Catechol-functionalized precursor with SWCNT hydrogel.

6.2.1 Metal-catecholate Complexes with SWCNT Hydrogel

In this strategy, the suitable polymer network precursor with catechol groups was prepared first. The candidates were PDMS (polydimethylsiloxane), PBS (polyborosiloxane), PAM (polyacrylamide), PEO (polyethylene oxide), PEG (polyethylene glycol), PMMA (polymethyl methacrylate), PAA (polyacrylic acid) and PVA (polyvinyl alcohol). Due to its biocompatibility and hydrophilicity and the presence of hydroxyl group facilitating further functionalization, the PAM backbone was selected having pendent short PEO/PEG chains with catechol unit or other functional groups. Then SWCNT hydrogel (removing out the surfactant and kept under appropriate pH conditions) was infiltrated in the polymer-catechol composite. Thirdly, metal ions, such as Fe^{3+}, Al^{3+}, Co^{2+}, Cu^{2+}, Zn^{2+} and Mg^{2+}, were added into the polymer-catechol

composite to build metal-ligand coordination complex via chelation reactions. The designed chemical structures are shown in Figs. 6.2 and 6.3.

The role of the metal ion cross linker is to help to quickly aggregate the free catechol groups and thus primarily stabilize the hydrogel. The metal-containing network typically improves by two or three orders of magnitude the stiffness because of the increased cross-link density introduced by the reversible metal-catecholate complexes [276]. The metal-catechol coordination complexes establish a macromolecular dynamic cross-linking process, which is mimicking what occurs in an aqueous environment [276]. Different metals contribute to dynamic covalent bonding in the protein structure in this order: $K^{+}<Na^{+}<Ca^{2+}<Mn^{2+}<Fe^{2+}<Co^{2+}\sim Ni^{2+}\sim Cu^{2+}<Zn^{2+}$ [279]. Finally, SWCNT hydrogel was added to the precursor.

Different chelation chemical structures were designed, targeted to self-healing properties via metal coordination crosslink dynamics. These are shown in Fig. 6.2 (a). In Fig. 6.2 (a), PEO/PEG was selected to the backbone, then pendent with catechol unit, o-Phenylenediamine, (S)-(-)-1,1′-Bi(2-naphthol) and (R)-(+)1,1′-Bi(2-naphthol) via chelation reactions. In Fig. 6.2 (b), PAM was used as the backbone, pendent with catechol unit, o-Phenylenediamine, (S)-(-)-1,1′-Bi(2-naphthol) and (R)-(+)1,1′-Bi(2-naphthol) via chelation reactions.

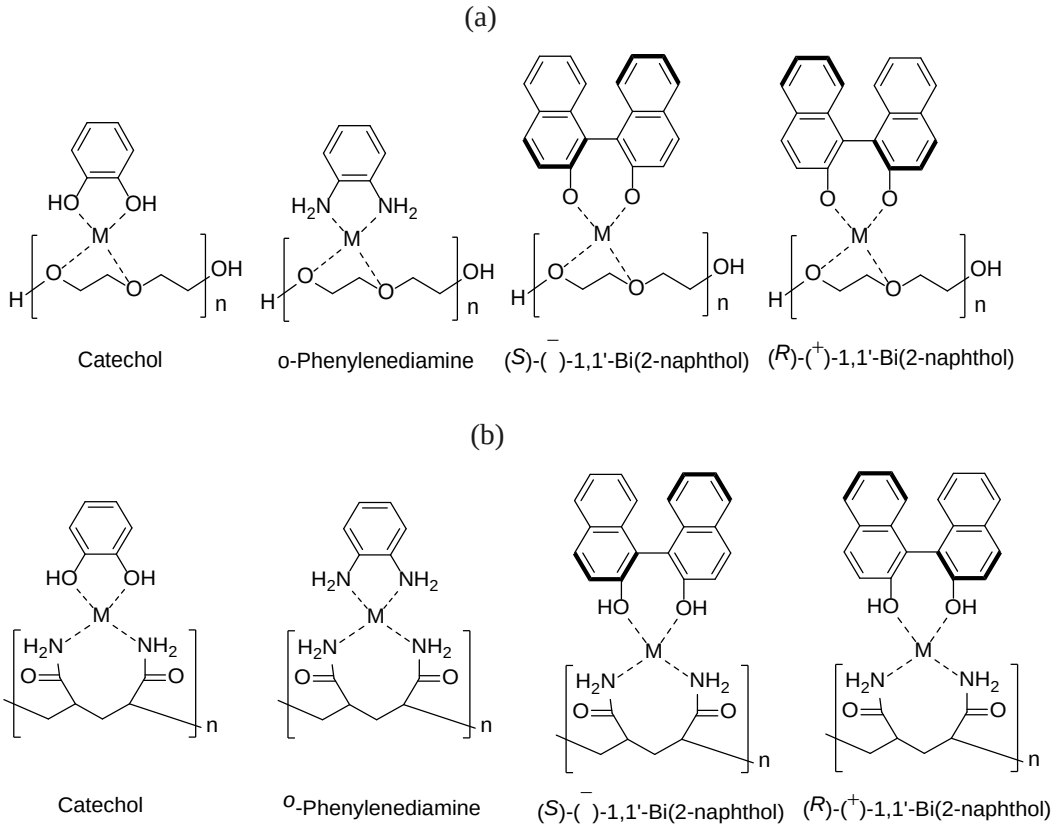

Figure 6.2: Designed chelation chemical structures based on different functional groups targeted for self-healing properties. (a) PEO/PEG backbone, pendent with catechol unit, o-Phenylenediamine, (S)-(-)-1,1′-Bi(2-naphthol) and (R)-(+)1,1′-Bi(2-naphthol) via chelation reactions. (b) PAM backbone, pendent with catechol unit, o-Phenylenediamine, (S)-(-)-1,1′-Bi(2-naphthol) and (R)-(+)1,1′-Bi(2-naphthol) via chelation reactions.

Coordination complexes between metals and catechol groups form metal–catechol coordination crosslinks that offer stiffness and strength (Fig. 6.2). These strongly depend on the coordination state and type of metals [278]. In these coordination complexes, metal ions cross-linkers have been used to establish different polymer networks with color changes. Several different metal ions were selected, namely Co^{2+}, Cu^{2+}, Zn^{2+}, Mg^{2+} and Fe^{3+}, to prepare various metal-catechol coordination complexes (Fig. 6.3). In Fig. 6.3, the sample preparation protocol is shown, and the dynamic metal–catechol coordination complexes explored as polymer crosslinks.

(a)

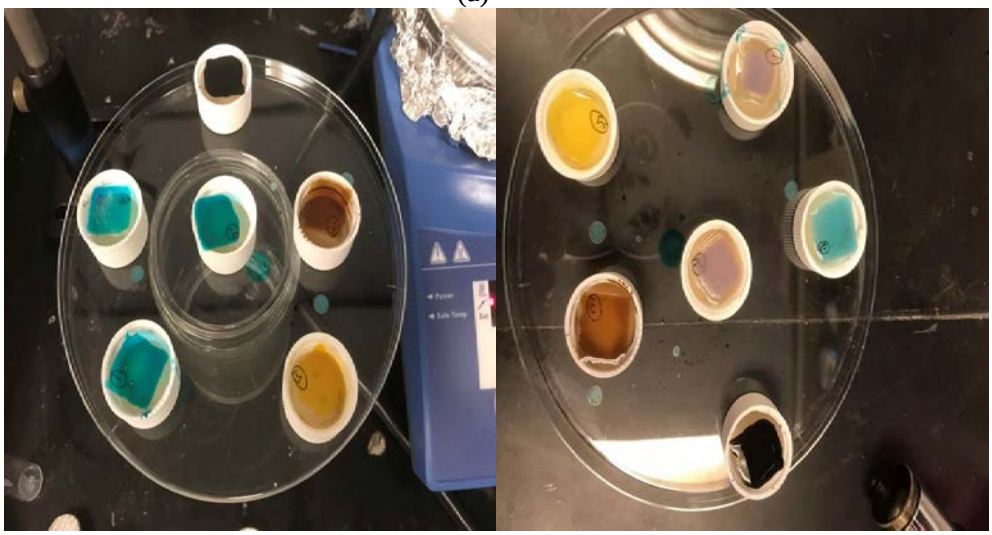

(b)

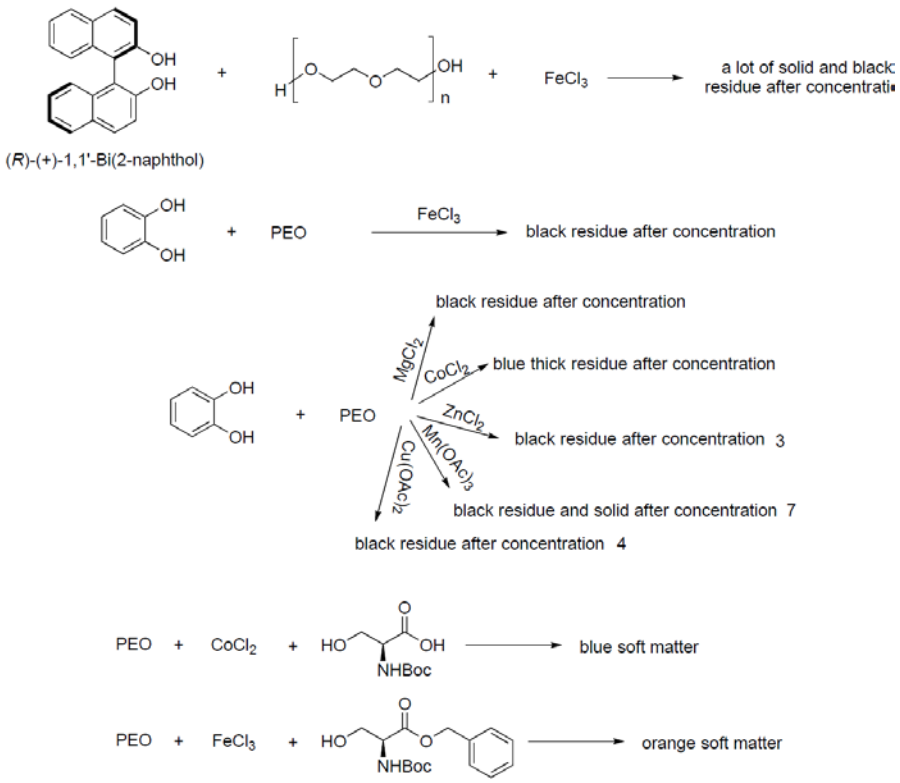

Fig. 6.3: Metal-catechol coordination polymer networks precursor.
Metal ions cross-linkers were used to establish different polymer networks with color changes.
(a) Dynamic metal–catechol coordination complexes explored as polymer crosslinks.
(b) Sample preparation protocol.

To test the self-healing properties of these prepared metal–catechol coordination complexes, finger printing and physical damage (i.e. knife wound) were applied to each sample. The results illustrate that finger printing on the PEO-catechol-Co^{2+} hydrogel disappears without external influence after about 2 hours and physical damage on the PEO-catechol-Co^{2+} hydrogel will also repair without external actuation after about 2 hours. This is attributed to catechol-Co^{2+} coordinate bonds that can cross-link automatically, at the suitable pH condition to ensure cross-link stability on the relevant time scales [274]. The mechanical properties of PEO-catechol-Co^{2+} polymer networks can be adjusted because the polymer networks behave according to the average lifetime of their catechol-Co^{2+} cross-links [274].

(a) Finger Printing Time 0 (b) Finger Printing after hours

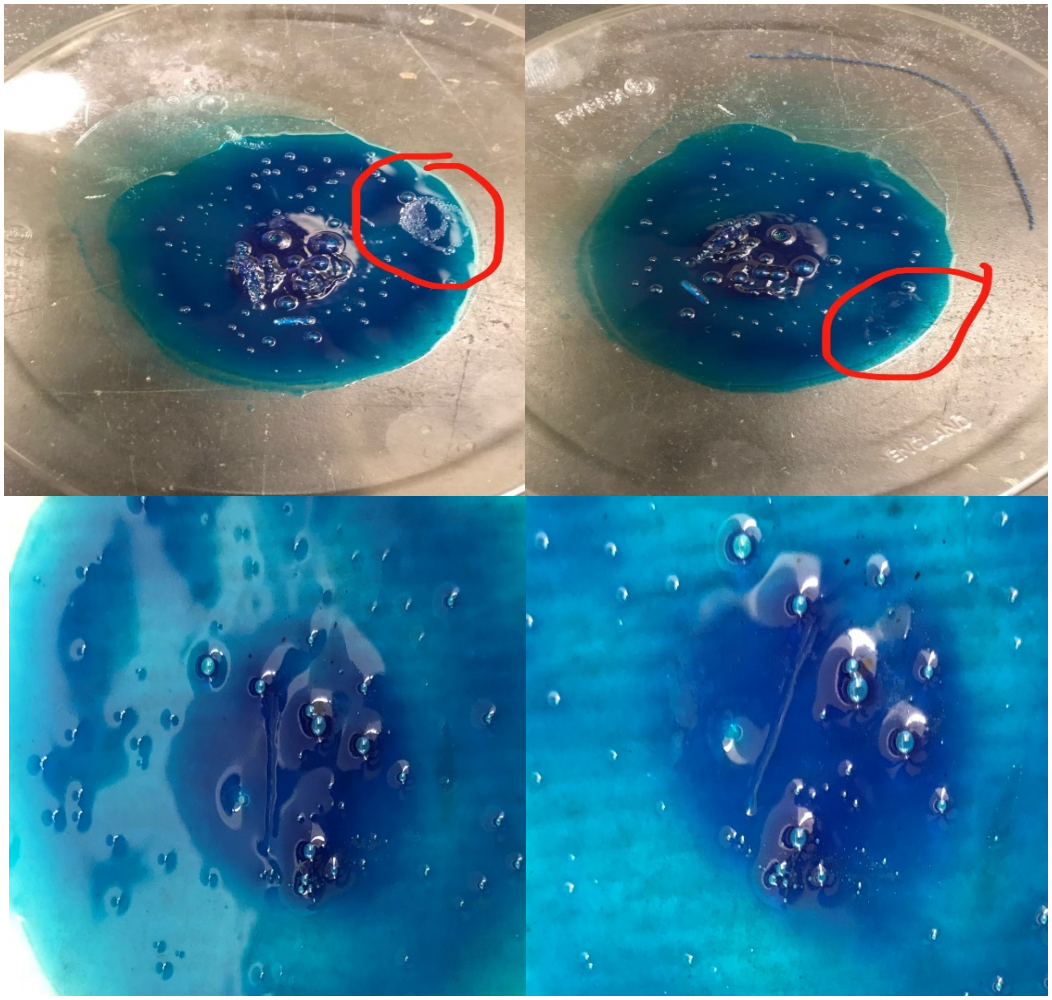

(c) Physical Damage Time 0 (d) Physical Damage after 2 hours

Figure 6.4: Images of PEO-catechol-Co^{2+} hydrogel undergo self-healing after physical damage. (a) and (b) Finger printing on the sample, which disappears without external influence after about 2 hours. (c) and (d) Physical damage (knife wound) on the sample, which will repair without external actuation after 2 hours.

6.3 Catechol-functionalized Precursor with SWCNT Hydrogel

This section explains that SWCNT hydrogel precursors were prepared first, then were embedded into the 3,4-Dihydroxy-L-phenylalanine-polyacrylamide (L-DOPA-PAM) hydrogel to form an L-DOPA-PAM-SWCNT hydrogel hybrid network, which maintains sufficient free catechol groups.

Optical microcopy, Raman spectroscopy and DMA were employed to characterize the L-DOPA-PAM-SWCNT hydrogel hybrid network.

6.3.1 Chemicals and Materials Synthesis

3,4-Dihydroxy-L-phenylalanine (L-DOPA, or Levodopa) was purchased from Fluka Chemie GmbH., Switzerland. Acrylamide (AM), ammonium persulfate (APS), *N,N'*-methylenebis (acrylamide) (BIS) and tetramethyl ethylenediamine (TEMA) were purchased from Sigma-Aldrich. Sodium dodecylbenzene sulfonate (SDBS) surfactant was purchased from Acros Organics and SWCNTs powder from CHASM Advanced Materials, Inc., USA.

6.3.2 Reaction Mechanism of L-DOPA–PAM Hydrogel

AM is toxic in its unpolymerized state, but is benign once polymerized [248]. Therefore, polymerization is mandatory to make it useful for practical applications. The monomer (AM) is polymerized in aqueous solution in the presence of small amounts of bifunctional cross-linker (BIS), resulting in an AM network with BIS links. This reaction occurs via a free-radical mechanism, where APS is used as an initiator, and a small volume of TEMA is used to stabilize the reaction.

Firstly, the L-DOPA powder was dissolved in a sodium hydroxide (NaOH) aqueous solution in an alkaline environment (pH=11). The L-DOPA was then left to self-polymerize for 20 min in air under magnetic stirring. Next, AM, BIS and TEMA were added into the L-DOPA solution in an ice bath under stirring. SWCNT hydrogel was added to the above solution in an ice bath under stirring for 1 h, then APS was added to the polymer network precursor solution and the mixture was kept stirred at 0 ℃ for 10 min. In this way, L-DOPA-PAM hydrogel is obtained.

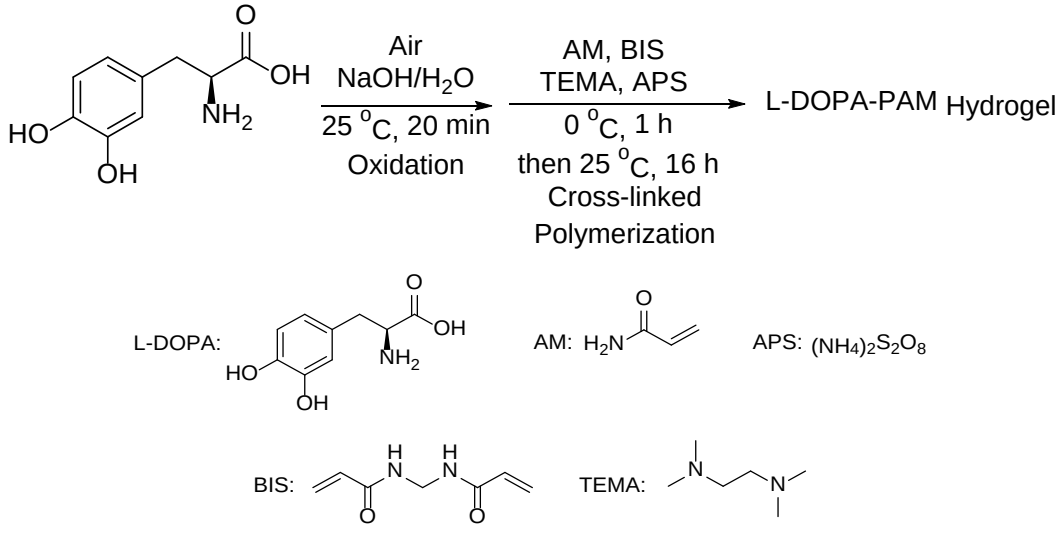

Figure 6.5: Synthetic process and reaction mechanism of the L-DOPA–PAM hydrogel.

6.3.3 Synthesis of L-DOPA-PAM-SWCNT Hydrogel Hybrid Network

The CG 300 SWCNT powder (0.03 g, average diameter: 0.84 nm, median length: 1 μm, carbon purity: ≥ 95 wt. %, specific surface area: ≥ 700 m^2/g) was suspended in deionized water (30 mL) using SDBS surfactant (0.3 g) at a SWCNT dispersion concentration of 1 mg/mL; the mass ratio of SWCNT with SDBS was 1:10. The solution was then tip-sonicated (VC 505, Sonics & Materials, Inc., USA) for 1 h at 100 W. During the sonication process, the temperature of the dispersion was maintained at room temperature using a water bath. Then the SWCNT dispersion was centrifuged at 1,500 rpm for 30 min (Fisher Scientific Marathon 21000R). After centrifugation, the SWCNTs suspension was concentrated by evaporating in a forced air oven (VWR Scientific 1330 FM) at 60 ˚C for 6 hours. The product was then poured into circular molds which were then covering with parafilm for 24 h in a humid ambient condition. After waiting for the gelation of the solution, the surfactant was removed by soaking in deionized water for 20 min, then in 1 M of nitric acid aqueous solution for 20 min. Different concentrations (20%, 40%, 60%, 80% and 100%) ethanol solutions were used to exchange the water in the samples.

The L-DOPA (10 mg, 4 wt. ‰ L-DOPA/AM) was dissolved in a beaker containing the NaOH aqueous solution (2.16 mL, pH = 11). With the vigorous magnetic stirring, L-DOPA was self-polymerized for 20 min under an atmosphere of air. After the reaction was cooled to 0 ˚C, APS (240 mg, 10 wt. % APS/AM), BIS (3 mg, 1.2 wt. ‰ BIS/AM) and TEMA (19 μL) were added to the L-DOPA solution. Then SWCNT hydrogel was also added into the above solution carefully and the resultant mixture was stirred carefully at 0 ˚C for 1 h. Finally, AM (2.4 g) was added into the polymer network precursor solution and the mixture was stirred slowly at 0 ˚C for 30 min. After that, the beaker was covered with parafilm and the reaction was stopped and then kept at room temperature overnight. After the polymerization, the SWCNT hydrogel was embedded into the L-DOPA-PAM polymer matrix. This produced the L-DOPA-PAM-SWCNT hydrogel hybrid network.

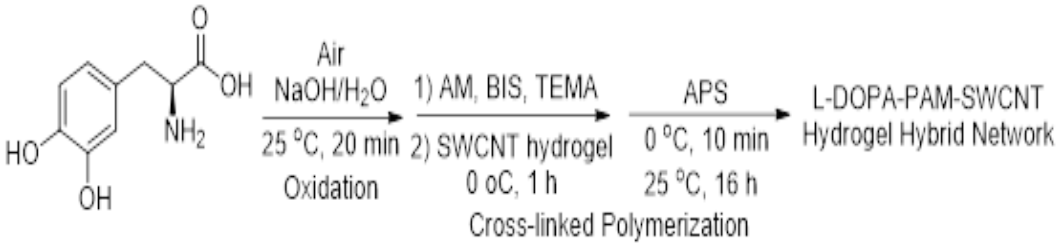

Figure 6.6: Synthetic process and reaction mechanism of the L-DOPA-PAM-SWCNT hydrogel hybrid network.

Figure 6.7: Synthetic process of L-DOPA-PAM-SWCNT hydrogel hybrid network.

6.4 Characterization of Obtained Samples

6.4.1 Optical Microscopy

To confirm the L-DOPA particles were infiltrated in the L-DOPA-PAM hydrogel properly, optical microscopy images were recorded using a Leica DMRX optical microscope with a 10x lens and a Zeiss Axiovert 135 optical microscope with a 100× oil immersion objective (N.A.=1.4). The L-DOPA–PAM hydrogel was cut off into a thin slice, sandwiched between 2 coverslips and then examined under the 100x oil immersion lens. Optical images of the L-PDOPA–PAM hydrogel is shown in Fig. 6.8.

Because the optical microscopy did not provide accurate scale information, I estimated the size of L-DOPA particles using a known colloid particle (d = 4 micron). The diameter of bigger particles (blue scale bar) is roughly around 30–40 micron. However, the L-DOPA particles were probably 50–100 nm in diameter unless the waiting time to create the hybrid network is very long; in that case the L-DOPA particles can grow to ~ several microns in diameter. In either case, the bigger particles are unlikely to infiltrate the SWCNT hydrogel. On the other hand, the small L-DOPA

oligomers (~ a few angstroms) will likely infiltrate and give the hybrid network its mechanical and self-healing properties.

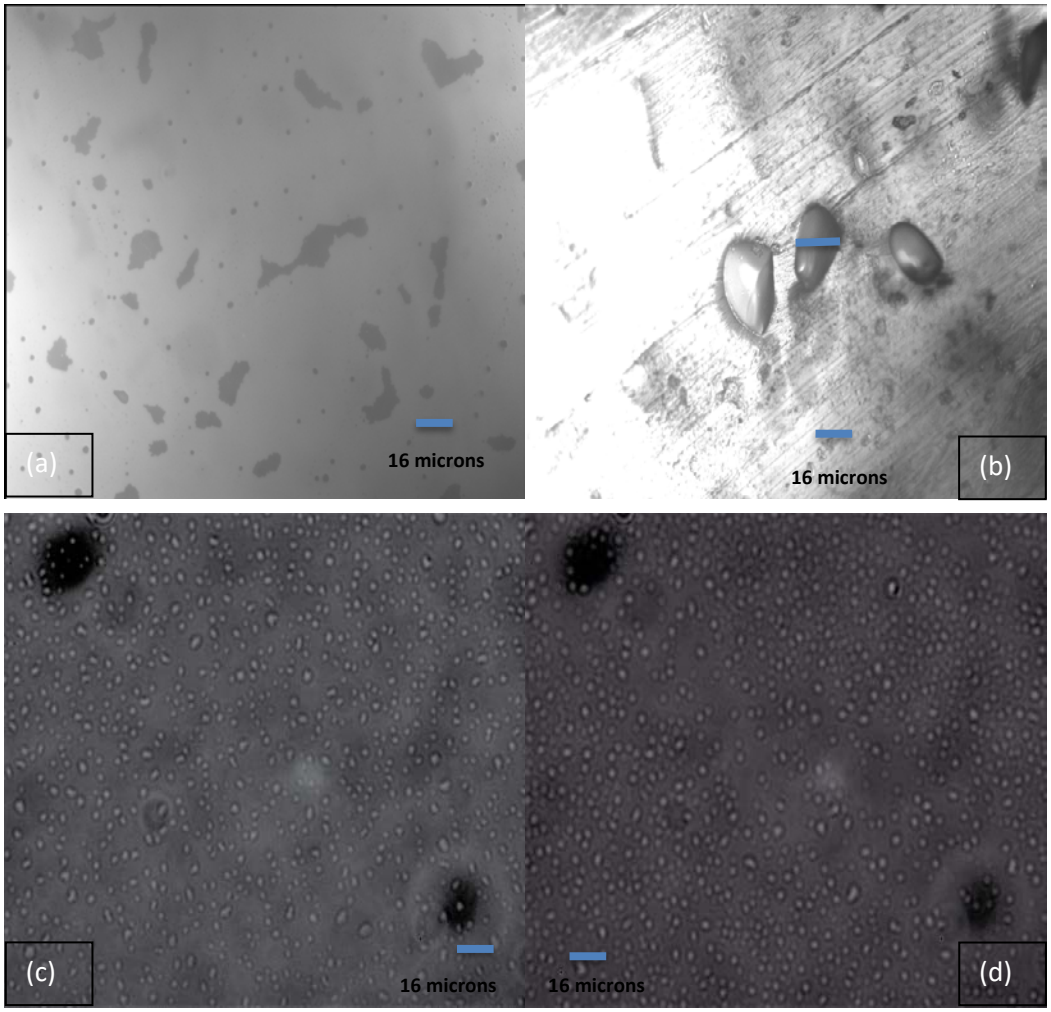

Figure 6.8: Optical microscopy images of L-PDOPA-PAM hydrogel.
(a) reference: colloid particles, d = 4 micron. (b) Leica DMRX optical microscopy 10x lens.
(c) and (d) Zeiss Axiovert 135 optical microscopy of L-PDOPA-PAM hydrogel
using 100x lens with immersion oil.

6.4.2 Raman Spectroscopy

To investigate the charge polarizability in the vibrational modes of the polymer structure, Raman spectra were measured on a Renishaw inVia^{TM} Raman spectrometer using a 633 nm He-Ne laser for excitation and 1800 l/mm gratings. The laser was focused on the sample via a Leica 50× long distance objective giving a laser spot size of about 1.5 μm. The laser beam power was adjustable from 10% to 100% of the source power in order to prevent sample damage and ensure a comparatively high SNR. Detection was achieved by an air-cooled CCD detector. The spectral resolution was about 3 cm^{-1} at 633 nm. Spectra were recorded in the regions of 60–4000 cm^{-1}. The calibration of this spectrometer is checked by using the line at 521 cm^{-1} of a silicon sample.

Fig. 6.9 shows the Raman spectra (60–4000 cm^{-1}) of the L-DOPA-PAM-SWCNT hydrogel hybrid network. There are several sharp peaks identified with the typical Raman peaks of SWCNTs, e.g.

258 cm^{-1} and 285 cm^{-1} (RBM), 845 cm^{-1} (oTO), 1050 cm^{-1} (oTO+LA), 1318 cm^{-1} (D), 1555 cm^{-1} (G^-), 1592 cm^{-1} (G^+) , 1731 cm^{-1} (M, overtone of oTO mode), 1924 cm^{-1} (iTOLA), 2617 cm^{-1} (2D) and 3186 cm^{-1} (2G) peaks [54,55,59,61]. This confirms that SWCNTs were present, which is expected since the synthesis was to design to embed SWCNT hydrogel precursors into the L-DOPA-PAM hydrogel to form the L-DOPA-PAM-SWCNT hydrogel hybrid network. Compared with the Raman spectra of SWCNT and SWCNT aerogel also at the excitation wavelength of 633 nm, this result shows the same Raman features (RBM, D, G^+ and G^- bands) with the L-DOPA–SWCNT hydrogel hybrid network and SWCNT aerogel [61,77]. This indicates that the SWCNT hydrogel embedded into the L-DOPA-PAM polymer matrix maintains its Raman features during the sample preparation process and that the properties of SWCNT did not change during the sample preparation. In Fig. 6.9 (b), there are 12 cm^{-1} shifts to the D band between L-DOPA-PAM-SWCNT hydrogel hybrid network (1318 cm^{-1}) and SWCNT aerogel (1306 cm^{-1}), 2 cm^{-1} shifts of the G^+ band (1590 cm^{-1} for L-DOPA-PAM-SWCNT hydrogel hybrid network, 1592 cm^{-1} for SWCNT aerogel) and G^- band (1556 cm^{-1} for L-DOPA-PAM-SWCNT hydrogel hybrid network, 1554 cm^{-1} for SWCNT aerogel). These shifts are likely to be due to the interaction between the SWCNT and their surroundings.

(a) Raman spectra from 60–4000 cm^{-1} (b) Zoom in the D, G^+ and G^- bands

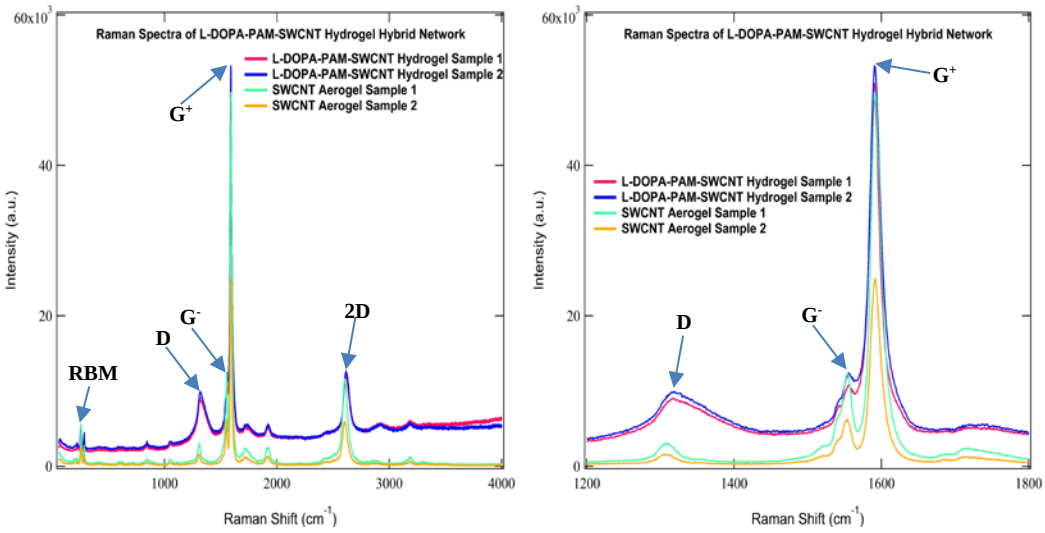

Figure 6.9: Raman spectra of L-DOPA-PAM-SWCNT hydrogel hybrid network and SWCNT aerogel.

6.4.3 Dynamic Mechanical Properties (Rheology)-Compression Test

The goal of rheological experiments is to quantify dynamic viscoelasticity over a range of temperature, time, and deformation scales, and ultimately to relate these viscoelastic properties to material structures [286,287]. This goal is achieved by using a DMA that mechanically imposes an oscillatory stress (the amount of force per unit area applied to the sample), or strain (the dimensionless degree to which the material deforms), upon soft materials being tested. The linear response is described by frequency-dependent shear moduli, including the storage modulus (*G′*,

elastic response) and loss modulus (G'', viscous response) that provide information on the structures and rheological timescales of soft materials [288,289].

In order to obtain the basic parameters, i.e. the relaxation time and frequency dependent modulus, of the L-DOPA-PAM-SWCNT hydrogel hybrid network, I preformed frequency sweeps (time dependent viscoelastic properties) of the dynamic modulus for samples using a NETZSCH 242 E Artemis DMA system at 23 °C. L-DOPA-PAM hydrogel was chosen as the reference sample. A piece of the L-DOPA-PAM-SWCNT hydrogel hybrid network (15 mm length × 15 mm width × 6.8 mm thickness) was placed between the clips of the DMA. It was compressed to a given distance at a rate of 15 mm/min, and then the distance was maintained for 60 s. Water loss during testing was negligible due to typical testing time < 30 min.

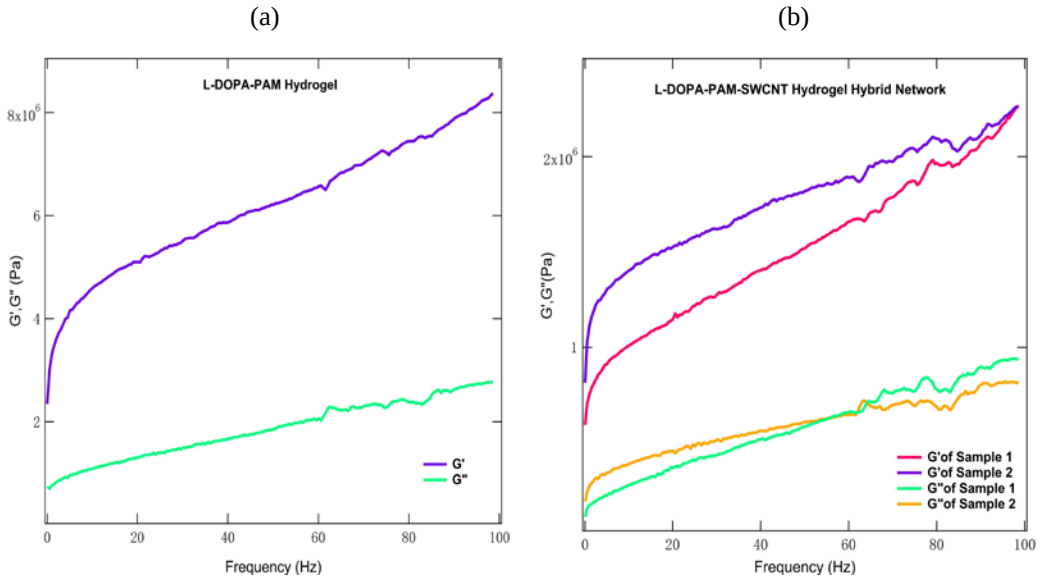

Figure 6.10: Frequency dependent modulus of L-DOPA-PAM-SWCNT hydrogel hybrid network. (a) Reference sample. (b) L-DOPA-PAM-SWCNT hydrogel hybrid network.

Fig. 6.10 presents the frequency dependent modulus of the L-DOPA-PAM-SWCNT hydrogel hybrid network in the frequency range 0.1–100 Hz with linear frequency sweep mode and dynamic single point mode. It was performed at constant 0.1% strain while measuring G' and G'. Both G' and G'' of L-DOPA-PAM-SWCNT hydrogel hybrid network show an increase as the frequency increases from 0.1 to 80 Hz. Minor oscillations also appear in the high frequency range (60–100 Hz). In the frequency range of 0.1–100 Hz, G' is always larger than G'', which means the sample of L-DOPA-PAM-SWCNT hydrogel hybrid network and its precursor, L-DOPA-PAM hydrogel, are likely to be physical gels. According to the behavior at the gel-point, both G' and G'' of L-DOPA-PAM-SWCNT hydrogel hybrid network decreased significantly (G'=2.3 MPa at 100 Hz) relative to those of L-DOPA-PAM hydrogel (8.2 MPa at 100 Hz). This is likely to be due to enhanced entanglement effects.

The tan δ curves of L-DOPA-PAM-SWCNT hydrogel hybrid network are shown in Fig. 6.11. When the frequency increases, the tan δ also increases (there are oscillations after 60 Hz in the high frequency range). It has been previously shown tan δ can reflect the crosslink degree of the

L-DOPA-PAM-SWCNT hydrogel; the smaller the tan δ is, the larger is the crosslinked degree of the network [290-292]. Peaks in the tan δ curves as a function of frequency imply phase transitions in the hydrogel hybrid network. Most hydrogel groups in this study produce an obvious viscoelastic response below 60 Hz. There are vibrations in both L-DOPA-PAM-SWCNT and L-DOPA-PAM-SWCNT hydrogels between 60 and 90 Hz (the high frequency range). The loss tangent curves also indicate a progressive softening of the L-DOPA-PAM hydrogel until saturation is reached after about 100 Hz. The loss tangent of L-DOPA-PAM-SWCNT hydrogel show a decreasing trend after 100 Hz. It is likely that the higher structural inhomogeneity of the L-DOPA-PAM-SWCNT hydrogel leads to nonuniform softening.

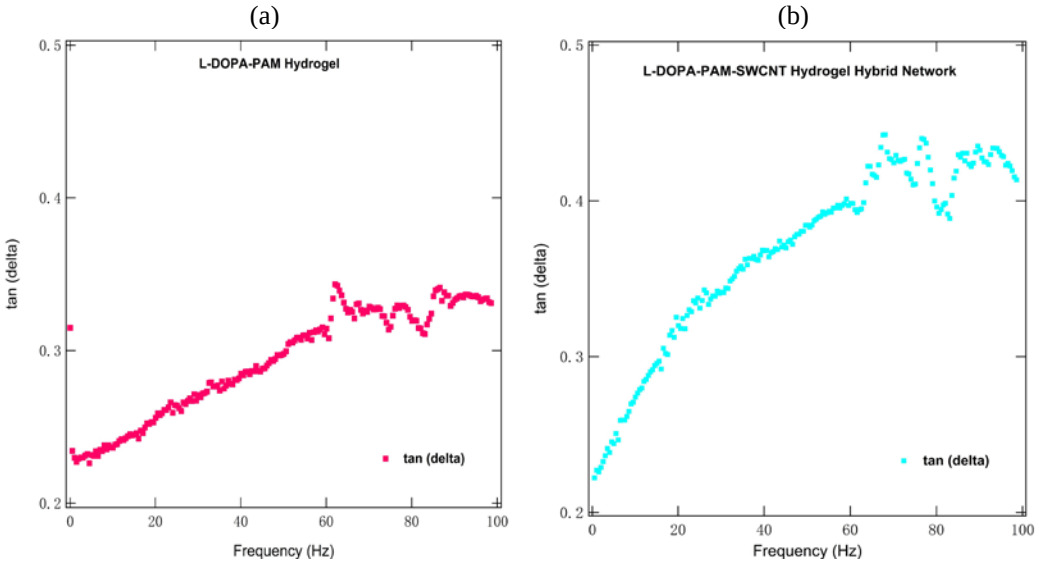

Figure 6.11: tan δ curves as a function of frequency of L-DOPA-PAM-SWCNT hydrogel hybrid network.
(a) Reference sample. (b) L-DOPA-PAM-SWCNT hydrogel hybrid network.

On the other hand, the lower the loss tangent of a dielectric material, the better is its performance in charge storage applications. The tan δ curves of L-DOPA-PAM-SWCNT hydrogel hybrid network increase as the frequency increases, which indicates a stronger charge storage ability of this L-DOPA-PAM-SWCNT hybrid system at lower frequency. The values of the loss tangent of L-DOPA-PAM-SWCNT hydrogel are larger (minimum 0.23) compared with that of other polymer systems, such as polystyrene incorporating core-shell copper nanowires (maximum 0.2 at the same concertation) [293]. It is thus demonstrated that our hydrogel system has the better charge storage ability and has potential applications in supercapacitors.

6.4.4 Piezoresistive Effect

Piezo-polymers and their composites are widely used as a result of their wide bandwidth, rapid electromechanical response, relatively low power requirements and high generative forces [294-298]. The piezoresistive response in polymers and their composites arises from electrical resistivity. This occurs because of the strain from the applied force impacts the material's band structure, which makes it easier or more difficult for electrons to be excited into the conduction

band and from the resulting change of the density of current carriers and the electrical resistance upon application of a mechanical stimulus [294-298]. Piezo-polymers were developed to advance energy harvesting technology due to their mechanical flexibility, high processing speed, low fabrication cost and biocompatibility. Other potential applications are to piezoresistive sensors, smart electronic devices, high-sensitive flexible electronic skin, MEMS, and micro fluid chips [299,300]. CNTs and another sp^2 carbon hybrid system, such as fullerenes (C_{60}), have been applied to improve the piezoresistive performance of the typical piezo-polymers through an increase of Young's modulus; for example, polyvinylidene fluoride (PVDF) and its copolymers, cellulose, and their derivatives [301-304].

The piezoresistive response of numerous polymer composites have been characterized and reported and theoretical models developed to explain the piezoresistivity in conductor-polymer composites, such as the tunneling mechanism linked to a percolation model [305-310]. In the tunneling model, based on the interparticle separation change under the applied stress, the relative resistance will decrease with an increase of applied stress in the electrically conducting composites composed of a conducting filler into the polymeric matrix [306]. The resistance is affected by the applied stress (σ), filler particle diameter (D), filler volume fraction (θ), matrix compressive modulus (M), and barrier height (φ), and is quantitively described in Eq. 6.1 [307]:

$$\frac{R}{R_0} = \left(1 - \frac{\sigma}{M}\right) exp\left\{-\frac{4\pi}{h}(2m\varphi)^{-\frac{1}{2}} D\left[\left(\frac{\pi}{6}\right)^{\frac{1}{3}}\theta^{-\frac{1}{3}} - 1\right]\frac{\sigma}{M}\right\} = f(\sigma, M, D, \theta, \varphi) \quad (6.1)$$

where R_0 is the original electrical resistance without the applied stress.

The interparticle separation change of the polymer matrix is also a function of time. This causes the creep behavior of polymer matrix [308]:

$$\frac{R(t)}{R_0} = \frac{1-\varepsilon(t)}{1-\varepsilon_0} exp\{-\gamma s_0[\varepsilon(t) - \varepsilon_0]\} = \left(1 - \frac{\psi\sigma t^n}{1-\varepsilon_0}\right) exp\left\{-\gamma\psi\sigma D\left[\left(\frac{\pi}{6}\right)^{\frac{1}{3}}\theta^{-\frac{1}{3}} - 1\right] t^n\right\}$$
$$= f(\sigma, D, \theta, \varphi, \varepsilon_0, \psi, n) \quad (6.2)$$

where ε_0 is the original strain under the applied stress, ψ and n are constants, and s_0 is the original interparticle separation, $\gamma = \frac{4\pi}{h}(2m\varphi)^{-\frac{1}{2}}$.

The L-DOPA-PAM hydrogel was put in the sample holder with a pressing stage, which was fabricated by polymethyl methacrylate (PAAM, or Perspex), to keep the samples in place. The sample was of cylindrical shape, with radius of 1 cm, a circular cross-sectional area of 3.14 cm^2 and thickness 1 mm. The sample was connected to the high-performance digital multimeter (RIGOL DM3061, Suzhou, China) using brass electrodes arranged at each side for two-probe measurements. The sample holder prevented transverse movement of the sample under stress and ensured that the applied stress was uniaxial [307]. Different weights (0.01 kg, 0.03 kg, 0.05 kg, 0.1 kg, 0.15 kg, 0.2 kg, 0.25 kg, 0.3 kg, 0.35 kg, 0.4 kg, 0.45 kg and 0.5 kg) with the corresponding pressures of 0.31 kPa, 0.94 kPa, 1.56 kPa, 3.12 kPa, 4.68 kPa, 6.24 kPa, 7.80 kPa, 9.36 kPa, 10.9 kPa, 12.48 kPa, 14.05 kPa and 15.61 kPa, were applied to the top of the sample holder as a static

load. Once the load is applied, the force generated by weights was enough to ensure good electrical contact. For all measurements, values of electrical resistance reach their final stabilization around 5 minutes. Stability and repeatability were analyzed by multiple sampling.

(a) Group A

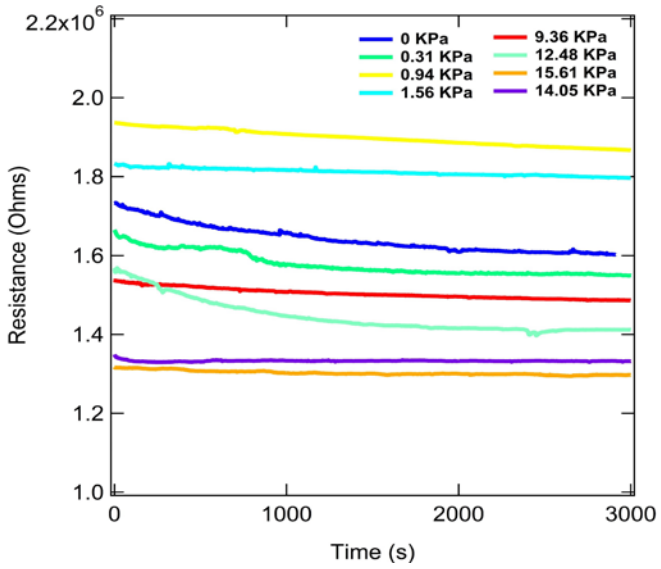

(b) Group B

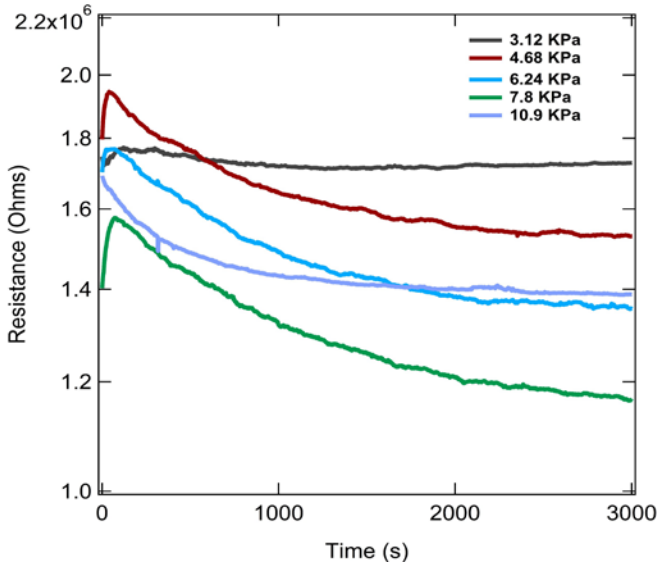

Figure 6.12: Electrical resistance as a function of pressure and time of L-DOPA–PAM hydrogel (at ambient temperature 23 °C).

Fig. 6.12 presents the electrical resistance as a function of pressure and time of L-DOPA-PAM hydrogel at ambient temperature of 23 °C. Measurements under each of the uniaxial pressures were performed for 3000 s. This data shows that the electrical resistance on average decreases with an increase of applied stress; and the electrical resistance generally decreases with time under the same pressure, which may be attributed to the creep behavior of the polymer matrix [308]. For clarity, these are plotted in two groups: group A and B, respectively. In group A (at pressures 0 kPa < P < 1.56 kPa, and 9.4 kPa < P < 14 kPa), the electrical resistance generally decreases with time under the same pressure. In group B (at pressures 3.1 kPa < P < 10.9 kPa), the electrical

resistance initially increases and then decreases with time under the same pressure. At pressures for which the strongest change of resistance with time is observed, the resistance initially increases with time (approximately in the first minute after applying the pressure). Then, the resistance peaks, followed by a decrease in resistance with time.

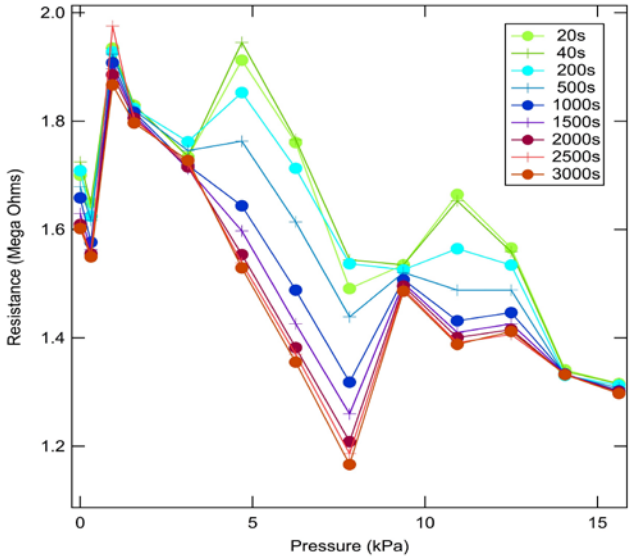

Figure 6.13: Electrical resistance as a function of pressure of L-DOPA–PAM hydrogel. (at ambient temperature 23 °C)

Fig. 6.13 shows the electrical resistance as a function of pressure (kPa) at ambient temperature of 23 °C, as obtained from Fig. 6.12. For P < 3.1 kPa, 9.4 kPa, and 14 kPa and more, the electrical resistance does not depend on time (or has little time dependence); that is, $R(t)$ always has the same value for up to 3000 s. At pressures 3.1 kPa < P < 9.4 kPa, and 9.4 kPa < P < 14 kPa, $R(T)$ is in a transitional state, changing with time. This may be associated with the potential barriers that need to be overcome by the application of pressure, so that the distance between conducting fibers can slowly decrease with time as the polymer creeps. The value of the pressure reflects the energy density applied to the sample. The hypothesis is that the polymer does not creep under pressure until at a certain pressure corresponding to an internal energy barrier is overcome. From that point onward, the polymer fibers start moving slowly, producing a change of the distance between conducting fibers. Because of this, the resistance changes with time (resistance is mainly contributed by the tunneling between conducting fibers through the polymer). Then, at a certain pressure (i.e. 9.4 kPa) the pressure induces fast enough polymer creep to overcome the initial barrier, so that there is no time dependence observed. However, higher pressure than that drives the polymer toward a second energy barrier that needs to be overcome, curtailing further creep, and changing the electrical resistance with time. This continues until 14 kPa, at which pressure no polymer creep occurs, and the electrical resistance no longer changes with time. In order to assess the noise level (and oscillations) in Fig 6.12, the electrical resistance measured at 40 s is plotted vs. pressure (kPa) with error bars in Fig. 6.14.

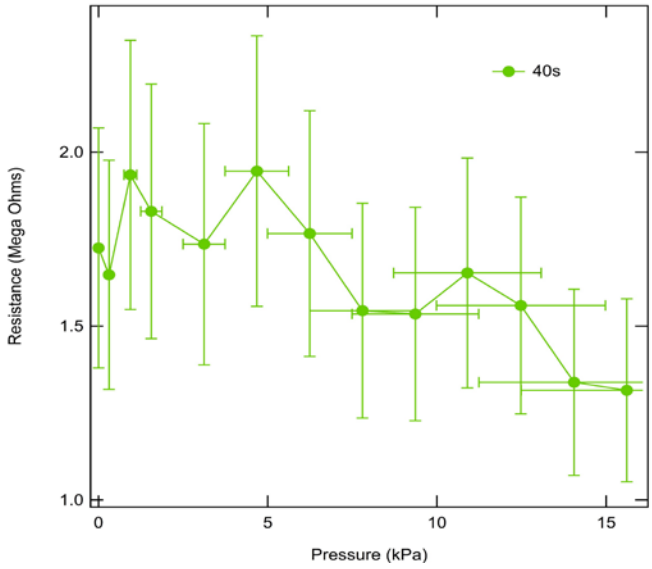

Figure 6.14: Electrical resistance vs. pressure of L-DOPA–PAM hydrogel measured at 40 s with error bars.

To explain this electrical resistance dependent behavior, two main assumptions have been made: 1. there are fibers in the sample that are more conducting than the sample "matrix". The electrical conductivity changes as the connectivity between these fibers changes as the matrix "creeps" in time; and 2. there are at least two types of energy barriers associated with this creep. Each of them is overcome at a distinct pressure, after which the matrix creeps, changing the connectivity between the conducting fibers.

It is noted that there is also initial increase of R with time for $P < 3.1$ kPa, indicating an increase of the distance between conducting fibers as pressure is applied. However, the increase of R also occurs in the first ~500 s after the first energy barrier is overcome at 3.1 kPa. For $P > 7.8$ kPa, the increase of R always occurs. R becomes independent of time at 9.4 kPa.

6.5 Conclusion

In this chapter, a novel functional hydrogel was prepared combining the advantages of CNT hydrogels and polydopamine with self-healing ability. SWCNT hydrogel precursors were successfully embedded into an L-DOPA-PAM polymer matrix to form an L-DOPA-PAM-SWCNT hydrogel hybrid network. The L-DOPA-PAM-SWCNT hydrogel hybrid network was characterized by optical and mechanical methods. Piezoresistive and electrical resistance properties of the L-DOPA-PAM hydrogel and their dependence on time and pressure were also investigated. The electrical resistance decreases with an increase of applied stress; the electrical resistance decreases with time at constant pressure. A physical explanation of the pressure- and time-sensitivities of the L-DOPA-PAM hydrogel is along the lines that the dominant mechanisms are a combination of polymer creep two different energy barriers in this hydrogel hybrid network. This offers a possible candidate for tactile sensing, supercapacitors, self-healing electronic skin with bioelectronic applications.

Chapter 7

Conclusion and Outlook

In this chapter, I summarize the general conclusions that may be drawn from this PhD thesis. I also outline some perspectives and the outlook arising from this work.

7.1 Conclusion

The main goal of this doctoral work was to investigate the vibrational spectroscopy (Raman spectroscopy and synchrotron TH/Far-IR spectroscopy) and temperature dependent electrical transport properties of Aerographite and SWCNT aerogel at THz and IR frequencies. Furthermore, as a potential material for flexible electronics manufacturing and biomedical applications, a novel functional L-DOPA-PAM-SWCNT hydrogel hybrid network was prepared and characterized.

In the Chapter 3, the Raman spectra of Aerographite were studied in comparison to graphite oxide, kish graphite and graphite flakes, and quantitatively analyzed to yield their respective intensity ratios, as a function of the laser excitation energy. The Raman features of Aerographite may be divided into two parts: first, the typical Raman features of graphitic materials, namely the G, D, and 2D bands; and, second, distinctive Raman features due to Aerographite's 3D interconnected carbon foam structure on a hollow tetrapod skeleton. The D and 2D bands of Aerographite exhibit a blue-shift (to higher energies) as the excitation energy increases, but the positions of the G band does not obviously shift with excitation energy. While all the samples give Raman bands characteristic for graphitic systems, the bands for Aerographite and graphite oxide are broadened. While the intensity ratio of the D to G band (I_D/I_G) increases linearly with laser wavelength with all wavelengths used for kish graphite and graphite flakes, it saturates at the longest wavelengths for Aerographite and graphite oxide. However, all samples show a linear increase in the energy of D band over all laser wavelengths used. A physical model is proposed to explain these phenomena that is based on the double resonant Raman scattering mechanism. This model was employed to interpret the energy dependence of the D band. It takes into account the effects of defects on the phonon density of states. This explains the observed saturation in (I_D/I_G) vs. λ_L at long laser wavelengths for highly disordered graphitic materials, as exemplified in this work by Aerographite and graphite oxide.

Temperature dependent synchrotron THz/Far-IR and Raman spectral studies of Aerographite and SWCNT aerogel are presented in Chapter 4. New IR absorption bands of Aerographite and SWCNT aerogel were observed in the temperature range from 6–300 K. Some low frequency IR absorption bands show a red-shift (to lower energies) with increasing temperature. Variable temperature Raman results reveal frequency shifts of phonon modes with the change of temperature over the range 80–300 K. The Raman peak positions of Aerographite and SWCNT aerogel also show a red-shift (to lower energies) with increasing temperature. This behavior is

attibuted to carbon-carbon bond stretching, which is due to the thermal expansion in the lattice and the anharmonic coupling of phonon modes. The 2D peaks of Aerographite and SWCNT aerogel both show a blue-shift (to higher energy) with temperature. This may be explained either through the increasing distance between covalently bonded carbon structures and possible charge redistribution within the covalent bonds, or through the double resonant Raman scattering mechanism. Measurements of both red-shift and blue-shift offer a tool for studying the intricacies of inter- and intra-molecular bonds for a range of different molecular solids. In addition, multiple low frequency Raman features are identified and assigned in the THz region.

In Chapter 5, the temperature dependent electrical transport properties of Aerographite and SWCNT aerogel were studied over the temperature range 2–300 K under varying magnetic fields. The experimental data were successfully fitted by the fluctuation-induced tunneling conduction (FITC) model for Aerographite and the variable range hopping (VRH) model for SWCNT aerogel. The statistical length and diameter distributions of the SWCNTs were quantitively determined using atomic force microscopy (AFM). Aerographite shows a metallic conductive behavior down to low temperatures, that is, resistance decreasing with increasing temperature. On the other hand, SWCNT aerogel displays a semiconducting behavior at very low temperature (resistance decreasing with temperature). Structural disorder and the variable charge carrier density are advanced as important reasons for the observed temperature dependent electrical transport properties of Aerographite and SWCNT aerogel.

A stimulus-responsive hydrogel hybrid network, L-DOPA-PAM, was prepared, combining the advantages of CNTs hydrogel and polydopamine with demonstrated self-healing ability. Piezoresistive properties as a function of time and pressure for this material were investigated. It was found that the electrical resistance decreases with an increase of applied stress, and that the electrical resistance at constant pressure decreases with time. A physical explanation based on the creep behavior and quantum tunneling effect across barriers was proposed to explain these experimental results.

7.2 Outlook

The unusual properties of carbon aerogels suggest their suitability for various applications in the military, industry and high technology including aerospace [311], thermal insulation [312], supercapacitor [313], energy storage and conversion [314], water purification and pollution management (oil and metal absorption) [315], sensing technology [316], architectural and building technology [317], and electrocatalysis and enzyme catalysis [318].

The results that have been presented in this PhD thesis serve as the foundation for further investigations or experiments that can be done. The PhD thesis has provided insights into the optical, vibrational, and electrical transport properties of Aerographite and SWCNT aerogel at THz and IR frequencies. However, there remain many challenges and more investigations that

beckon to further the understanding of the fine structures of carbon aerogels, physical properties of carbon aerogels, and to explore advanced THz and IR applications of new carbon-based nanostructures, such as active THz metamaterial devices and THz metasurfaces.

1. Since the first- and second-order Raman spectra are related to the graphitization degree and the magneto-structural correlations of carbons, the first-order Raman spectra are especially sensitive to the extent of the 2D graphitic ordering, and the second-order Raman spectra are sensitive to the graphitization processes which give rise to the 3D ordering of hexagonal graphite. It is important to investigate the magnetic susceptibility χ of carbon allotropes, which is sensitive to the size of ordered 2D regions in the graphite layers [319,320]. Magnetic susceptibility depends on the existence of localized electrons with unpaired spins and the modulation of DOS around the Fermi level [321]. When charge transfers from graphite π electron to the localized edge states (edge shapes, quantum size effect and surface effects) it results in a shifting of the Fermi level, which determines the Raman G-peak position and magnetic properties of these nanosized π-electron states in the graphitization process and the magnetic susceptibility in sp^2 and sp^3 carbon systems [320,322-324]. To confirm this, the temperature-dependence of magnetic susceptibility in sp^2 and sp^3 carbon systems are required.

2. DFT simulations for the vibrational mode analysis of Aerographite and SWCNT aerogel might precisely identify the vibrational modes of carbon aerogel at THz and IR frequencies.

3. The physical model proposed to explain the temperature dependent electrical transport properties of Aerographite and SWCNT aerogel still needs refining. We only had limited access to Monte Carlo simulations based on percolation theory. Future work might open up a deeper understanding of the electrical conductivity behavior of carbon aerogels, resulting from these interesting amorphous morphologies.

It is possible to consider new carbon aerogels or other cellular carbon structures (carbon foams, mesogels, 3D architectures) for THz and IR applications in terahertz devices and electromagnetic interference shielding; for example, a MWCNT aerogel sheet supporting surface plasmon polaritons excitation THz polarizer, a macroscopic 3D graphene foam-based THz absorber, a graphene aerogel-based bloomer for Far-IR sensing, a spherical MWCNT aerogel in state of acoustic levitation for THz wave scattering, and a flexible and robust Kevlar nanofiber aerogel film for IR stealth imaging [325-330].

References

[1] (a) S. S. Kistler, "Coherent Expanded Aerogels and Jellies", *Nature*, **127**, 741 (1931); (b) S. S. Kistler, "Coherent Expanded-Aerogels", *J. Phys. Chem.* **36**, 52 (1932).

[2] H. D. Gesser and P. C. Goswami, "Aerogels and Related Porous Materials", *Chem. Rev.* **89**, 765 (1989).

[3] N. Hüsing and U. Schubert, "Aerogels-Airy Materials: Chemistry, Structure, and Properties", *Angew. Chem. Int. Ed.* **37**, 22 (1998).

[4] NASA Jet Propulsion Laboratory: https://stardust.jpl.nasa.gov/photo/aerogel.html

[5] AZO Materials: https://www.azom.com/article.aspx?ArticleID=6499

[6] M. Antonietti, N. Fechler and T. P. Fellinger, "Carbon Aerogels and Monoliths: Control of Porosity and Nanoarchitecture via Sol−Gel routes", *Chem. Mater.* **26**, 196 (2014).

[7] N. A. Peppas, J. Z. Hilt, A. Khademhosseini and R. Langer, "Hydrogels in Biology and Medicine: From Molecular Principles to Bionanotechnology", *Adv. Mat.* **18**, 1345 (2006).

[8] Y. S. Zhang and A. Khademhosseini, "Advances in Engineering Hydrogels", *Science* **356**, 500 (2017).

[9] A. W. P. Fung, Z. H. Wang, K. Lu, M. S. Dresselhaus and R. W. Pekala, "Characterization of Carbon Aerogels by Transport Measurements", *J. Mater. Res.* **8**, 1875 (1993).

[10] S. Chandrasekaran, P. G. Campbell, T. F. Baumann and M. A. Worsley, "Carbon Aerogel Evolution: Allotrope, Graphene-Inspired, and 3D-Printed Aerogels", *J. Mater. Res.* **32**, 4166 (2017).

[11] J. Biener, M. Stadermann, M. Suss, M. A. Worsley, M. M. Biener, K. A. Rose and T. F. Baumann, "Advanced Carbon Aerogels for Energy Applications", *Energy Environ. Sci.* **4**, 656 (2011).

[12] M. Mecklenburg, A. Schuchardt, Y. K. Mishra, S. Kaps, R. Adelung, A. Lotnyk, L. Kienle and K. Schulte, "Aerographite: Ultra Lightweight, Flexible Nanowall, Carbon Microtube Material with Outstanding Mechanical Performance", *Adv. Mater.* **24**, 3486 (2012).

[13] S. Garlof, M. Mecklenburg, D. Smazna, Y. K. Mishra, R. Adelung, K. Schulte and B. Fiedler, "3D Carbon Networks and Their Polymer Composites: Fabrication and Electromechanical Investigation of Neat Aerographite and Aerographite-based PNCs under Compressive Load", *Carbon*, **111**, 103 (2017).

[14] Scientists from Germany Produce the Lightest Material in the World: http://www.uni-kiel.de/aktuell/pm/2012/2012-212-aerographit-e.shtml.

[15] (a) M. A. Worsley, P. J. Pauzauskie, T. Y. Olson, J. Biener, J. H. Satcher, Jr. and T. F. Baumann, "Synthesis of Graphene Aerogel with High Electrical Conductivity", *J. Am. Chem. Soc.* **132**, 40 (2010); (b) Y. X. Xu, K. X. Sheng, C. Li and G. Q. Shi, "Self-Assembled Graphene Hydrogel via a One-Step Hydrothermal Process", *ACS Nano* **4**, 4324 (2010); (c) H. Hu, Z. B. Zhao, W. B. Wan, Y. Gogotsi and J. S. Qiu, "Ultralight and Highly Compressible Graphene Aerogels", *Adv. Mat.* **25**, 2219 (2013); (d) M. A. Worsley, T. T.

Pham, A. Yan, S. J. Shin, J. R. I. Lee, M. Bagge-Hansen, W. Mickelson and A. Zettl, "Synthesis and Characterization of Highly Crystalline Graphene Aerogels", *ACS Nano* **8**, 11013 (2014).

[16] (a) H. Y. Sun, Z. Xu and C. Gao, "Multifunctional, Ultra-Flyweight, Synergistically Assembled Carbon Aerogels", *Adv. Mat.* **25**, 2554 (2013); (b) F. Guo, Y. Q. Jiang, Z. Xu, Y. H. Xiao, B. Fang, Y. J. Liu, W. W. Gao, P. Zhao, H. T. Wang and C. Gao, "Highly Stretchable Carbon Aerogels", *Nat. Commun.* **9**, 881 (2018); (c) C. Zhu, T. Y. J. Han, E. B. Duoss, A. M. Golobic, J. D. Kuntz, C. M. Spadaccini and M. A. Worsley, "Highly Compressible 3D Periodic Graphene Aerogel Microlattices", *Nat. Commun.* **6**, 6962 (2015).

[17] M. B. Bryning, D. E. Milkie, M. F. Islam, L. A. Hough, J. M. Kikkawa and A. G. Yodh, "Carbon Nanotube Aerogels", *Adv. Mat.* **19**, 661 (2007).

[18] (a) M. B. Bryning, M. F. Islam, J. M. Kikkawa and A. G. Yodh, "Very Low Conductivity Threshold in Bulk Isotropic Single-Walled Carbon Nanotube-Epoxy Composites", *Adv. Mat.* **17**, 1186 (2005); (b) K. H. Kim, Y. Oh and M. F. Islam, "Mechanical and Thermal Management Characteristics of Ultrahigh Surface Area Single-Walled Carbon Nanotube Aerogels", *Adv. Funct. Mater.* **23**, 377 (2013).

[19] J. H. Zou, J. H. Liu, A. S. Karakoti, A. Kumar, D. Joung, Q. Li, S. I. Khondaker, S. Seal and L. Zhai, "Ultralight Multiwalled Carbon Nanotube Aerogel", *ACS Nano* **4**, 7293 (2010).

[20] (a) P. J. Pauzauskie, J. C. Crowhurst, M. A. Worsley, T. A. Laurence, A. L. David Kilcoyne, Y. Wang, T. M. Willey, K. S. Visbeck, S. C. Fakra, W. J. Evans, J. M. Zaug and J. H. Satcher Jr., "Synthesis and Characterization of a Nanocrystalline Diamond Aerogel", *PNAS*, **108**, 8550 (2011); (b) S. Manandhar, P. B. Roder, J. L. Hanson, M. Lim, B. E. Smith, A. Mann and P. J. Pauzauskie, "Rapid Sol–Gel Synthesis of Nanodiamond Aerogel", *J. Mater. Res.* **29**, 2905 (2014).

[21] R. A. Lewis, *Terahertz Physics*, Cambridge University Press, Cambridge, UK, 2012.

[22] Y.-S. Lee, *Principles of Terahertz Science and Technology*, Springer Science+Business Media, New York, NY, USA, 2008.

[23] E. Bründermann, H. W. Hübers and M. F. Kimmitt, *Terahertz Techniques*, Springer-Verlag, Berlin, Germany, 2012.

[24] X.-C. Zhang and J. Z. Xu, *Introduction to Terahertz Wave Photonics*, Springer Science+Business Media, New York, NY, USA, 2010.

[25] (a) Zomega Terahertz Corporation, *The Terahertz Wave eBook-Technical Overview*, Troy, NY, USA, 2012; (b) L. Duvillaret, F. Garet and J. L. Coutaz, "A Reliable Method for Extraction of Material Parameters in Terahertz Time-Domain Spectroscopy", *IEEE J. Sel. Top. Quantum Electron.* **2**, 739 (1996); (c) L. Duvillaret, F. Garet and J. L. Coutaz, "Highly Precise Determination of Optical Constants and Sample Thickness in Terahertz Time-Domain Spectroscopy", *Appl. Opt.* **38**, 409 (1999); (d) L. Duvillaret, F. Garet and J. L. Coutaz, "Influence of Noise on the Characterization of Materials by Terahertz Time-Domain Spectroscopy", *J. Opt. Soc. Am. B* **17**, 452 (2000).

[26] B. Ferguson and X.-C. Zhang, "Materials for Terahertz Science and Technology," *Nat. Mater*. **1**, 26 (2002).

[27] R. A. Lewis, "A Review of Terahertz Sources", *J. Phys. D: Appl. Phys.* **47**, 374001 (2014).

[28] V. Vylet and J. Liu, "Synchrotron Facilities and Free Electron Lasers", *Invited talk presented at Health Physics Society, Professional Development School, Topics in Accelerator Health Physics*, 1/31/2008-2/2/2008, Oakland, CA, USA.

[29] Australian Synchrotron: http://archive.synchrotron.org.au/aussyncbeamlines/ftir/introduction.

[30] (a) W. Withayachumnankul and M. Naftaly, "Fundamentals of Measurement in Terahertz Time-Domain Spectroscopy", *J. Infrared Millim. Terahertz Waves*, **35**, 610 (2014); (b) W. Withayachumnankul, B. M. Fischer and D. Abbott, "Material Thickness Optimization for Transmission-Mode Terahertz Time-Domain Spectroscopy", *Opt. Exp.* **16**, 7382 (2008); (c) W. Withayachumnankul, B. M. Fischer, H. Lin and D. Abbott, "Uncertainty in Terahertz Time-domain Spectroscopy Measurement", *J. Opt. Soc. Am. B* **25**, 1059 (2008); (d) T. D. Dorney, R. G. Baraniuk and D. M. Mittleman, "Materials Parameter Estimation with Terahertz Time-Domain Spectroscopy", *J. Opt. Soc. Am. A* **18**, 1562 (2001); (e) R. Fastampa, L. Pilozzi and M. Missori, "Cancellation of Fabry-Perot Interference Effects in Terahertz Time-Domain Spectroscopy of Optically Thin Samples", *Phys. Rev. A* **95**, 063831 (2017).

[31] M. S. Sherwin, C. A. Schmuttenmaer and P. H. Bucksbaum, "Opportunities in THz Science", Report of a DOE-NSF-NIH Workshop, February 12–14, 2004, Arlington, VA, USA.

[32] R. A. Lewis, "A Review of Terahertz Detectors", *J. Phys. D: Appl. Phys.* **52**, 433001 (2019).

[33] P. L. Richards, "Bolometers for Infrared and Millimeter Waves", *J. Appl. Phys*. **76**, 1 (1994).

[34] R. A. Lewis, "Physical Phenomena in Electronic Materials in the Terahertz Region", *Proc. IEEE*, **95**, 1641 (2007).

[35] P. U. Jepsen, D. G. Cooke and M. Koch, "Terahertz Spectroscopy and Imaging–Modern Techniques and Applications", *Laser Photon. Rev.* **5**, 1 (2011).

[36] P. Y. Han, M. Tani, M. Usami, and S. Kono, R. Kersting and X.-C. Zhang, "A Direct Comparison between Terahertz Time-Domain Spectroscopy and Far-Infrared Fourier Transform Spectroscopy", *J. Appl. Phys*. **89**, 2357 (2001).

[37] R. Ulbricht, E. Hendry, J. Shan, T. F. Heinz and M. Bonn, "Carrier Dynamics in Semiconductors Studied with Time-Resolved Terahertz Spectroscopy", *Rev. Mod. Phys.* **83**, 543 (2011).

[38] D. N. Basov, R. D. Averitt, D. van der Marel, M. Dressel and K. Haule, "Electrodynamics of Correlated Electron Materials", *Rev. Mod. Phys.* **83**, 471 (2011).

[39] M. A. Gilmore, S. Kamal, D. M. Broun and J. S. Dodge, "Determination of Electron-Phonon Interaction Parameters from Time-Domain Terahertz Spectroscopy", *Appl. Phys. Lett.* **88**, 141910 (2006).

[40] Q. L. Zhou, Y. L. Shi, B. Jin and C. L. Zhang, "Ultrafast Carrier Dynamics and Terahertz Conductivity of Photoexcited GaAs under Electrical Field", *Appl. Phys. Lett.* **93**, 102103 (2008).

[41] (a) P. A. George, J. Strait, J. Dawlaty, S. Shivaraman, M. Chandrashekhar, F. Rana and M. G. Spencer, "Ultrafast Optical-Pump Terahertz-Probe Spectroscopy of the Carrier Relaxation and Recombination Dynamics in Epitaxial Graphene", *Nano Lett.* **8**, 42428 (2008); (b) K. C. Lin, M. Y. Li, L. J. Li, D. C. Ling, C. C. Chi and J. C. Chen, "Ultrafast Dynamics of Hot Electrons and Phonons in Chemical Vapor Deposited Graphene", *J. Appl. Phys.* **113**, 133511 (2013).

[42] (a) A. E. Miroshnichenko, S, Flach and Y. S. Kivshar, "Fano Resonances in Nanoscale Structures", *Rev. Mod. Phys.* **82**, 2257 (2010); (b) M. F. Limonov, M. V. Rybin, A. N. Poddubny and Y. S. Kivshar, "Fano Resonances in Photonics", *Nat. Photonics* **11**, 543 (2017).

[43] P. Y. Yu and M. Cardona, *Fundamentals of Semiconductors*-4th Ed., Springer-Verlag, Berlin, Germany, 2010.

[44] (a) M. Fox, *Optical Properties of Solids*, Oxford University Press, Oxford, UK, 2001; (b) S. Nudelman and S. S. Mitra, *Optical Properties of Solids*, Plenum Press, New York, NY, USA, 1969.

[45] M. S. Dresselhaus, G. Dresselhaus and A. Jorio, *Group Theory-Application to the Physics of Condensed Matter*, Springer-Verlag, Berlin, Germany, 2008.

[46] R. Saito, G. Dresselhaus and M. S. Dresselhaus, *Physical Properties of Carbon Nanotubes*, Imperial College Press, London, UK, 1998.

[47] (a) F. Tuinstra and J. L. Koenig, "Raman Spectrum of Graphite", *J. Chem. Phys.* **53**, 1126 (1970); (b) S. Reich and C. Thomsen, "Raman Spectroscopy of Graphite", *Phil. Trans. R. Soc. Lond. A* **362**, 2271 (2004); (c) J. Maultzsch, S. Reich, C. Thomsen, H. Requardt and P. Ordejón, "Phonon Dispersion of Graphite", *Phys. Rev. Lett.* **92**, 075501 (2004); (d) L. Wirtz and A. Rubio, "The Phonon Dispersion of Graphite Revisited", *Solid State Commun.* **131**, 141 (2004); (e) M. Mohr, J. Maultzsch, E. Dobardžić, S. Reich, I. Milošević, M. Damnjanović, A. Bosak, M. Krisch and C. Thomsen, "Phonon Dispersion of Graphite by Inelastic X-Ray Scattering", *Phys. Rev. B* **76**, 035439 (2007).

[48] M. S. Dresselhaus, G. Dresselhaus, S. B. Cronin and A. G. Souza Filho, *Solid State Properties from Bulk to Nano*, Springer-Verlag, Berlin, Germany, 2018.

[49] A. M. Rao, E. Richter, S. Bandow, B. Chase, P. C. Eklund, K. A. Williams, S. Fang, K. R. Subbaswamy, M. Menon, A. Thess, R. E. Smalley, G. Dresselhaus and M. S. Dresselhaus, "Diameter-Selective Raman Scattering from Vibrational Modes in Carbon Nanotubes", *Science*, **275**, 187 (1997).

[50] S. Reich, C. Thornsen and J. Maultzsch, *Carbon Nanotubes-Basic Concepts and Physical Properties*, Wiley-VCH Verlag, Weinheim, Germany, 2004.

[51] (a) M. S. Dresselhaus and P. C. Eklund, "Phonons in Carbon Nanotubes", *Adv. Phys.* **49**,

705 (2000); (b) P. C. Eklund, J. M. Holden and R. A. Jishi, “Vibrational Modes of Carbon Nanotubes: Spectroscopy and Theory”, *Carbon*, **33**, 959 (1995).

[52] M. S. Dresselhaus, A. Jorio and R. Saito, “Characterizing Graphene, Graphite, and Carbon Nanotubes by Raman Spectroscopy”, *Annu. Rev. Condens. Matt. Phys.* **1**, 89 (2010).

[53] M. S. Dresselhaus, A. Jorio, M. Hofmann, G. Dresselhaus and R. Saito, “Perspectives on Carbon Nanotubes and Graphene Raman Spectroscopy”, *Nano Lett.* **10**, 751 (2010).

[54] R. Saito, M. Hofmann, G. Dresselhaus, A. Jorio and M. S. Dresselhaus, “Raman Spectroscopy of Graphene and Carbon Nanotubes”, *Adv. Phys.* **60**, 413 (2011).

[55] M. S. Dresselhaus, G. Dresselhaus, R. Saito and A. Jorio, “Raman Spectroscopy of Carbon Nanotubes”, *Phys. Rep.* **409**, 47 (2005).

[56] L. M. Malard, M. A. Pimenta, G. Dresselhaus and M. S. Dresselhaus, “Raman Spectroscopy of Graphene”, *Phys. Rep.* **473**, 51 (2009).

[57] A. C. Ferrari, “Raman Spectroscopy of Graphene and Graphite: Disorder, Electron–Phonon Coupling, Doping and Nonadiabatic Effects”, *Solid State Commun.* **143**, 47 (2007).

[58] M. J. Matthews, M. A. Pimenta, G. Dresselhaus, M. S. Dresselhaus and M. Endo, “Origin of Dispersive Effects of the Raman D Band in Carbon Materials”, *Phys. Rev. B* **59**, R6585 (1999).

[59] M. S. Dresselhaus, G. Dresselhaus, A. Jorio, A. G. Souza Filho and R. Saito, “Raman Spectroscopy on Isolated Single Wall Carbon Nanotubes”, *Carbon* **40**, 2043 (2002).

[60] M. A. Pimenta, G. Dresselhaus, M. S. Dresselhaus, L. G. Cançado, A. Jorio and R. Saito, “Studying Disorder in Graphite-Based Systems by Raman Spectroscopy”, *Phys. Chem. Chem. Phys.*, **9**, 1276 (2007).

[61] A. Jorio, R. Saito, G. Dresselhaus and M. S. Dresselhaus, *Raman Spectroscopy in Graphene Related Systems*, Wiley-VCH, Weinheim, Germany, 2011.

[62] C. Thomsen and S. Reich, “Double Resonant Raman Scattering in Graphite”, *Phys. Rev. Lett.* **85**, 5214 (2000).

[63] J. Maultzsch, C. Thomsen and S. Reich, “Double-Resonant Raman Scattering in Graphite: Interference Effects, Selection Rules, and Phonon Dispersion”, *Phys. Rev. B* **70**, 155403 (2004).

[64] R. Saito, A. Jorio, A. G. Souza Filho, G. Dresselhaus, M. S. Dresselhaus and M. A. Pimenta, “Probing Phonon Dispersion Relations of Graphite by Double Resonance Raman Scattering”, *Phys. Rev. Lett.* **88**, 027401 (2002).

[65] R. Saito, A. Grueneis, L. G. Cancado, M. A. Pimenta, A. Jorio, G. Dresselhaus, M. S. Dresselhaus and A. G. Souza Filho, “Double Resonance Raman Spectra in Disordered Graphite and Single Wall Carbon Nanotubes”, *Mol. Cryst. Liq. Cryst.* **387**, 63 (2002).

[66] S. O. Kasap, *Principle of Electronic Materials and Devices*, 4th ed., McGraw-Hill Education, New York, NY, USA, 2018.

[67] D. J. Griffith, *Introduction to Quantum Mechanics*, 2nd ed., Pearson Education, Upper Saddle River, NJ, USA, 2005.

[68] P. W. Anderson, "Absence of Diffusion in Certain Random Lattices", *Phys. Rev.* **109**, 1492 (1958).

[69] P. A. Lee and T. V. Ramakrishnan, "Disordered Electronic Systems", *Rev. Mod. Phys.* **57**, 287 (1985).

[70] P. Sheng, *Introduction to Wave Scattering, Localization and Mesoscopic Phenomenon*, 2nd ed., Springer-Verlag, Berlin, Germany, 2006.

[71] (a) N. F. Mott, "Conduction in Glasses Containing Transition Metal Ions", *J. Non-Crystal Solids*, **1**, 1 (1968); (b) N. F. Mott and E. A. Davis, *Electronic Processes in Non-Crystalline Materials*, 2nd ed., Oxford University Press, Oxford, UK, 2012.

[72] B. I. Shklovskii and A. L. Efros, *Electronic Properties of Doped Semiconductors*, Springer-Verlag, Berlin, Germany, 1984.

[73] D. Stauffer and A. Aharony, *Introduction to Percolation Theory*, 2nd revised ed., Taylor and Francis, London, UK, 2003.

[74] S.-S. Yan, *Fundamental of Solid State Physics* (Chinese), 3rd ed., Peking University Press, Beijing, China, 2011; S.-S. Yan, *An Introduction to Modern Solid State Physics* (Chinese), Peking University Press, Beijing, China, 2008.

[75] (a) J. Kurkijärvi, "Hopping Conductivity in One Dimension", *Phys. Rev. B* **8**, 922 (1973); (b) V. K. S. Shante, C. M. Varma and A. N. Bloch, "Hopping Conductivity in One-Dimensional Disordered Compounds", *Phys. Rev. B* **8**, 4885 (1973).

[76] (a) M. Büttiker, Y. Imry, R. Landauer and S. Pinhas, "Generalized Many-Channel Conductance Formula with Application to Small Rings", *Phys. Rev. B* **31**, 6207 (1985); (b) M. Büttiker, "Four-Terminal Phase-Coherent Conductance", *Phys. Rev. Lett.* **57**, 1761 (1986).

[77] R. Landauer, "Spatial Variation of Currents and Fields Due to Localized Scatterers in Metallic Conduction", *IBM J. Res. Dev.* **1**, 233 (1957).

[78] (a) D. Feng and G.-J. Jin, *Introduction to Condensed Matter Physics*, Vol. 1, World Scientific, Singapore, 2005; (b) D. Feng and G.-J. Jin, *Condensed Matter Physics* (Chinese), Vols. 1 and 2, Higher Education Press, Beijing, China, 2013.

[79] S. Datta, *Electronic Transport in Mesoscopic Systems*, Cambridge University Press, Cambridge, UK, 1995.

[80] (a) N. W. Ashcroft and N. D. Mermin, *Solid State Physics*, Saunders College Publishing, Philadelphia, PA, USA, 1976; (b) C. Kittel, *Introduction to Solid State Physics*, 8th ed., John Wiley & Sons, Hoboken, NJ, USA, 2005; (c) W. A. Harrison, *Solid State Theory*, 1st ed., Dover Publications, Mineola, NY, USA, 1980.

[81] TeraView TeraPulse 4000 User's Guide, TeraView Ltd, Cambridge, UK, 2017.

[82] (a) B. Stuart, *Infrared Spectroscopy: Fundamentals and Applications*, John Wiley & Sons, Inc., Hoboken, NJ, USA, 2004; (b) B. C. Smith, *Infrared Spectral Interpretation: A Systematic Approach*, CRC Press, Boca Raton, FL, USA, 1999; (c) B. C. Smith, *Fundamentals of Fourier Transform Infrared Spectroscopy*, 2nd ed., CRC Press, Boca Raton,

FL, USA, 2010; (d) P. R. Griffiths and J. A. de Haseth, *Fourier Transform Infrared Spectroscopy*, 2nd ed., John Wiley & Sons, Inc., Hoboken, NJ, USA, 2007; (e) G. Socrates, *Infrared and Raman Characteristic Group Frequencies*, John Wiley & Sons, Chichester, West Sussex, UK, 2001.

[83] (a) D. Creagh, J. McKinlay and P. Dumas, "The Design of the Infrared Beamline at the Australian Synchrotron", *Vib. Spectrosc.* **41**, 213 (2006); (b) R. Plathe, D. Martin, M. J. Tobin and D. Appadoo, "The Far-Infrared/THz Beamline at the Australian Synchrotron: Performance & Applications", *IEEE Proc. IRMMW-THz 2011* (*36th International Conference on Infrared, Millimeter, and Terahertz Waves*), Houston, TX, USA, 2011; (c) Bruker Optics, Guide for Infrared Spectroscopy, Billerica, MA, USA, 2009.

[84] Cyro Industries of America Cryogen Free Products, online available: http://www.cryoindustries.com/CryogenFreeProductPage.html.

[85] Renishaw Raman spectroscopy explained, online available: https://resources.renishaw.com/en/details/brochure-raman-spectroscopy-explained--104782.

[86] Quantum Design Physical Property Measurement System® DynaCool™ User's Manual, online available: https://www.qdusa.com/products/dynacool.html.

[87] S. A. Speakman, *Basics of X-Ray Powder Diffraction*, Massachusetts Institute of Technology, online available: http://prism.mit.edu/xray/Basics%20of%20X-Ray%20Powder%20Diffraction.pdf.

[88] JEOL Field Emission Scanning Electron Microscope Introduction, online available: https://aiim.uow.edu.au/content/groups/public/@web/@aiim/documents/doc/uow154681.pdf.

[89] Oxford Instruments Asylum Research AFM Systems Introduction, online available: https://afm.oxinst.com/products/mfp-3d-afm-systems/mfp-3d-origin-afm.

[90] NETZSCH Dynamic Mechanical Analysis, online available: https://www.netzsch-thermal-analysis.com/en/products-solutions/dynamic-mechanical-thermal-analysis/dma-242-e-artemis/.

[91] A. C. Ferrari and D. M. Basko, "Raman Spectroscopy as a Versatile Tool for Studying the Properties of Graphene", *Nat. Nanotechnol.* **8**, 235 (2013).

[92] (a) F. Tuinstra and J. L. Koenig, "Raman Spectrum of Graphite", *J. Chem. Phys.* **53**, 1126 (1970); (b) F. Tuinstra and J. L. Koenig, "Characterization of Graphite Fiber Surfaces with Raman Spectroscopy", *J. Comp. Mater.* **4**, 492 (1970).

[93] J.-B. Wu, M.-L. Lin, X. Cong, H.-N. Liu and P.-H. Tan, "Raman Spectroscopy of Graphene-based Materials and Its Applications in Related Devices", *Chem. Soc. Rev.* **47**, 1822 (2018).

[94] Y. Kawashima and G. Katagiri, "Fundamentals, Overtones, and Combinations in the Raman Spectrum of Graphite", *Phys. Rev. B* **52**, 10053 (1995).

[95] R. J. Nemanich and S. A. Solin, "First- and Second-Order Raman Scattering from Finite-Size Crystals of Graphite", *Phys. Rev. B* **20**, 392 (1979).

[96] M. S. Dresselhaus and G. Dresselhaus, “Intercalation Compounds of Graphite”, *Adv. Phys.* **51**, 1 (2002).

[97] (a) P.-H. Tan, S. Dimovski and Y. Gogotsi, “Raman Scattering of Non–Planar Graphite: Arched Edges, Polyhedral Crystals, Whiskers and Cones”, *Phil. Trans. R. Soc. Lond. A*, **362**, 2289 (2004); (b) P.-H. Tan, C.-Y. Hu, J. Dong, W.-C. Shen and B.-F. Zhang, “Polarization Properties, High-Order Raman Spectra, and Frequency Asymmetry between Stokes and Anti-Stokes Scattering of Raman Modes in a Graphite Whisker”, *Phys. Rev. B* **64**, 214301 (2001); (c) P.-H. Tan, J. Zhang, X.-C. Wang, G.-Y. Zhang and E.-G. Wang, “Raman Scattering from an Individual Tubular Graphite Cone”, *Carbon*, **5**, 1116 (2007).

[98] Y. Wang, D. C. Alsmeyer and R. L. McCreery, “Raman Spectroscopy of Carbon Materials: Structural Basis of Observed Spectra”, *Chem. Mater.* **2**, 557 (1990).

[99] N. Shimodaira and A. Masui, “Raman Spectroscopic Investigations of Activated Carbon Materials”, *J. Appl. Phys.* **92**, 902 (2002).

[100] L. M. Malard, M. A. Pimenta, G. Dresselhaus and M. S. Dresselhaus, “Raman Spectroscopy in Graphene”, *Phys. Rep.* **473**, 51 (2009).

[101] C. Casiraghi, A. Hartschuh, H. Qian, S. Piscanec, C. Georgi, A. Fasoli, K. S. Novoselov, D. M. Basko and A. C. Ferrari, “Raman Spectroscopy of Graphene Edges”, *Nano Lett.* **9**, 1433 (2009).

[102] (a) P. Bindu and S. Thomas, “Estimation of Lattice Strain in ZnO Nanoparticles: X-Ray Peak Profile Analysis”, *J. Theor. Appl. Phys.* **8**, 123 (2014); (b) A. F. Abdulrahman, S. M. Ahmed, N. M. Ahmed and M. A. Almessiere, “Fabrication, Characterization of ZnO Nanorods on the Flexible Substrate (Kapton Tape) via Chemical Bath Deposition for UV Photodetector Applications”, *AIP Conf. Proc.* **1875**, 020004 (2017); (c) J. Y. Howe, C. J. Rawn, L. E. Jones and H. Ow, “Improved Crystallographic Data for Graphite”, *Powder Diffr.* **18**, 150 (2003); (d) H. E. Swanson, H. F. McMurdie, M. C. Morris and E. H. Evans, Standard X-Ray Diffraction Powder Patterns, National Bureau of Standards Monograph 25-Section 5, Washington D. C., USA, 1967; (e) S.-J. Mu, Y.-C. Su, L.-H. Xiao, S.-D. Liu, T. Hu and H.-B. Tang, “X-Ray Diffraction Pattern of Graphite Oxide”, *Chin. Phys. Lett.* **30**, 096101 (2013); (f) Y.-G. Sun, J. Tang, K. Zhang, J.-S. Yuan, J. Li and D.-M. Zhu, K. Ozawa and L.-C. Qin, “Comparison of Reduction Products from Graphite Oxide and Graphene Oxide for Anode Applications in Lithium-Ion Batteries and Sodium-ion Batteries”, *Nanoscale*, **9**, 2585 (2017); (g) I. Y. Jeon, S. H. Shin, S. M. Jung, H. J. Choi, J. Xu and J. B. Baek, “One-Pot Purification and Iodination of Waste Kish Graphite into High-Quality Electrocatalyst”, *Part. Part. Syst. Charact.* **34**, 1600426 (2017).

[103] R. P. Vidano, D. B. Fischbach, L. J. Willis and T. M. Lohr, “Observation of Raman Band Shifting with Excitation Wavelength for Carbons and Graphites”, *Solid State Commun.* **39**, 341 (1981).

[104] M. S. Dresselhaus, A. Jorio, M. Hofmann, G. Dresselhaus and R. Saito, “Perspectives on Carbon Nanotubes and Graphene Raman Spectroscopy”, *Nano Lett.* **10**, 751 (2010).

[105]A. Eckmann, A. Felten, A. Mishchenko, L. Britnell, R. Krupke, K. S. Novoselov and C. Casiraghi, “Probing the Nature of Defects in Graphene by Raman Spectroscopy”, *Nano. Lett.* **12**, 3925 (2012).

[106](a) P.-H. Tan, W.-P. Han, W.-J. Zhao, Z.-H. Wu, K. Chang, H. Wang, Y.-F. Wang, N. Bonini, N. Marzari, N. Pugno, G. Savini, A. Lombardo and A. C. Ferrari, “The Shear Mode of Multilayer Graphene”, *Nat. Mater.* **11**, 294 (2012); (b) C. Cong and T. Yu, “Enhanced Ultra-Low-Frequency Interlayer Shear Modes in Folded Graphene Layers”, *Nat. Commun.* **5**, 4709 (2014).

[107]E. H. Martins Ferreira, M. V. O. Moutinho, F. Stavale, M. M. Lucchese, R. B. Capaz, C. A. Achete and A. Jorio, “Evolution of the Raman Spectra from Single-, Few-, and Many-layer Graphene with Increasing Disorder”, *Phys. Rev. B* **82**, 125429 (2010).

[108](a) J. Hong, M. K. Park, E.-J. Lee, D. Lee, D.-S. Hwang and S. Ryu, “Origin of New Broad Raman D and G peaks in Annealed Graphene”, *Sci. Rep.* **3**, 2700 (2013); (b) I. A. Verzhbitskiy, M. D. Corato, A. Ruini, E. Molinari, A. Narita, Y. Hu, M. G. Schwab, M. Bruna, D. Yoon, S. Milana, X. Feng, K. Müllen, A. C. Ferrari, C. Casiraghi and D. Prezzi, “Raman Fingerprints of Atomically Precise Graphene Nanoribbons”, *Nano Lett.* **16**, 3442 (2016).

[109]A. Sadezky, H. Muckenhuber, H. Grothe, R. Niessner and U. Pöschl, “Raman Microspectroscopy of Soot and Related Carbonaceous Materials: Spectral Analysis and Structural Information”, *Carbon*, **43**, 1731 (2005).

[110]Z. Luo, C. Cong, J. Zhang, Q. Xiong and T. Yu, “The Origin of Sub-bands in the Raman D-band of Graphene”, *Carbon*, **50**, 4252 (2012).

[111]S. Piscanec, M. Lazzeri, F. Mauri, A. C. Ferrari and J. Robertson, “Kohn Anomalies and Electron-Phonon Interactions in Graphite”, *Phys. Rev. Lett.* **93**, 185503 (2004).

[112]M. J. Matthews, M. A. Pimenta, G. Dresselhaus, M. S. Dresselhaus and M. Endo, “Origin of Dispersive Effects of the Raman D Band in Carbon Materials”, *Phys. Rev. B* **59**, R6585 (1999).

[113]C. Cong, T. Yu and H. Wang, “Raman Study on the G Mode of Graphene for Determination of Edge Orientation”, *ACS Nano*, **4**, 3175 (2010).

[114]X.-R. Wang and H.-J. Dai, “Etching and Narrowing of Graphene from the Edges”, *Nat. Chem.* **2**, 661 (2010).

[115]L. Yang, M. L. Cohen and S. G. Louie, “Excitonic Effects in the Optical Spectra of Graphene Nanoribbons”, *Nano Lett.* **7**, 3112 (2007).

[116]R. Denk, M. Hohage, P. Zeppenfeld, J. Cai, C. A. Pignedoli, H. Söde, R. Fasel, X. Feng, K. Müllen, S. Wang, D. Prezzi, A. Ferretti, A. Ruini, E. Molinari and P. Ruffieux, “Exciton-dominated Optical Response of Ultra-Narrow Graphene Nanoribbons”, *Nat. Commun.* **5**, 4253 (2014).

[117]I. Pócsik, M. Hundhausen, M. Koós and L. Ley, “Origin of the D Peak in the Raman Spectrum of Microcrystalline Graphite”, *J. Non-Cryst. Solids* **1083**, 227 (1998).

[118]A. K. Sooda, R. Gupta and S. A. Asher, “Origin of the Unusual Dependence of Raman D Band on Excitation Wavelength in Graphite-like Materials”, *J. Appl. Phys.* **90**, 4494 (2001).

[119]A. C. Ferrari and J. Robertson, “Interpretation of Raman Spectra of Disordered and Amorphous Carbon”, *Phys. Rev. B* **61**, 14095 (2000).

[120]G. Katagiri, H. Ishida and A. Ishitani, “Raman Spectra of Graphite Edge Planes”, *Carbon*, **26**, 565 (1988).

[121](a) M. S. Dresselhaus, A. Jorio, A. G. Souza Filho and R. Saito, “Defect Characterization in Graphene and Carbon Nanotubes using Raman Spectroscopy”, *Phil. Trans. R. Soc. A* **368**, 5355 (2010); (b) A. C Ferrari and J. Robertson, “Resonant Raman Spectroscopy of Disordered, Amorphous, and Diamondlike Carbon”, *Phys. Rev. B* **64**, 075414 (2001).

[122](a) R. Al-Jishi and G. Dresselhaus, “Lattice-Dynamical Model for Graphite”, *Phys. Rev. B* **26**, 4514 (1982); (b) P. Lespade, R. Al-Jishi and M. S. Dresselhaus, “Model for Raman Scattering from Incompletely Graphitized Carbons”, *Carbon*, **20**, 427 (1982).

[123]T. P. Mernagh, R. P. Cooney and R. A. Johnson, “Raman Spectra of Graphon Carbon Black”, *Carbon*, **22**, 39 (1984).

[124]L. G. Cançado, K. Takai, T. Enoki, M. Endo, Y. A. Kim, H. Mizusaki, A. Jorio, L. N. Coelho, R. Magalhães-Paniago and M. A. Pimenta, “General Equation for the Determination of the Crystallite Size L_a of Nanographite by Raman Spectroscopy”, *Appl. Phys. Lett.* **88**, 163106 (2006).

[125](a) A. Jorio, M. M. Lucchese, F. Stavale and C. A. Achete, “Raman spectroscopy Study of Ar^+ Bombardment in Highly Oriented Pyrolytic Graphite”, *Phys. Satus. Solidi (b)* **246**, 2689 (2009); (b) A. Jorio, M. M. Lucchese, F. Stavale, E. H. Martins Ferreira, M. V. O. Moutinho, R. B. Capaz and C. A. Achete, “Raman Study of Ion-Induced Defects in *N*-Layer Graphene”, *J. Phys. Condens. Matter* **22**, 334204 (2010); (c) M. M. Lucchese, F. Stavale, E. H. Martins Ferreira, C. Vilani, M. V. O. Moutinho, R. B. Capaz, C. A. Achete and A. Jorio, “Quantifying Ion-Induced Defects and Raman Relaxation Length in Graphene”, *Carbon*, **48**, 1592 (2010); (d) L. G. Cançado, A. Jorio, E. H. Martins Ferreira, F. Stavale, C. A. Achete, R. B. Capaz, M. V. O. Moutinho, A. Lombardo, T. S. Kulmala and A. C. Ferrari, “Quantifying Defects in Graphene via Raman Spectroscopy at Different Excitation Energies”, *Nano. Lett.* **11**, 3190 (2011).

[126]B.-L. Huang, M.-C. Chang and C.-Y. Mou, “Density of States in Graphene in the Presence of Strong Point Defects”, *Phys. Rev. B* **82**, 155462 (2010).

[127](a) V. Adamyan and V. Zavalniuk, “Phonons in Graphene with Point Defects”, *J. Phys.: Condens. Matter* **23**, 015402 (2011); (b) D. L. Nika and A. A. Balandin, “Phonons and Thermal Transport in Graphene and Graphene-related Materials”, *Rep. Prog. Phys.* **80**, 036502 (2017).

[128](a) S. Baroni, S. de Gironcoli, A. Dal Corso and P. Giannozzi, “Phonon and Related Crystal Properties from Density-Functional Perturbation Theory”, *Rev. Mod. Phys.* **73**, 515 (2001);

(b) P. Giannozzi, *et al.*, "Quantum ESPRESSO: A Modular and Open-source Software Project for Quantum Simulation of Materials", *J. Phys.: Condens. Matter* **21**, 395502 (2009); (c) P. Giannozzi, *et al.*, "Advanced Capacities for Materials Modelling with Quantum ESPRESSO", *J. Phys.: Condens. Matter* **29**, 465901 (2017).

[129] K. L. VanAken, C. R. Pérez, Y. Oh, M. Beidaghi, Y. J. Jeong, M. F. Islam and Y. Gogotsi, "High Rate Capacitive Performance of Single-Walled Carbon Nanotube Aerogels", *Nano Energy* **15**, 662 (2015).

[130] S. R. Meier, "Reflectance and Scattering Properties of Highly Absorbing Black Appliqués Over a Broadband Spectral Region", *Appl. Opt.* **40**, 6260 (2000).

[131] E. B. Barros, N. S. Demir, A. G. Souza Filho, J. Mendes Filho, A. Jorio, G. Dresselhaus and M. S. Dresselhaus, "Raman Spectroscopy of Graphitic Foam", *Phys. Rev. B* **71**, 165422 (2005).

[132] A. C. Ferrari, J. C. Meyer, V. Scardaci, C. Casiraghi, M. Lazzeri, F. Mauri, S. Piscanec, D. Jiang, K. S. Novoselov, S. Roth and A. K. Geim, "Raman Spectrum of Graphene and Graphene Layers", *Phys. Rev. Lett.* **97**, 187401 (2006).

[133] (a) A. Jorio, R. Saito, J. H. Hafner, C. M. Lieber, M. Hunter, T. McClure, G. Dresselhaus and M. S. Dresselhaus, "Structural (n, m) Determination of Isolated Single-Wall Carbon Nanotubes by Resonant Raman Scattering", *Phys. Rev. Lett.* **86**, 1118 (2001); (b) A. Jorio, A. G. Souza Filho, G. Dresselhaus, M. S. Dresselhaus, A. K. Swan, M. S. Ünlü, B. B. Goldberg, M. A. Pimenta, J. H. Hafner, C. M. Lieber, and R. Saito, "*G*-band Resonant Raman Study of 62 Isolated Single-Wall Carbon Nanotubes", *Phys. Rev. B* **65**, 155412 (2002).

[134] (a) P. Chamorro-Posada, J. Vázquez-Cabo, Ó. Rubiños-López, J. Martín-Gil, S. Hernández-Navarro, P. Martín-Ramos, F. M. Sánchez-Arévalo, A. V. Tamashausky, C. Merino-Sánchez and R. C. Dante, "THz TDS Study of Several sp^2 Carbon Materials: Graphite, needle Coke and Graphene Oxides", *Carbon*, **98**, 484 (2016); (b) T. Kampfrath, L. Perfetti, F. Schapper, C. Frischkorn and M. Wolf, "Strongly Coupled Optical Phonons in the Ultrafast Dynamics of the Electronic Energy and Current Relaxation in Graphite", *Phys. Rev. Lett.* **95**, 187403 (2005); (c) M. Scheuch, T. Kampfrath, M. Wolf, K. von Volkmann, C. Frischkorn and L. Perfetti, "Temperature Dependence of Ultrafast Phonon Dynamics in Graphite", *Appl. Phys. Lett.* **99**, 211908 (2011).

[135] (a) H.-N. Liu, X. Cong, M.-L. Lin and P.-H. Tan, "The Intrinsic Temperature-Dependent Raman Spectra of Graphite in the Temperature Range from 4 K to 1000 K", *Carbon*, **152**, 451 (2019); (b) P.-H. Tan, Y.-M. Deng and Q. Zhao, "Temperature-Dependent Raman Spectra and Anomalous Raman Phenomenon of Highly Oriented Pyrolytic graphite", *Phys. Rev. B* **58**, 5435 (1998); (c) P.-H. Tan, Y.-M. Deng, Q. Zhao and W.-C. Cheng, "The Intrinsic Temperature Effect of the Raman Spectra of Graphite", *Appl. Phys. Lett.* **74**, 1818 (1999).

[136] (a) P. V. Huong, R. Cavagnat, P. M. Ajayan and O. Stephan, "Temperature-Dependent Vibrational Spectra of Carbon Nanotubes", *Phys. Rev. B* **51**, 10048 (1995); (b) N. R.

Raravikar, P. Keblinski, A. M. Rao, M. S. Dresselhaus, L. S. Schadler and P. M. Ajayan, "Temperature Dependence of Radial Breathing Mode Raman Frequency of Single-Wall Carbon Nanotubes", *Phys. Rev. B* **66**, 235424 (2002); (c) F. Huang, K.-T. Yue, P.-H. Tan, S.-L. Zhang, Z. Shi, X. Zhou and Z. Gu, "Temperature Dependence of the Raman Spectra of Carbon Nanotubes", *J. Appl. Phys.* **84**, 4022 (1998); (d) H.-D. Li, K.-T. Yue, Z.-L. Lian, Y. Zhan, L.-X. Zhou, S.-L. Zhang, Z.-J. Shi, Z.-N. Gu, B.-B. Liu, R.-S. Yang, H.-B. Yang, G.-T. Zou, Y. Zhang and S. Iijima, "Temperature Dependence of the Raman Spectra of Single-Wall Carbon Nanotubes", *Appl. Phys. Lett.* **76**, 2053 (2000); (e) M. N. Iliev, A. P. Litvinchuk, S. Arepalli, P. Nikolaev and C. D. Scott, "Fine Structure of the Low-Frequency Raman Phonon Bands of Single-Wall Carbon Nanotubes", *Chem. Phys. Lett.* **316**, 217 (2000); (f) L. Song, W. Ma, Y. Ren, W. Zhou, S.-S. Xie, T.-H. Tan and L. Sun, "Temperature Dependent Raman Spectra of Single-walled Carbon Nanotube Rings", *Appl. Phys. Lett.* **92**, 121905 (2008); (g) Z. Zhou, X. Dou, L. Ci, L. Song, D. Liu, Y. Gao, J. Wang, L. Liu, W. Zhou, S.-S. Xie and D. Wan, "Temperature Dependence of the Raman Spectra of Individual Carbon Nanotube", *J. Phys. Chem. B* **110**, 1206 (2006); (h) L.-J. Ci, Z.-P. Zhou, L. Song, X.-Q. Yan, D.-F. Liu, H.-J. Yuan, Y. Gao, J.-X. Wang, L.-F. Liu, W.-Y. Zhou, G. Wang and S.-S. Xie, "Temperature Dependence of Resonant Raman Scattering in Double-Wall Carbon Nanotubes", *Appl. Phys. Lett.* **82**, 3098 (2003); (i) Y. Ouyang and Y. Fang, "Temperature Dependence of the Raman Spectra of Carbon Nanotubes with 1064 nm Excitation", *Physica E* **24**, 222 (2004); (j) N. D. Sharma, J. Singh and A. Vijay, "Temperature Dependent Raman Investigation of Multiwall Carbon Nanotubes", *J. Appl. Phys.* **123**, 155101 (2018); (k) X. Zhang, F. Yang, D. Zhao, L. Cai, P.-S. Luan, Q. Zhang, W.-B. Zhou, N. Zhang, Q.-X. Fan, Y.-C. Wang, H.-P. Liu, W.-Y. Zhou and S.-S. Xie, "Temperature Dependent Raman Spectra of Isolated Suspended Single-Walled Carbon Nanotubes", *Nanoscale*, **6**, 3949 (2014).

[137] http://archive.synchrotron.org.au/aussyncbeamlines/ftir/introduction.

[138] M. T. Islam, R. M. Trevoraha, D. R. T. Appadoo, S. P. Best, C. T. Chantlera, "Methods and Methodology for FTIR Spectral Correction of Channel Spectra and Uncertainty, Applied to Ferrocene", *Spectrochimica Acta Part A: Mol. and Biomol. Spectrosc.* **177**, 86 (2017).

[139] (a) R. J. Nemanich, G. Lucovsky and S. A. Solin, "Infrared Active Optical Vibrations in Graphite", *Solid State Commun.* **23**, 117 (1977); (b) G. S. Jeon and G. D. Mahan, "Microscopic Origin of Infrared Activity of Graphite", *Phys. Rev. B* **71**, 184306 (2005); (c) M. Manzardo, E. Cappelluti, E. van. Heumen and A. B. Kuzmenko, "Infrared Phonon Activity in Pristine Graphite", *Phys. Rev. B* **86**, 054302 (2012).

[140] (a) R. Saito, A. Grüneis, Ge. G. Samsonidze, V. W. Brar, G. Dresselhaus, M. S. Dresselhaus, A. Jorio, L. G. Cançado, C. Fantini and M. A. Pimenta, "Double Resonance Raman Spectroscopy of Single-Wall Carbon Nanotubes", *New J. Phys.* **5**, 157 (2003); (b) J. Maultzsch, H. Telg, S. Reich and C. Thomsen, "Radial Breathing Mode of Single-Walled Carbon Nanotubes: Optical Transition Energies and Chiral-index Assignment", *Phys. Rev. B* **72**, 205438 (2005); (c) V. N. Popov and P. Lambin, "Radius and Chirality Dependence of

the Radial Breathing Mode and the G-Band Phonon Modes of Single-Walled Carbon Nanotubes", *Phys. Rev. B* **73**, 085407 (2006); (d) C. Tyborski, A. Vierck, R. Narula, V. N. Popov and J. Maultzsch, "Double-Resonant Raman Scattering with Optical and Acoustic Phonons in Carbon Nanotubes", *Phys. Rev. B* **97**, 214306 (2018).

[141](a) U. Kulhmann, H. Jantolljak, N. Pfänder, P. Bernier, C. Journet and C. Thomsen, "Infrared Active Phonons in Single-Walled Carbon Nanotubes", *Chem. Phys. Lett.* **294**, 237 (1998); (b) U. J. Kim, X. M. Liu, C. A. Furtado, G. Chen, R. Saito, J. Jiang, M. S. Dresselhaus and P. C. Eklund, "Infrared-Active Vibrational Modes of Single-Walled Carbon Nanotubes", *Phys. Rev. Lett.* **95**, 157402 (2005); (c) J. L. Bantignies, J. L. Sauvajol, A. Rahmani and E. Flahaut, "Infrared-Active Phonons in Carbon Nanotubes", *Phys. Rev. B* **74**, 195425 (2006); (d) K. Sbai, A. Rahmani, H. Chadli, J.-L. Bantignies, P. Hermet and J.-L. Sauvajol, "Infrared Spectroscopy of Single-Walled Carbon Nanotubes", *J. Phys. Chem. B* **110**, 12388 (2006); (e) S. E. Rodil, "Infrared Spectra of Amorphous Carbon Based Materials", *Diam. Relat. Mater*. **14**, 1262 (2005).

[142](a) O. E. Alon, "Number of Raman- and Infrared-Active Vibrations in Single-Walled Carbon Nanotubes", *Phys. Rev. B* **63**, 201403R (2001); (b) O. E. Alon, "From Spatial Symmetry to Vibrational Spectroscopy of Single-Walled Nanotubes", *J. Phys.: Condens. Matter* **15**, S2489 (2003); (c) E. B. Barros, A. Jorio, G. G. Samsonidze, R. B. Capaz, A. G. Souza Filho, J. M. Filho, G. Dresselhaus and M. S. Dresselhaus, "Review on the Symmetry-Related Properties of Carbon Nanotubes", *Phys. Rep.* **431**, 261 (2006).

[143](a) C. Zhang, D. M. Dabbs, L.-M. Liu, I. A. Aksay, R. Car and A. Selloni, "Combined Effects of Functional Groups, Lattice Defects, and Edges in the Infrared Spectra of Graphene Oxide", *J. Phys. Chem. C* **119**, 18167 (2015); (b) T. Xing, L.-H. Li, L. Hou, X. Hu, S. Zhou, R. Peter, M. Petravic and Y. Chen, "Disorder in Ball-milled Graphite Revealed by Raman Spectroscopy", *Carbon*, **57**, 515 (2013).

[144](a) L.-B. Liang, J. Zhang, B. G. Sumpter, Q.-H. Tan, P.-H. Tan and V. Meunier, "Low-Frequency Shear and Layer-Breathing Modes in Raman Scattering of Two Dimensional Materials", *ACS Nano* **11**, 11777 (2017); (b) G. Dolling and B. N. Brockhouse, "Lattice Vibrations in Pyrolitic Graphite", *Phys. Rev.* **128**, 1120 (1962); (c) M. S. Dresselhaus, G. Dresselhaus, P. C. Eklund and D. D. L. Chung, "Lattice Vibrations in Graphite and Intercalation Compounds in Graphite", *Mat. Sci. Eng*. **31**, 141 (1977); (d) J.-Z. Shang, C.-X. Cong, J. Zhang, Q.-H. Xiong, G. G. Gurzadyan and T. Yu, "Observation of Low-Wavenumber Out-of-Plane Optical Phonon in Few-Layer Graphene", *J. Raman Spectrosc.* **44**, 70 (2013).

[145](a) J.-J. Wang, M.-Y. Zhu, R.A. Outlaw, X, Zhao, D. M. Manos, B. C. Holloway and V. P. Mammana, "Free-Standing Subnanometer Graphite Sheets", *Appl. Phys. Lett.* **85**, 1265 (2004); (b) J. Zhou and J.-M. Dong, "Vibrational Property and Raman Spectrum of Carbon Nanoribbon", *Appl. Phys. Lett.* **91**, 173108 (2007); (c) F. Yu, H.-Q. Zhou, Z.-X. Zhang, D.-S. Tang, M.-J. Chen, H.-C. Yang, G. Wang, H.-F. Yang, C.-Z. Gu and L.-F. Sun, "Experimental Observation of Radial Breathing-Like Mode of Graphene Nanoribbons",

Appl. Phys. Lett. **100**, 101904 (2012); (d) J.-K. Lee, K. P. S. S. Hembram, Y. Park, S.-G. Lee, J.-G. Kim, W. Lee and D. J. Moon, "Raman Radial Mode Revealed from Curved Graphene", *J. Phys. Chem. Lett.* **8**, 2597 (2017).

[146] N. Bonini, M. Lazzeri, N. Marzari and F. Mauri, "Phonon Anharmonicities in Graphite and Graphene", *Phys. Rev. Lett.* **99**, 176802 (2007).

[147] A. Ugawa, A. G. Rinzler and D. B. Tanner, "Far-Infrared Gaps in Single-Wall Carbon Nanotubes", *Phys. Rev. B* **60**, R11305 (1999).

[148] P. Giura, N. Bonini, G. Creff, J. B. Brubach, P. Roy and M. Lazzeri, "Temperature Evolution of Infrared- and Raman-Active Phonons in Graphite", *Phys. Rev. B* **86**, 121404R (2012).

[149] (a) N. J. Everall, J. Lumsdon and D. J. Christopher, "The Effect of Laser-Induced Heating Upon the Vibrational Raman Spectra of Graphites and Carbon Fibres", *Carbon* **29**, 133 (1991); (b) I. Chatzakis, H. Yan, D. Song, S. Berciaud and T. F. Heinz, "Temperature Dependence of the Anharmonic Decay of Optical Phonons in Carbon Nanotubes and Graphite", *Phys. Rev. B* **83**, 205411 (2011); (c) I. Calizo, A. A. Balandin, W. Bao, F. Miao and C. N. Lau, "Temperature Dependence of the Raman Spectra of Graphene and Graphene Multilayers", *Nano Lett.* **7**, 2645 (2007); (d) G. Montagnac, R. Caracas, E. Bobocioiu, F. Vittoz and B. Reynard, "Anharmonicity of Graphite from UV Raman Spectroscopy to 2700 K", *Carbon* **54**, 68 (2013).

[150] (a) Y.-Y. Zhang, L.-M. Xie, J. Zhang, Z.-Y. Wu and Z.-F. Liu, "Temperature Coefficients of Raman Frequency of Individual Single-Walled Carbon Nanotubes", *J. Phys. Chem. C* **111**, 14031 (2007); (b) M. Paillet, T. Michel, J. C. Meyer, V. N. Popov, L. Henrard, S. Roth and J. L. Sauvajol, "Raman Active Phonons of Identified Semiconducting Single-Walled Carbon Nanotubes", *Phys. Rev. Lett.* **96**, 257401 (2006); (c) A. Jorio, C. Fantini, M. S. S. Dantas, M. A. Pimenta, A. G. Souza Filho, Ge. G. Samsonidze, V. W. Brar, G. Dresselhaus, M. S. Dresselhaus, M. S. Ünlü, B. B. Goldberg and R. Saito, "Linewidth of the Raman Features of Individual Single-Wall Carbon Nanotubes", *Phys. Rev. B* **66**, 115411 (2002).

[151] C. Zhang, X. Yan, L. Wang, Y. Kitahama, Y. Ozaki and Y. Fang, "The Effect of Temperature on the Resonance of the Interband Transition Energy in Single-Walled Carbon Nanotube with Excitation Laser Energy by Raman Spectroscopy", *Appl. Phys. Lett.* **103**, 231902 (2013).

[152] O. Dubay and G. Kresse, "Accurate Density Functional Calculations for the Phonon Dispersion Relations of Graphite Layer and Carbon Nanotubes", *Phys. Rev. B* **67**, 035401 (2003).

[153] M. Lazzeri, S. Piscanec, F. Mauri, A. C. Ferrari and J. Robertson, "Phonon Linewidths and Electron-Phonon Coupling in Graphite and Carbon Nanotubes", *Phys. Rev. B* **73**, 155426 (2006).

[154] L. M. Lepodise, J. Horvat and R. A. Lewis, "Terahertz Spectroscopy of 2,4-Dinitrotoluene

over a Wide Temperature Range (7–245 K)", *J. Phys. Chem. A* **119**, 263 (2015).

[155] G. A. Slack, "Anisotropic Thermal Conductivity of Pyrolytic Graphite", *Phys. Rev.* **127**, 694 (1962).

[156] (a) A. M. Rao, J. Chen, E. Richter, U. Schlecht, P. C. Eklund, R. C. Haddon, U. D. Venkateswaran, Y.-K. Kwon and D. Tomanek, "Effect of van der Waals Interactions on the Raman Modes in Single Walled Carbon Nanotubes", *Phys. Rev. Lett.* **86**, 3895 (2001); (b) A. M. Rao, P. C. Eklund, S. Bandow, A. Thess and R. E. Smalley, "Evidence for Charge Transfer in Doped Carbon Nanotube Bundles from Raman Scattering", *Nature* **388**, 257 (1997); (c) C. Thomsen, S. Reich, A. R. Goñi, H. Jantoljak, P.M. Rafailov, I. Loa, K. Syassen, C. Journet and P. Bernier, "Intermolecular Interaction in Carbon Nanotube Ropes", *Phys. Stat. Sol. (b)* **215**, 435 (1999).

[157] (a) S. Sahoo, A. P. S. Gaur, M. Ahmadi, M. J.-F. Guinel and R. S. Katiyar, "Temperature-Dependent Raman Studies and Thermal Conductivity of Few-Layer MoS_2", *J. Phys. Chem. C* **117**, 9042 (2013); (b) S. Luo, X. Qi, H. Yao, X. Ren, Q. Chen and J. Zhong, "Temperature-Dependent Raman Responses of the Vapor-Deposited Tin Selenide Ultrathin Flakes", *J. Phys. Chem. C* **121**, 4674 (2017).

[158] M.-L. Lin, J.-B. Wu, X.-L. Liu and P.-H. Tan, "Probing the Shear and Layer Modes in Multilayer Graphene by Raman Spectroscopy", *J. Raman Spectrosc.* **49**, 19 (2018).

[159] P.-H. Tan, W.-P. Han, W.-J. Zhao, Z.-H. Wu, K. Chang, H. Wang, Y.-F. Wang, N. Bonini, N. Marzari, N. Pugno, G. Savini, A. Lombardo and A. C. Ferrari, "The Shear Mode of Multilayer Graphene", *Nat. Mater.* **11**, 294 (2012).

[160] C.-X. Cong and T. Yu, "Enhanced Ultra-Low-Frequency Interlayer Shear Modes in Folded Graphene Layers", *Nat. Commun.* **5**, 4709 (2014).

[161] (a) E. P. J. Parrott and J. A. Zeitler, "Terahertz Time-Domain and Low-Frequency Raman Spectroscopy of Organic Materials", *Appl. Spectrosc.* **69**, 1 (2015); (b) D. Bertoldo Menezes, A. Reyer, Y. Yüksel, B. Bertoldo Oliveira and M. Musso, "Introduction to Terahertz Raman Spectroscopy", *Spectrosc. Lett.* **51**, 438 (2018).

[162] J.-W. Jiang, H. Tang, B.-S. Wang and Z.-B. Su, "Raman and Infrared Properties and Layer Dependence of the Phonon Dispersions in Multilayered Graphene", *Phys. Rev. B* **77**, 235421 (2008).

[163] (a) S. K. Saha, U. V. Waghmare, H. R. Krishnamurthy and A. K. Sood, "Phonons in Few-Layer Graphene and Interplanar Interaction: A First-Principles Study", *Phys. Rev. B* **78**, 165421 (2008); (b) V. N. Popov and C. V. Alsenoy, "Low-Frequency Phonons of Few-Layer Graphene within a Tight-Binding Model", *Phys. Rev. B* **90**, 245429 (2014).

[164] C. S. Casari, A. Li Bassi, A. Baserga, L. Ravagnan, P. Piseri, C. Lenardi, M. Tommasini, A. Milani, D. Fazzi, C. E. Bottani and P. Milani, "Low-Frequency Modes in the Raman Spectrum of *sp-sp*^{2} Nanostructured Carbon", *Phys. Rev. B* **77**, 195444 (2008).

[165] C.-H. Lui, L. M. Malard, S. H. Kim, G. Lantz, F. E. Laverage, R. Saito and T. F. Heinz, "Observation of Layer-Breathing Mode Vibrations in Few-Layer Graphene through

Combination Raman Scattering", *Nano Lett.* **12**, 5339 (2012).

[166]R. He, T.-F. Chung, C. Delaney, C. Keiser, L.A. Jauregui, P. M. Shand, C. C. Chancey, Y. Wang, J. Bao and Y.-P. Chen, "Observation of Low Energy Raman Modes in Twisted Bilayer Graphene", *Nano Lett.* **13**, 3594 (2013).

[167]C.-H. Lui and T. F. Heinz, "Measurement of Layer Breathing Mode Vibration in Few-Layer Graphene", *Phys. Rev. B* **87**, 121404(R) (2013).

[168]C.-H. Lui, Z. Ye, C. Keiser, X. Xiao and R. He, "Temperature-Activated Layer-Breathing Vibrations in Few-Layer Graphene", *Nano Lett.* **14**, 4615 (2014).

[169]J. Wu, H. Xu, W. Mu, L. Xie, X. Ling, J. Kong, M. S. Dresselhaus and J. Zhang, "Observation of Low-Frequency Combination and Overtone Raman Mode in Misoriented Graphene", *J. Phys. Chem. C* **118**, 3636 (2014).

[170]M. S. Dresselhaus, G. Dresselhaus, J. C. Charlier and E. Hernández, "Electronic, Thermal and Mechanical Properties of Carbon Nanotubes", *Phil. Trans. R. Soc. Lond. A* **362**, 2065 (2004).

[171](a) P. Sheng, E. K. Sichel and J. Gittleman, "Fluctuation-Induced Tunneling Conduction in Carbon-Polyvinylchloride Composites", *Phys. Rev. Lett.* **40**, 1197 (1978); (b) P. Sheng, "Fluctuation-Induced Tunneling Conduction in Disordered Materials", *Phys. Rev. B* **21**, 2180 (1980); (c) H. Xie and P. Sheng, "Fluctuation-Induced Tunneling Conduction through Nanoconstrictions", *Phys. Rev. B* **79**, 165419 (2009).

[172](a) N. F. Mott, "Conduction in Glasses Containing Transition Metal Ions", *J. Non-Crystal Solid* **1**, 1 (1968); (b) N. F. Mott and E. A. Davis, *Electronic Process in Non-Crystalline Materials*, Clarendon Press, Oxford, UK, 1979.

[173]B. I. Shklovskii and A. L. Efros, *Electronic Properties of Doped Semiconductors*, Springer Verlag, Berlin, Germany, 1984.

[174]M. Pollak and B. I. Shklovskii, *Hopping Transport in Solids*, Elsevier Science Publishers B.V., Amsterdam, Netherlands, 1991.

[175]V. Ambegaokar, B. I. Halperin and J. S. Langer, "Hopping Conductivity in Disordered Systems", *Phys. Rev. B* **4**, 8 (1971).

[176]P. Stallinga, "Electronic Transport in Organic Materials: Comparison of Band Theory with Percolation/ (Variable Range) Hopping Theory", *Adv. Mater.* **23**, 3356 (2011).

[177]S. Ilani and Paul L. McEuen, "Electron Transport in Carbon Nanotubes", *Annu. Rev. Condens. Matter Phys.* **1**, 1 (2010).

[178]R. Bhatia, K. Kumari, R. Rani, A. Suri, U. Pahuja and D. Singh, "A Critical Review of Experimental Results on Low Temperature Charge Transport in Carbon Nanotubes-Based Composites", *Rev. in Phys.* **3**, 15 (2018).

[179]A. B. Kaiser, "Electronic Transport Properties of Conducting Polymers and Carbon Nanotubes", *Rep. Prog. Phys.* **64**, 1 (2001).

[180]A. B. Kaiser, G. Düsberg and S. Roth, "Heterogeneous Model for Conduction in Carbon Nanotubes", *Phys. Rev. B* **57**, 3 (1998).

[181]M. Salvato, M. Cirillo, M. Lucci, S. Orlanducci, I. Ottaviani, M. L. Terranova and F. Toschi, "Charge Transport and Tunneling in Single-Walled Carbon Nanotube Bundles", *Phys. Rev. Lett.* **101**, 246804 (2008).

[182]L. V. Govor, M. Goldbach, I. A. Bashmakov, I. B. Butylina and J. Parisi, "Electrical Properties of Self-Assembled Carbon Networks", *Phys. Rev. B* **62**, 3 (2000).

[183](a) M. S. Fuhrer, W. Holmes, P. L. Richards, P. Delaney, S. G. Louie and A. Zettl, "Nonlinear Transport and Localization in Single-Walled Carbon Nanotubes", *Synth. Met.* **103**, 2529 (1999); (b) V. Skakalová, A. B. Kaiser, Y.-S. Woo and S. Roth, "Electronic Transport in Carbon Nanotubes: From Individual Nanotubes to Thin and Thick Networks", *Phys. Rev. B* **74**, 085403 (2006).

[184](a) Y. Yosida and I. Oguro, "Variable Range Hopping Conduction in Multiwalled Carbon Nanotubes", *J. Appl. Phys.* **83**, 4985 (1998); (b) Y. Yosida and I. Oguro, "Variable Range Hopping Conduction in Bulk Samples Composed of Single-Walled Carbon Nanotubes", *J. Appl. Phys.* **86**, 999 (1999).

[185]Z. H. Khan, M. Husain, T. P. Perng, N. Salah and S. Habib, "Electrical Transport via Variable Range Hopping in an Individual Multi-Wall Carbon Nanotube", *J. Phys.: Condens. Matter*, **20**, 475207 (2008).

[186]R. Kamalakannan, K. Ganesan, S. Ilango, N. Thirumurugan, V. N. Singh, M. Kamruddin, B. R. Mehta and A. K. Tyagi, "The Role of Structural Defects on the Transport Properties of a Few-Walled Carbon Nanotube Networks", *Appl. Phys. Lett.* **98**, 192105 (2011).

[187]R. Fu, B. Zheng, J. Liu, M. S. Dresselhaus, G. Dresselhaus, J. H. Satcher, Jr. and T. F. Baumann, "The Fabrication and Characterization of Carbon Aerogels by Gelation and Supercritical Drying in Isopropanol", *Adv. Funct. Mat.* **13**, 558 (2003).

[188]K.-J. Zhang, A. Yadav, K. H. Kim, Y. Oh, M. F. Islam, C. Uher and K. P. Pipe, "Thermal and Electrical Transport in Ultralow Density Single-Walled Carbon Nanotube Networks", *Adv. Mater.* **25**, 2926 (2013).

[189]K. H. Kim, Y. Oh and M. F. Islam, "Mechanical and Thermal Management Characteristics of Ultrahigh Surface Area Single-Walled Carbon Nanotube Aerogels", *Adv. Funct. Mat.* **23**, 377 (2013).

[190](a) Z.-H. Wang, K. Ichimura, M. S. Dresselhaus and G. Dresselhaus, "Electronic Transport Properties of K_xC_{70} Thin Films", *Phys. Rev. B* **48**, 10657 (1993); (b) Z.-H. Wang, M. S. Dresselhaus, G. Dresselhaus, K.-A. Wang and P. C. Eklund, "Electronic Transport Properties of K_xC_{70} Thin Films. II", *Phys. Rev. B* **49**, 15891 (1994).

[191]S. Paschen, M. N. Bussac, L. Zuppiroli, E. Minder and B. Hilti, "Tunnel Junctions in a Polymer Composite", *J. Appl. Phys.* **78**, 3230 (1995).

[192](a) Y.-H. Lin, S. P. Chiu and J.-J. Lin, "Thermal Fluctuation-Induced Tunneling Conduction through Metal Nanowire Contacts", *Nanotechnology* **19**, 365201 (2008); (b) Y.-H. Lin and J.-J. Lin, "Fluctuation-Induced Tunneling Conduction through R_uO_2 Nanowire Contacts", *J. Appl. Phys.* **110**, 064318 (2011).

[193]A. Bajpai and A. K. Nigam, "Fluctuation-Induced Tunneling Conductance and Enhanced Magnetoresistance in Polycrystalline C_rO_2 and its Composites", *Phys. Rev. B* **75**, 064403 (2007).

[194]S. J. Konezny, C. Richter, R. C. Snoeberger, III, A. R. Parent, G. W. Brudvig, C. A. Schmuttenmaer and V. S. Batista, "Fluctuation-Induced Tunneling Conductivity in Nanoporous T_iO_2 Thin Films", *J. Phys. Chem. Lett.* **2**, 1931 (2011).

[195]Z. Wu, X. Chen, M. Zhang, L. Wang, Y. Han, S. Xu, T. Han, J. Lin, L. An, J. Wang, X. Cai, R. Shi, C. Cheng and N. Wang, "Fluctuation-Induced Tunneling Conduction in Iodine-Doped Bilayer Graphene", *J. Appl. Phys.* **123**, 244302 (2018).

[196]J. Marx, A. Brouschkin, S. Roth, D. Smazna, Y.K. Mishra, H. Wittich, K. Schulte, R. Adelung and B. Fiedler, "Fundamentals of the Temperature-Dependent Electrical Conductivity of a 3D Carbon Foam-Aerographite", *Synth. Met.* **235**, 145 (2018).

[197](a) J. E. Fischer, H. Dai, A. Thess, R. Lee, N. M. Hanjani, D. L. Dehaas and R. E. Smalley, "Metallic Resistivity in Crystalline Ropes of Single-Wall Carbon Nanotubes", *Phys. Rev. B* **55**, R4921 (1997); (b) M. Bockrath, D. H. Cobden, P. L. McEuen, N. G. Chopra, A. Zettl, A. Thess and R. E. Smalley, "Single-Electron Transport in Ropes of Carbon Nanotubes", *Science*, **275**, 1922 (1997).

[198](a) M. Bockrath, D. H. Cobden, J. Lu, A. G. Rinzler, R. E. Smalley, L. Balents and P. L. McEuen, "Luttinger-Liquid Behavior in Carbon Nanotubes", *Nature*, **397**, 598 (1999); (b) Z. Yao, H. W. Ch. Postma, L. Balents and C. Dekker, "Carbon Nanotube Intramolecular Junctions", *Nature*, **402**, 273 (1999); (c) M. Shiraishi and M. Ata, "Tomonaga-Luttinger-Liquid Behavior in Single-Walled Carbon Nanotube Networks", *Solid State Commun.* **127**, 215 (2003); (d) T. Tanaka, K.-I. Mori, E. Sano, B. Fugetsu and H.-W. Yu, "The Luttinger-Liquid Behavior in Single-Walled Carbon Nanotube Networks", *Physica E*, **44**, 997 (2012).

[199]E. Kymakis and G. A. J. Amaratunga, "Electrical Properties of Single-Wall Carbon Nanotube-Polymer Composite Films", *J. Appl. Phys.* **99**, 084302 (2006).

[200](a) A. B. Kaiser, "Systematic Conductivity Behavior in Conducting Polymers: Effects of Heterogeneous Disorder", *Adv. Mater.* **13**, 927 (2001); (b) A. N. Aleshin, "Polymer Nanofibers and Nanotubes: Charge Transport and Device Applications", *Adv. Mater.* **18**, 17 (2006).

[201](a) G. A. M. Reynolds, A. W. P. Fung, Z. H. Wang, M. S. Dresselhaus and R. W. Pekala, "Morphological Effects on the Transport and Magnetic Properties of Polymeric and Colloidal Carbon Aerogels", *Phys. Rev. B* **50**, 590 (1994); (b) H. Liu, H. S. Choe, Y. Chen, J. Suh, C. Ko, S. Tongay and J. Wu, "Variable Range Hopping Electric and Thermoelectric Transport in Anisotropic Black Phosphorus", *Appl. Phys. Lett.* **111**, 102101 (2017).

[202]D. Joung and S. I. Khondaker, "Efros-Shklovskii Variable-Range Hopping in Reduced Graphene Oxide Sheets of Varying Carbon sp^2 Fraction", *Phys. Rev. B* **86**, 235423 (2012).

[203](a) C. L. Kane, E. J. Mele, R. S. Lee, J. E. Fischer, P. Petit, H. Dai, A. Thess, R. E. Smalley, A. R. M. Verschueren, S. J. Tans and C. Dekker, "Temperature-Dependent Resistivity of

Single-Wall Carbon Nanotubes", *Europhys. Lett.* **41**, 683 (1998); (b) C. L. Kane and E. J. Mele, "Size, Shape, and Low Energy Electronic Structure of Carbon Nanotubes", *Phys. Rev. Lett.* **78**, 1932 (1997); (c) L. Balents and M. P. A. Fisher, "Correlation Effects in Carbon Nanotubes", *Phys. Rev. B* **55**, R11973 (1997); (d) Z. Yao, C. L. Kane and C. Dekker, "High-Field Electrical Transport in Single-Wall Carbon Nanotubes", *Phys. Rev. Lett.* **84**, 2941 (2000).

[204] C. Li, E. T. Thostenson and T.-W. Chou, "Dominant Role of Tunneling Resistance in the Electrical Conductivity of Carbon Nanotube–Based Composites", *Appl. Phys. Lett.* **91**, 213114 (2007).

[205] Y. Yu, G. Song and L. Sun, "Determinant Role of Tunneling Resistance in Electrical Conductivity of Polymer Composites Reinforced by Well Dispersed Carbon Nanotubes", *J. Appl. Phys.* **108**, 084319 (2010).

[206] (a) W.-S. Bao, S. A. Meguid, Z.-H. Zhu and M. J. Meguid, "Modeling Electrical Conductivities of Nanocomposites with Aligned Carbon Nanotubes", *Nanotechnology* **22**, 485704 (2011); (b) W.-S. Bao, S. A. Meguid, Z.-H. Zhu and G.-J. Weng, "Tunneling Resistance and Its Effect on the Electrical Conductivity of Carbon Nanotube Nanocomposites", *J. Appl. Phys.* **111**, 093726 (2012); (c) W.-S. Bao, S. A. Meguid, Z.-H. Zhu, Y. Pan and G.-J. Weng, "Effect of Carbon Nanotube Geometry Upon Tunneling Assisted Electrical Network in Nanocomposites", *J. Appl. Phys.* **113**, 234313 (2013).

[207] G. R. Fiuschau, S. Yoshikawa and R. E. Newnham, "Resistivities of Conductive Composites", *J. Appl. Phys.* **72**, 953 (1992).

[208] A. V. Kyrylyuk and P. van der Schoot, "Continuum Percolation of Carbon Nanotubes in Polymeric and Colloidal Media", *PNAS*, **105**, 11451 (2008).

[209] Z. Rubin, S. A. Sunshine, M. B. Heaney, I. Bloom and I. Balberg, "Critical Behavior of the Electrical Transport Properties in a Tunneling-Percolation System", *Phys. Rev. B* **59**, 12 (1999).

[210] D. Toker, D. Azulay, N. Shimoni, I. Balberg and O. Millo, "Tunneling and Percolation in Metal-Insulator Composite Materials", *Phys. Rev. B* **68**, 041403 (2003).

[211] S. Kirkpatrick, "Percolation and Conduction", *Rev. Mod. Phys.* **45**, 574 (1973).

[212] D. Stauffer and A. Aharony, *Introduction to Percolation Theory*-2nd revised ed., Taylor and Francis, London, UK, 2003.

[213] M. Sahimi, *Application of Percolation Theory*, Taylor and Francis, London, UK, 1994.

[214] C.-W. Nan, Y. Shen and J. Ma, "Physical Properties of Composites near Percolation", *Annu. Rev. Mater. Res.* **40**, 131 (2010).

[215] M. Pollak, "A Percolation Treatment of DC Hopping Conduction", *J. Non-Cryst. Solids* **11**, 1 (1972).

[216] Y. M. Strelniker, S. Havlin, R. Berkovits and A. Frydman, "Resistance Distribution in the Hopping Percolation Model", *Phys. Rev. E* **72**, 016121 (2005).

[217] H. P. Huinink, P. A. Bobbert, W. F. Pasveer and M. A. J. Michels, "Structure and

Conductivity of Clusters Generated by Variable-Range Hopping Percolation", *Phys. Rev. B* **73**, 224204 (2006).

[218] C. Gau, C.-Y. Kuo and H.-S. Ko, "Electron Tunneling in Carbon Nanotube Composites", *Nanotechnology*, **20**, 395705 (2009).

[219] X. Zeng, X. Xu, P. M. Shenai, E. Kovalev, C. Baudot, N. Mathews and Y. Zhao, "Characteristics of the Electrical Percolation in Carbon Nanotubes/Polymer Nanocomposites", *J. Phys. Chem. C*, **115**, 21685 (2011).

[220] M. S. Fuhrer, J. Nygråd, L. Shih, M. Forero, Y.-G. Yoon, M. S. C. Mazzoni, H. J. Choi, J. Ihm, S. G. Louie, A. Zettl and P. L. McEuen, "Crossed Nanotube Junctions", *Science* **288**, 494 (2000).

[221] (a) E. Burstein and S. Lundqvist (Ed.), *Tunneling Phenomenon in Solids*, Plenum Press, New York, NY, USA, 1969; (b) P. Esquinazi (Ed.), *Tunneling Systems in Amorphous and Crystalline Solids*, Springer, Berlin, Germany, 1998.

[222] (a) J. G. Simmons, "Generalized Formula for the Electric Tunnel Effect between Similar Electrodes Separated by a Thin Insulating Film", *J. Appl. Phys.* **34**, 1793 (1963); (b) J. G. Simmons, "Electric Tunnel Effect between Dissimilar Electrodes Separated by a Thin Insulating Film", *J. Appl. Phys.* **34**, 2581 (1963); (c) W. F. Brinkman, R. C. Dynes and J. M. Rowell, "Tunneling Conductance of Asymmetrical Barriers", *J. Appl. Phys.* **41**, 1915 (1970).

[223] (a) S. Gong, Z.-H. Zhu and E. I. Haddad, "Modeling Electrical Conductivity of Nanocomposites by Considering Carbon Nanotube Deformation at Nanotube Junctions", *J. Appl. Phys.* **114**, 074303 (2013); (b) S. Gong, Z.-H. Zhu, J. Li and S. A. Meguid, "Modeling and Characterization of Carbon Nanotube Agglomeration Effect on Electrical Conductivity of Carbon Nanotube Polymer Composites", *J. Appl. Phys.* **116**, 194306 (2014).

[224] J. Li, P.-C. Ma, W.-S. Chow, C.-K. To, B.-Z. Tang and J.-K. Kim, "Correlations Between Percolation Threshold, Dispersion State, and Aspect Ratio of Carbon Nanotubes", *Adv. Funct. Mat.* **17**, 3207 (2007).

[225] J. M. Benoit, B. Corraze and O. Chauvet, "Localization, Coulomb Interactions, and Electrical Heating in Single-Wall Carbon Nanotubes/Polymer Composites", *Phys. Rev. B* **65**, 24140501 (2002).

[226] M. B. Bryning, M. F. Islam, J. M. Kikkawa and A. G. Yodh, "Very Low Conductivity Threshold in Bulk Isotropic Single-Walled Carbon Nanotube–Epoxy Composites", *Adv. Mater.* **17**, 1186 (2005).

[227] F. Du, J. E. Fischer and K. I. Winey, "Effect of Nanotube Alignment on Percolation Conductivity in Carbon Nanotube/Polymer Composites", *Phys. Rev. B* **72**, 121404 (2005).

[228] S. I. White, B. A. DiDonna, M. Mu, T. C. Lubensky and K. I. Winey, "Simulations and Electrical Conductivity of Percolated Networks of Finite Rods with Various Degrees of Axial Alignment", *Phys. Rev. B* **79**, 024301 (2009).

[229] E. Kymakis and G. A. J. Amaratunga, "Electrical Properties of Single-Wall Carbon

Nanotube-Polymer Composite Films", *J. Appl. Phys.* **99**, 084302 (2006).

[230]R. Kamalakannan, K. Ganesan, S. IIango, N. Thirumurugan, V. N. Singh, M. Kamruddin, B. R. Mehta and A. K. Tyagi, "The Role of Structural Defects on the Transport Properties of a Few-Walled Carbon Nanotube Networks", *Appl. Phys. Lett.* **98**, 192105 (2011).

[231]R. Tamura and M. Tsukada, "Electronic Transport in Carbon Nanotube Junctions", *Solid State Commun.* **101**, 601 (1997).

[232]R. Saito, G. Dresselhaus, and M. S. Dresselhaus, *Physical Properties of Carbon Nanotubes*, Imperial College Press, London, UK, 1998.

[233]Y. Imry and R. Landauer, "Conductance Viewed as Transmission", *Rev. Mod. Phys.* **71**, S306 (1999).

[234]A. Buldum and J.-P. Lu, "Contact Resistance Between Carbon Nanotubes", *Phys. Rev. B* **63**, 161403 (2001).

[235]P. E. Lyons, S. De, F. Blighe, V. Nicolosi, L. F. C. Pereira, M. S. Ferreira and J. N. Coleman, "The Relationship Between Network Morphology and Conductivity in Nanotube Films", *J. Appl. Phys.* **104**, 044302 (2008).

[236]Y. R. Lai, K.-F. Yu, Y.-H. Lin, J.-C. Wu and J.-J. Lin, "Observation of Fluctuation-Induced Tunneling Conduction in Micrometer-Sized Tunnel Junctions", *AIP Adv.* **2**, 032155 (2012).

[237]T. R. N. Kutty and S. Ezhilvalavan, "The Role of Silica in Enhancing the Nonlinearity Coefficients by Modifying the Trap States of Zinc Oxide Ceramic Varistors", *J. Phys. D.* **29**, 809 (1996).

[238]M. Wei, C.-F. Li, X.-R. Deng and H. Deng, "Surface Work Function of Transparent Conductive ZnO Films", *Energy Procedia* **16**, 76 (2012).

[239]I. M. Seró, F. F. Santiago, B. Denier, J. Bisquert, R. T. Zaera, J. Elias and C. L. Clément, "Determination of Carrier Density of ZnO Nanowires by Electrochemical Techniques", *Appl. Phys. Lett.* **89**, 203117 (2006).

[240]K. D. Nam, S. K. Kwak, J. M. Lee, K. D. Nam, S. K. Kwak and J. M. Lee, "Synthesis of ZnO Nanorods by the Thermal Reduction Process of a Mixture of ZnO and Al Powder", *Cryst. Res. Technol.* **46**, 1323 (2011).

[241]L. J. Brillson and Y.-C. Lu, "ZnO Schottky Barriers and Ohmic Contacts", *J. Appl. Phys.* **109**, 121301 (2011).

[242]M. F. Islam, E. Rojas, D. M. Bergey, A. T. Johnson and A. G. Arjun, "High Weight Fraction Surfactant Solubilization of Single-Wall Carbon Nanotubes in Water", *Nano Lett.* **3**, 269 2003.

[243]S. Wang, Z. Liang, B. Wang and C. Zhang, "Statistical Characterization of Single-Wall Carbon Nanotube Length Distribution", *Nanotechnology*, **17**, 634 (2006).

[244]S. Dehghani and M. K. Moravvej-Farshi, "Temperature Dependence of Electrical Resistance of Individual Carbon Nanotubes and Carbon Nanotubes Network", *Mod. Phys. Lett. B* **26**, 1250136 (2012).

[245]T. W. Ebbesen, H.J. Lezect, H. Hiura, J. W. Bennett, H. F. Ghaemi and T. Thio, "Electrical

Conductivity of Individual Carbon Nanotubes", *Nature*, **382**, 54 (1996).

[246] T. Watanabe, E.-H. S. Sadki, T. Yamaguchi and Y. Takano, "Electrical Transport Properties of Small Diameter Single-Walled Carbon Nanotubes Aligned on ST-Cut Quartz Substrates", *Nanoscale Res. Lett.* **9**, 374 (2014).

[247] R. M. Ottenbrite, K. Park and T. Okano, *Biomedical Applications of Hydrogel Handbook*, Springer, New York, NY, USA, 2010.

[248] A. Hoffman, "Hydrogels for Biomedical Applications", *Adv. Drug Deliv. Rev.*, **54**, 3 (2002).

[249] M. L. Oyen, "Mechanical Characterization of Hydrogel Materials", *Int. Mat. Rev.*, **59**, 44 (2014).

[250] (a) D. L. Taylor and M. in het Panhuis, "Self-Healing Hydrogels", *Adv. Mat.*, 28, 9060 (2016); (b) J. Fu and M. in het Panhuis, "Hydrogel Properties and Applications", *J. Mat. Chem. B*, **7**, 1523 (2019).

[251] J. Kang, J. B.-H. Tok and Z. Bao, "Self-healing Soft Electronics", *Nat. Electron.*, **2**, 144 (2019).

[252] N. S. Satarkar, D. Biswal and J. Z. Hilt, "Hydrogel Nanocomposites: A Review of Applications as Remote-Controlled Biomaterials", *Soft Matter*, **6**, 2364 (2010).

[253] G. Cirillo, S. Hampel, U.G. Spizzirri, O.I. Parisi, N. Picci and F. Iemma, "Carbon Nanotubes Hybrid Hydrogels in Drug Delivery: A Perspective Review", *Biomed. Res. Int.* **2014**, 1 (2014).

[254] A. A. Adewunmi, S. Ismail and A.S. Sultan, "Carbon Nanotubes Nanocomposite Hydrogels Developed for Various Applications: A Critical Review", *J. Inorg. Organomet. Polym.*, **26**, 717 (2016).

[255] A. Vashist, A. Kaushik, A. Vashist, V. Sagar, A. Ghosal, Y. K. Gupta, S. Ahmad and M. Nair, "Advances in Carbon Nanotubes-Hydrogel Hybrids in Nanomedicine for Therapeutics", *Adv. Healthcare Mater.* **7**, 1701213 (2018).

[256] E. Lee, J. Park, S. G. Im and C. Song, "Synthesis of Single-Walled Carbon Nanotube-Incorporated Polymer Hydrogels via Click Chemistry", *Polm. Chem.*, **3**, 2451 (2012).

[257] S. Dai, X. Zhou, S. Wang, J. Ding and N. Yuan, "A self-Healing Conductive and Stretchable Aligned Carbon Nanotube/Hydrogel Composite with a Sandwich Structure", *Nanoscale*, **10**, 19360 (2018).

[258] B. Joddar, E. Garcia, A. Casas and C. M. Stewart, "Development of Functionalized Multi-Walled Carbon Nanotube-Based Alginate Hydrogels for Enabling Biomimetic Technologies", *Sci. Rep.*, **6**, 32456 (2016).

[259] S. R. Shin, S. M. Jung, M. Zalabany, K. Kim, P. Zorlutuna, S. B. Kim, M. Nikkhah, M. Khabiry, M. Azize, J. Kong, K.-T. Wan, T. Palacios, M. R. Dokmeci, H. Bae, X. Tang and A. Khademhosseini, "Carbon-Nanotube-Embedded Hydrogel Sheets for Engineering Cardiac Constructs and Bioactuators", *ACS Nano*, **7**, 2369 (2013).

[260] E. P. Gilshteyn, S. Lin, V. A. Kondrashov, D. S. Kopylova, A. P. Tsapenko, A. S. Anisimov, A. J. Hart, X. Zhao and A, G. Nasibulin, "A One-Step Method of Hydrogel Modification by

Single-Walled Carbon Nanotubes for Highly Stretchable and Transparent Electronics", *ACS Appl. Mater. Interfaces*, **10**, 28069 (2018).

[261] L. Saeednia, L. Yao, K. Cluff and R. Asmatulu, "Sustained Releasing of Methotrexate from Injectable and Thermosensitive Chitosan-Carbon Nanotube Hybrid Hydrogels Effectively Controls Tumor Cell Growth", *ACS Omega*, **4**, 4040 (2019).

[262] B. K. Ahn, D. W. Lee, J. N. Israelachvili and J. H. Waite, "Surface-Initiated Self-Healing of Polymers in Aqueous Media", *Nat. Mat.* **13**, 867 (2014).

[263] J. J. Wilker, "Self-Healing Polymer: Sticky When Wet", *Nat. Mat.* **13**, 849 (2014).

[264] L. Han, L.-W. Yan, K.-F. Wang, L.-M. Fang, H.-P. Zhang, Y.-H. Tang, Y.-H. Ding, L.-T. Weng, J.-L. Xu, J. Weng, Y.-J. Liu, F.-Z. Ren and X. Lu, "Tough, Self-Healable and Tissue-Adhesive Hydrogel with Tunable Multifunctionality", *NPG Asia Mat.*, **9**, e372 (2017).

[265] L. Han, K.-Z. Liu, M.-H. Wang, K.-F. Wang, L.-M. Fang, H.-T. Chen, J. Zhou and X. Lu, "Mussel-Inspired Adhesive and Conductive Hydrogel with Long-Last Moisture and Extreme Temperature Tolerance", *Adv. Funct. Mater.*, **28**, 1704195 (2018).

[266] R. A. L. Jones, *Soft Condensed Matter*, Oxford University Press, Oxford, UK, 2002.

[267] L. S. Hirst, *Fundamentals of Soft Matter Science*, CRC Press, Boca Raton, FL, USA, 2013.

[268] M. Krogsgaard, V. Nue and H. Birkedal, "Mussel-Inspired Materials: Self-Healing through Coordination Chemistry", *Chem. Eur. J.*, **22**, 844 (2016).

[269] (a) J.-P. Gong, Y. Katsuyama, T. Kurokawa and Y. Osada, "Double-Network Hydrogels with Extremely High Mechanical Strength", *Adv. Mat.* **15**, 1155 (2003); (b) J.-P. Gong, "Why Are Double Network Hydrogels So Tough?" *Soft Matter*, **6**, 2583 (2010); (c) M. A. Haque, T. Kurokawa and J.-P. Gong, "Super Tough Double Network Hydrogels and Their Application as Biomaterials", *Polymer*, **53**, 1805 (2012).

[270] Q. Chen, H. Chen, L. Zhu and J. Zheng, "Fundamentals of Double Network Hydrogels", *J. Mat. Chem. B* **3**, 3654 (2015).

[271] N. Bruns and A. F. M. Kilbinger, *Bio-Inspired Polymers*, The Royal Society of Chemistry, Cambridge, UK, 2017.

[272] (a) J. H. Waite and M. L. Tanzer, "Polyphenolic Substance of *Mytilus edulis*: Novel Adhesive Containing L-Dopa and Hydroxyproline", *Science*, **212**, 1038 (1981); (b) H. Lee, S. M. Dellatore, W. M. Miller and P. B. Messersmith, "Mussel-Inspired Surface Chemistry for Multifunctional Coatings", *Science*, **318**, 426 (2007); (c) W. Zhang, R.-X. Wang, Z.-M. Sun, X.-W. Zhu, Q. Zhao, T.-F. Zhang, A. Cholewinski, F. Yang, B.-X. Zhao, R. Pinnaratip, P. K. Forooshani and B. P. Lee, "Catechol-Functionalized Hydrogels: Biomimetic Design, Adhesion Mechanism, and Biomedical Applications", *Chem. Soc. Rev.*, **49**, 433 (2020).

[273] H. Lee, B. P. Lee and P. B. Messersmith, "A Reversible Wet/Dry Adhesive Inspired by Mussels and Geckos", *Nature*, **448**, 338 (2007).

[274] N. Holten-Andersen, M. J. Harrington, H. Birkedal, B. P. Lee, P. B. Messersmith, K. Y. Lee and J. H. Waite, "pH-Induced Metal-Ligand Cross-Links Inspired by Mussel Yield Self-

Healing Polymer Networks with Near-Covalent Elastic Moduli", *PNAS*, **108**, 2651 (2011).

[275](a) P. K. Forooshani and B. P. Lee, "Recent Approaches in Designing Bioadhesive Materials Inspired by Mussel Adhesive Protein", *J. Polym. Sci. Part A: Polym. Chem.* **55**, 9 (2017); (b) L. Li, W. Smitthipong and H. Zeng, "Mussel-Inspired Hydrogels for Biomedical and Environmental Applications", *Polym. Chem.*, **6**, 353 (2015).

[276]E. Filippidi, T. R. Cristiani, C. D. Eisenbach, J. H. Waite, J. N. Israelachvili, B. K. Ahn and M. T. Valentine, "Toughening Elastomers Using Mussel-Inspired Iron-Catechol Complexes", *Science*, **358**, 502 (2017).

[277]N. Holten-Andersen, T. E. Mates, M. S. Toprak, G. D. Stucky, F. W. Zok and J. H. Waite, "Metals and the Integrity of a Biological Coating: The Cuticle of Mussel", *Langmuir*, **25**, 3323 (2009).

[278]N. Holten-Andersen, A. Jaishankar, M. J. Harrington, D. E. Fullenkamp, Genevieve DiMarco, L. He, G. H. McKinley, P. B. Messersmith and K. Y. Lee, "Metal-Coordination: Using one of Nature's Tricks to Control Soft Materials Mechanics", *J. Mat. Chem. B* **2**, 2467 (2014).

[279]Z. Xu, "Mechanics of Metal-Catecholate Complexes: The Roles of Coordination State and Metal Types", *Sci. Rep.* **3**, 2914 (2013).

[280]B. P. Lee, A. Narkar and R. Wilharm, "Effect of Metal Ion Type on the Movement of Hydrogel Actuator Based on Catechol-Metal Ion Coordination Chemistry", *Sensor Actuat. B-Chem.* **227**, 248 (2016).

[281]Y.-L. Liu, K.-L. Ai and L.-H. Lu, "Polydopamine and Its Derivative Materials: Synthesis and Promising Applications in Energy, Environmental, and Biomedical Fields", *Chem. Rev.*, **114**, 5057 (2014).

[282]J. Sedó, J. Saiz-Poseu, F. Busqué and D. Ruiz-Molina, "Catechol-Based Biomimetic Functional Materials", *Adv. Mat.*, **25**, 653 (2013).

[283]E. Faurea, C. Falentin-Daudréa, C. Jérôme, J. Lyskawa, D. Fournier, P. Woisel and C. Detrembleur, "Catechols as Versatile Platforms in Polymer Chemistry", *Prog. Polym. Sci.*, **38**, 236 (2013).

[284] (a) S. K. Ghosh, *Self-Healing Materials: Fundamentals, Design Strategies, and Applications*, Wiley-VCH, Weinheim, Germany, 2009; (b) G. Wypych, *Self-Healing Materials: Principles and Technology*, ChemTec Publishing, Toronto, ON, Canada, 2017.

[285]C. E. Carraher Jr., *Introduction to Polymer Chemistry*-4th Ed., CRC Press, Boca Raton, FL, USA, 2017.

[286]D. T. N. Chen, Q. Wen, P. A. Janmey, J. C. Crocker and A. G. Yodh, "Rheology of Soft Materials", *Annu. Rev. Condens. Matt. Phys.* **1**, 301 (2010).

[287]T. G. Mezger, *The Rheology Handbook*-4th Ed., Vincentz Network, Hanover, Germany, 2014.

[288]G. K. Baker, *Test Methods for the Dynamic Mechanical Properties of Polymeric Materials*, *Bendix*, Kansas City, MO, USA, 1980.

[289]A. J. Pattison, M. McGarry, J. B. Weaver and K. D. Paulsen, "A Dynamic Mechanical Analysis Technique for Porous Media", *IEEE T. Bio-Med. Eng.*, **62**, 443 (2015).

[290](a) S. S. Bafna, "Is the Cross-Over Modulus a Reliable Measure of Polymeric Polydispersity?", *J. Appl. Polym. Sci.*, **63**, 111 (1997); (b) R. R. Rahalkar, "Correlation between the Crossover Modulus and the Molecular Weight Distribution using the Doi-Edwards Theory of Reptation and the Rouse Theory", *Rheol. Acta.*, **28**, 166 (1989).

[291]Q. Zhang, X. Zhu, C.-H. Li, Y. Cai, X. Jia and Z. Bao, "Disassociation and Reformation Under Strain in Polymer with Dynamic Metal-Ligand Coordination Cross-Linking", *Macromolecules*, **52**, 660 (2019).

[292](a) M. Rubinstein and R. H. Colby, *Polymer Physics*, Oxford University Press, New York, NY, USA, 2003; (b) R. K. Gupta, *Polymer and Composite Rheology*-2nd Ed., Marcel Dekker, Inc. New York, NY, USA, 2000.

[293]L. He and S.-C. Tjong, "High Dielectric Permittivity and Low Loss Tangent of Polystyrene Incorporated with Hydrophobic Core-Shell Copper Nanowires", *RSC Adv.*, **5**, 38452 (2015).

[294]F. Avilés, A. I. Oliva-Avilés and M. Cen-Puc, "Piezoresistivity, Strain, and Damage Self-Sensing of Polymer Composites Filled with Carbon Nanostructures", *Adv. Eng. Mater.* **20**, 1701159 (2018).

[295]M. N. Tsui and M. F. Islam, "Creep-and Fatigue-Resistant, Rapid Piezoresistive Responses of Elastomeric Graphene-Coated Carbon Nanotube Aerogels over a Wide Pressure Range", *Nanoscale*, **9**, 1128 (2017).

[296]L. Chen, G. H. Chen and L. Lu, "Piezoresistive Behavior Study on Finger-Sensing Silicone Rubber/Graphite Nanosheet Nanocomposites", *Adv. Funct. Mater.* **17**, 898 (2007).

[297]T. Wu and B. Chen, "Autonomous Self-Healing Multiwalled Carbon Nanotube Nanocomposites with Piezoresistive Effect", *RSC Adv.* **7**, 20422 (2017).

[298]S. Cravanzola, G. Haznedar, D. Scarano, A. Zecchina and F. Cesano, "Carbon-based Piezoresistive Polymer Composites: Structure and Electrical Properties", *Carbon*. 2013, **62**, 270 (2013).

[299]L. Li, W.-W. Ng and J. Sharp, *Polymer Composites for Energy Harvesting, Conversion, and Storage*, ACS Symposium Series ebooks, Washington DC, USA, 2014.

[300]L. Pan, A. Chortos, G. Yu, Y. Wang, S. Isaacson, R. Allen, Y. Shi, R. Dauskardt and Z. Bao, "An Ultra-Sensitive Resistive Pressure Sensor Based on Hollow-Sphere Microstructure Induced Elasticity in Conducting Polymer Film", *Nat. Commun.*, **5**, 3002 (2013).

[301]T. V. Sreekumar, T. Liu, B.-G. Min, H. Guo, S. Kumar, R. H. Hauge and R. E. Smalley, "Polyacrylonitrile Single-Walled Carbon Nanotube Composite Fibers", *Adv. Mat.*, **16**, 58 (2004).

[302]L. Wang and Z. Dang, "Carbon Nanotube Composites with High Dielectric Constant at Low Percolation Threshold", *Appl. Phys. Lett.*, **87**, 042903 (2005).

[303]A. Salehi-Khojin, M. R. Hosseini and N. Jalili, "Underlying Mechanics of Active Nanocomposites with Tunable Properties", *Comps. Sci. Technol.*, **69**, 545 (2009).

[304]C. Baur, J. R. DiMaio, E. McAllister, R. Hossini, E. Wagener, J. Ballato, S. Priya, A. Ballato and D. W. Smith Jr., "Enhanced Piezoelectric Performance from Carbon Fluoropolymer Nanocomposites", *J. Appl. Phys.*, **112**, 124104 (2012).

[305]A. I. Oliva-Avilés and F.Avilés, "Electrical and Piezoresistive Properties of Multi-Walled Carbon Nanotube/Polymer Composite Films Aligned by an Electric Field", *Carbon*, **49**, 2989 (2011).

[306]B. C.-K. Tee, C. Wang, R. Allen and Z. Bao, "An Electrically and Mechanically Self-Healing Composite with Pressure- and Flexion-Sensitive Properties for Electronic Skin Applications", *Nat. Nanotechnol.*, **7**, 825 (2012).

[307]T. R. Arslanov, A. A. Babaev, R. K. Arslanov, P. P. Khokhlachev, E. I. Terukov and A. K. Filippov, "High-Pressure Resistance Reversibility of Polymer Composites based on Multiwalled Carbon Nanotubes", *Appl. Phys. Lett.*, **105**, 203103 (2014).

[308]X.-W. Zhang, Y. Pan, Q. Zheng and X.-S. Yi, "Time Dependence of Piezoresistance for the Conductor-Filled Polymer Composites", *J. Polym. Sci., Part B: Polym. Phys.*, **38**, 2739 (2000).

[309]A. D. Lantada, P. Lafont, J. L. M. Sanz, J. M. Munoz-Guijosa and J. E. Otero, "Quantum Tunneling Composites: Characterisation and Modelling to Promote Their Applications as Sensors", *Sens. Actuators, A* **164**, 46 (2010).

[310]M. Wang, R. Gurunathan, K. Imasato, N. R. Geisendorfer, A. E. Jakus, J. Peng, R. N. Shah, M. Grayson and G. J. Snyder, "A Percolation Model for Piezoresistivity in Conductor-Polymer Composites", *Adv. Theory Simul.*, **2**, 1800125 (2019).

[311]J. P. Randall, M. A. B. Meador and S. C. Jana, "Tailoring Mechanical Properties of Aerogels for Aerospace Applications", *ACS Appl. Mater. Interfaces* **3**, 613 (2011).

[312]H.-J. Zhan, K.-J. Wu, Y.-L. Hu, J.-W. Liu, H. Li, X. Guo, J. Xu, Y. Yang, Z.-L. Yu, H.-L. Gao, X.-S. Luo, J.-F. Chen, Y. Ni and S.-H. Yu, "Biomimetic Carbon Tube Aerogel Enables Super-Elasticity and Thermal Insulation", *Chem* **5**, 1 (2019).

[313](a) Y. Xu, Z. Lin, X. Huang, Y. Wang, Y. Huang and X. Duan, "Functionalized Graphene Hydrogel-Based High-Performance Supercapacitors", *Adv. Mater.* **25**, 5779 (2013); (b) X.-N. Tang, C.-Z. Liu, X.-R. Chen, Y.-Q. Deng, X.-H. Chen, J.-J. Shao and Q.-H. Yang, "Graphene Aerogel Derived by Purification-Free Graphite Oxide for High Performance Supercapacitor Electrodes", *Carbon* **146**, 147 (2019).

[314]Z. Wang, H. Gao, Q. Zhang, Y. Liu, J. Chen and Z. Guo, "Recent Advances in 3D Graphene Architectures and Their Composites for Energy Storage Applications", *Small* **15**, 1803858 (2019).

[315](a) X. Zhou, F. Zhao, Y. Guo, B. Rosenberger and G. Yu, "Architecting Highly Hydratable Polymer Networks to Tune the Water State for Solar Water Purification", *Sci. Adv.* 5, 5484 (2019); (b) S. Kabiri, D. N. H. Tran, T. Altalhi and D. Losic, "Outstanding Adsorption Performance of Graphene–Carbon Nanotube Aerogels for Continuous Oil Removal", *Carbon* **80**, 523 (2014); (c) X. Mi, G. Huang, W. Xie, W. Wang, Y. Liu and J. Gao,

"Preparation of Graphene Oxide Aerogel and Its Adsorption for Cu^{2+} Ions", *Carbon* **50**, 4856 (2012); (d) J. Li, J. Li, H. Meng, S. Xie, B. Zhang, L. Li, H. Ma, J. Zhang and M. Yu, "Ultra-Light, Compressible and Fire-Resistant Graphene Aerogel as a Highly Efficient and Recyclable Absorbent for Organic Liquids", *J. Mater. Chem. A* **2**, 2934 (2014).

[316] L. Li, S. He, M. Liu, C. Zhang and W. Chen, "Three-Dimensional Mesoporous Graphene Aerogel-Supported SnO_2 Nanocrystals for High-Performance NO_2 Gas Sensing at Low Temperature", *Anal. Chem.* **87**, 1638 (2015).

[317] S. B. Riffat and G. Qiu, "A Review of State-of-the-Art Aerogel Applications in Buildings", *Int. J. Low-Carbon Tec.* **8**, 1 (2013).

[318] (a) Z.-S. Wu, S. Yang, Y. Sun, K. Parvez, X. Feng and K. Müllen, "3D Nitrogen-Doped Graphene Aerogel-Supported Fe_3O_4 Nanoparticles as Efficient Electrocatalysts for the Oxygen Reduction Reaction", *J. Am. Chem. Soc.* **134**, 9082 (2012); (b) L. Chen, B. Wei, X. Zhang and C. Li, "Bifunctional Graphene/γ-Fe_2O_3 Hybrid Aerogels with Double Nanocrystalline Networks for Enzyme Immobilization", *Small* **9**, 13, 2331 (2013).

[319] Z. He, H. Xia, X. Zhou, X. Yang, Y. Song and T. Wang, "Raman Study of Correlation between Defects and Ferromagnetism in Graphite", *J. Phys. D: Appl. Phys.* **44**, 085001 (2011).

[320] A. Milev, D. M. A. S. Dissanayake, G. S. K. Kannangara and A. R. Kumarasinghe, "Defect Induced Electronic States and Magnetism in Ball-milled Graphite", *Phys. Chem. Chem. Phys.*, **15**, 16294 (2013).

[321] (a) T. L. Makarova and F. Palacio (Eds.), *Carbon Based Magnetism-An Overview of the Magnetism of Metal Free Carbon-Based Compounds and Materials*, Elsevier, Amsterdam, Netherlands, 2006; (b) O. V. Yazyev, "Emergence of Magnetism in Graphene Materials and Nanostructures", *Rep. Prog. Phys.* **73**, 056501 (2010); (c) M. A. Akhukov, M. I. Katsnelson and A. Fasolino, "Structure and Magnetism of Disordered Carbon", *J. Phys.: Condens. Phys.*, **25**, 255301 (2013); (d) R. R. Nair, M. Sepioni, I.-L. Tsai, O. Lehtinen, J. Keinonen, A. V. Krasheninnikov, T. Thomsen, A. K. Geim and I. V. Grigorieva, "Spin-half Paramagnetism in Graphene induced by Point Defects", *Nat. Phys.* **8**, 199 (2012).

[322] (a) P. Esquinazi, A. Setzer, R. Höhne, C. Semmelhack, Y. Kopelevich, D. Spemann, T. Butz, B. Kohlstrunk and M. Lösche, "Ferromagnetism in Oriented Graphite Samples", *Phys. Rev. B* **66**, 024429 (2002); (b) A. V. Rode, E. G. Gamaly, A. G. Christy, J. G. Fitz Gerald, S. T. Hyde, R. G. Elliman, B. Luther-Davies, A. I. Veinger, J. Androulakis and J. Giapintzakis, "Unconventional Magnetism in All-carbon Nanofoam", *Phys. Rev. B* **70**, 054407 (2004); (c) D. Arěon, Z. Jagličič, A. Zorko, A. V. Rode, A. G. Christy, N. R. Madsen, E. G. Gamaly and B. Luther-Davies, "Origin of Magnetic Moments in Carbon Nanofoam", *Phys. Rev. B* **74**, 014438 (2006); (d) H. Xia, W. Li, Y. Song, X. Yang, X. Liu, M. Zhao, Y. Xia, C. Song, T.-W. Wang, D. Zhu, J. Gong and Z. Zhu, "Tunable Magnetism in Carbon-Ion-Implanted Highly Oriented Pyrolytic Graphite", *Adv. Mat.* **20**, 4679 (2008).

[323] Y. Shibayama, H. Sato and T. Enoki, "Disordered Magnetism at the Metal-Insulator Threshold in Nano-Graphite-Based Carbon Materials", *Phys. Rev. Lett.* **84**, 1744 (2000).

[324]B. L. V. Prasad, H. Sato, T. Enoki, Y. Hishiyama, Y. Kaburagi, A. M. Rao, P. C. Eklund, K. Oshida and M. Endo, "Heat-treatment effect on the nanosized graphite π-electron system during diamond to graphite conversion", *Phys. Rev. B* **62**, 11209 (2000).

[325]T. D. Nguyen, S. Liu, M. D. Lima, S. Fang, R. H. Baughman, A. Nahata and Z. V. Vardeny, "Terahertz Surface Plasmon Polaritons on Freestanding Multi-Walled Carbon Nanotube Aerogels Sheets", *Opt. Mater. Express* **2**, 782 (2012).

[326]M. H. Bergen, J. Reich, T. Ho, F. Clark, M. Reid and J. F. Holzman, "Terahertz Field Depolarization and Absorption with Composite Media", *Appl. Phys.* Lett. **115**, 041901 (2019).

[327]Z. Huang, H. Chen, Y. Huang, Z. Ge, Y. Zhou, Y. Yang, P. Xiao, J. Liang, T. Zhang, Q. Shi, G. Li and Y. Chen, "Ultra-Broadband Wild-Angle Terahertz Absorption Properties of 3D Graphene Foam", *Adv. Mat.* **28**, 1704363 (2018).

[328]Y. Xie, M. Han, R. Wang, H. Zobeiri, X. Ding, P. Zhang and X. Wang, "Graphene Aerogel Based Bolometer for Ultrasensitive Sensing from Ultraviolet to Far-Infrared", *ACS Nano* **13**, 5385 (2019).

[329](a) I. O. Dorofeev, V. I. Suslyaev, S. I. Moseenkov, V. L. Kuznetsov and K. V. Dorozhkin, "Interaction of Multiwalled Carbon Nanotube Aerogels with Quasi-Optical Terahertz Beams", *Phys. Status Solidi B* 1900251 (2019); (b) A. V. Badin, G. E. Kuleshov, K. V. Dorozhkin, G. E. Dunaevskii, V. I. Suslyaev and V. A. Zhuravlev "Anisotropy of Electrical Properties of 3D-Printing MWCNT Composites at the THz Frequency Range", *43rd International Conference on Infrared, Millimeter, and Terahertz Waves ("IRMMW-THz 2018")*, Nagoya, Japan (2018); (c) A.V. Badin, I. O. Dorofeev, G. E. Dunaevskii, V. I. Suslyaev, D. S. Bodazhkov, K. V. Simonova, S. I. Moseenkov and V. L. Kuznetsov, "Scattering of THz Radiation by Spherical MWCNTs Aerogel in State of Acoustic Levitation", *44th International Conference on Infrared, Millimeter, and Terahertz Waves ("IRMMW-THz 2019")*, Paris, France (2019).

[330]J. Lyu, Z. Liu, X. Wu, G. Li, D. Fang and X. Zhang, "Nanofibrous Kevlar Aerogel Films and Their Phase-Change Composites for Highly Efficient Infrared Stealth", *ACS Nano* **13**, 2236 (2019).

Appendices

Appendix 1: List of Publications

Refereed Journal Articles

1. Aerographite Phonon Density of States Affects Double Resonant Raman Scattering, **H. Zhang**, J. Horvat, R. A. Lewis, R. Adelung, B. Fiedler and Y. K. Mishra, *J. Phys. Chem. A*, under review.
2. Temperature Dependent Raman Scattering Spectral Spectra of Aerographite and Single-Walled Carbon Nanotube Aerogel, **H. Zhang**, J. Horvat, R. A. Lewis, R. Adelung, B. Fiedler, Y. K. Mishra, M. F. Islam and A. G. Yodh, *J. Phys. Chem. A*, under review.
3. Synchrotron-based Temperature Dependent Terahertz and Far-Infrared Spectra of Aerographite and Single-Walled Carbon Nanotube Aerogel, **H. Zhang**, J. Horvat, R. A. Lewis, R. Adelung, B. Fiedler, Y. K. Mishra, M. F. Islam and A. G. Yodh, *J. Phys. Chem. A*, under review.
4. Temperature Dependent Electrical Transport Properties of Aerographite and Single-Walled Carbon Nanotube Aerogel, **H. Zhang**, J. Tian, M. H. Mohammed, J. Horvat, R. A. Lewis, R. Adelung, B. Fiedler, Y. K. Mishra, M. F. Islam and A. G. Yodh, *Phys. Rev. B*, in preparation.
5. Piezoresistive and Electrical Resistance Dependent Properties of poly L-DOPA-Polyacrylamide Single-Walled Carbon Nanotube Hydrogel Hybrid Network, **H. Zhang**, Q. Yan, J. Horvat, R. A. Lewis, M. F. Islam and A. G. Yodh, *ACS Appl. Polym. Mater.*, under review.

Refereed Conference Paper

6. **H. Zhang**, J. Horvat and R. A. Lewis, "Terahertz Spectroscopic Characterization for Carbon-based Materials," *IEEE Proceedings of the 41st International Conference on Infrared, Millimeter, and Terahertz Waves* ("*IRMMW-THz 2016*"), Copenhagen, Denmark, September 26th - 30th, 2016.
7. **H. Zhang**, J. Horvat and R. A. Lewis, "Low-Frequency Terahertz Raman Spectra of Graphite Flakes and Single-Walled Carbon Nanotube Aerogel," *IEEE Proceedings of the 45th International Conference on Infrared, Millimeter, and Terahertz Waves* ("*IRMMW-THz 2020*"), Buffalo, NY, USA, November 8th - 13th, 2020.

Conference Posters

8. **H. Zhang**, J. Horvat and R. A. Lewis, "Terahertz Spectroscopic Characterizations for Graphite Nanofibers and Graphite," *The 40th Annual Condensed Matter and Materials Meeting* ("*Wagga 2016*"), Wagga Wagga, New South Wales, Australia, February 2nd - 5th, 2016.
9. **H. Zhang**, J. Horvat and R. A. Lewis, "Terahertz Spectroscopic Characterizations for

Carbon-based Materials," *The 41st Annual Condensed Matter and Materials Meeting* ("*Wagga 2017*"), Wagga Wagga, New South Wales, Australia, January 31st - February 3rd, 2017.

10. J. Archer, **H. Zhang**, J. Horvat and R. A. Lewis, "Reflectance of Materials as a Function of Angle of Incidence," *The 43th Annual Condensed Matter and Materials Meeting* ("*Wagga 2019*"), Wagga Wagga, New South Wales, Australia, February 5th - 8th, 2019.

Grants

Australian Synchrotron Research Program (AS181/THz/Far/IR/13120): Terahertz and Far-Infrared Spectroscopic Characterizations for Aerographite and Related sp^2 Carbon-based Materials, AU$ 98,352.

Appendix 2: MATLAB Code for FTIC and VRH Fittings

I. FITC Model:

```
A=zeros(360,1);
B=zeros(360,1);
C=zeros(360,1);
A=S(:,1);
B=S(:,2);
plot(A,B,'ko--');
hold on
f=@(a,x)exp(a(1)./(x+a(2))+a(3));
c=nlinfit(A,B,f,[1 1 1]);
plot(A,exp(c(1)./(A+c(2))+c(3)),'rv--');
C(:)=exp(c(1)./(A(:)+c(2))+c(3));
format long
c(:)
```

II. VRH Model:

```
A=zeros(360,1);
B=zeros(360,1);
C=zeros(360,1);
A=S(:,1);
B=S(:,2);
plot(A,B,'ko--');
hold on
%f=@(a,x)exp((a(1)./x).^a(2)+a(3));
f=inline('exp(a(1)*(x^a(2))+a(3))','b','x');
c=nlinfit(A,B,f,[1 1 1]);
plot(A,exp((c(1)./A).^c(2)+c(3)),'rv--');
C(:)=exp((c(1)./ A(:)).^c(2)+c(3));
format long
c(:)
```